

**INVESTIGATION OF NEW BIODEGRADABLE MAGNESIUM ALLOY
WITH IMPROVED BIOCORROSION, BIOCOMPATIBILITY AND
MECHANICAL PROPERTIES FOR USE IN TEMPORARY
CARDIOVASCULAR STENTS**

By

Mandana Bornapour

A Thesis Submitted to the Faculty of Graduate Studies and Research in Partial
Fulfillment of the Requirements for the Degree of Doctor of Philosophy



Department of Mining and Materials Engineering

McGill University

Montreal, Canada

December 2014

© Mandana Bornapour

ABSTRACT

Biodegradable Magnesium (Mg) alloys have received increasing interest for biomedical applications over the past few years. Current metallic cardiovascular implants cause restenosis, endothelial dysfunction and chronic inflammatory reactions, which necessitate subsequent interventions. Mg is an interesting candidate that biodegrades via corrosion reaction in the body and disappears once its role has ended. The major drawback of Mg as a temporary biomaterial is its fast degradation rate, which leads to a release of a high volume of hydrogen gas and early loss of mechanical integrity. Alloying is an effective technique to tailor the corrosion rate of Mg.

This research focused on developing a new biodegradable Mg alloy with a controlled degradation rate, optimum mechanical properties and biocompatibility. This was done by studying the corrosion behavior, microstructure and biological performance of Mg-Sr and Mg-Ca-Sr alloys and by detecting the role of Sr as an alloying element in the biocorrosion mechanism of Mg. Experimental techniques such as optical microscopy (OM), scanning electron microscopy (SEM), energy dispersive spectroscopy (EDS), electron probe micro-analysis (EPMA), transmission electron microscopy (TEM), X-ray diffraction (XRD), and X-ray photoelectron spectroscopy (XPS) were used for microstructural and surface characterization. In vitro and in vivo biocompatibility was studied via cytocompatibility assays and animal trials.

In the first part of the research, the bio-corrosion of as-cast Mg-Sr alloys ($0.3 < \text{Sr} < 2.5\%$) was evaluated via an in vitro corrosion test in simulated body fluid (SBF). The Mg-0.5Sr alloy showed the slowest corrosion rate (2 mg/day/cm^2) in this range of composition. Microstructural and surface characterization showed the possibility of the formation of a Sr-substituted hydroxyapatite (Sr-HA) scale, which was present as a thin layer at the interface between the Mg-0.5Sr alloy and the corrosion products on the surface. Indirect cytotoxicity assays using human umbilical vascular endothelial cells (HUVECs) indicated that Mg-0.5Sr did not cause any inhibitory effect on the viability of the cells. Animal implantation did not show any thrombosis after 3 weeks of implantation of Mg-0.5Sr stent into the femoral artery.

The second part of the research focused on the effect of the combined addition of Sr with Ca. In vitro corrosion tests in SBF showed that 0.3 wt.% Sr and 0.3 wt.% Ca in combination decreased the corrosion rate of Mg more effectively than the single addition of either alloying

element. The improved mechanical and corrosion resistance of Mg-0.3Sr-0.3Ca over the binary alloys was related (i) to the presence of a new intermetallic phase in the as-solidified microstructure, and (ii) to the third element effect where increased corrosion is obtained at lower solute levels in ternary alloys compared to binary alloys. The Mg-0.3Sr-0.3Ca alloy also showed better thermal stability than the binary alloy.

In the final part of the study, static and dynamic immersion tests were used to evaluate the effect of pH change on the degradation of Mg-0.3Sr-0.3Ca. Surface analysis showed the formation of the Sr-HA layer as a thin layer at the interface between the Mg-0.3Sr-0.3Ca alloy and the corrosion products. This layer slowed down the degradation rate of Mg-0.3Sr-0.3Ca alloy over time. Indirect cytotoxicity assays using HUVECs showed that Mg-0.3Sr-0.3Ca improves the viability of the cells after one week. The *in vivo* biocompatibility of Mg-0.3Sr-0.3Ca was evaluated during 5 weeks implantation into the femoral artery of an animal. Histological analysis showed no thrombosis caused by the Mg-0.3Sr-0.3Ca stent. Microstructural analysis on the material-tissue interface confirmed the surface-active effect of Sr that leads to the formation of Sr-HA on the surface of this stent, which is a key advantage in the use of Sr-containing Mg alloys as materials for biodegradable implants.

RÉSUMÉ

Les alliages de magnésium (Mg) biodégradables ont suscité un intérêt grandissant pour les applications biomédicales au cours des années passées. Les implants métalliques actuels causent le rétrécissement des artères, le recouvrement interne des artères et des réactions inflammatoires. Mg est ainsi un candidat potentiel intéressant qui se biodégrade via une réaction de corrosion dans le corps et par la même occasion s'élimine quand son rôle est terminé. L'inconvénient majeur du magnésium comme biomatériau est son taux de dégradation rapide qui conduit à la libération d'un volume élevé d'hydrogène et à une perte rapide d'intégrité mécanique. L'alliage est alors une technique qui permet de maîtriser le taux de corrosion du Mg.

Ce travail de recherche est orienté vers le développement d'un nouvel alliage de Mg biodégradable avec un taux de dégradation contrôlé, des propriétés mécaniques optimales et une biocompatibilité. Ce projet a été réalisé par l'étude du comportement à la corrosion, la microstructure et la performance biologique des alliages de Mg-Sr et Mg-Ca-Sr, ainsi que l'analyse du rôle du Sr comme élément d'alliage dans le mécanisme de biocorrosion du Mg. Les techniques expérimentales utilisées ont été les suivantes : la microscopie optique, la microscopie électronique à balayage, la spectroscopie par énergie dispersive des rayons-X, l'analyse par micro sonde électronique, la microscopie électronique à transmission, la diffraction des rayons-x et la spectroscopie par l'émission des photoélectrons émis par les rayons-X pour l'étude de la caractérisation de la microstructure et de la surface. La biocompatibilité in-vitro et in-vivo a été étudiée via la viabilité des cellules et par des essais sur des animaux.

Dans la première partie de ce travail de recherche la bio-corrosion des alliages de Mg-Sr tels que coulés contenant de 0.3 à 2.5 de Sr a été étudiée par la réalisation des essais de corrosion in-vitro en utilisant du plasma synthétique. L'alliage Mg-0.5Sr a démontré le plus faible taux de corrosion (2mg/jour/cm^2) dans cette gamme de composition. L'analyse de la microstructure et de la surface a démontré la formation d'un substrat composé d'oxyde de Sr-hydroxyapatite (Sr-HA) qui était présent sous la forme d'une couche mince formée à l'interface de l'alliage Mg-0.5Sr et les produits de corrosion sur la surface. Des essais indirects de cytotoxicité en utilisant des cellules d'un vaisseau d'endothélium ombilical humain (HUVECs) ont montré que l'alliage Mg-0.5Sr n'a pas causé de toxicité et aucun effet d'inhibition n'a été observé sur la viabilité des

cellules. L'implantation sur un animal n'a pas montré non plus d'effet de thrombose dans l'endoprothèse composée de l'alliage Mg-0.5Sr après 3 semaines.

La seconde partie de cette recherche a été orientée sur l'effet de la combinaison du Sr avec le Ca. Des essais de corrosion in-vitro en utilisant du plasma synthétique ont montré que l'alliage de Mg avec 0.3Sr et 0.3Ca a permis de diminuer la corrosion du Mg de façon plus significative que l'addition simple de chacun des éléments. L'augmentation de la résistance mécanique et de la corrosion de l'alliage Mg-0.3Sr-0.3Ca comparée aux alliages binaires sont par conséquent reliées à (i) la présence d'un nouveau composé intermétallique dans la microstructure tel que solidifiée et (ii) l'effet du troisième élément étant l'augmentation du taux de corrosion qui a été obtenu en fonction des niveaux de soluté plus bas dans les alliages ternaires en comparaison avec les alliages binaires. L'alliage Mg-0.3Sr-0.3Ca a aussi démontré une meilleure stabilité thermique que l'alliage binaire.

Dans la partie finale de cette étude, des essais par immersion statique et dynamique ont été réalisés afin d'évaluer l'effet de changement du pH sur le taux de dégradation de l'alliage Mg-0.3Sr-0.3Ca. Une analyse systématique de la surface a permis de constater la formation d'un substrat Sr-HA sous la forme d'une mince couche à l'interface entre l'alliage Mg-0.3Sr-0.3Ca et les produits de corrosion. Cette couche stabilise la surface de l'alliage Mg-0.3Sr-0.3Ca et ralentie son taux de dégradation en fonction du temps. Des essais indirects de cytotoxicité avec des cellules d'un vaisseau de HUVEC ont démontré que le milieu d'extraction de l'alliage de Mg-0.3Sr-0.3Ca améliore la viabilité des cellules après une semaine. La biocompatibilité de l'alliage Mg-0.3Sr-0.3Ca a été évaluée pour une durée de 5 semaines dans l'artère fémoral d'un animal. L'analyse histologique n'a pas révélé de thrombose causée par la présence de l'endoprothèse fabriquée avec l'alliage Mg-0.3Sr-0.3Ca. L'analyse microstructurale de l'interface tissu-matériau a confirmé l'effet d'activation de la surface du Sr qui a conduit à la formation d'un substrat Sr-HA sur la surface de l'endoprothèse ce qui par conséquent constitue un avantage de premier plan pour l'utilisation des alliages de Mg contenant du Sr pour la fabrication des implants biodégradables.

ACKNOWLEDGEMENTS

First, I would like to express my sincere gratitude to Prof. Mihriban Pegguleryuz for giving me the opportunity to work under her supervision and overseeing my PhD degree at McGill University. I was impressed not only by her solid knowledge of material engineering, but also by her personality and dedication to her students. Throughout this journey, her helpful nature and positive attitude always motivated me to carry out my research successfully.

I would like to sincerely thank Prof. Marta Cerruti for her supervision, especially in the field of surface characterization. I am also grateful for her prompt responses, good advice and support. I would like to thank Dr. Dominique Shum-Tim, who provided a great deal of assistance in the animal study part of this work. He kindly provided me with great discussions and guided me with valuable advice in his area of expertise during our meetings. I am grateful to Prof. Sasha Omanovic as well as Prof. Hojatollah Vali for their invaluable discussions and support. I would like to thank Dr. Majid Hoseini for his assistance at the first stage of this project and for providing me with access to mechanical testing facilities. Thanks also extended to Dr. Naser Muja for his guidance and useful discussion regarding cell culture experiments.

Special thanks are directed to Pierre Vermette for his very generous assistance in the casting and all other experimental work throughout this project. I thank all the present and past members of Prof. Pegguleryuz and Prof. Cerruti's research group for their help and support. My appreciation also extends to my friends in the department, especially Neslihan Alpay, Shirin Kaboli, Bamidele Akinrinlola, Deniz Aydin, Amir Nazari, Jinke Xu and Kaiwen Hu. Special thanks to Line Mongeon, Monique Riendeau, Courtney Jelaco, Terry Zatylny and Barbara Hanley.

Last, but not least, I would like to express my sincere appreciation to my husband, friend and colleague, Hesam, for his constant support and encouragement. He has always motivated me to strive for something better in life. My deepest gratitude goes to my parents and my brother. If it were not for them, I would not be standing here today. I am forever grateful and indebted to them for all that they have done for me throughout my life. Their unconditional love, heartfelt support and encouragement has accompanied me throughout this venture.

THESIS STRUCTURE AND CONTRIBUTIONS OF AUTHORS

This thesis was prepared according to the guidelines of a manuscript-based thesis published by Graduate and Postdoctoral Studies office of McGill University. This thesis is comprised of eight chapters. Chapter 1 places the work in context, presents the objectives and describes the thesis structure. Chapter 2 presents the literature review that focuses on the biodegradation behavior of magnesium, recent studies conducted to control its degradation rate via alloying and the biocompatibility evaluation of Mg alloys. Chapter 3 details the experimental procedures that are not fully described in the manuscripts and focuses on error analysis. The next three chapters (Ch. 4-6) contain four manuscripts that reports the results of the PhD research. All the manuscripts have been published, accepted or submitted for publication as indicated.

Chapter 4 investigates the effect of Sr on degradation rate and biological performance of Mg. It involves in vitro corrosion tests, microstructural analysis and biocompatibility evaluations. It has been published as a journal article (Publication 1)

(1) M. Bornapour, N. Muja, D. Shum-Tim, M. Cerruti, M. Pekguleryuz, "Biocompatibility and biodegradability of Mg-Sr alloys: the formation of Sr-substituted hydroxyapatite," *Acta Bio Mater.*, v. 9, n. 2, 2013, pp. 5319-5330.

Chapter 5 examines the combined addition of Sr and Ca and elucidates the role of the third element effect and the phases on the biodegradation, microstructure and mechanical properties of Mg-Sr-Ca. The effect of thermal exposure is also discussed to determine the optimum manufacturing condition. Chapter 5 has been published as two journal articles, appearing as sections 5.1 and 5.2 (publication 2 and Publication 3)

(2) M. Bornapour, M. Celikin, M. Cerruti, M. Pekguleryuz, "Magnesium implant alloy with low levels of strontium and calcium: the third element effect and phase selection improve bio-corrosion resistance and mechanical performance," *Mat. Sci. Eng. C*, v. 35, n. 1, 2014, pp. 267-282.

(3) M. Bornapour, M. Celikin, M. Pekguleryuz, "Thermal exposure effects on the in-vitro degradation and mechanical properties of Mg-Sr and Mg-Ca-Sr biodegradable implant alloys and the role of the microstructure," *Mat. Sci. Eng. C*, v. 46, n. 1, 2015, pp. 16-24.

In Chapter 6, the effect of Sr addition on the chemistry and the morphology of corrosion products is investigated via *in vitro* and *in vivo* tests. This chapter also reports the interaction between Mg-Sr-Ca and surrounding tissue and evaluates the biocompatibility of this alloy as a candidate alloy for cardiovascular stent. The results have been submitted as a journal article (Publication 4)

(4) M. Bornapour, H. Mahjoubi, H. Vali, D. Shum-Tim, M. Cerruti, M. Pektuleryuz, "Biodegradable Mg-0.3Sr-0.3Ca alloy as temporary cardiovascular stent: Surface characterization, *in vitro* and *in vivo* biocompatibility evaluation, " submitted to *Biomaterials*, 2014.

Chapter 7 draws the major conclusions from this research and gives suggestions for future work. Chapter 8 summarizes the contribution of this PhD thesis to original knowledge.

All the manuscripts are co-authored by Prof. Mihriban Pektuleryuz, the research main supervisor. She guided me throughout the project and reviewed all the manuscripts. Manuscripts 1, 2 and 4 are co-authored by Prof. Marta Cerruti, the research co-supervisor. She reviewed mentioned manuscripts and gave useful inputs in surface characterization sections. All the experimental works were planned and performed by the candidate. Manuscripts 1 and 4 include Dr. Dominique Shum-Tim (cardiothoracic surgeon at Royal Victoria Hospital) for performing animal surgery. Manuscript 1 includes Dr. Naser Muja as co-author. I learned the procedure of cell culture from him and he gave me useful information regarding HUVEC cell line. Manuscripts 2 and 3 include Dr. Mert Celikin for his help in TEM studies and analysis of diffraction patterns. Manuscript 4 includes Hesameddin Mahjoubi for his collaboration in cytotoxicity evaluations. Manuscript 4 also includes Dr. Hojatollah Vali for his guidance in microscopic and histological evaluation. All the work presented in this thesis, apart from the co-author contributions mentioned above, was performed by me.

TABLE OF CONTENTS

ABSTRACT.....	i
RÉSUMÉ	iii
ACKNOWLEDGEMENTS.....	v
THESIS STRUCTURE AND CONTRIBUTIONS OF AUTHORS.....	vi
TABLE OF CONTENTS.....	xiii
LIST OF FIGURES	xii
LIST OF TABLES.....	xix
GLOSSARY OF BIOLOGICAL TERMS	xxi
CHAPTER 1: INTRODUCTION.....	1
CHAPTER 2: LITERATURE REVIEW	10
2. 1. An overview of Biodegradable stents.....	10
2. 1. 1. Cardiovascular implants.....	11
2. 1. 2. Biodegradable cardiovascular implants	14
2. 2. Mg As A Biomaterial.....	16
2. 2. 1. Biological performance of Mg.....	18
2. 2. 2. Biochemistry of Mg.....	20
2. 2. 3. Mg as biodegradable orthopedic implant.....	21
2. 2. 4. Early stages of Mg biodegradable stents	21
2. 3. Current Research Activities on the Development of Biodegradable Mg Stents.....	25
2. 3. 1. Corrosion mechanisms of Mg and its alloys.....	25
2. 3. 2. Alloying approach to control the degradation rate of Mg and preclinical studies....	30
2. 4. Testing methods used in the evaluation of biodegradable Mg biomaterials.....	37
2. 4. 1 In vitro testing and characterization.....	37
2. 4. 2. Biocompaibility evaluation, in vivo testing and post-implant histological studies .	39
2. 5. References.....	41

CHAPTER 3: EXPERIMENTAL PROCEDURE.....	50
3. 1. Alloy synthesis and casting.....	50
3. 2. Immersion test.....	51
3. 3. Electrochemical test.....	55
3. 4. Optical microscopy.....	55
3. 5. Scanning electron microscopy (SEM).....	56
3. 6. Transmission electron microscopy (TEM).....	56
3. 7. X-ray diffraction.....	57
3. 8. X-ray photoelectron spectroscopy (XPS).....	57
3. 9. Mechanical testing.....	58
3. 10. Cytocompatibility assay.....	59
3. 11. Animal study and histological evaluation.....	60
CHAPTER 4: BIODEGRADATION BEHAVIOR AND BIOCOMPATIBILITY OF Mg-Sr ALLOYS AS TEMPORARY BIOMATERIALS.....	62
4. 0. Biocompatibility and biodegradability of Mg-Sr alloys: the formation of Sr-substituted hydroxyapatite.....	63
4. 1. ABSTRACT.....	63
4. 2. INTRODUCTION.....	64
4. 3. EXPERIMENTAL PROCEDURE.....	66
4. 3. 1. Alloy Synthesis and Plate Casting.....	66
4. 3. 2. Immersion Experiments.....	66
4. 3. 3. Electro-Polarization Test.....	67
4. 3. 4. Microstructure and Surface Analysis.....	67
4. 3. 5. Cytotoxicity Evaluation.....	68
4. 3. 6. Animal Implantation.....	69
4. 4. RESULTS AND DISCUSSION.....	70
4. 4. 1. Degradation Behavior in SBF.....	70
4. 4. 2. Cytotoxicity Evaluation.....	82
4. 4. 3. Implantation and Post-Implantation Analysis.....	83
4. 5. CONCLUSIONS.....	86

4. 6. REFERENCES	86
CHAPTER 5: COMBINED ADDITION OF Sr AND Ca ON BIOCORROSION, MICROSTRUCTURE AND MECHANICAL PROPERTIES OF Mg	93
5.1. Magnesium implant alloy with low levels of strontium and calcium: the third element effect and phase selection improve bio-corrosion resistance and mechanical performance.....	95
5. 1. 1. ABSTRACT.....	95
5. 1. 2. INTRODUCTION	96
5. 1. 3. EXPERIMENTAL PROCEDURE	98
5. 1. 3. 1. Alloy synthesis and sample preparation	98
5. 1. 3. 2. Immersion test.....	99
5. 1. 3. 3. Electrochemical measurements.....	99
5. 1. 3. 4. Microstructural and surface characterization.....	100
5. 1. 3. 5. Mechanical properties.....	101
5. 1. 4. RESULTS AND DISCUSSION	101
5. 1. 4. 1. As-cast microstructure and phase analysis	101
5. 1. 4. 2. Corrosion tests in SBF	110
5. 1. 4. 3. Mechanical Properties.....	120
5. 1. 5. CONCLUSIONS	124
5. 1. 6. REFERENCES	125
5.2. Thermal exposure effects on the in-vitro degradation and mechanical properties of Mg-Sr and Mg-Ca-Sr biodegradable implant alloys and the role of the microstructure.....	133
5. 2. 1. ABSTRACT.....	133
5. 2. 2. INTRODUCTION	134
5. 2. 3. EXPERIMENTAL PROCEDURE	135
5. 2. 3. 1. Alloy synthesis and sample preparation	135
5. 2. 3. 2. Immersion test.....	136
5. 2. 3. 3. Electrochemical measurements.....	136
5. 2. 3. 4. Microstructural and surface characterization.....	137
5. 2. 3. 5. Mechanical properties.....	137
5. 2. 4. RESULTS AND DISCUSSION	138

5. 2. 4. 1. Corrosion tests in SBF	138
5. 2. 4. 2. Microstructure and phase analysis	142
5. 2. 4. 3. Mechanical properties	147
5. 2. 5. CONCLUSIONS	152
5. 2. 6. REFERENCES	153
CHAPTER 6: DEGRADATION MECHANISM AND BIOCOMPATIBILITY OF Mg-0.3Sr-0.3Ca AS A TEMPORARY CARDIOVASCULAR STENT	157
6. 0. Biodegradable Mg-0.3Sr-0.3Ca alloy as temporary cardiovascular stent: Surface characterization, in vitro and in vivo biocompatibility evaluation	158
6. 1. ABSTRACT	158
6. 2. INTRODUCTION	159
6. 3. EXPERIMENTAL PROCEDURE	161
6. 3. 1. Materials	161
6. 3. 2. Immersion Test	162
6. 3. 3. Surface Analysis	163
6. 3. 4. Cytotoxicity Evaluation	163
6. 3. 5. Animal Implantation	164
6. 4. RESULTS AND DISCUSSION	166
6. 4. 1. Degradation behavior, role of immersion time and pH	166
6. 4. 2. Analysis of the surface layer	169
6. 4. 3. Cytotoxicity evaluation	172
6. 4. 4. Implantation and post-implantation analysis	175
6. 5. BIOCORROSION MECHANISM	180
6. 6. CONCLUSIONS	183
6. 7. REFERENCES	184
CHAPTER 7: CONCLUSIONS AND RECOMMENDATIONS FOR FUTURE WORK	190
7. 1. CONCLUSIONS	190
7. 2. RECOMMENDATIONS FOR FUTURE WORK	194
CHAPTER 8: CONTRIBUTION TO ORIGINAL KNOWLEDGE	196

LIST OF FIGURES

Fig. 1. 1. An illustration of a coronary stent implantation: (a) the catheter delivers the stent to the site of blockage, (b) balloon inflation deploys the stent to push the plaque and open the narrowed artery, (c) the catheter is removed and the stent remains to support the artery and restore the blood flow [25].	3
Fig. 2. 1. Illustration of coronary stent implantation: (a) delivery to the blocked artery by a catheter, (b) expansion to push and open the narrowed artery, (c) the catheter leaves and the stent remains to support the artery and restore the blood flow [12]	12
Fig. 2. 2. Illustration of an ideal compromise between mechanical integrity and degradation of a biodegradable stent [13].	13
Fig. 2. 3. Biodegradable iron stents: (a) NOR-I stent expanded to 3.5 mm diameter [26] and (b) X-ray photograph of iron stent (Biotronik, Erlangen, Germany) after implantation in porcine coronary artery [27]	14
Fig. 2. 4. Extent of degradation in implanted wires. Clean iron wire before implantation (A) and wires retrieved from the arterial wall after 1.5 (B) and 3 (C) months. Iron wires retrieved from the artery lumen after 9 months at central (D) or wall locations (E). Clean magnesium wire before implantation (F), magnesium wires implanted in the arterial wall after 3 weeks (G and H), where (G) shows the in situ image of implanted magnesium with localized pits on the surface (yellow arrow in G) and subsequent fragmentation after 3 weeks (green arrows in H), and magnesium wires implanted in artery lumen in contact with blood after 3 weeks (I).	16
Fig. 2. 5. Mg ion in an octahedral coordination with six water molecules [41]	20
Fig. 2. 6. Schematic images of a typical (a) hip joint, (b) shoulder and (c) knee implant replacement after surgery as some examples of hard tissue application [2].	21
Fig. 2. 7. Mg (left) vs stainless steel (right) stent at 30 days of implantation [17]	23
Fig. 2. 8. Schematic presentation of recoil and negative luminal remodeling after 4 months of implantation with PROGRESS AMS-1 trial Biotronik-Germany [45]	24
Fig. 2. 9. Lekton Magic coronary stent made from WE43: (a) before and (b) after expansion [26]	24

Fig. 2. 10. Illustration of an (a) external galvanic corrosion and (b) internal galvanic corrosion in Mg alloys.	25
Fig. 2. 11. Electromotive force series [53]	26
Fig. 2. 12. Microstructure of AZ91D [53]	26
Fig. 2. 13. Pourbaix diagram of Mg ± H ₂ O system at 25°C. The region of water stability lies between the lines marked (a) and (b). The different regions are separated by the following reactions: (1) Mg + 2 H ₂ O → Mg(OH) ₂ + H ₂ ; (2) Mg ²⁺ + H ₂ O → MgO + 2H ⁺ ; (3) Mg → Mg ²⁺ + 2 e [±] [53].....	28
Fig. 2. 14. Appearance of (a) Mg, (b) AZ31, (c) Mg with 0.3 mass%-La and (d) Mg with 0.6 mass%-La after 50 h immersion in salt water [63].....	31
Fig. 2. 15. (a) Immunofluorescence images from the morphology of HUVECs in the control medium and extraction medium from JDBM, WE43 and AZ31 (from left to right) for 24 h. The cells were fixed and stained for cytoskeleton (phalloidin: green) and nuclei (DRAQ5: magenta). (b) Live cell observation of HUVECs direct attachment and elongation on JDBM, WE43 and AZ31 metallic substrates (from left to right) after 24 h.....	32
Fig. 2. 16. Schematic curves obtain from Tafel extrapolation method [91]	38
Fig. 3. 1. Casting procedure: (a) melting in graphite crucible with induction furnace, (b) pouring the melt into the preheated die, (c) thin plate cast sample, (d) drill used to obtain the chips.	50
Fig. 3. 2. Experimental set-up for in vitro immersion test in SBF (a) and the close-up from the sample hung into the solution (b).....	54
Fig. 3. 3. Side view (a) and top view (b) of the experimental set-up used for three-electrode cell electrochemical test in SBF.	55
Fig. 3. 4. Tensile (a), compression (b) and bending (c) samples tested at room temperature.	58
Fig. 3. 5. Indirect cytotoxicity assay: (a) extracting ions from Mg samples and (b) cell seeding onto 96-well cell culture plates.	60
Fig. 3. 6. Post-implantation analysis on retrieved Mg stent samples: (a) cut and dehydrated for microscopic observation, (b) embedded and sectioned for histology and (c) stained using H&E.	61
Fig. 4. 1 . The average corrosion rate (mg/day/cm ²) in terms of mass loss and hydrogen evolution for Mg-Sr samples with various Sr content after immersion in SBF at 37°C.	71

Fig. 4. 2. (a) The average corrosion rate of Mg-0.5Sr in terms of mass loss (M) and hydrogen evolution (H ₂) after immersion in SBF for different times. (b) The relationship between mass loss (M) and hydrogen evolution (H ₂) in SBF immersion fitted as $H_2 \approx -1.3 M^2 + 3.8 M$	73
Fig. 4. 3. Change in pH of SBF during the immersion of the Mg-0.5Sr alloy as a function of immersion time.	73
Fig. 4. 4. Polarization curves of as-cast pure Mg (CP Mg) and Mg-0.5Sr in Hank's solution.....	74
Fig. 4. 5. The surface appearance of as-cast Mg-0.5Sr removed from SBF after (a) 1 day, (b) 2 days (c) 3 days, and (d) pure Mg after 1 day of immersion at 37°C. A significant amount of the surface of pure Mg exhibits extensive corrosion even after one day of immersion.	75
Fig. 4. 6. Optical micrograph from cross-section of as cast Mg-0.5Sr after immersion in SBF for (a) 1 day, (b) 2 days, and (c) 3 days showing the depth corrosion on the sample surface....	75
Fig. 4. 7. (a) Secondary electron images from the cross-section of Mg-0.5Sr after immersion in SBF for 1 day and, (b) EDS spectroscopy from the grain boundary region marked with an arrow.	76
Fig. 4. 8. Secondary electron images from the cross-section of Mg-0.5Sr after immersion in SBF for (a) 1 day, and (b) 3 days showing the white surface scale on the sample.....	77
Fig. 4. 9. Secondary electron image and EDS analysis from the surface of (a & b) Mg-0.5Sr and (c & d) pure Mg after immersion in SBF. Thin layer of containing Ca, P, Mg and O formed on the surface.	78
Fig. 4. 10. X-ray diffraction patterns correspond to corrosion products formed on the surface of Mg-0.5Sr after 3 days immersion in SBF. Hydroxyapatite was detected in the 2theta range 15-35°	79
Fig. 4. 11. Secondary electron image from the surface of (a) Mg-0.5Sr and (b) pure Mg after removing the corrosion products.	80
Fig. 4. 12. High resolution XPS spectra of Ca _{2p} , P _{2p} and Sr _{3p} on the surface of Mg-0.5Sr after 1 day immersion test and removing the corrosion products.	81
Fig. 4. 13. Cell viability expressed as a percentage of the viability of cells in the control (F-12K) after 1, 4 and 7 days of exposure to the extraction of Mg-0.5Sr and WE43 alloys.....	83
Fig. 4. 14. The Tubular Mg-0.5Sr stent (a) before and (b) after 3 weeks implantation into the right femoral artery of the animal.	84

Fig. 4. 15. SEM images from the longitudinal cross section of (a) Mg-0.5Sr and (b) WE43 implanted in the right and left femoral artery of a dog respectively. Both samples were retrieved 3 weeks after operation. The wall thicknesses of retrieved Mg stents were marked with arrow. The initial wall thickness of the stents was 0.27 mm.	84
Fig. 5. 1. Optical micrograph from cross-sections of as-cast (a) Mg-0.5Sr, (b) Mg-0.6Ca, (c) Mg-0.3Sr-0.3Ca, and (d) Mg-0.5Sr-0.6Ca.	102
Fig. 5. 2. X-ray diffraction patterns of (a) Mg-0.5Sr, (b) Mg-0.6Ca, (c) Mg-0.3Sr-0.3Ca, and (d) Mg-0.5Sr-0.6Ca. α -Mg, $Mg_{17}Sr_2$ and Mg_2Ca were detected.	102
Fig. 5. 3. Secondary electron images from the longitudinal cross sections of (a & b) Mg-0.5Sr, (c & d) Mg-0.6Ca, (e & f) Mg-0.3Sr-0.3Ca and (g & h) Mg-0.5Sr-0.6Ca. Regions marked as A, B and C on the high-magnification images correspond to areas where EDS was performed (see Table 5. 3).	103
Fig. 5. 4. EPMA micrographs of as-cast Mg-0.3Sr-0.3Ca (a) and Mg-0.5Sr-0.6Ca (d), and their corresponding Sr (b & e) and Ca (c & f) elemental maps.	105
Fig. 5. 5. (a) TEM image showing the intermetallic/Mg phases in the interdendritic eutectic phase in Mg-0.3Sr-0.3Ca; (b) SAED patterns obtained from interdendritic phase at $B = [0\bar{1}\bar{1}0]$ and $B = [\bar{7}\bar{2}\bar{5}3]$; (c) EDS analysis from the interdendritic phase.	107
Fig. 5. 6. (a) TEM image of the globular phase in Mg-0.3Sr-0.3Ca at different magnifications; (b, left) SAED pattern obtained from globular phase at $B=[\bar{1}\bar{2}\bar{1}\bar{3}]$ and (b, right) reciprocal lattice drawn using same lattice parameters; (c) EDS analysis from the globular phase.	108
Fig. 5. 7. (a) TEM dark field and bright field image of the needle-shaped phase near a nano-scale globular phase in Mg-0.3Sr-0.3Ca; (b) Line scan across the nano-scale globular phase and needle-shaped phases along the direction shown with an arrow in (a) for Ca (blue), Mg (red) and Sr (green); (c) high resolution line scan of Ca and Sr in (b) without Mg.	109
Fig. 5. 8. The average corrosion rate ($mg/day/cm^2$) in terms of mass loss and hydrogen evolution for pure Mg and Mg binary and ternary alloys after immersion in SBF at 37°C.	110
Fig. 5. 9. (a) pH measured in SBF and (b) hydrogen volume released from different Mg samples during the immersion test as a function of immersion time.	111
Fig. 5. 10. Polarization curves of pure Mg and binary and ternary Mg alloys in SBF.	113
Fig. 5. 11. SEM and EDS of the surface of corroded (a) Mg-0.5Sr, (b) Mg-0.6Ca, (c) Mg-0.3Sr-0.3Ca and (d) Mg-0.5Sr-0.6Ca after 1 day immersion in SBF at 37 °C.	115

Fig. 5. 12. High resolution XPS spectra of (a) Ca _{2p} , (b) P _{2p} , (c) C _{1s} , (d) O _{1s} and (e) Mg _{2p} measured on the surface of Mg-0.3Sr-0.3Ca after 1 day immersion in SBF at 37 °C. Surface layer represents the XPS spectra on the surface before sputtering, whereas 100 s sputtering corresponds to the at least 30 nm of sputtering. Figs. (c) and (d) show the fits corresponding to the peak components of the surface layer spectra. Fig. (e) shows the peak fittings on the spectrum obtained after 100 s sputtering.	119
Fig. 5. 13. X-ray diffraction pattern of the corrosion products formed on the surface of Mg-0.3Sr-0.3Ca after 1 day immersion in SBF at 37°C.	120
Fig. 5. 14. Tensile stress-strain curved of as-cast Mg-0.5Sr, Mg-0.6Ca, Mg-0.3Sr-0.3Ca and pure Mg generated at room temperature.	121
Fig. 5. 15. SEM fractographs of tensile tested (a) pure Mg, (b) Mg-0.6Ca, (c) Mg-0.5Sr and (d) Mg-0.3Sr-0.3Ca.	122
Fig. 5. 16. Force-displacement curve generated by three-point bending test of as-cast Mg-0.5Sr, Mg-0.6Ca, Mg-0.3Sr-0.6Ca and pure Mg at room temperature.	124
Fig. 5. 17. The average corrosion rate (mg/day/cm ²) in terms of mass loss and hydrogen evolution for as-cast and heat-treated Mg-0.5Sr and Mg-0.3Sr-0.3Ca after immersion in SBF at 37°C.	139
Fig. 5. 18. pH measured in SBF containing as-cast and 8h heat-treated Mg-0.5Sr and Mg-0.3Sr-0.3Ca samples during the immersion test as a function of immersion time.	140
Fig. 5. 19. Polarization curves of as-cast and 8h heat-treated Mg-0.3Sr-0.3Ca in Hank's solution.	142
Fig. 5. 20. Secondary electron images from the longitudinal cross sections of as-cast and 8h heat-treated (a & b) Mg-0.5Sr and (c & d) Mg-0.3Sr-0.3Ca.	143
Fig. 5. 21. EPMA micrographs of (a) as-cast and (d) 8h heat-treated Mg-0.3Sr-0.3Ca samples, and their corresponding Sr (b & e) and Ca (c & f) elemental maps.	144
Fig. 5. 22. TEM image of the globular phase in (a) as-cast and (b) heat-treated Mg-0.3Sr-0.3Ca. (c-f) EDS analysis from various regions with different contrast within the globular phase (marked as I-IV in b) after 8h heat treatment at 400 °C shows the variation of Ca/Sr ratio as listed in Table 5. 12. (g, left) SAED pattern obtained from the brighter regions in the globular phase after heat treatment at B=[1213] and (g, right) reciprocal lattice drawn using same lattice parameters.	146

Fig. 5. 23. Mechanical properties of Mg-0.5Sr (binary) and Mg-0.3Sr-0.3Ca (ternary) samples before and after 8h heat treatment at 400 °C; (a) Ultimate tensile strength and ultimate tensile strain (b) Tensile yield strength (c) Ultimate compressive strength and ultimate compressive strain (d) Compressive yield strength.	150
Fig. 5. 24. SEM fractographs of tensile tested samples of as-cast versus 8h heat-treated at 400 °C of Mg-0.5Sr (a & b) and Mg-0.3Sr-0.3Ca (c & d). Tensile test was performed at room temperature.	151
Fig. 5. 25. (a) Three-point bend tester used on Mg alloys; (b) Mg sample after bending experiment and (c) force-displacement curve generated by three-point bending test of as-cast and 8h heat-treated samples of Mg-0.5Sr and Mg-0.3Sr-0.3Ca.	152
Fig. 6. 1. (a) Average corrosion rate (mg/day/cm ²) of Mg-0.3Sr-0.3Ca in terms of mass loss and H ₂ evolution during interrupted immersion test without SBF renewal. (b) Comparison of pH change of the solution containing Mg-0.3Sr-0.3Ca in experiments with and without SBF renewal. (c) Average corrosion rate (mg/day/cm ²) of Mg-0.3Sr-0.3Ca in terms of mass loss and H ₂ evolution after immersion tests with and without SBF renewal.	167
Fig. 6. 2. Raman spectra of corrosion product scratched off the surface of Mg-0.3Sr-0.3Ca after 1 day immersion in SBF compared with HA powders as control.....	170
Fig. 6. 3. High resolution XPS spectra of Mg2p, P2p, Sr3p and Ca2p on the surface of Mg-0.3Sr-0.3Ca after 1 day immersion test and removing the corrosion products.	172
Fig. 6. 4. Cell viability expressed as a percentage of the viability of HUVEC cells in the control media (F-12K) after (a) 1 day, (b) 4 days and (c) 7 days of exposure to different concentration of extractions obtained from Mg-0.3Sr-0.3Ca, pure Mg and WE43 alloys (*P < 0.05). (d) Comparison of viability of HUVEC cells in contact with 10% extraction medium of Mg-0.3Sr-0.3Ca, pure Mg and WE43 with time of exposure (*P < 0.05).	174
Fig. 6. 5. The tubular Mg-0.3Sr-0.3Ca stent (a) before and (b) after implantation into the right femoral artery of the animal.....	175
Fig. 6. 6. Artery condition after 5 weeks implantation of (a) Mg-0.3Sr-0.3Ca and (b) WE43 in the right and left femoral artery respectively. The stented area of the artery is marked in the figures. Blood flow is illustrated by epinephrine injection before sacrificing the animal.	176

Fig. 6. 7. Optical and histology images (H&E staining) of vascular tissue surrounding (a & b) Mg-0.3Sr-0.3Ca and (c & d) WE43 tubular stent samples implanted in right and left femoral artery for 5 weeks..... 177

Fig. 6. 8. (a) SEM image and EDS mapping of elemental distribution for (b) Mg, (c) O, (d) Ca, and (e) P at the interface of Mg-03Sr-0.3Ca and its surrounding tissue after 5 weeks implantation (EDS compositional analysis obtained from different points is shown in Table 6. 4). 179

Fig. 6. 9. Schematic presentation of the Mg-0.3Sr-0.3Ca alloy biocorrosion interface in physiological environment: a) galvanic corrosion and Mg dissolution; b) formation of partially protective layer consists of $Mg(OH)_2$ and CaH_2 ; c) diffusion of Cl^- ions and inward shift of corrosion interface, thus creating a dynamic scale formation/dissolution equilibrium with b); d) Sr-substituted HA formation; and e) formation of a compact and homogenous layer of HA on the surface. The thickness of the layers is exaggerated to better visualize the mechanism. 182

LIST OF TABLES

Table 2. 1: Physical and mechanical properties of some biomaterials and natural bone [9].....	17
Table 2. 2: Distribution and concentrations of magnesium in the body of a healthy adult [39]...	19
Table 2. 3: Voltaic potential differences of the micro-constituents determined by SKPFM.....	27
Table 2. 4: Magnesium Stent Alloys, Present Efforts and Future Considerations	36
Table 2. 5: Mechanical properties of primary metallic materials used as biomedical implants...	37
Table 3. 1: Composition of SBF used for immersion test (Hank's solution)	54
Table 4. 1: The chemical composition of the alloys	66
Table 4. 2: The concentration of inorganic salts in F-12K formulation	69
Table 4. 3: Corrosion potential and corrosion current density of Mg alloys in SBF obtained by linear fitting on both cathodic and anodic parts of polarization curves	74
Table 4. 4: Atomic concentration found by XPS from the surface of Mg-0.5Sr and pure Mg before and after sputtering with Ar ions for successive 50 second cycles.....	79
Table 4. 5: XPS analysis from the surface of Mg-0.5Sr and pure Mg after removing the corrosion products and after a few seconds of etching with Ar ions.	80
Table 4. 6: Initial Dimension, volume and mass of Mg-0.5Sr and WE43 stents before and after implantation	85
Table 5. 1: The actual chemical composition of the alloys.....	98
Table 5. 2: Composition of Hank's simulated body fluid.....	99
Table 5. 3: Composition of different regions of the as-cast microstructure of Mg binary and ternary alloys in wt% (marked as A, B and C in Fig. 3) obtained by EDS.	104
Table 5. 4: Crystal structure of the intermetallic compounds.....	105
Table 5. 5: Corrosion current density (I_{corr}) and corrosion potential (E_{corr}) of Mg alloys in SBF derived from the polarization curves.	113
Table 5. 6: Atomic percent composition and Ca/P ratio measured by XPS before (0 s etching time) and after (200 s etching time) removing the top layer from the surface of Mg-0.5Sr, Mg-0.6Ca and MG-0.3Sr-0.3Ca immersed for 1 day in SBF.....	116

Table 5. 7: Atomic percent composition and Ca/P, Mg/O and Mg/Ca ratios obtained by XPS from the surface of Mg-0.3Sr-0.3Ca immersed for 1 day in SBF, before and after sputtering with Ar ions. Every 100 s etching is corresponds to at least 30 nm sputtering.	117
Table 5. 8: Tensile properties of as-cast Mg, Mg-0.5Sr, Mg-0.6Ca, and Mg-0.3Sr-0.3Ca.	123
Table 5. 9: The actual chemical composition of the alloys.....	136
Table 5. 10: Corrosion potential and corrosion current density of as-cast and heat-treated Mg-0.3Sr-0.3Ca in SBF obtained by linear fitting on both cathodic and anodic parts of polarization curves.	142
Table 5. 11: Composition of different regions of the as-cast and heat-treated microstructure of Mg-0.5Sr alloy in wt% (marked as A and B regions in Fig. 5. 20a & b) obtained by EPMA-WDS.....	144
Table 5. 12: Variation of Ca/Sr ratio obtained by EDS analysis from different regions of globular Ca-Sr (Mg) phase in Mg-0.3Sr-0.3Ca after 8h heat treatment at 400 °C.	147
Table 6. 1: The actual chemical composition of the as-cast Mg-0.3Sr-0.3Ca obtained by ICP-AES.....	162
Table 6. 2: The concentration of metallic ions (mg/l) in the SBF measured by ICP after immersion of Mg-0.3Sr-0.3Ca in SBF, with and without daily renewal. Values include the ions pre-existing in Hank’s solution. The amount of Sr was very low and not traceable. .	168
Table 6. 3: XPS analysis from the surface of Mg-0.3Sr-0.3Ca after removing the corrosion products and after sputtering with Ar ions for successive 50-second cycles.....	171
Table 6. 4: EDS compositional analysis obtained from of different regions at the interface of the tubular Mg-0.3Sr-0.3Ca stent and its surrounding tissue after 5 weeks implantation at right femoral artery (spots marked from 1 to 8 in Fig. 6. 8).....	180

GLOSSARY OF BIOLOGICAL TERMS

Balloon angiography	A procedure in which a catheter equipped with a tiny balloon at the tip is inserted into an artery that has been narrowed by the accumulation of fatty deposits. The balloon is then inflated to clear the blockage and widen the artery.
Biocompatibility	The condition of being compatible with living tissue or a living system by not being toxic or injurious and not causing immunological rejection.
Cytotoxicity	The degree to which an agent possesses a specific destructive action on certain cells or the possession of such action.
Endothelial cells	The cells lining the inner walls of the blood vessels.
Histology	The science concerned with the minute structure of cells, tissues, and organs in relation to their function.
HUVEC	Human umbilical vein endothelial cell. HUVECs are cells derived from the endothelium of veins from the umbilical cord.
Hyperplasia	An abnormal increase in cells. The causes of benign prostatic hyperplasia are not fully understood.
In vitro	An experiment that is performed with cells or biological molecules outside their normal biological context; in a test tube, in glass; outside the body, or a living system.
In vivo	An experiment that is done in vivo is done in the body of a living organism as opposed to in a laboratory method that does not use the living organism as the host of the test. In vivo is the opposite of in vitro.

Neointima	The scar tissue that forms within tubular anatomical structures such as blood vessels, as the intima is the innermost lining of these structures. Neointima can form as a result of vascular surgery such as angioplasty or stent placement. It is actually due to proliferation of smooth muscle cells in the media giving rise to appearance of fused intima and media.
Restenosis	The narrowing of an opening or passage-way in the body. In arteries, stenosis is caused by a build-up of atherosclerotic plaque, disease, or other disorder.
Thrombosis	The formation or presence of a blood clot in a blood vessel. The vessel may be any vein or artery as, for example, in a deep vein thrombosis or a coronary (artery) thrombosis. The clot itself is termed a thrombus.
VSMC	Vascular smooth muscle. VSMCs refer to the particular type of smooth muscle found within, and composing the majority of the wall of blood vessels.

CHAPTER 1

INTRODUCTION

Magnesium (Mg) has a low density (1.74 g/cm^3), high strength-to-weight ratio and its Young's modulus is close to that of natural bone [1]. Mg is the fourth most abundant cation in the human body, followed by Ca, K, and Na [1, 2]. It is one of the essential elements for human metabolism and plays the role of stabilizer in many enzymatic reactions [2, 3]. These unique properties make Mg an attractive material for medical applications [4, 5]. Metallic biomaterials are extensively used as implants to repair or replace damaged tissues. Two major application areas are temporary intravascular stents and orthopedic implants.

Currently, metallic stents are made of stainless steel, Nitinol, or cobalt-chromium alloys [4, 6]. These materials cause restenosis due to the irritation of the endothelium and the resulting hyperplasia [7, 8]. Some of their other shortcomings include:

- (i) the release of toxic ions and particles as a result of corrosion and wear processes that can cause infection and immune response in the body [1],
- (ii) the large differences in the mechanical behavior of the stented and the non-stented vessel areas, which leads to growth restrictions in the case of pediatric patients [8, 9],
- (iii) non-permissive or disadvantageous characteristics for later surgical revascularization, which make it difficult or impossible to perform subsequent angioplasty or bypass graft surgery,
- (iv) a likelihood to cause thrombogenicity, permanent physical irritation, long-term endothelial dysfunction, and chronic inflammatory reactions [8-10].

Thus, a second surgery is needed to remove these permanent biomaterials from the body after the healing process is completed, which is expensive for health care system and dangerous for the patient.

Mg has attracted considerable interest as an important candidate for bioresorbable implant applications. Mg biodegrades via corrosion reaction in the body and disappears once its role is completed [1, 11]. This eliminates the stimulus for hyperplasia and reduces the tendency to

restenosis [12]. Mg has an advantage over biodegradable polymeric stents in that a smaller mass can result in an equal mechanical performance. A large bulk of polymer must be used in order to have good mechanical integrity [12, 13]. Compared to current metallic implants, the mechanical properties of Mg are closer to that of natural tissues such as bone [1]. Mg alloys also have better visibility in CT scans compared to stainless steel biomaterials.

The main shortcoming of Mg as a temporary implant material is its fast corrosion rate, which produces high volumes of hydrogen gas released during the biodegradation reaction, which can be detrimental to the surrounding tissue, especially in cardiovascular applications [4, 14, 15]. While a rapid degradation rate may be an advantage in certain applications such as drug elution, which does not require an extensive implant duration, much slower biodegradation is needed in other stent applications to provide adequate time for tissue healing. Another complication of Mg is its loss of mechanical integrity before the healing process is complete [16]. In the case of stent applications, the main role of biomaterial is to provide mechanical support for the arterial wall and avoid early recoil until the healing process is completed [17]. There are several possibilities to tailor the corrosion rate of Mg. Alloying is one of the most effective ways to reduce the degradation rate and enhance the mechanical properties. However, there are limited elements that can be used in the body without harmful effects on other organs [18]. For example, the addition of aluminum may slow down the biodegradation rate of Mg but is neurotoxic to the human body [19-21]. Zinc is highly cytotoxic and, at high levels, causes genotoxicity [22, 23]. Therefore, alloying elements should improve the biodegradation behavior without compromising the biocompatibility.

Cardiovascular diseases are a major cause of death globally that are estimated to reach up to 23.6 million people by 2030. Seventy percent of these deaths result from coronary artery disease, which is caused by the blockage of the artery by cholesterol build-up [24]. An effective standard treatment to remove the blockage of the artery is balloon angiography. Currently, about sixty percent of balloon angioplasties are associated with stent implantation [17]. In this process, a stent, which is a wire metal mesh tube, is inserted and then expanded and locked inside of the artery to keep it properly open (Fig. 1. 1). The price of stents has come down in past few years due to its competitive market but there are still niches, such as pediatric patients and drug delivery applications, that require biodegradable stents, which make stents commercially interesting. The global market for cardiovascular stents is forecast to increase to 9.8 billion US

dollars by 2017 [24]. Consequently, new technological approaches in stent development and fabrication are essential to meet the clinical requirements and fulfill the increasing market demand.

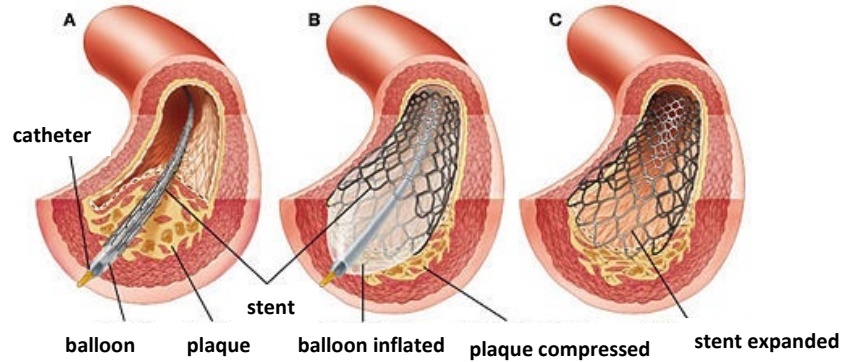


Fig. 1.1. An illustration of a coronary stent implantation: (a) the catheter delivers the stent to the site of blockage, (b) balloon inflation deploys the stent to push the plaque and open the narrowed artery, (c) the catheter is removed and the stent remains to support the artery and restore the blood flow [25].

The company Biotronik (Germany) started clinical studies on biodegradable stents with Mg-7RE [26]. Their follow-up studies [27, 28] revealed early restenosis in the aorto-pulmonary collateral of a baby; at the beginning, there was a significant increase in vessel diameter but 4 months later, significant restenosis occurred. Biotronik developed its next generation stent with the WE43 (Mg-4Y-3Nd) alloy, which showed better mechanical integrity in animal studies. Clinical studies showed the formation of thick neo-intima and thrombosis [29]. They are still working on their new generation by integrating the stent with drug-eluting polymer coating to resolve these issues. This reveals the need for further refinements in Mg alloy stent technology, especially in view of its promising potential for intervention in children where permanent stent placement is unsuitable [30, 31].

Presently, from an economic perspective, metallic permanent stents have decreased slightly in price, making it less attractive for major medical device companies to maintain their stent business. On the other hand, niche applications for stents, such as biodegradable stents for pediatric use or drug elution, offer important business potential for these companies.

Objectives of the project

The general goals of this PhD project are:

- (1) to design novel Mg alloys with a controlled degradation rate and improved mechanical and biocompatibility properties;
- (2) to evaluate their biocorrosion, biocompatibility, and mechanical properties via in vitro and in vivo tests;
- (3) to understand the corrosion mechanism of Mg and the role of alloying during its corrosion in a physiological condition.

Alloy design strategy: The strategy in alloying is to improve biocorrosion resistance while maintaining biocompatibility and mechanical performance. One of the alloying elements selected for this purpose is strontium (Sr). Sr is a novel candidate material for use in medical applications. Prof. Pekguleryuz and her research team have been studying the addition of Sr to Mg alloys over the past decades [32]. Sr is a grain refiner for Mg and can improve the mechanical properties of some Mg alloys [33], as well as improve the corrosion resistance of Mg by altering its surface due to its surface active nature [32, 34-37]. Sr is a component of human bones, and its critical role in bone, heart, and muscle function was shown in the 1950s and 1960s [38]. Sr is known to promote the growth of osteoblasts and prevent bone resorption [39-43]. It also improves osteoblast function and bone formation [44-46]. We have therefore adopted Sr as one of the alloying elements for our new stent alloy.

There is also a significant number of studies on the addition of Ca to Mg for biomedical applications, especially as orthopedic implants [47-50]. Ca, with a density of 1.55 g/cm^3 , is an alkaline-earth element like Mg. It is a major component of bones and an essential element for cell chemical signaling [51]. Several studies have analyzed Ca and Mg interactions in vivo and in vitro. Ca seems to better incorporate into bones in the presence of Mg ions [52]. It has been demonstrated that optimal amounts of Ca improve the mechanical properties and increase the corrosion resistance of Mg [53]. Therefore, we investigated the effect of Sr addition into Mg-Ca alloys and evaluated the combined additional effect of Sr and Ca simultaneously.

Mechanical properties are very important during fabrication since the material usually undergoes several mechanical and thermal processes during its fabrication into cardiovascular stents (e.g., extrusion, heat-treatment, laser machining); it is also essential for the material to have proper mechanical properties after fabrication during the implantation and tissue healing

processes. The mechanical properties of these alloys need to be evaluated to ascertain the stability of the microstructure and the retention of the properties during fabrication, processing, and service.

During this PhD project, a comprehensive evaluation of the surface chemistry of candidate Mg-Sr and Mg-Ca-Sr alloys was conducted through various characterization techniques to understand the effect of Sr, the morphology of the corrosion product, and the mechanism through which these alloys biodegrade in physiological condition. Finally, the biocompatibility of these alloys was evaluated via cytocompatibility assays and in vivo animal trials. Improved alloys will be candidates for subsequent pre-clinical trials in the future to evaluate their use in cardiovascular implants, especially for pediatric patients.

References

- [1] Staiger MP, Pietak AM, Huadmai J, Dias G. Magnesium and its alloys as orthopedic biomaterials: A review. *Biomaterials*. 2006;27:1728-34.
- [2] Saris NEL, Mervaala E, Karppanen H, Khawaja JA, Lewenstam A. Magnesium - An update on physiological, clinical and analytical aspects. *Clinica Chimica Acta*. 2000;294:1-26.
- [3] Brink EJ, Beynen AC. Nutrition and magnesium absorption - a review. *Progress in Food and Nutrition Science*. 1992;16:125-62.
- [4] Witte F. The history of biodegradable magnesium implants: A review. *Acta Biomaterialia*. 2010;6:1680-92.
- [5] Zeng R, Dietzel W, Witte F, Hort N, Blawert C. Progress and challenge for magnesium alloys as biomaterials. *Advanced Engineering Materials*. 2008;10:B3-B14.
- [6] Witte F, Fischer J, Nellesen J, Crostack HA, Kaese V, Pisch A, et al. In vitro and in vivo corrosion measurements of magnesium alloys. *Biomaterials*. 2006;27:1013-8.
- [7] Gu XN, Zhou WR, Zheng YF, Cheng Y, Wei SC, Zhong SP, et al. Corrosion fatigue behaviors of two biomedical Mg alloys-AZ91D and WE43-In simulated body fluid. *Acta Biomaterialia*. 2010;6:4605-13.
- [8] Heublein B, Rohde R, Kaese V, Niemeyer M, Hartung W, Haverich A. Biocorrosion of magnesium alloys: a new principle in cardiovascular implant technology? *Heart*. 2003;89:651-6.
- [9] Yaremchuk MJ, Fiala TGS, Barker F, Ragland R. The effects of rigid fixation on craniofacial growth of rhesus-monkeys. *Plastic and Reconstructive Surgery*. 1994;93:1-10.

- [10] Gilardino MS, Chen E, Bartlett SP. Choice of internal rigid fixation materials in the treatment of facial fractures. *Craniofacial trauma & reconstruction*. 2009;2:49-60.
- [11] Song G. Control of biodegradation of biocompatible magnesium alloys. *Corrosion Science*. 2007;49:1696-701.
- [12] Waksman R, Pakala R, Kuchulakanti PK, Baffour R, Hellings D, Seabron R, et al. Safety and efficacy of bioabsorbable magnesium alloy stents in porcine coronary arteries. *Catheterization and Cardiovascular Interventions*. 2006;68:607-17.
- [13] Erne P, Schier M, Resink TJ. The road to bioabsorbable stents: Reaching clinical reality? *Cardiovascular and Interventional Radiology*. 2006;29:11-6.
- [14] Witte F, Kaese V, Haferkamp H, Switzer E, Meyer-Lindenberg A, Wirth CJ, et al. In vivo corrosion of four magnesium alloys and the associated bone response. *Biomaterials*. 2005;26:3557-63.
- [15] Kuhlmann J, Bartsch I, Willbold E, Schuchardt S, Holz O, Hort N, et al. Fast escape of hydrogen from gas cavities around corroding magnesium implants. *Acta Biomaterialia*. 2013;9:8714-21.
- [16] Song Y, Shan D, Chen R, Zhang F, Han E-H. Biodegradable behaviors of AZ31 magnesium alloy in simulated body fluid. *Materials Science & Engineering C-Biomimetic and Supramolecular Systems*. 2009;29:1039-45.
- [17] Moravej M, Mantovani D. Biodegradable Metals for Cardiovascular Stent Application: Interests and New Opportunities. *International Journal of Molecular Sciences*. 2011;12:4250-70.
- [18] Kirkland NT, Staiger MP, Nisbet D, Davies CHJ, Birbilis N. Performance-driven design of Biocompatible Mg alloys. *Jom*. 2011;63:28-34.
- [19] Gu X, Zheng Y, Cheng Y, Zhong S, Xi T. In vitro corrosion and biocompatibility of binary magnesium alloys. *Biomaterials*. 2009;30:484-98.
- [20] Witte F, Hort N, Vogt C, Cohen S, Kainer KU, Willumeit R, et al. Degradable biomaterials based on magnesium corrosion. *Current Opinion in Solid State & Materials Science*. 2008;12:63-72.
- [21] Abd El-Rahman SS. Neuropathology of aluminum toxicity in rats (glutamate and GABA impairment). *Pharmacological Research*. 2003;47:189-94.
- [22] Fosmire GJ. Zinc toxicity. *American Journal of Clinical Nutrition*. 1990;51.

- [23] Wataha JC. Biocompatibility of dental casting alloys: A review. *Journal of Prosthetic Dentistry*. 2000;83.
- [24] Fang G, Ai W-J, LeeFlang S, Duszczyc J, Zhou J. Multipass cold drawing of magnesium alloy minitubes for biodegradable vascular stents. *Materials science & engineering C, Materials for biological applications*. 2013;33:3481-8.
- [25] <http://www.britannica.com/EBchecked/topic/720793/cardiovascular-disease>.
- [26] Ramcharitar S, Serruys PW. Fully Biodegradable Coronary Stents Progress to Date. *American Journal of Cardiovascular Drugs*. 2008;8:305-14.
- [27] McMahon CJ, Oslizlok P, Walsh KP. Early restenosis following biodegradable stent implantation in an aortopulmonary collateral of a patient with pulmonary atresia and hypoplastic pulmonary arteries. *Catheterization and Cardiovascular Interventions*. 2007;69:735-8.
- [28] Waksman R, Erbel R, Di Mario C, Bartunek J, de Bruyne B, Eberli FR, et al. Early- and Long-Term Intravascular Ultrasound and Angiographic Findings After Bioabsorbable Magnesium Stent Implantation in Human Coronary Arteries. *Jacc-Cardiovascular Interventions*. 2009;2:312-20.
- [29] Peuster M, Beerbaum P, Bach FW, Hauser H. Are resorbable implants about to become a reality? *Cardiology in the Young*. 2006;16:107-16.
- [30] Schranz D, Zartner P, Michel-Behnke I, Akinturk H. Bioabsorbable metal stents for percutaneous treatment of critical reocclusion of the aorta in a newborn. *Catheterization and Cardiovascular Interventions*. 2006;67:671-3.
- [31] Zartner P, Buettner M, Singer H, Sigler M. First biodegradable metal stent in a child with congenital heart disease: Evaluation of macro and histopathology. *Catheterization and Cardiovascular Interventions*. 2007;69:443-6.
- [32] Pekguleryuz M. An overview of the effects of calcium and strontium on the properties of aluminum and magnesium alloys. IMMC (15th International Metallurgy and Materials Congress). Istanbul, Turkey2010.
- [33] Fan Y, Wu G, Zhai C. Effect of strontium on mechanical properties and corrosion resistance of AZ91D. 2007. p. 567-70.
- [34] Suganthi RV, Elayaraja K, Joshy MIA, Chandra VS, Girija EK, Kalkura SN. Fibrous growth of strontium substituted hydroxyapatite and its drug release. *Materials Science & Engineering C-Materials for Biological Applications*. 2011;31:593-9.

- [35] Zeng XQ, Wang YX, Ding WJ, Luo AA, Sachdev AK. Effect of strontium on the microstructure, mechanical properties, and fracture behavior of AZ31 magnesium alloy. *Metallurgical and Materials Transactions a-Physical Metallurgy and Materials Science*. 2006;37A:1333-41.
- [36] Pekguleryuz M, Kainer K, Kaya E. The alloying behaviour of magnesium. *Fundamentals of magnesium metallurgy*. Cambridge, UK: Woodhead; 2013.
- [37] Pekguleryuz M, Avedesian MM. Magnesium Alloying- Some Metallurgical Aspects. In: Mordike BL, Hehman F, editors. *Magnesium Alloys & their Applications*. Germany: DGM; 1992. p. 213-20.
- [38] Nielsen SP. The biological role of strontium. *Bone*. 2004;35:583-8.
- [39] Dahl SG, Allain P, Marie PJ, Mauras Y, Boivin G, Ammann P, et al. Incorporation and distribution of strontium in bone. *Bone*. 2001;28:446-53.
- [40] Marie PJ. Strontium ranelate: a novel mode of action optimizing bone formation and resorption. *Osteoporosis International*. 2005;16:S7-S10.
- [41] Taylor A. Therapeutic uses of trace-elements. *Clinics in Endocrinology and Metabolism*. 1985;14:703-24.
- [42] Zhang W, Shen Y, Pan H, Lin K, Liu X, Darvell BW, et al. Effects of strontium in modified biomaterials. *Acta Biomaterialia*. 2011;7:800-8.
- [43] Bigi A, Boanini E, Capuccini C, Gazzano M. Strontium-substituted hydroxyapatite nanocrystals. *Inorganica Chimica Acta*. 2007;360:1009-16.
- [44] Kung K-C, Lee T-M, Lui T-S. Bioactivity and corrosion properties of novel coatings containing strontium by micro-arc oxidation. *Journal of Alloys and Compounds*. 2010;508:384-90.
- [45] Pramatarova L, Pecheva E, Presker R, Pham MT, Maitz MF, Stutzmann M. Hydroxyapatite growth induced by native extracellular matrix deposition on solid surfaces. *European cells & materials*. 2005;9:9-12.
- [46] Boanini E, Gazzano M, Bigi A. Ionic substitutions in calcium phosphates synthesized at low temperature. *Acta Biomaterialia*. 2010;6:1882-94.
- [47] Li Z, Gu X, Lou S, Zheng Y. The development of binary Mg-Ca alloys for use as biodegradable materials within bone. *Biomaterials*. 2008;29:1329-44.

- [48] Gu XN, Zheng W, Cheng Y, Zheng YF. A study on alkaline heat treated Mg-Ca alloy for the control of the biocorrosion rate. *Acta Biomaterialia*. 2009;5:2790-9.
- [49] Wang HX, Guan SK, Wang X, Ren CX, Wang LG. In vitro degradation and mechanical integrity of Mg-Zn-Ca alloy coated with Ca-deficient hydroxyapatite by the pulse electrodeposition process. *Acta Biomaterialia*. 2010;6:1743-8.
- [50] Zhou P, Gong HR. Phase stability, mechanical property, and electronic structure of an Mg-Ca system. *Journal of the Mechanical Behavior of Biomedical Materials*. 2012;8:154-64.
- [51] Ilich JZ, Kerstetter JE. Nutrition in bone health revisited: A story beyond calcium. *Journal of the American College of Nutrition*. 2000;19.
- [52] Serre CM, Papillard M, Chavassieux P, Voegel JC, Boivin G. Influence of magnesium substitution on a collagen-apatite biomaterial on the production of a calcifying matrix by human osteoblasts. *Journal of Biomedical Materials Research*. 1998;42:626-33.
- [53] Wan Y, Xiong G, Luo H, He F, Huang Y, Zhou X. Preparation and characterization of a new biomedical magnesium-calcium alloy. *Materials & Design*. 2008;29:2034-7.

CHAPTER 2

LITERATURE REVIEW

Mg alloys have attracted the interest of biomedical researchers over the past two decades due to their low density, biocompatibility and good mechanical properties. Yet, the use of Mg as biomedical implants is impeded by its rapid corrosion rate. The focus of this literature review is four-fold:

1. An overview of biodegradable stents is provided in section 2.1.
2. Mg as a *biomaterial* including the biological role of Mg, its use in biodegradable implants and early studies on Mg cardiovascular implants are presented in section 2.2.
3. Current research activities on the development of biodegradable Mg stents, including the corrosion resistance of Mg, the effects of alloying elements on corrosion resistance and studies on the evaluation of Mg alloys for corrosion and biocompatibility are reviewed in section 2.3.
4. Testing methods (in vitro corrosion and surface characterization) used for the evaluation of biodegradable Mg alloys are presented in section 2.4.

2. 1. An overview of Biodegradable stents

The term “biomaterials” has been defined in various ways. In general, a biomaterial is one (or several) synthetic or natural material(s) that can be used in any period of time as an entire or a part of a system and treats or replaces any tissue, organ or function of the body [1]. The range of biomaterials is expanding extremely rapidly [2]; even so, biomaterials can be classified into five general categories: metals and alloys, ceramics, composites, synthetic polymers and biologically derived substances [1, 2]. They can repair, restore and replace damaged or failed tissue. Some of these materials can be developed in an interdisciplinary effort as the combined activity of material science and engineering together with biology and clinical sciences [1, 3, 4].

Metallic materials play an important role in biomedical engineering. Every day, many people lose tissues or organs because of accidents or other unexpected incidents. Engineering the damaged organ or tissue is the best way to treat these patients [4]. Different kinds of biomaterials help us repair or replace natural damaged tissues and organs. In the case of load-bearing applications, metals are more suitable compared to other types of biomaterials, such as ceramics and polymers [5]. Among all the biomaterials, metals have the longest history of use. Metallic biomaterials have high mechanical strength and fracture toughness, making them uniquely suitable for certain applications [5, 6]. Currently, stainless steel, titanium and cobalt-chromium alloys are commonly used metallic biomaterials [7, 8], although one of their major shortcomings is their high elastic moduli, which are not well matched with the modulus of natural bone tissue. This mismatch can cause stress shielding effects, decelerate new bone growth and decrease implant stability [9]. Another limitation of these metallic biomaterials is the release of toxic metallic ions or particles into the body during the corrosion and wear processes, which can cause infection and tissue loss and reduce biocompatibility. Furthermore, these specific metallic biomaterials are used as permanent fixtures (plate, screw and pin) that remain inside the human body until natural tissue has repaired sufficiently. They must be subsequently removed by a second surgery after the healing process has completed; this second intervention is expensive for the health care system and painful for the patient [5, 8, 9].

2. 1. 1. Cardiovascular implants

Cardiovascular diseases are a major cause of death in the world. It is predicted that the number of deaths due to the cardiovascular diseases will reach 23.6 million by 2030. Seventy percent of these deaths are caused by coronary artery disease, which is the blockage of the artery by cholesterol build up [10] that leads to insufficient supply of blood and oxygen to different organs in the body. A standard effective treatment to remove the blockage of the artery is balloon angiography. Currently, about 60% of balloon angioplasties are associated with stent implantation [11]. In this process, a stent, which is a wire metal mesh tube, is inserted and then expanded and locked inside of the artery to keep it properly open (Fig. 2. 1). The global market for cardiovascular stent is forecast to increase to 9.8 billion US dollars by 2017 [10]. Consequently, new technological approaches in stent development and fabrication are essential to meet the clinical requirements and fulfill the increasing market demand.

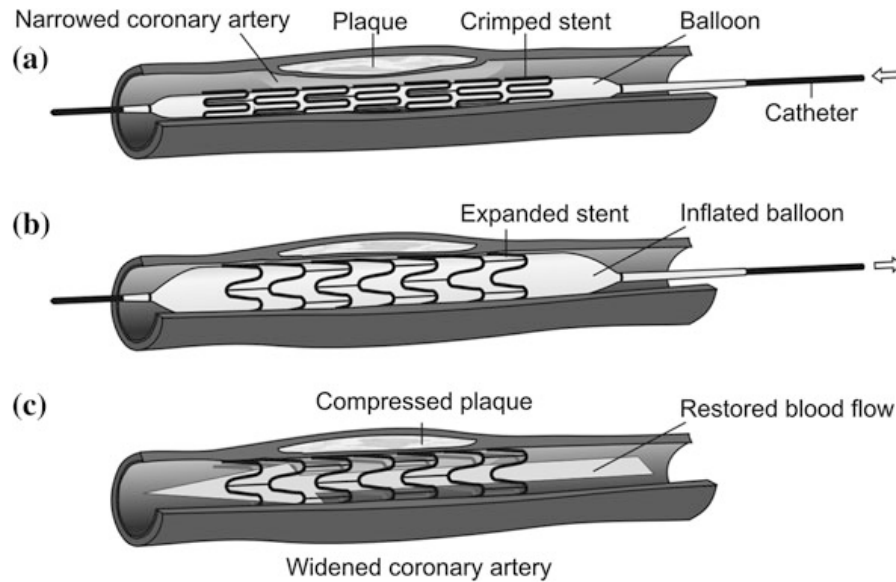


Fig. 2. 1. Illustration of coronary stent implantation: (a) delivery to the blocked artery by a catheter, (b) expansion to push and open the narrowed artery, (c) the catheter leaves and the stent remains to support the artery and restore the blood flow [12]

The main functions of the stent are to scaffold the arterial wall and provide mechanical support to avoid early recoil until the healing process is completed. The stents currently used clinically are mainly made of corrosion resistance metals, such as stainless steel, titanium and cobalt-chromium alloys [10, 11, 13]. These metallic stents provide good mechanical support, prevent early shrinkage of the artery and thereby reduce the restenosis (re-blocking of the artery) after angioplasty [14]. However, the long-term presence of these permanent metallic stents in the body is associated with serious complications, the limitations of which detract from the benefits. Although these materials are known to be corrosion resistant, their long-term presence leads to the release of metallic ions, which can be toxic to the body. For example, stainless steel and Ni-Ti stents are prone to releasing nickel, chrome and molybdenum ions, which are reported as carcinogenic by the International Agency for Research on Cancer (IARC) [15]. These toxic ions can cause inflammatory and allergic reactions in the body. The long-term presence of these stents can also inhibit the growth and remodeling processes of the arteries and stimulate in-stent restenosis after the angioplasty. Presently, in-stent restenosis is reported to occur in about 25% of angiographies [16]. The other limitations of permanent metallic stents are thrombosis (clotting within the stent), chronic inflammatory local reaction, physical irritation and the large

differences in the mechanical behavior of the stented and the non-stented vessel areas [17]. The use of the permanent stents are also very restrictive in the case of pediatric patients due to the lack of growth potential [18].

From a clinical point of view, the stent in the body is desired to play only a temporary function. After stent implantation, the arterial walls start remodeling due to the mechanical stress induced by the stent [19]. The stent is required to remain in place and scaffold the artery during the remodeling process, which can take 6–12 months [13]. The presence of the stent beyond the remodeling period does not have any beneficial effects; on the contrary; it can cause several complications (hyperplasia, restenosis, tissue irritation).

In view of these complications, the development of biodegradable stents has been highlighted as a promising solution. Biodegradable stents reduce the stimulus for hyperplasia, minimize the tendency to restenosis and eliminate the chance of local tissue irritation [20, 21]. An ideal biodegradable stent should balance its mechanical integrity and degradation rate until the healing process is completed (Fig. 2. 2). The material should degrade slowly to maintain sufficient mechanical integrity during arterial remodeling. While the healing process progresses, the degradation happens at a slow rate, with a tolerable accumulation of degradation products and a gradual decrease in mechanical integrity [11, 17]. In an ideal case, only the healed artery vessel remains after the stent degrades completely, i.e., a period of 12–24 months after implantation. This period, however, depends on various parameters, such as type of material and the condition of the stenting area [13].

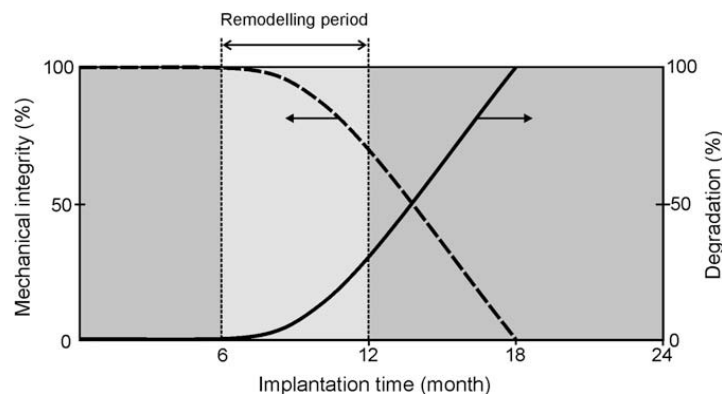


Fig. 2. 2. Illustration of an ideal compromise between mechanical integrity and degradation of a biodegradable stent [13]

2. 1. 2. Biodegradable cardiovascular implants

Two classes of materials have been studied for the development of biodegradable stents: polymers and metals. Polymers, such as poly-L-lactic acid (PLLA), were the first choice for biomedical application due to their high biocompatibility [22]. Coronary stents made of PLLA showed very good biocompatibility, minimal inflammatory response and small neointimal formation in porcine coronary arteries [23]. The main challenge in the use of biodegradable polymeric stents has been their low mechanical properties [24]. Since they have low radial force compared to metallic stents (degradable or non-degradable), a larger thickness is required to ensure adequate mechanical support.

Metallic stents have an advantage over biodegradable polymeric stents in that they can have smaller mass for equal mechanical performance [20]. Polymeric stents also have difficulties expanding completely with balloon dilatation during angiography [25]. Degradable metallic stents with superior mechanical strength have attracted more interest than polymeric ones and, therefore, have reached the commercial development stage rather rapidly. Based on biocompatibility and mechanical performance considerations, iron and magnesium have been singled out as the promising candidate materials for this application [11].

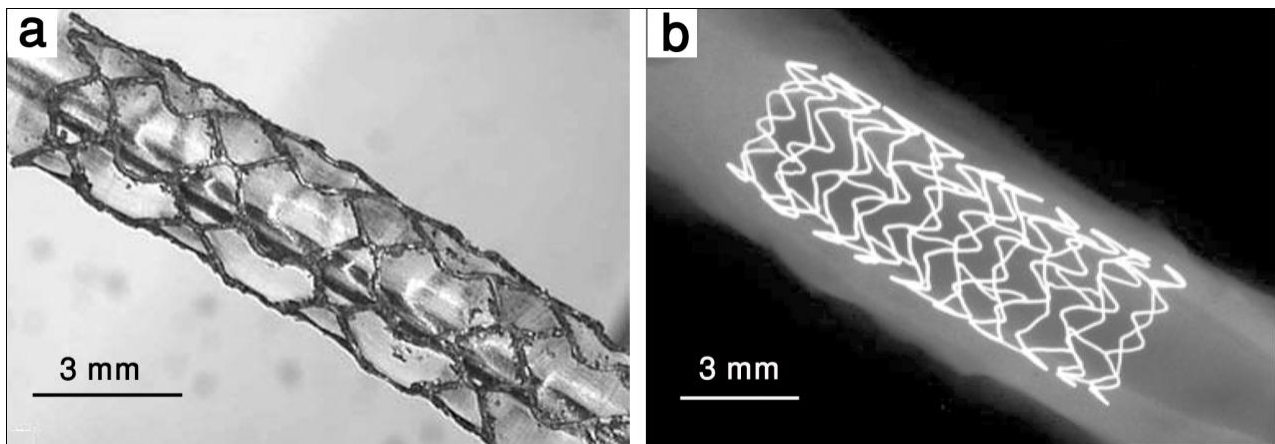


Fig. 2. 3. Biodegradable iron stents: (a) NOR-I stent expanded to 3.5 mm diameter [26] and (b) X-ray photograph of iron stent (Biotronik, Erlangen, Germany) after implantation in porcine coronary artery [27]

Pure iron has high strength and ductility that are desirable for stent applications. It also has high radial strength due to the high modulus of elasticity, which allows easier stent implantation.

However, it should be noted that iron, although an essential element for the body, can cause harmful effects in excess amounts [13]. The results from previous investigations show no significant inflammatory response and neointimal proliferation related to iron stents. Fig. 2. 3 shows two biodegradable iron stents implanted in animal models. The implantation studies also indicate that the iron stent does not corrode completely within the set time and faster degradation rates would be required [28]. Future studies for biodegradable iron stent need to focus on accelerating its bio-corrosion.

Magnesium is another attractive element for use as a biodegradable stent. It is biocompatible and has low thrombogenicity due to its fibrinolytic and anticoagulative properties [26]. It is an essential element in the body that is involved in many biological mechanisms and metabolic reactions. Magnesium is also known to be non-carcinogenic for the body [29]. The amount of recommended magnesium intake is 6 to 10 mg per kg body weight, with a systemic toxic level of about 7 to 10 millimoles per lit of serum [26].

Pierson et al [25] used a new model to study the short- and long-term degradation behavior of two candidate stent materials—iron and magnesium. He implanted wire metals (2 cm length × 0.25 mm diameter) into the abdominal aorta of rats (Fig. 2. 4). The wires were deployed in the artery lumen and artery wall to simulate both stent blood contact and stent matrix contact. The results showed that the degradation products from the iron wire implanted within the arterial wall remained in the artery in an expanded form after 9 months. The iron degradation products appeared to be stable in the physiological environment; the concern here is the fact that the residues can affect the mechanical integrity of artery walls and cause long-term retention. The iron wire in contact with blood showed minimal degradation after 9 months. The wire/blood interface was more resistant to corrosion compared to the wire/artery wall interface.

These researchers found that the magnesium wire corroded very rapidly when implanted in the arterial wall with non-homogenous corrosion and localized pits on the wire surface and consequent fragmentation of magnesium wires implanted in the artery wall. Unlike the iron wire, none of the magnesium wires showed evidence of retention of degradation product in the surrounding tissues. Magnesium wires in contact with blood experienced insignificant degradation after 3 weeks. Fig. 2. 4 shows iron vs. magnesium wire implanted in the arterial wall and lumen after 1.5, 3 and 9 months.

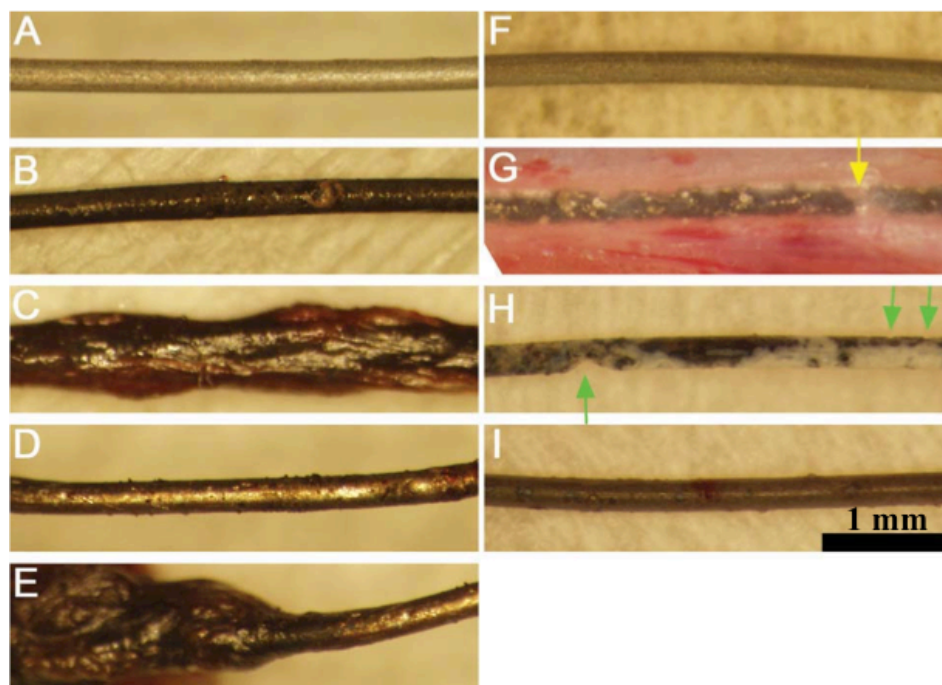


Fig. 2. 4. Extent of degradation in implanted wires. Clean iron wire before implantation (A) and wires retrieved from the arterial wall after 1.5 (B) and 3 (C) months. Iron wires retrieved from the artery lumen after 9 months at central (D) or wall locations (E). Clean magnesium wire before implantation (F), magnesium wires implanted in the arterial wall after 3 weeks (G and H), where (G) shows the in situ image of implanted magnesium with localized pits on the surface (yellow arrow in G) and subsequent fragmentation after 3 weeks (green arrows in H), and magnesium wires implanted in artery lumen in contact with blood after 3 weeks (I).

2.2. Mg As A Biomaterial

Magnesium (Mg) has an old and interesting history. In 1618, when a farmer tried to give his cows water from a well, they refused to drink because of the specific bitter taste of the water. Soon they found that this spring water had a healing ability, in the form of Epsom salt, which quickly became popular around the world. In 1695, N. Grew discovered that magnesium sulphate (MgSO_4) is the main constituent of Epsom salts. This was the first entry of Mg into medicine. In 1707, J. Black recognized Mg as an element [30]. In 1808, Sir Humphrey Davy identified Mg for the first time; he found a mixture of magnesium oxide and mercurit oxide and then isolated the metals by distilling off the mercury. In 1828, A.A. Bussy prepared the metal in good purity by

reducing anhydrous magnesium chloride with potassium [30]. In 1833, Michael Faraday, Davy's assistant, was the first to produce Mg via the electrolysis of molten magnesium chloride, which has been the main method in the industrial production of Mg before the advent of thermal processes, such as the carbothermic and ferrosilicon techniques [30].

Mg has unique properties that make it commendable for use as a metallic biomaterial. It is one of the lightest metals discovered in the world, with a density of 1.74 g/cm^3 . Mg is 1.6 and 4.5 times lighter than aluminum and steel respectively [9]. It also has good mechanical properties in comparison to ceramics and other polymeric biomaterials [22]. The Young's modulus and compressive yield strength of Mg are lower than those of aluminum and steel and closer to that of natural bone tissue, as a result of which Mg does not cause stress shielding effect [31]. Some of the important properties of Mg compared to other biomaterials and natural bone are listed in Table 2. 1. Mg is also one of the most important and essential elements for human metabolism. It is the fourth most abundant cation in the human body and acts as a stabilizer in many enzymatic reactions [9, 22].

Table 2. 1. Physical and mechanical properties of some biomaterials and natural bone [9]

	Density (g/cm^3)	Elastic modulus (GPa)	Compressive yield strength (MPa)	Fracture toughness ($\text{MPam}^{1/2}$)
Natural bone	1.8-2.1	3-20	130-180	3-6
Magnesium	1.74-2.0	41-45	65-100	15-40
Ti alloy	4.4-4.5	110-117	758-1117	55-115
Co-Cr alloy	8.3-9.2	230	450-1000	N/A
Stainless steel	7.9-8.1	189-205	170-310	50-200
Synthetic hydroxyapatite	3.1	73-117	600	0.7

However, the main problem of Mg in many engineering applications is its low corrosion resistance. In fact, the high rate of degradation in corrosive media, especially in electrolytic, aqueous environments, is the Achilles heel of Mg in most of the engineering applications as well as the biomedical domain [32, 33]. Interestingly, the *in vivo* use of Mg as a biomaterial leads to the formation of a soluble and non-toxic oxide that is not harmful for the human body and could be excreted into the urine without any problems [34]. Because of the functional role of Mg in human metabolism, it may stimulate the growth of new natural tissue and accelerate the healing process [35]. Therefore, Mg and its alloys can be applied as biocompatible, biodegradable and bioresorbable lightweight biomaterials that can remain inside the body and maintain mechanical integrity for certain periods while the healing process is being completed and Mg is gradually replaced by natural tissue [33]. Consequently, second surgical processes would be avoided by using Mg biomaterials and the patient would not suffer from permanent physical irritation and chronic inflammatory, problems that are very often associated with “old” permanent implants [9].

On the other hand, pure Mg can corrode very rapidly, especially in physiological conditions (pH= 7.4-7.6) and in the presence of chlorides. This high rate of corrosion leads to a loss of mechanical integrity before the damaged tissue is sufficiently healed. Another complication arising from the high corrosion rate of Mg is the excessive amount of hydrogen gas produced during the corrosion process, which can be damaging to the host tissue [22, 32]. Actually, 1.081 liters of H₂ is released from 1 g corroded Mg [36]. Fortunately, there are several possible ways to improve the corrosion resistance of Mg, such as alloying, surface modification and mechanical preprocessing [9]. These methods, of course, should result in producing a non-toxic, biocompatible material.

Mg alloys can be used to repair or replace hard tissue such as bones and joints. They can also be used to repair or support soft tissues such as coronary arteries. Orthopedic and cardiovascular implants are two major application areas of Mg as biomaterials.

2. 2. 1. Biological performance of Mg

The importance of Mg in living organisms was first determined when people started to use Mg-rich mineral water to cure scratches and wounds in ancient times. Mg is the fourth most abundant cation in human body followed by Ca, K and Na, and the second most abundant cation within the

cells. It is an essential mineral for various physiological reactions, such as cellular functions, ions transportation, energy metabolism, cell signaling and cell proliferation. Moreover, regarding genomic stability, Mg has an important and critical effect in DNA replication and protein synthesis [37, 38]. Consequently, Mg deficiency leads to very serious disorders [39]. A 70 kg adult contains approximately 1 mol (24 g) of Mg [9]. This amount of Mg is distributed between different organs and compartments according to the concentrations needed [39, 40].

Table 2. 2. Distribution and concentrations of Mg in the body of a healthy adult [39]

Percent distribution	Concentration
Bone (60–65%)	0.5% of bone ash
Muscle (27%)	6–10 mmol/kg wet weight
Other cells (6–7%)	6–10 mmol/kg wet weight
Erythrocytes	2.5 mmol/l
Serum	0.7–1.1 mol/l
Mononuclear blood cells	2.3–3.5 fmol/cell
Cerebrospinal fluid	1.25 mmol/l
Sweat	0.3 mmol/l (in hot environment)
Secretions	0.3–0.7 mmol/l
Total body Mg: 20–28 g.	

Table 2. 2 presents the Mg distribution in different parts of the human body. The majority of body Mg is located in the bones (more than half) and the rest is spread in muscles, soft tissues and other organs. Only 1% of the total Mg in the human body is in the plasma. Also, almost 90% of Mg is bound and only 10% is free [39]. It has been demonstrated that bone Mg has a critical role in making equilibrium in extracellular Mg. In fact bone Mg serves as a reservoir for extracellular Mg by releasing or absorbing Mg from the bone surface and keeping extracellular Mg in a constant range. Usually the total amount of Mg for a body can be provided by a healthy diet containing 2–7.5 mg Mg/kg weight [39]. For instance, 300–400 mg/day is recommended for adults. The normal circulation of Mg in the body involves absorption from the gut, distribution to

the cells, and excretion of the surplus by the kidneys. Intestinal absorption mainly accrues in the ileum and jejunum, and Mg is usually absorbed as an ion. Afterward, Mg is transported to various organs when needed and the surplus is excreted by the kidney [34].

2. 2. 2. Biochemistry of Mg

Mg is positively charged and so can bind electrostatically to negatively charged molecules such as phospholipids, nucleic acids, proteins and even small molecules (e.g., nucleotides). Mg is also very interesting because it binds with oxygen donor ligands, such as negatively charged carboxylates and phosphates. Mg is a small ion with relatively low ionic radius (0.86 \AA) but high hydration energy (-1922 KJ/mol) compared to adjacent metals in the periodic table. Ionized Mg tends to attract water molecules because of the high hydration energy that leads to a large ionic radius. In the case of $\text{MgSO}_4 (7\text{H}_2\text{O})$ or $\text{MgCl}_2 (6\text{H}_2\text{O})$, ionized Mg can coordinate with 6–7 molecules of water whereas other metal ions such as Ca and Ba usually coordinate with 2 or 1 molecules of water respectively as seen in CaCl_2 and BaCl_2 . Typically, the coordination between Mg and H_2O takes place in octahedral conformation (Fig. 2. 5) with six rigid coordination bonds that makes the Mg molecule bigger and more stable with a slower water exchange compared to other elements such as Ca [41]. The chemico-physical properties of Mg make it the most versatile cation in the body and lead to the incorporation of Mg ion in a wide range of enzymatic reactions and biological functions.

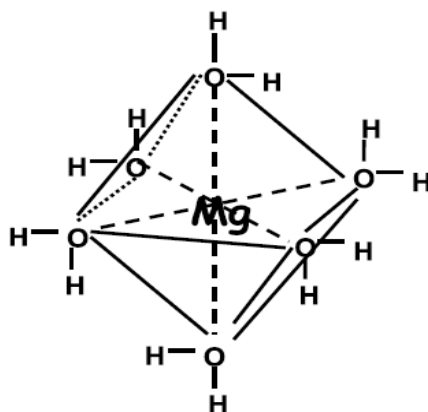


Fig. 2. 5. Mg ion in an octahedral coordination with six water molecules [41]

2. 2. 3. Mg as biodegradable orthopedic implant

Mg has drawn attention as a biodegradable lightweight biomaterial for load-bearing applications, such as orthopedic implants [4, 8]. Orthopedic implants are generally used to replace a damaged bone and joint or to provide fixation and mechanical integrity until natural bone tissues are repaired. They are available for knees, shoulders, hips and elbows. Biomedical implants increase mobility and decrease pain. In some cases, they can cause infection or malfunction [42]. Commercial implants are mainly made of stainless steel and titanium alloys because of their high mechanical properties [2, 4].

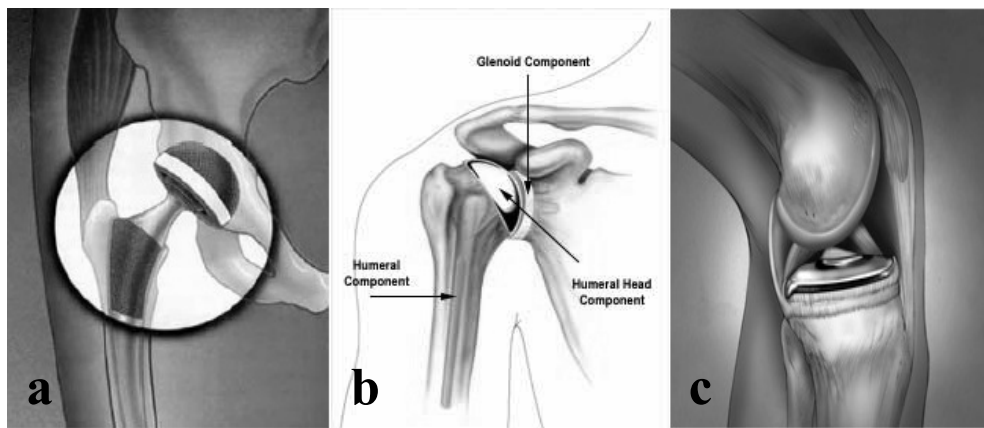


Fig. 2. 6. Schematic images of a typical (a) hip joint, (b) shoulder and (c) knee implant replacement after surgery as some examples of hard tissue application [2].

Mg implants have been introduced in last century with significant advantages, such as a high strength to weight ratio and mechanical properties closer to those of natural bone. These implants are biocompatible and biodegradable. Fig. 2. 6a shows a hip implant, which is perhaps one of the most important implants with high load capacity. Other typical examples of shoulder and knee orthopedic implants are seen in Fig. 2. 6b and c respectively [2].

2. 2. 4. Early stages of Mg biodegradable stents

In 1916, Charles Stent used the word “stent” for the first time as a dental impression compound. In 1969, Charles Theodore Dotter implanted a coronary stent in a dog for the first time. In 1986, Jacques Puel inserted the first coronary stent for a patient. The initial trials of Mg for cardiovascular applications date back to 1878, when Huse used Mg wires to successfully stop

bleeding vessels. In 1900, Payr introduced tubular Mg cylinders with thin walls to use as vessel connector [33], which he tested on pigs and the femoral artery of dogs. Payr observed that the vessels at the connection point became solid after 8 days. He also observed highly thickened intima and the formation of a fibrous ring on the outer side at the anastomosis. Payr reported that the thickness of the vessel returned to normal after a waiting period of more than 8 days; he observed that only the intravascularly placed Mg cylinders caused thrombotic blood clotting at the end of the tubes, whereas extravascularly placed tubes caused no thrombosis effect [33]. In 1910, Lespinasse suggested a new design for Mg plate with a punched hole to connect and fix the vessel ends. He did not observe any significant thrombosis in his experiments using these Mg plates [43].

In 1998, Heublein et al [20] restarted the use of Mg as a biodegradable stent. In 2003, they reported the preliminary results from in vitro and in vivo evaluation after the implantation of six Mg alloys into the coronary artery of domestic pigs. In vitro evaluation showed that the biocompatibility of the Mg alloys was high but diminished fast with the release of Al ions present in the alloys. In vivo inflammatory tests on subcutaneous pockets of rats showed that the AE21 (Mg-2Al-1RE where RE=rare-earth)¹ gave minimum inflammatory reactions and H₂ production (which may cause tissue and cell damage). Coronary animal study evaluating WE21 (Mg-2Y-1RE) showed 28 days of stent integrity, good biocompatibility with endothelial and smooth muscle cells. From 2003–2007, animal studies and pre-clinical trials with humans consistently reported safe biodegradation and suggested a desirable prolonged degradation time of Mg alloy stents. In 2006, Waksman et al [21] deployed Mg stents and 316L stainless steel (SS) stents in coronary arteries of domestic or mini-pigs and evaluated in vivo biocompatibility over 3 months. They observed that Mg alloy stents are safe and associated with very low neointima. Its advantages over 316L stent were: (i) a reduction in neointimal formation (Fig. 2. 7), (ii) positive vessel remodeling at the stent site (30–56 days), (iii) complete stent absorption after 56 days, (iv) no evidence of fibrin or thromboembolic events and (v) a minimal degree of inflammation, much lower than 316L stents (Fig. 2. 7). The low thrombogenicity of Mg was attributed to its high electronegativity, compared to other metals, in contact with blood. In 2007, Waksman observed less intimal hyperplasia and an improved lumen area by using adjunct vascular brachytherapy (VBT). However, VBT did not affect the late recoil of the stent [44].

¹ *All alloy compositions in this chapter are in weight% unless otherwise specified.*

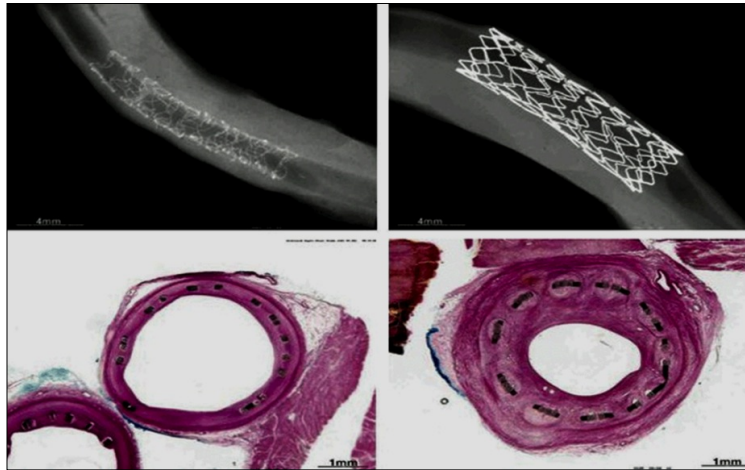


Fig. 2. 7. Mg (left) vs stainless steel (right) stent at 30 days of implantation [17]

The company Biotronik (Germany) evaluated a Mg-7RE (laser cut) stent [45] in a clinical study (PROGRESS-AMS), which demonstrated the Mg alloy stent safety after 12 months in 63 patients, with no incidence of stent thrombosis, heart attack or death [46-48]. Mg stents have been used in pediatric patients with congenital heart disease, and other clinical trials with Mg alloys have been undertaken [46]. Ca and P replaced Mg over time through the body's natural processes. They observed 13.5% vessel thickening around the stented vessel area and 41% in-stent neointimal hyperplasia after 4 months (Fig. 2. 8) [45]. Results after 12 months showed: (i) 47.5% restenosis, (ii) 27% recurrent ischaemia (lack of blood flow to the tissues) and (iii) intervention for vessel reopening (24%). Follow-up studies [49, 50] of the Biotronik stent in the PROGRESS-AMS trial revealed early restenosis in aorto-pulmonary collateral of a baby where, despite the significant initial increase in vessel diameter, restenosis occurred 4 months later. This study stressed again the need for further refinements in Mg alloy stent technology, especially in view of its promising potential for the intervention in children where permanent stent placement is unsuitable [51, 52]. The conclusions from the in vivo studies and pre-clinical trials are: (1) new alloys/methods must be developed to slow down the corrosion rate of Mg stents, (2) the mechanical integrity of Mg alloys must be improved to maintain good vascular support during tissue healing and (3) thick neointima formation must be prevented. The results show that Mg is a promising candidate for use as biodegradable cardiovascular stent material [53, 54], but that it needs to be further developed as a biodegradable stent material.

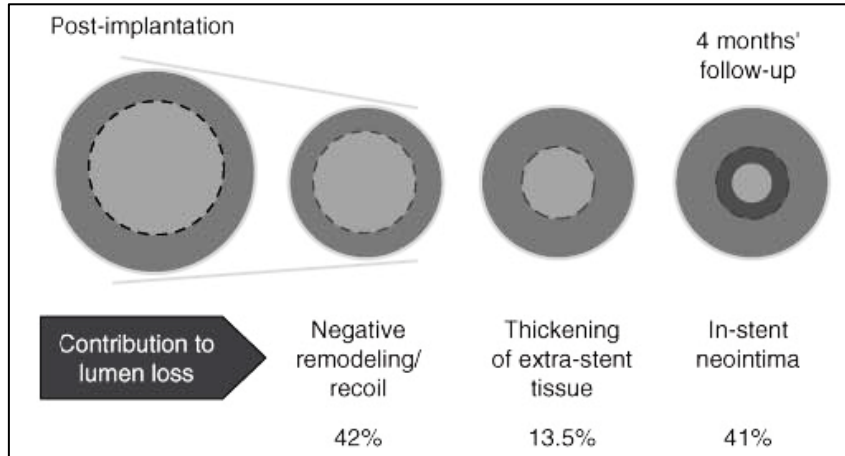


Fig. 2. 8. Schematic presentation of recoil and negative luminal remodeling after 4 months of implantation with PROGRESS AMS-1 trial Biotronik-Germany [45]

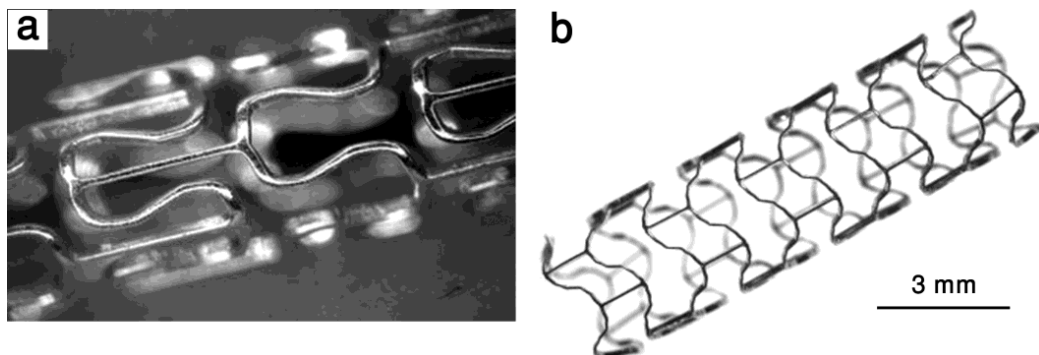


Fig. 2. 9. Lekton Magic coronary stent made from WE43: (a) before and (b) after expansion [26]

The Biotronik developed their second-generation stent with the WE43 (Mg-4Y-3Nd) alloy, which showed better mechanical integrity in animal studies. Fig. 2. 9 shows non-expanded and expanded states of the Lekton Magic coronary stent (Biotronik, Bulach, Switzerland) made from the WE43 alloy for animal study on mini-pigs. The company has been working on their third-generation stent, which is integrated with drug-eluting polymer coating to address the issues related to thick neo-intima and risk of thrombosis and to accelerate tissue healing.

2. 3. Current Research Activities on the Development of Biodegradable Mg Stents

In recent years, Mg alloy development activities have begun focusing on improving biocorrosion behavior and mechanical integrity while maintaining biocompatibility. Current activities can be classified in two groups: (a) the development of improved Mg alloys for biodegradable stents especially with improved corrosion resistance and (b) in vivo and preclinical studies using stents made of certain Mg alloys. The goal has been to have new Mg stents with lower corrosion rate (low mass loss & H₂ evolution) and sufficient mechanical support that contains biocompatible alloying element(s). Various experimental alloys have been evaluated. In this section, the corrosion mechanism of Mg and its alloys, the current research related to the alloying approach to improve the corrosion resistance of Mg and the preclinical studies on biodegradable Mg stents are reviewed.

2. 3. 1. Corrosion mechanisms of Mg and its alloys

The major drawback of Mg as a biodegradable material is its rapid degradation rate. Therefore, understanding the corrosion behavior and the corrosion mechanism can help us overcome this problem and obtain the proper corrosion rate for specific applications [32]. Generally, the mechanism of corrosion in Mg alloys depends on the chemical composition and environmental conditions. There are different forms of corrosion that can occur in Mg alloys: galvanic corrosion, intergranular corrosion, localized corrosion, stress corrosion cracking and corrosion fatigue [53, 55, 56]. Galvanic corrosion is the most probable type of corrosion in Mg alloys in aqueous environments, which can be external when Mg is in contact with another element or internal when there is a secondary phase and impurities in Mg (Fig. 2. 10) [53].

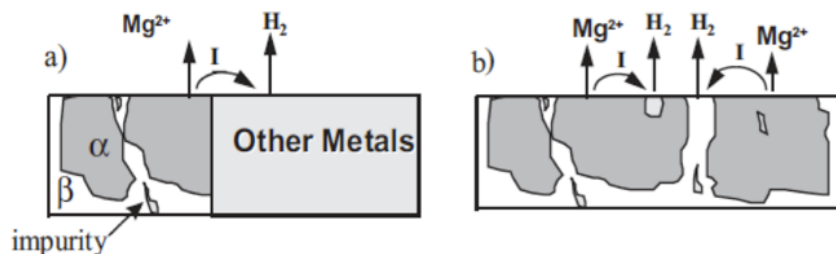


Fig. 2. 10. Illustration of an (a) external galvanic corrosion and (b) internal galvanic corrosion in Mg alloys.

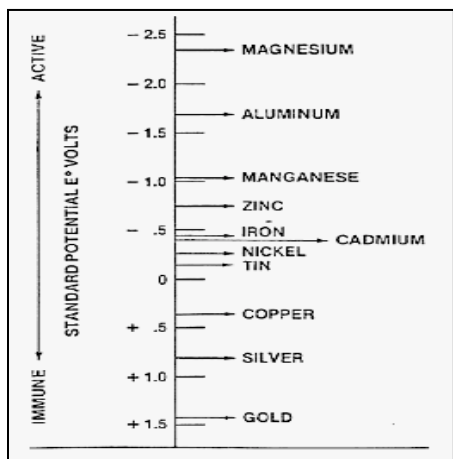


Fig. 2. 11. Electromotive force series [53]

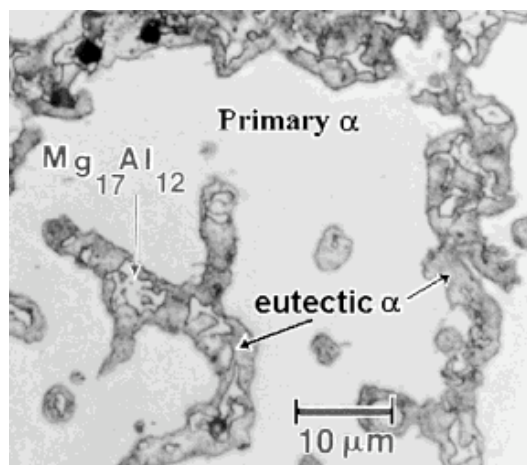


Fig. 2. 12. Microstructure of AZ91D [53]

Due to low hydrogen overvoltage, impurities such as Fe, Ni and Cu promote galvanic corrosion with Mg. Moreover, alloying elements such as Al, Zn and Ce lead to the formation of intermetallic phases usually concentrated in the grain or interdendritic boundaries [53, 56]. Depending on the type of alloying element and its standard potential compared to that of Mg (-2.37 V_{nhe}), the intermetallic phase could be the anode or cathode in galvanic corrosion. As an example, in the case of Al as added to Mg, Mg has lower standard potential compared to Al (Fig. 2. 11). Thus, the intermetallic compounds, such as Mg₁₇Al₁₂, act as a cathode in contact with the Mg matrix especially in the corroding media, such as body fluids containing chloride ions, and make an electrochemical galvanic cell in which Mg is the anode. Fig. 2. 12 shows the microstructure of die cast AZ91D (Mg-9Al-1Zn) where the α -Mg matrix is the anode for the intermetallic phase and corrodes sacrificially [53].

Certain elements, such as Ca, have lower standard potential compared to Mg, such that the Mg matrix will be the cathode in the galvanic corrosion process and the intermetallic phases corrodes during the reaction [57]. Alloying elements with very low standard potential can stimulate the galvanic corrosion in Mg unless there are other mechanisms involved in altering the microstructure and decelerating the corrosion process [53]. Li et al [58] reported that the simultaneous formation of Mg(OH)₂ and hydroxyapatite on the surface of Mg-1Ca alloy slows down its degradation rate in physiological condition. Zhang et al [31] observed the formation of phosphate containing Mg/Ca attached to the surface that prolongs the in vitro degradation of the Mg-6Zn alloy. He also reported that Zn elevates the corrosion potential of Mg alloys and

improves their corrosion resistance. One should consider that the amount of intermetallic phase also plays an important role in Mg alloy corrosion. As an example, we can note that in the case of Mg-Al based cast alloys, the $Mg_{17}Al_{12}$ intermetallic phase (Fig. 2. 12) has two effects on the corrosion depending on its volume fraction and distribution: as a barrier that improves the corrosion resistance and as a galvanic cathode that increases the corrosion rate. Coy et al [59] have investigated the corrosion potential differences between certain intermetallics and the Mg matrix in rare earth containing Mg alloys (Table 2. 3).

Table 2. 3. Voltaic potential differences of the micro-constituents determined by SKPFM [59]

Alloy	Micro-constituent	ΔV (mV)
ZE41 as-cast	Grain boundary	-80 ± 5
	T-phase (Mg_7Zn_3RE)	$+100 \pm 5$
	Zr-Zn-rich	$+180 \pm 10$
WE43-T6 sand-cast	$M_{12}(RE,Y)$	$+25 \pm 5$
	Zn-rich	$+170 \pm 10$
	Y-rich	$+50 \pm 10$
	β -phase	$+15 \pm 5$
WE43-T6 wrought	$M_{12}(RE,Y)$	$+25 \pm 5$
	Zn-rich	$+180 \pm 10$
	Y-rich $< 1\mu m$	$+90 \pm 10$
	β -phase	$+15 \pm 5$
WE54-T6 wrought	$M_{12}(RE,Y)$	$+25 \pm 5$
	Zn-rich	$+250 \pm 10$
	Y-rich	$+50 \pm 10$
	β -phase	$+15 \pm 5$

The corrosion of Mg in aqueous solution can be expressed in three reactions:

- 1) $Mg \rightarrow Mg^{2+} + 2e^-$
- 2) $2H_2O + 2e^- \rightarrow H_2 + 2 OH^-$
- 3) $Mg^{2+} + 2 OH^- \rightarrow Mg(OH)_2$

Mg dissolves in the anodic reaction and hydrogen is reduced in the cathode, which is mostly in the grain boundaries. Continuous Mg dissolution leads to a significant increase in pH value to basic levels. Mg^{2+} and OH^- combine with each other in the interface of the material and the surrounding solution and form a $\text{Mg}(\text{OH})_2$ layer, which can serve as a protective surface film. Thermodynamics shows that this hydroxide layer can provide protection after certain pH levels [53], as is shown in the Pourbaix diagram in Fig. 2. 13. There are many investigations on the corrosion mechanism of Mg to explain the electrochemical reaction in the bulk, on the surface of Mg and in the solution. Four models have been suggested in the literature for pure Mg and its alloys: (1) partially protective surface film: breakage of protective surface film of Mg during anodic dissolution; (2) mono-valent Mg ion model: mono-valent ion Mg^+ produced electrochemically from Mg reacts with H^+ to release hydrogen gas; (3) particle undermining model: most of the intermetallic particles are cathodic to the Mg matrix, which suffers local galvanic corrosion in the grain boundaries; (4) magnesium hydride (MgH_2) model: MgH_2 , which is very reactive in water, forms on the surface of Mg and subsequently decomposes into Mg^{2+} and H_2 [53].

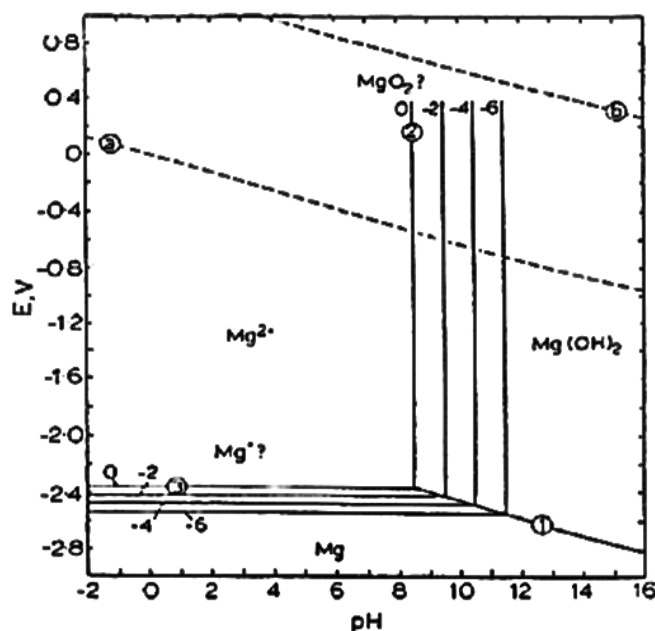
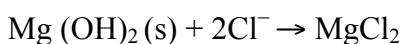
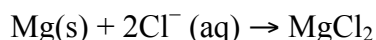


Fig. 2. 13. Pourbaix diagram of $\text{Mg} \pm \text{H}_2\text{O}$ system at 25°C . The region of water stability lies between the lines marked (a) and (b). The different regions are separated by the following reactions: (1) $\text{Mg} + 2 \text{H}_2\text{O} \rightarrow \text{Mg}(\text{OH})_2 + \text{H}_2$; (2) $\text{Mg}^{2+} + \text{H}_2\text{O} \rightarrow \text{MgO} + 2\text{H}^+$; (3) $\text{Mg} \rightarrow \text{Mg}^{2+} + 2 e^-$ [53].

The high rate of degradation of commercially pure Mg is the major drawback for its use in biomedical applications. If a piece of Mg is exposed to a normal atmosphere, a gray oxide layer of magnesium hydroxide ($\text{Mg}(\text{OH})_2$) forms on the surface that has slight solubility in water and slows down the corrosion of Mg. However, in the physiological environment where there is a high concentration of chloride ions (around 150 mmol/L), $\text{Mg}(\text{OH})_2$ film tends to react with Cl^- and produce highly soluble magnesium chloride and hydrogen gas. The corrosion reaction of Mg can be summarized in the following reactions [9]:



Hydrogen is a by-product of the corrosion reaction. The amount of hydrogen gas released from material is a critical point when it is to be used in human body. The hydrogen bubbles evolved from the corrosion of Mg, accumulate in gas pockets close to the biomaterial and postpone the healing process at the surgery region and cause death of tissues due to the separation between tissue layers [60]. Unfortunately, in some cases this can be fatal if it leads to the presence of large hydrogen bubbles in the blood circulation system, especially if Mg is used as a vascular stent [36, 61]. Song observed that a small piece of Mg ($1 \times 1 \times 1 \text{ cm}^3$) could increase the pH value of 250 ml neutral Hank's solution to 10 after 15 h [61]. Moreover, it has been found that in a neutral solution the pH value is always more than 10 in the vicinity of Mg and at the surface of biomaterials due to the formation of OH^- as another by-product of corrosion reactions. This local alkalization can make disturbance in pH-dependent physiological reactions at the region very close to biomaterial and also can cause poisoning if the in vivo pH goes over 7.8 in certain regions [60].

The hydrogen evolution rate is a substantial and accurate parameter to study of biodegradation of Mg. First of all, hydrogen evolution damages the healing process and restricts the development of biodegradable Mg. Moreover, almost 1 ml H_2 releases from 1 mg of dissolved Mg [56]. Thus, measuring hydrogen evolution is one of the simplest ways to evaluate the degradation or corrosion rate of Mg. On the other hand, the evolution of 1 mole H_2 is equal to 2 mole OH^- production [56]. In this way, hydrogen evolution can be used as a good parameter to measure the degree of alkalization in the solution. Consequently, hydrogen evolution can be used as a significant way to investigate biodegradation and corrosion behavior of Mg and its alloys.

The amount of hydrogen gas released from biomaterial during degradation should be less than the tolerable level for the host tissue to absorb or pass hydrogen bubbles through themselves. If large amounts of hydrogen are produced during the degradation process, the host tissue would not be able to accommodate it, which may lead to inflammation and infection around the biomaterial [9, 62]. Fortunately, in most of previous research, it has been observed that hydrogen evolution starts off at a very high rate and then slows down to a stable level. This high amount of hydrogen released during the first days of implantation can be simply removed from the body by syringe [35].

It is clear that the amount of hydrogen evolved from biomaterial is very crucial from a biomedical point of view and needs to be controlled before using Mg as biomedical material. Several techniques exist to control corrosion rate and the subsequent hydrogen evolution rate of Mg, among which alloying element is the most widespread technique used to enhance corrosion resistance and mechanical properties simultaneously.

2. 3. 2. Alloying approach to control the degradation rate of Mg and preclinical studies

In general, commercial Mg alloys designed for other engineering applications have good mechanical properties and corrosion resistance. There are two important classes of these alloys: (i) Mg alloys containing aluminum (Al) (usually between 2-10 wt.%) with small amounts of zinc and manganese, such as AZ31 (3wt.% aluminum, 1 wt.% zinc) and AZ91 (9wt.% aluminum, 1 wt.% zinc), (ii) Mg alloys containing rare earth elements (Y, Ce, Nd, etc.), such as WE43 (71 wt.% Nd, 8 wt.% Ce, 6 wt.% La) and LAE442 (51 wt.% Ce, 22 wt.% La, 16 wt.% Nd, 8 wt.% Pr) [9]. Alloying is an effective technique to improve the mechanical properties, control the degradation rate and facilitate the manufacturing process of Mg biomaterials.

Al and/or rare earth (RE) containing Mg alloys:

Mg alloys (both Al-containing alloys and RE-containing alloys) were used in initial studies related to Mg biomaterials. It is reported that adding RE elements to Mg may lead to improved corrosion resistance [35]. Since the corrosion of biomaterials usually starts from the surface, the surface oxide film plays an important role in their resistivity to corrosion. RE elements may also change the surface oxide film and make it more stable in physiological conditions. Fig. 2. 14

shows the appearance of Mg alloys after an in vitro corrosion test of 50 h immersion in salt water for AZ31 and Mg with and without La. Mg without La is highly degraded [63].

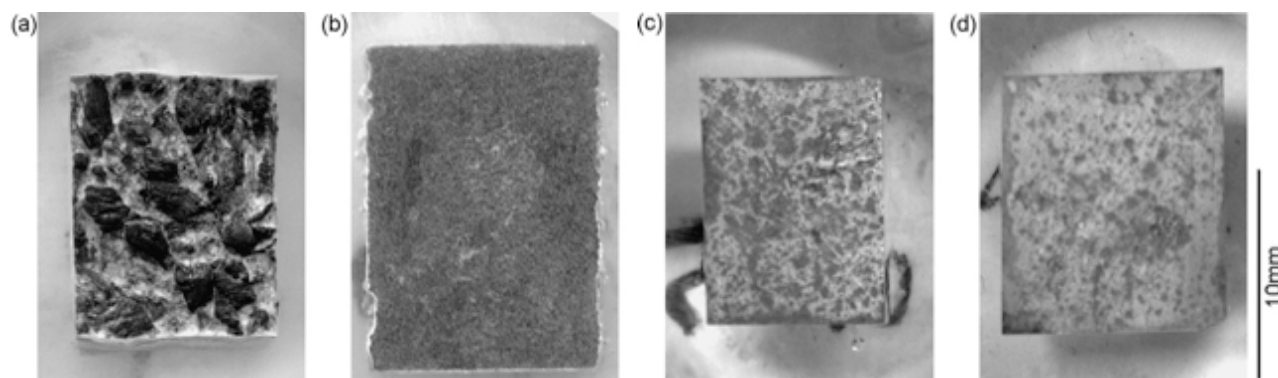


Fig. 2. 14. Appearance of (a) Mg, (b) AZ31, (c) Mg with 0.3 mass%-La and (d) Mg with 0.6 mass%-La after 50 h immersion in salt water [63]

Witte et al [35] demonstrated that rare earth elements could improve the corrosion resistivity of Mg by investigating the degradation mechanisms of different Mg alloys at the bone-implant interface. It was seen that the degradation rate of Mg-based implants depends on the alloy composition. The comparison between in vivo results after 6 and 18 weeks for four different Mg based alloys (AZ31, AZ91, WE43 and LAE442) revealed a significant effect of the alloying elements in the degradation process of Mg biomaterial. AZ31 and AZ91 showed higher corrosion rates, as did WE43, when compared to LAE442 at the same immersion time.

Zhou et al [64] studied the addition of Li to develop a new Mg alloy for cardiovascular stents. Mg-3.5Li, Mg-8.5Li and Mg-8.5Li-1Al did not affect the cell proliferation of VSMCs after 5 days exposure, while Mg-3.5Li-2Al-2RE, Mg-3.5Li-4Al-2RE and Mg-8.5Li-2Al-2RE suppressed the proliferation of these cells. Zhou et al [64] also studied the viability of human umbilical vein endothelial cells (ECV304) in contact with Mg-Li-(Al)-(RE) alloys. Other than Mg-8.5Li-2Al-2RE, none of the samples showed negative effect on the viability of ECV304. However, the presence of Al ions is a concern when using these alloys.

Mao et al [65] introduced a Mg-RE alloy with the chemical composition of Mg-2.5Nd-0.2Zn-0.4Zr (known as JDBM) for use as biodegradable vascular stent. They observed that solution-treated (T4), extruded and annealed JDBM samples have lower degradation rates with homogenous corrosion surface after immersing in artificial plasma when compared to WE43 and AZ31 (Mg-3Al-1Zn) commercial alloys prepared with the same procedure. HUVECs (human

umbilical endothelial cells) in contact with the extraction medium of JDBM alloy showed normal growth and viability except during the first day of exposure, which showed slightly lower viability (grade 2). Cells exposed to JDBM ions had flattened spindle morphology and looked healthier than WE43 and AZ31 after 24 h incubation (Fig. 2. 15a). They also seeded HUVECs directly on the metal substrates of JDBM, WE43 and AZ31 and observed significant differences. Cells showed pseudopodial spreading on the surface of JDBM and WE43 (marked with arrows in Fig. 2. 15b), whereas they appeared as rounded morphology with minimal spreading on AZ31. Results showed that AZ31 does not allow HUVECs to attach and spread easily. Mao et al [66] evaluated long-term in vivo durability and biocompatibility of JDBM; a tubular stent (14 mm length \times 3 mm diameter) made out of JDBM that was implanted in rabbit abdominal aorta showed good tissue compatibility and long-term mechanical integrity after 16 weeks.

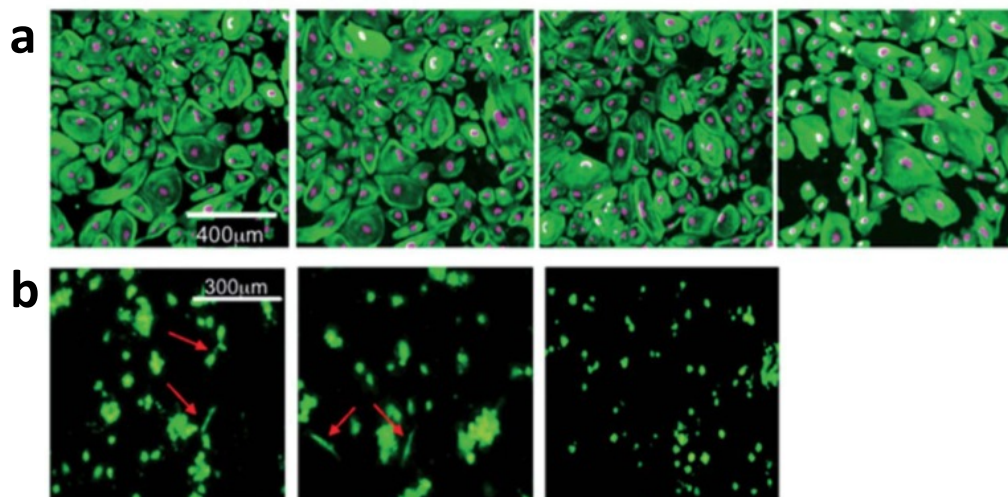


Fig. 2. 15. (a) Immunofluorescence images from the morphology of HUVECs in the control medium and extraction medium from JDBM, WE43 and AZ31 (from left to right) for 24 h. The cells were fixed and stained for cytoskeleton (phalloidin: green) and nuclei (DRAQ5: magenta). (b) Live cell observation of HUVECs direct attachment and elongation on JDBM, WE43 and AZ31 metallic substrates (from left to right) after 24 h.

Hänzi et al [67] studied the suitability of Mg-Y-Zn alloys as biodegradable stents. In vitro corrosion evaluation in simulated physiological media showed homogeneous degradation on the surface with slower hydrogen evolution. Cytocompatibility studies revealed that HUVECs could

tolerate the corrosion products existing in the extraction medium of Mg-Y-Zn. The viability and the metabolic activity of HUVECs decreased with increase in the concentration of the extraction medium, which is due to the dilution of the growth medium and a pH increase from the corrosion products of the reaction. Considering the fact that the concentration of degradation products in the cytocompatibility evaluation is much higher than in the in vivo condition, Mg-Y-Zn is considered to be a potential alloying system as biodegradable stent application. Animal implantation of the Mg-Y-Zn alloy in the abdomen and abdominal wall of mini-pigs showed good wound healing with no inflammatory reactions. Further animal tests had to be considered to evaluate the material's behavior specifically for stent applications. Hänzi et al [67] found Mg-Y-Zn alloys as potential materials for biodegradable cardiovascular stents. These alloys had good combination of electrochemical, mechanical and biological properties. WZ21 (Mg-2Y-1Zn) and ZW21 (Mg-2Zn-1Y) showed good cytocompatibility effect on HUVECs. WZ21 also revealed good in vivo performance and promising biocompatibility in animal study. Mg-1.5Y-1.2Zn-0.44Zr showed superior mechanical properties and good biocompatibility as a biodegradable implant application [68].

However, these alloys are not optimized for biocompatibility. Aluminum-containing Mg alloys release Al ions into the body, which bind to inorganic phosphate causing a lack of phosphate in the body. A high concentration of Al ions in the brain is known to increase the risk of Alzheimer disease [69, 70]. It was reported that rare earth elements such as yttrium, cerium and praseodymium should be used very cautiously due to a high toxicity effect [70].

Newer generation Mg alloys for cardiovascular implants:

In the past few years, there has been growing interest in developing a new Mg system through the addition of various elements such as Ca, Zn, Mn, Li, Sr, etc. that are deemed to offer better biocompatibility.

Calcium (Ca) has low density (1.55 g/cm^3) and is known to have better incorporation into bone in the presence of Mg. The Mg-Ca system with a closer density to bone that stimulates the bone-healing process has been studied as potential material for biodegradable bone implants. Li et al [58] recorded that Mg-1Ca has the best mechanical properties, a lower corrosion rate and acceptable biocompatibility among Mg-xCa ($x=1-3 \text{ wt.}\%$) binary alloys. Wan et al [71] studied the behavior of Mg-Ca alloys with various calcium content and found that Mg alloy containing

0.6 wt.% calcium has the best mechanical and corrosion properties. Hassel et al [36] also demonstrated that Mg-0.6Ca has minimum toxic potential and good workability as well as a very slow corrosion rate. Other investigations also report that the best combination of mechanical and corrosion behavior could be attained in binary Mg-Ca alloys with optimum calcium content ($0.6 < \text{Ca} < 1$ wt.%) and some of these have been considered as biocompatible candidates for biomedical applications [58, 72, 73]. These alloys have been evaluated as bone implants rather than cardiovascular stents. Ca in high doses may not be compatible for the cardiovascular environment; therefore the alloys for stent applications should target low Ca content. Drynda et al [74] increased the corrosion resistance and the mechanical integrity of Mg-Ca alloys by fluoride (MgF_2) coating. Fluoride-coated Mg-Ca samples showed better mechanical properties and slower degradation kinetics in in vitro evaluation. Fluoride-coated Mg-Ca alloys with Ca content of 0.4–0.8 wt.% showed the lowest degradation rate. These samples exhibited good cytocompatibility on human vascular smooth muscle cells (VSMCs) and endothelial cells (ECs) after 10 days.

Zinc (Zn) is another essential element in the body. It participates in nucleic acid metabolism, gene expression and signal transduction. Zinc also interacts with various organic ligands in the body [75]. It increases the mechanical strength of Mg and reduces the corrosion rate. Wang et al [76] coated the surface of Mg-1Zn-0.2Mn with biodegradable poly(1,3-trimethylene carbonate) (PTMC) and observed a significant decrease in the corrosion rate compared to bare Mg. PTMC-coated Mg alloys exhibited good hemocompatibility during in vitro blood testing and maintained ~ 55% of its initial thickness after 16 weeks subcutaneous implantation in rats. Bowen et al [77] considered zinc for coronary stent applications and studied its biocompatibility by deploying 4 wire sample for 1.5 to 6 months in the abdominal aorta of a Sprague–Dawley rat. He found zinc to be a promising biodegradable element to be considered for cardiovascular applications. Zhang et al [31] demonstrated that the addition of 0.6 wt.% Zn reduces the degradation rate of Mg in simulated body fluid (SBF). This alloy shows good biocompatibility; a rod of Mg-0.6Zn, implanted into the femoral shaft of rabbit, degraded with rate of 2.32 mm/yr and did not show any negative effect on the surrounding organs. This alloy was also harmless to L-929 cells. Xu et al [29] studied the combined addition of Zn and Mn on the degradation behavior of Mg. Mg-1.2Mn-1.0Zn accelerates the deposition rate of biological calcium phosphate apatite and the formation of new bone tissue around the implant. ZM21 (Mg-

2Zn-1Mn) is also known to have preferable mechanical properties for use as a biodegradable vascular stent [10].

Strontium (Sr) is also a potential element for medical applications. It is a component of bone and is known to stimulate the growth of osteoblasts and prevent bone resorption [78, 79]. The incorporation of Sr to hydroxyapatite (HA) improves osteoblast function and bone formation [80, 81]. Sr increases the mechanical properties of Mg partly due to its grain refining effect [82]. It also improves the corrosion resistance of Mg because of its surface active effect [83]. Mg-Sr alloys have been recently studied as biodegradable implants. Gu et al [84] evaluated in vivo and in vitro degradation of Mg alloys containing 1-4 wt.% Sr and found that as-rolled Mg-2Sr has the highest corrosion resistance and mechanical strength in this range of composition. This alloy showed acceptable in vitro and in vivo biocompatibility. Brar et al [85] studied the mechanical properties and biodegradation rate of heat-treated Mg-Sr and Mg-Sr-Zn alloys. They found the lowest degradation rate in Mg-2Zn-0.5Sr with moderate mechanical properties. Mg-0.5Sr showed the lowest biodegradation rate among Mg-xSr (x = 0.5, 1, 1.5 wt.%) binary alloys. Li et al [86] evaluated Mg-Zr-Sr alloys (Zr/Sr = 0-5 wt.%) as biodegradable implant material for load-bearing applications. The addition of Zr and Sr improved the mechanical strength and ductility as well as the corrosion resistance of the Mg implant. Mg-1Zr-2Sr, Mg-2Zr-5Sr and Mg-5Zr showed the best cytocompatibility in osteoblast-like SaOS₂ cell. Mg-1Zr-2Sr showed the best in vivo biocompatibility and biodegradability in rabbit model study. They found that the presence of Sr in this alloy increases in vitro biocompatibility and in vivo bone formation. Guan et al [87] evaluated a ZnSr41 (Mg-4Zn-1Sr) alloy for similar load-bearing applications. ZnSr41 showed higher mechanical properties after rolling and aging at 175 °C for 8 h, an ultimate tensile strength of 270 MPa and 12.8% elongation. They observed a significant decrease in corrosion current density from 1.67 mA/mm² in pure Mg to 0.41 mA/mm² in ZSr41. Sr-containing Mg alloys have never been considered as biodegradable cardiovascular stents in the past. Moreover, the exact mechanism through which these alloys corrode and the role of Sr to reduce the degradation rate of Mg have not been understood.

Table 2. 4 gives a summary of the advantages and disadvantages of Mg alloys for stent applications. It also lists research directions needed to be taken to attain fuller development of these alloys before they can be used for biodegradable cardiovascular stents.

Table 2. 4. Mg Stent Alloys, Present Efforts and Future Considerations

Alloy	Advantages	Disadvantages	Future considerations
Mg-Al with Li and/or REs [20, 76]	Mechanical properties	Release of Al ions	Systematic studies on the effect of Al
Mg-RE alloys [45-52, 65-67]	Bio-corrosion resistance and mechanical properties	Risk of thrombosis	Studies on cell proliferation
Mg alloys containing Ca and/or Sr [58, 72-74, 88]	Bio-corrosion resistance; enhanced bio-compatibility, potential to minimize the risk of thrombosis; Mechanical properties	Lack of long-term pre-clinical studies;	Studies on blood compatibility; long-term pre-clinical studies; histological studies

The mechanical properties of biomaterial affect their therapeutical function and need to be optimized for specific use as cardiovascular stent material. The mechanical performance depends on both material properties and the design of the stent (e.g. tubular stents and coil stents). Mathematical modeling has been used to evaluate and optimize the stent design for specific lesions [89-91]. Among the key mechanical performance requirements of metallic cardiovascular stents the following can be cited: stent deployment pressure, elastic recoil, resistance to radial compression forces, foreshortening and flexibility. Table 2.5 lists the mechanical properties of most common metallic materials which has been used as biomedical implants to date [90]. An ideal stent should have high elastic modulus to prevent recoil. Stiffness, however, is both a material property and a design attribute; stiffness can be increased by using a high wall thickness which is more easily achieved with materials of low density. Both elasticity and plasticity are needed for stent expansion during balloon dilatation. Lower yield strength facilitates stent expansion at acceptable balloon pressures and eases the insertion and implantation of the stent through the delivery system. High elastic modulus and low yield together will also prevent spring back of the stent to its original position after dilatation. Low yield strength and high elastic modulus is desired for stent application as outlined above. Smaller Yield stress²/Elastic modulus (Y^2/E) prevents spring back and recoil of material after dilatation. Among materials listed in Table 2.5, the highest Y^2/E ratio is attributed to titanium alloys whereas the lowest Y^2/E ratio is attributed to stainless steel, cobalt-base alloys and Mg-base alloys.

Once the stent is inserted, high tensile property is preferred to ensure high radial strength with less volume of implanted material, which allows the use of thinner designs with more flexibility and deliverability. Higher ductility is very important to prevent stent failure during balloon dilatation [91]. The material needs to be carefully selected for each application, as these properties are difficult to obtain in one material. For instance, materials with high tensile strength usually have high yield strength. In the case of stent applications, high tensile strength to provide high radial strength is favorable whereas high yield strength causes undesired recoil after balloon deflation.

Table 2. 5: Mechanical properties of primary metallic materials used as biomedical implants

Alloy	Density g/cm ³	Elastic Modulus (E) GPa	Ultimate Tensile Strength, MPa	0.2% Yield Strength (Y), MPa	Elongation (%)	Y ² /E
Fe-18Cr-14Ni-2.5Mo	7.95	193	670	340	48	0.6
Fe-21Cr-10Ni-3.5Mn-2.5Mo	7.90	195	740	430	35	0.9
Fe-22Cr-13Ni-5Mn	7.88	193	827	448	45	1.0
Fe-23Mn-21Cr-1Mo-1N	7.63	190	931	607	49	1.9
Co-20Cr-15W-10Ni	9.10	243	820-1200	380-780	35-55	0.6-2.5
Co-20Cr-35Ni-10Mo	8.43	233	930	414	45	0.7
Ti-6Al-4V	4.43	105	860	795	10	6
Ti-6Al-7Nb	4.74	106	1000	900	12	7.6
NITINOL Martensitic	6.45	40	1200	200-300	25	1-2.2
Mg-3Al-1Z	1.8	45	255	162	10-25	0.6

2. 4. Testing methods used in the evaluation of biodegradable Mg biomaterials

2.4.1 In vitro testing and characterization

The corrosion behavior of metallic alloys for biomedical applications is usually studied through electrochemical and immersion tests. In both techniques, samples need to be tested in simulated body fluid. Among the various electrochemical testing methods, the potentiodynamic polarization test has been used widely to evaluate the corrosion rate of biodegradable Mg samples. In this technique, the sample is placed in a three-electrode cell containing an SBF solution. The main parameters of this test are the anodic and cathodic curves, anodic Tafel slope

(β_a) and the cathodic Tafel slope (β_c), which are shown in Fig. 2. 16. The E_{corr} and i_{corr} values can be estimated using the Tafel extrapolation method and linear fit to the anodic and cathodic parts of the polarization curves. The corrosion rate of the sample can be estimated using E_{corr} and i_{corr} [31, 64, 86, 92, 93]. Due to the fast degradation rate of Mg alloys, the electrochemical test alone cannot give much information about the degradation behavior of Mg samples. In vitro immersion of Mg samples in SBF provides the opportunity to study the degradation behavior of Mg samples step by step. The corrosion rate of the Mg sample can be monitored in terms of mass loss and the volume of hydrogen gas produced during the reaction. The in vitro immersion test has been described in detail in Chapter 3 of this thesis.

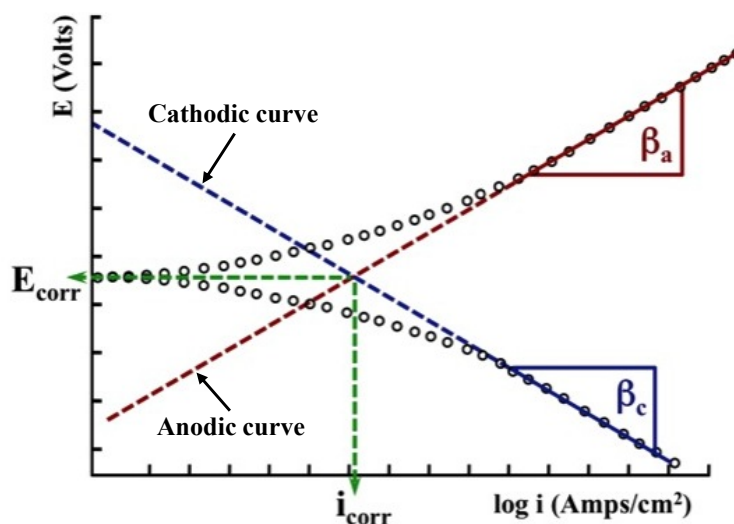


Fig. 2. 16. Schematic curves obtain from Tafel extrapolation method [94]

SEM characterization is usually used for general observation on the surface morphology of Mg samples after the immersion test. EDS and XRD analyses also assist in the evaluation of the chemical composition and crystal structure of the corrosion products formed on the surface. However, the information obtained from these techniques comes from a larger volume underneath the surface. More accurate surface analysis techniques are needed to analyze the surface composition and elucidate the corrosion mechanism of Mg alloys. X-ray photoelectron spectroscopy (XPS) is the most widely used surface characterization technique for Mg alloys. Feliu et al [95, 96] applied XPS to understand the surface chemistry and atmospheric corrosion of Mg alloys such as AZ31, AZ80 and AZ91D. He observed ~ 3 nm thin oxide film on the

surface of Mg-Al alloy in contact with air. A similar sample showed corrosion film with more than 1 μm thickness (mostly consist of carbonate) after exposure to humid atmosphere [97]. Wang et al [98] used XPS to study the surface chemistry of AZ31 and AZ91 immersed in NaCl solution for aerospace and automotive applications. Brar et al [99] analyzed the chemical composition of the oxide layer formed on the surface of Mg-3Sc-3Y to be used as biodegradable implant material. He reported that the presence of additional elements leads to the formation of more stable oxide surface compared to original oxide (MgO) film and reduces the initial degradation rate.

The formation of a passive layer can act as a barrier on the surface of the implant material and reduces the degradation rate in the physiological environment. This layer can form on the surface of the material naturally, such as oxide, hydroxide and carbonate, or it can be deposited on the surface due to various surface treatment techniques.

Researchers have used hydroxyapatite (HA), $\text{Ca}_{10}(\text{PO}_4)_6(\text{OH})_2$, as a biocompatible coating to improve the corrosion resistance of Mg implants [100]. HA is a biological mineral of the apatite family that is widely used as a biomaterial. Geng et al [101] observed that the biocompatibility of pure Mg increases by adding β -TCP (β -tricalcium phosphate) coating on the surface; β -TCP is a precursor of HA. It is also reported that some of Ca ions in the crystal structure of HA can be replaced with other elements such as Mg, Sr, Zn and Y, which produce substituted HA. Ergun et al [102] observed that the grain size of these substituted apatites are smaller than those of pure HA. Kung et al [103] found that Sr-containing HA coating can improve the bioactivity and bio-corrosion resistance of titanium alloys. Sr-HA is also known to have better biocompatibility, thermal stability and surface reactivity compared to pure HA [104].

2. 4. 2. Biocompatibility evaluation, in vivo testing and post-implant histological studies

Biocompatibility evaluation techniques for biomaterials are classified in two major groups: in vitro and in vivo tests. In vitro studies are usually the first step of biocompatibility evaluation, since these studies are generally cheaper and easier to carry out compared to in vivo studies. Cells, proteins and tissues are used for in vitro tests to examine the cytotoxicity of materials and their components. The most commonly used method to evaluate in vitro biocompatibility is to examine the cell viability in the presence of the material. This test can be performed as direct or indirect assays. In direct cell viability assay, cells are adhered to and grown on the surface of the material, whereas in indirect viability assay, cells are exposed to the medium containing

extracted ions from the sample [31, 86, 105]. The cytocompatibility of biodegradable Mg implants has been evaluated via both techniques using different types of cells; osteoblast-like cells such as MC3T3-E1 and vascular cells such as HUVEC are common cell lines used for bone and cardiovascular applications respectively [67, 105].

In vivo biocompatibility evaluation involves surgery on animal models to study the interaction between material and host tissue and to predict the performance and effectiveness of medical device in the body. Animal study is usually employed after in vitro tests to better understand the effects of new material on living organism. Animals such as mice, rats, rabbits, dogs, pigs, etc. are used for animal trials depending on the type and size of the medical device [67, 86, 105]. Witte et al [35] implanted biodegradable Mg-based rods into the femora of guinea pigs for 6 and 18 weeks to evaluate the bone cell activation effect of Mg ions. Li et al [86] implanted cylindrical samples of Mg alloys by drilling a cavity into the cortical bone on a rabbit model to evaluate the in vivo bone formation. Höpfner used a dog model for the implantation of Mg as a vessel connector [33]. Payr implanted a vessel connector made of a Mg sample in the femoral artery of both pigs and dogs [33].

During animal testing, radiographic evaluation and other clinical test are often used to study the performance and effect of material on treating process. Once the treatment is completed, histological evaluation is performed to study the structure of both the tissue and the cells. In this process the tissue is preserved in formalin (fixation process), dehydrated, embedded in paraffin and sectioned into small slices of the tissue. Following that, the sample is mounted on microscopic slides and stained to identify different cells and tissues. This will allow the observation of features that are not possible to distinguish otherwise. Hematoxylin and eosin (H&E) are the most widely used stains in histology. When applied on the tissue, hematoxylin marks negatively charged features like DNA with a blue color. Eosin, as the counterstain, marks the other cellular structure with a red color to provide the necessary contrast among different cell components [106]. Microscopic observation is also performed on post-implantation samples and/or tissue to investigate the material-tissue interaction [5]. In the case of various groups for animal studies, the analysis of variation (ANOVA) is usually conducted for statistical analysis and to evaluate the differences between groups.

There are also other in vitro and in vivo techniques to evaluate the blood-material interactions (BMT test), such as blood compatibility, thrombogenicity and platelet adhesion [5].

These techniques are beyond the scope of this PhD project, which is focused on the field of materials engineering rather than biomedical engineering.

2. 5. References

- [1] Clinical Applications of Biomaterials: National Institutes of Health (NIH); 1982.
- [2] Batchelor A, Chandrasekaran M. Service characteristics of biomedical materials and implants2004.
- [3] Temenoff JS, Mikos AG. Review: tissue engineering for regeneration of articular cartilage. *Biomaterials*. 2000;21:431-40.
- [4] Stupp SI, Donners J, Li LS, Mata A. Expanding frontiers in biomaterials. *Mrs Bulletin*. 2005;30:864-73.
- [5] Ratner BD, Hoffman AS, Schoen FJ, Lemons JE. *Biomaterials Science: An Introduction to Materials in Medicine*: Elsevier Academic Press 2004.
- [6] Navarro M, Michiardi A, Castano O, Planell JA. Biomaterials in orthopaedics. *Journal of the Royal Society Interface*. 2008;5.
- [7] Niinomi M, Nakai M, Hieda J. Development of new metallic alloys for biomedical applications. *Acta Biomaterialia*. 2012;8.
- [8] Niinomi M. Recent metallic materials for biomedical applications. *Metallurgical and Materials Transactions a-Physical Metallurgy and Materials Science*. 2002;33:477-86.
- [9] Staiger MP, Pietak AM, Huadmai J, Dias G. Magnesium and its alloys as orthopedic biomaterials: A review. *Biomaterials*. 2006;27:1728-34.
- [10] Fang G, Ai W-J, Lee S, Duszczek J, Zhou J. Multipass cold drawing of magnesium alloy minitubes for biodegradable vascular stents. *Materials science & engineering C, Materials for biological applications*. 2013;33:3481-8.
- [11] Moravej M, Mantovani D. Biodegradable Metals for Cardiovascular Stent Application: Interests and New Opportunities. *International Journal of Molecular Sciences*. 2011;12:4250-70.
- [12] Hermawan H, Mantovani D. Degradable metallic biomaterials: the concept, current developments and future directions. *Minerva Biotechnologica*. 2009;21:207-16.
- [13] Hermawan H, Dube D, Mantovani D. Developments in metallic biodegradable stents. *Acta Biomaterialia*. 2010;6:1693-7.

- [14] Saito S. New horizon of bioabsorbable stent. *Catheterization and Cardiovascular Interventions*. 2005;66:595-6.
- [15] Boffetta P. Carcinogenicity of trace-elements with reference to evaluations made by the international-agency-for-research-on-cancer. *Scandinavian Journal of Work Environment & Health*. 1993;19:67-70.
- [16] Chan AW, Moliterno DJ. In-stent restenosis: Update on intracoronary radiotherapy. *Cleveland Clinic Journal of Medicine*. 2001;68:796-803.
- [17] Erne P, Schier M, Resink TJ. The road to bioabsorbable stents: Reaching clinical reality? *Cardiovascular and Interventional Radiology*. 2006;29:11-6.
- [18] Mirensky TL, Nelson GN, Brennan MP, Roh JD, Hibino N, Yi T, et al. Tissue-engineered arterial grafts: long-term results after implantation in a small animal model. *Journal of Pediatric Surgery*. 2009;44:1127-33.
- [19] Grewe PH, Thomas D, Machraoui A, Barmeyer J, Muller KM. Coronary morphologic findings alter stent implantation. *American Journal of Cardiology*. 2000;85:554-8.
- [20] Heublein B, Rohde R, Kaese V, Niemeyer M, Hartung W, Haverich A. Biocorrosion of magnesium alloys: a new principle in cardiovascular implant technology? *Heart*. 2003;89:651-6.
- [21] Waksman R, Pakala R, Kuchulakanti PK, Baffour R, Hellenga D, Seabron R, et al. Safety and efficacy of bioabsorbable magnesium alloy stents in porcine coronary arteries. *Catheterization and Cardiovascular Interventions*. 2006;68:607-17.
- [22] Tan LL, Yu XM, Wan P, Yang K. Biodegradable Materials for Bone Repairs: A Review. *Journal of Materials Science & Technology*. 2013;29:503-13.
- [23] Tsuji T, Tamai H, Igaki K, Kyo E, Kosuga K, Hata T, et al. Biodegradable Polymeric Stents. *Curr Interv Cardiol Rep*. 2001;3:10-7.
- [24] Serruys PW, Ong ATL. Coronary-artery stents - Reply. *New England Journal of Medicine*. 2006;354:2078-.
- [25] Pierson D, Edick J, Tauscher A, Pokorney E, Bowen P, Gelbaugh J, et al. A simplified in vivo approach for evaluating the bioabsorbable behavior of candidate stent materials. *Journal of Biomedical Materials Research Part B-Applied Biomaterials*. 2012;100B:58-67.
- [26] Peuster M, Beerbaum P, Bach FW, Hauser H. Are resorbable implants about to become a reality? *Cardiology in the Young*. 2006;16:107-16.

- [27] Waksman R, Pakala R, Baffour R, Seabron R, Hellinga D, Tio FO. Short-term effects of biocorrosible iron stents in porcine coronary arteries. *Journal of Interventional Cardiology*. 2008;21:15-20.
- [28] Peuster M, Wohlsein P, Brugmann M, Ehlerding M, Seidler K, Fink C, et al. A novel approach to temporary stenting: degradable cardiovascular stents produced from corrodible metal - results 6-18 months after implantation into New Zealand white rabbits. *Heart*. 2001;86:563-9.
- [29] Xu L, Yu G, Zhang E, Pan F, Yang K. In vivo corrosion behavior of Mg-Mn-Zn alloy for bone implant application. *Journal of Biomedical Materials Research Part A*. 2007;83A:703-11.
- [30] Durlach J. Overview of magnesium research: History and current trends. *New Perspectives in Magnesium Research: Nutrition and Health*. 2007:3-10.
- [31] Zhang S, Zhang X, Zhao C, Li J, Song Y, Xie C, et al. Research on an Mg-Zn alloy as a degradable biomaterial. *Acta Biomaterialia*. 2010;6:626-40.
- [32] Zeng R, Dietzel W, Witte F, Hort N, Blawert C. Progress and challenge for magnesium alloys as biomaterials. *Advanced Engineering Materials*. 2008;10:B3-B14.
- [33] Witte F. The history of biodegradable magnesium implants: A review. *Acta Biomaterialia*. 2010;6:1680-92.
- [34] Saris NEL, Mervaala E, Karppanen H, Khawaja JA, Lewenstam A. Magnesium - An update on physiological, clinical and analytical aspects. *Clinica Chimica Acta*. 2000;294:1-26.
- [35] Witte F, Kaese V, Haferkamp H, Switzer E, Meyer-Lindenberg A, Wirth CJ, et al. In vivo corrosion of four magnesium alloys and the associated bone response. *Biomaterials*. 2005;26:3557-63.
- [36] Hassel T, Bach F-W, Golovko A, Krause C. Investigation of the mechanical properties and the corrosion behavior of low alloyed magnesium-calcium-alloys for use as absorbable biomaterial in the implant technique. In: Pegguleryuz M, Mackenzie L, editors. 45th Annual Conference of Metallurgists of CIM. Montreal: Magnesium Technology in the Global Age; 2006. p. 359.
- [37] Romani A, Scarpa A. Regulation of cell magnesium. *Archives of Biochemistry and Biophysics*. 1992;298:1-12.
- [38] Hartwig A. Role of magnesium in genomic stability. *Mutation Research-Fundamental and Molecular Mechanisms of Mutagenesis*. 2001;475:113-21.

- [39] Vormann J. Magnesium: nutrition and metabolism. *Molecular aspects of medicine*. 2003;24:27-37.
- [40] Brink EJ, Beynen AC. Nutrition and magnesium absorption - a review. *Progress in Food and Nutrition Science*. 1992;16:125-62.
- [41] Wolf FI, Cittadini A. Chemistry and biochemistry of magnesium. *Molecular aspects of medicine*. 2003;24:3-9.
- [42] Nagels J, Stokdijk M, Rozing PM. Stress shielding and bone resorption in shoulder arthroplasty. *Journal of Shoulder and Elbow Surgery*. 2003;12:35-9.
- [43] Lespinasse VD, Fisher GC, Eisenstaedt J. A practical mechanical method of end-to-end anastomosis of blood-vessels - Using absorbable magnesium rings. *Journal of the American Medical Association*. 1910;55:1785-90.
- [44] Waksman R, Pakala R, Okabe T, Hellings D, Chan R, Tio MO, et al. Efficacy and safety of absorbable metallic stents with adjunct intracoronary beta radiation in porcine coronary arteries. *Journal of interventional cardiology*. 2007;20:367-72.
- [45] Ramcharitar S, Serruys PW. Fully Biodegradable Coronary Stents Progress to Date. *American Journal of Cardiovascular Drugs*. 2008;8:305-14.
- [46] Zartner P, Cesnjevar R, Singer H, Weyand M. First successful implantation of a biodegradable metal stent into the left pulmonary artery of a preterm baby. *Catheterization and Cardiovascular Interventions*. 2005;66:590-4.
- [47] Di Mario C, Griffiths H, Goktekin O, Peeters N, Verbist J, Bosiers M, et al. Drug-eluting bioabsorbable magnesium stent. *Journal of interventional cardiology*. 2004;17:391-5.
- [48] LANCET. New Biodegradable Magnesium Stents For Coronary Arteries. <http://www.medicalnewstoday.com/releases/72981.php>. 2007.
- [49] McMahan CJ, Oslizlok P, Walsh KP. Early restenosis following biodegradable stent implantation in an aortopulmonary collateral of a patient with pulmonary atresia and hypoplastic pulmonary arteries. *Catheterization and Cardiovascular Interventions*. 2007;69:735-8.
- [50] Waksman R, Erbel R, Di Mario C, Bartunek J, de Bruyne B, Eberli FR, et al. Early- and Long-Term Intravascular Ultrasound and Angiographic Findings After Bioabsorbable Magnesium Stent Implantation in Human Coronary Arteries. *Jacc-Cardiovascular Interventions*. 2009;2:312-20.

- [51] Schranz D, Zartner P, Michel-Behnke I, Akinturk H. Bioabsorbable metal stents for percutaneous treatment of critical recoarctation of the aorta in a newborn. *Catheterization and Cardiovascular Interventions*. 2006;67:671-3.
- [52] Zartner P, Buettner M, Singer H, Sigler M. First biodegradable metal stent in a child with congenital heart disease: Evaluation of macro and histopathology. *Catheterization and Cardiovascular Interventions*. 2007;69:443-6.
- [53] Song GL, Atrens A. Corrosion mechanisms of magnesium alloys. *Advanced Engineering Materials*. 1999;1:11-33.
- [54] Levesque J, Hermawan H, Dube D, Mantovani D. Design of a pseudo-physiological test bench specific to the development of biodegradable metallic biomaterials. *Acta Biomaterialia*. 2008;4:284-95.
- [55] Song GL, Atrens A. Understanding magnesium corrosion - A framework for improved alloy performance. *Advanced Engineering Materials*. 2003;5:837-58.
- [56] Song GL. Recent progress in corrosion and protection of magnesium alloys. *Advanced Engineering Materials*. 2005;7:563-86.
- [57] Suedholz AD, Kirkland NT, Buchheit RG, Birbilis N. Electrochemical Properties of Intermetallic Phases and Common Impurity Elements in Magnesium Alloys. *Electrochemical and Solid State Letters*. 2011;14:C5-C7.
- [58] Li Z, Gu X, Lou S, Zheng Y. The development of binary Mg-Ca alloys for use as biodegradable materials within bone. *Biomaterials*. 2008;29:1329-44.
- [59] Coy AE, Viejo F, Skeldon P, Thompson GE. Susceptibility of rare-earth-magnesium alloys to micro-galvanic corrosion. *Corrosion Science*. 2010;52:3896-906.
- [60] Song G. Control of biodegradation of biocompatible magnesium alloys. *Corrosion Science*. 2007;49:1696-701.
- [61] Song G, Song S. Magnesium as a possible degradable bio-compatible material. In: Pekguleryuz M, Mackenzie L, editors. 45th Annual Conference of Metallurgists of CIM. Montreal: Magnesium Technology in the Global Age; 2006. p. 359.
- [62] Li LC, Gao JC, Wang Y. Evaluation of cyto-toxicity and corrosion behavior of alkali-heat-treated magnesium in simulated body fluid. *Surface & Coatings Technology*. 2004;185:92-8.
- [63] Takenaka T, Ono T, Narazaki Y, Naka Y, Kawakami M. Improvement of corrosion resistance of magnesium metal by rare earth elements. *Electrochimica Acta*. 2007;53:117-21.

- [64] Zhou WR, Zheng YF, Leeftang MA, Zhou J. Mechanical property, biocorrosion and in vitro biocompatibility evaluations of Mg-Li-(Al)-(RE) alloys for future cardiovascular stent application. *Acta Biomaterialia*. 2013;9:8488-98.
- [65] Mao L, Yuan GY, Wang SH, Niu JL, Wu GH, Ding WJ. A novel biodegradable Mg-Nd-Zn-Zr alloy with uniform corrosion behavior in artificial plasma. *Materials Letters*. 2012;88:1-4.
- [66] Mao L, Shen L, Niu J, Zhang J, Ding W, Wu Y, et al. Nanophasic biodegradation enhances the durability and biocompatibility of magnesium alloys for the next-generation vascular stents. *Nanoscale*. 2013;5:9517-22.
- [67] Haenzi AC, Gerber I, Schinhammer M, Loeffler JF, Uggowitzer PJ. On the in vitro and in vivo degradation performance and biological response of new biodegradable Mg-Y-Zn alloys. *Acta Biomaterialia*. 2010;6.
- [68] Fan J, Qiu X, Niu XD, Tian Z, Sun W, Liu XJ, et al. Microstructure, mechanical properties, in vitro degradation and cytotoxicity evaluations of Mg-1.5Y-1.2Zn-0.44Zr alloys for biodegradable metallic implants. *Materials Science & Engineering C-Materials for Biological Applications*. 2013;33:2345-52.
- [69] Hort N, Huang Y, Fechner D, Stoermer M, Blawert C, Witte F, et al. Magnesium alloys as implant materials - Principles of property design for Mg-RE alloys. *Acta Biomaterialia*. 2010;6:1714-25.
- [70] Feyerabend F, Fischer J, Holtz J, Witte F, Willumeit R, Druecker H, et al. Evaluation of short-term effects of rare earth and other elements used in magnesium alloys on primary cells and cell lines. *Acta Biomaterialia*. 2010;6:1834-42.
- [71] Wan Y, Xiong G, Luo H, He F, Huang Y, Zhou X. Preparation and characterization of a new biomedical magnesium-calcium alloy. *Materials & Design*. 2008;29:2034-7.
- [72] Ilich JZ, Kerstetter JE. Nutrition in bone health revisited: A story beyond calcium. *Journal of the American College of Nutrition*. 2000;19.
- [73] Gu XN, Zheng W, Cheng Y, Zheng YF. A study on alkaline heat treated Mg-Ca alloy for the control of the biocorrosion rate. *Acta Biomaterialia*. 2009;5:2790-9.
- [74] Drynda A, Hassel T, Hoehn R, Perz A, Bach F-W, Peuster M. Development and biocompatibility of a novel corrodible fluoride-coated magnesium-calcium alloy with improved degradation kinetics and adequate mechanical properties for cardiovascular applications. *Journal of Biomedical Materials Research Part A*. 2010;93A:763-75.

- [75] Hambidge KM, Krebs NF. Zinc deficiency: A special challenge. *Journal of Nutrition*. 2007;137:1101-5.
- [76] Wang J, He Y, Maitz MF, Collins B, Xiong K, Guo L, et al. A surface-eroding poly(1,3-trimethylene carbonate) coating for fully biodegradable magnesium-based stent applications: Toward better biofunction, biodegradation and biocompatibility. *Acta biomaterialia*. 2013;9:8678-89.
- [77] Bowen PK, Drelich J, Goldman J. Zinc exhibits ideal physiological corrosion behavior for bioabsorbable stents. *Advanced materials (Deerfield Beach, Fla)*. 2013;25:2577-82.
- [78] Nielsen SP. The biological role of strontium. *Bone*. 2004;35:583-8.
- [79] Dahl SG, Allain P, Marie PJ, Mauras Y, Boivin G, Ammann P, et al. Incorporation and distribution of strontium in bone. *Bone*. 2001;28:446-53.
- [80] Zhang W, Shen Y, Pan H, Lin K, Liu X, Darvell BW, et al. Effects of strontium in modified biomaterials. *Acta Biomaterialia*. 2011;7:800-8.
- [81] Bigi A, Boanini E, Capuccini C, Gazzano M. Strontium-substituted hydroxyapatite nanocrystals. *Inorganica Chimica Acta*. 2007;360:1009-16.
- [82] Zeng XQ, Wang YX, Ding WJ, Luo AA, Sachdev AK. Effect of strontium on the microstructure, mechanical properties, and fracture behavior of AZ31 magnesium alloy. *Metallurgical and Materials Transactions a-Physical Metallurgy and Materials Science*. 2006;37A:1333-41.
- [83] Pegguleryuz M. An overview of the effects of Calcium and Strontium on the properties of Aluminum and Magnesium alloys. IMMC (15th International Metallurgy and Materials Congress). Istanbul, Turkey 2010.
- [84] Gu XN, Xie XH, Li N, Zheng YF, Qin L. In vitro and in vivo studies on a Mg-Sr binary alloy system developed as a new kind of biodegradable metal. *Acta Biomaterialia*. 2012;8:14.
- [85] Brar HS, Wong J, Manuel MV. Investigation of the mechanical and degradation properties of Mg-Sr and Mg-Zn-Sr alloys for use as potential biodegradable implant materials. *Journal of the mechanical behavior of biomedical materials*. 2012;7:87-95.
- [86] Li Y, Wen C, Mushahary D, Sravanthi R, Harishankar N, Pande G, et al. Mg-Zr-Sr alloys as biodegradable implant materials. *Acta biomaterialia*. 2012;8:3177-88.
- [87] Guan R-G, Cipriano AF, Zhao Z-Y, Lock J, Tie D, Zhao T, et al. Development and evaluation of a magnesium-zinc-strontium alloy for biomedical applications - Alloy processing,

microstructure, mechanical properties, and biodegradation. *Materials science & engineering C, Materials for biological applications*. 2013;33:3661-9.

[88] Kirkland NT, Staiger MP, Nisbet D, Davies CHJ, Birbilis N. Performance-driven design of Biocompatible Mg alloys. *Jom*. 2011;63:28-34.

[89] Etave F, Finet G, Boivin M, Boyer JC, Rioufol G, Thollet G. Mechanical properties of coronary stents determined by using finite element analysis. *Journal of Biomechanics*. 2001;34:1065-75.

[90] Poncin P, Proft J. Stent Tubing: Understanding the Desired Attributes. *Materials & Processes for Medical Devices: ASM international*; 2003.

[91] Dyet JF, Watts WG, Ettles DF, Nicholson AA. Mechanical Properties of Metallic Stents: How Do These Properties Influence the Choice of Stent for Specific Lesions? *Cardiovasc Intervent Radiol* 2000;23:47-54.

[92] Wang HX, Guan SK, Wang X, Ren CX, Wang LG. In vitro degradation and mechanical integrity of Mg-Zn-Ca alloy coated with Ca-deficient hydroxyapatite by the pulse electrodeposition process. *Acta Biomaterialia*. 2010;6:1743-8.

[93] Hong D, Saha P, Chou D-T, Lee B, Collins BE, Tan Z, et al. In vitro degradation and cytotoxicity response of Mg-4% Zn-0.5% Zr (ZK40) alloy as a potential biodegradable material. *Acta Biomaterialia*. 2013;9:8534-47.

[94] <http://www.gscsg.com/tafel-extrapolation.html>.

[95] Feliu S, Jr., Merino MC, Arrabal R, Coy AE, Matykina E. XPS study of the effect of aluminium on the atmospheric corrosion of the AZ31 magnesium alloy. *Surface and Interface Analysis*. 2009;41:143-50.

[96] Feliu S, Jr., Pardo A, Merino MC, Coy AE, Viejo F, Arrabal R. Correlation between the surface chemistry and the atmospheric corrosion of AZ31, AZ80 and AZ91D magnesium alloys. *Applied Surface Science*. 2009;255:4102-8.

[97] Feliu S, C M, Juan Carlos G, Angel P, Maria Concepción M, Raul A. The application of x-ray photoelectron spectroscopy in understanding corrosion mechanisms of magnesium and mg-al alloys. *The Open Surface Science Journal*. 2011;3:1-14.

[98] Wang L, Shinohara T, Zhang B-P. XPS study of the surface chemistry on AZ31 and AZ91 magnesium alloys in dilute NaCl solution. *Applied Surface Science*. 2010;256:5807-12.

- [99] Brar HS, Ball JP, Berglund IS, Allen JB, Manuel MV. A study of a biodegradable Mg-3Sc-3Y alloy and the effect of self-passivation on the in vitro degradation. *Acta Biomaterialia*. 2013;9:5331-40.
- [100] Pereiro I, Rodríguez-Valencia C, Serra C, Solla EL, Serra J, González P. Pulsed laser deposition of strontium-substituted hydroxyapatite coatings. *Applied Surface Science*. 2012;258:6.
- [101] Geng F, Tan LL, Jin XX, Yang JY, Yang K. The preparation, cytocompatibility, and in vitro biodegradation study of pure beta-TCP on magnesium. *Journal of Materials Science-Materials in Medicine*. 2009;20:1149-57.
- [102] Ergun C, Webster TJ, Bizios R, Doremus RH. Hydroxylapatite with substituted magnesium, zinc, cadmium, and yttrium. I. Structure and microstructure. *Journal of Biomedical Materials Research*. 2002;59:305-11.
- [103] Kung K-C, Lee T-M, Lui T-S. Bioactivity and corrosion properties of novel coatings containing strontium by micro-arc oxidation. *Journal of Alloys and Compounds*. 2010;508:384-90.
- [104] Suganthi RV, Elayaraja K, Joshy MIA, Chandra VS, Girija EK, Kalkura SN. Fibrous growth of strontium substituted hydroxyapatite and its drug release. *Materials Science & Engineering C-Materials for Biological Applications*. 2011;31:593-9.
- [105] Chou D-T, Hong D, Saha P, Ferrero J, Lee B, Tan Z, et al. In vitro and in vivo corrosion, cytocompatibility and mechanical properties of biodegradable Mg-Y-Ca-Zr alloys as implant materials. *Acta Biomaterialia*. 2013;9:8518-33.
- [106] Yuehuei HA, Kylie LM. *Handbook of Histology Methods for Bone and Cartilage*: Humana Press; 2003.

CHAPTER 3

EXPERIMENTAL PROCEDURE

This thesis is written in a manuscript-based format. Thus, most of the experimental procedures are described in the chapters containing the manuscripts (Chapters 4-6). However, additional detailed information on the experimental techniques employed is provided in this chapter.

3. 1. Alloy synthesis and casting

Pure Mg (99.9 wt.%), pure Sr (99.99 wt.%) and Mg-30Ca master alloy, all supplied by Applied Magnesium (Formerly Timminco), was used to synthesize all the Mg alloys with various strontium and calcium levels.



Fig. 3. 1. Casting procedure: (a) melting in graphite crucible with induction furnace, (b) pouring the melt into the preheated die, (c) thin plate cast sample, (d) drill used to obtain the chips.

Pure Mg was melted in a graphite crucible using Lindberg/Blue M Crucible Furnace (Fig. 3. 1). The melt temperature was constantly monitored via digital thermometer K-type (Chromel-Alumel) thermocouple and the melt was periodically stirred with a graphite rod to remove any formation of an oxide layer. When the molten Mg reached 690 °C, prescribed amounts of Sr and Ca were added and allowed to dissolve for 15 min. Thin plates were cast using a steel die coated with boron-nitride release coating and pre-heated to 400 °C. The melt was cast at 730 °C in a thin plate-shaped cavity of the preheated steel die. Recovery rates of 90% and 80% were used for Sr and Ca additions, respectively, based on previous experiments in the research team. CO₂ with 0.5% SF₆ was used at a flow rate of 1.1 L/min as a protective gas to prevent burning during melting and casting. Each sample was drilled to obtain ~2 g of specimen chips to analyze the actual chemical composition by inductively coupled plasma (ICP).

3. 2. Immersion test

Thin plate samples were cut into sections (2 cm × 4 cm × 6 mm) and polished down to 800 grit with silicon-carbide (SiC) paper. They were then cleaned with acetone and dried. The initial surface area and weight of each sample was measured before the immersion test. Immersion tests were carried out in simulated body fluid (SBF) using Hank's solution, which was prepared using the recipe given in Table 3. 1. The pH of the SBF solution was adjusted to 7.4 ± 0.1 using HCl 0.5N solution before immersing the samples, and the temperature was maintained at 37 °C using a hot plate during immersion testing. The ratio of SBF solution to the surface area of the sample was kept at 150 ml/cm² in all the experiments. A stirring rod was used to provide a homogenous solution during the test. Each sample was hooked on to a wire through a mounting hole drilled on its surface (using an instrument shown in Fig. 3. 1d) and attached to a funnel covered by an inverted silicon caulked burette full of SBF solution. All the hydrogen bubbles released from the corroded samples were collected and transferred to the burette. Fig. 3. 2. shows the experimental setup used for the in vitro immersion test. The pH variation in SBF and the volume of hydrogen gas evolved was monitored from the change of the SBF solution level during the corrosion test. The samples were removed from SBF after a certain time or until the amount of gas collected exceeded the volume of the inverted burette. Samples were cleaned of corrosion residues using chromium trioxide (CrO₃) according to ASTM G1-90, air dried and weighed immediately after the immersion tests. The weight change of the samples and the volume of hydrogen gas released as a corrosion product were measured for each sample. The average value of the corrosion rate in

terms of both mass loss and hydrogen evolution was calculated as average values of the triplicate corrosion tests. In some experiments, samples were dried without cleaning the corrosion products for further surface analysis.

The following equations were used to calculate the corrosion rate for every single sample:

In case of mass loss:

$$R = \left(\frac{m}{t * A} \right) * 24$$

In case of hydrogen production:

$$R = \left(\frac{V * \rho * MW_{alloy}}{t * A * MW_{H_2}} \right) * 24$$

Where: R : corrosion rate, m : mass loss, t : immersion time, A : surface area, V : volume of H_2 , ρ : density of H_2 , MW_{H_2} : molar mass of H_2 and MW_{alloy} : molar mass.

The experiment was repeated at least three times for each alloy composition and each test condition to ensure the reproducibility of the results. The average value was calculated and presented as the corrosion rate of the sample.

Although a high level of care was taken to assess the experiments with most accuracy, the corrosion rate values have some error due to the experimental detailed below. However, since all the experiments were performed under the same conditions, results obtained from various specimens are comparable. Sources of error in this experiment are as follow:

- i. The corrosion rate in terms of mass loss can vary depending on the accuracy of the weight measurement. Errors can arise due to insufficient cleaning of the samples from the corrosion products by not soaking the sample in chromic acid and acetone long enough. Also if the samples are not washed and dried completely after cleaning and some acid or acetone remains inside the pits, the mass loss obtained in this experiments will be impacted. These experimental errors can cause underestimations of the corrosion rate. The amount of error in each experiment varies in the range of 0.002–0.03 g for a sample with ~7.5 g weight depending on its corrosion rate. For instance, for Mg-0.3Sr-0.3Ca the amount of mass loss after immersion test has the variation of ± 0.002 g after at least 5 weight measurements. Another source of error comes from the physical detachment and separation of large chunks

of the specimen during the experiment that is not due to the corrosion reaction and increases the corrosion rate value.

- ii. The surface area measurement also affects the corrosion rate in terms of both mass loss and hydrogen evolution. Special care has been taken to ensure the samples are completely uniform with flat and parallel sides after the grinding process and an average of at least 5 points were obtained from each dimension to calculate the surface area. Moreover, the samples were suspended into the solution by a supporting hook through a drilled hole. The extra surface area of the sample created by drilling was not taken into account, which can be considered as another source of error in surface area measurement. The diameter of the hole drilled into the sample was 2 mm. Considering that the thickness of the sample varied between 0.5 and 0.6 mm after grinding and polishing, drilling this hole caused an extra surface area of 0.31–0.37 cm², which is 1.4–1.6 % of the total surface area of sample. It should be mentioned that the position of the wire that passed through the sample to hang it into the solution was very tight and the surface inside the hole was barely exposed to the SBF solution. Therefore, the error caused by disregarding this extra surface area was negligible.
- iii. The corrosion rate in terms of hydrogen evolution is a function of volume of hydrogen gas collected during the experiment. In theory, 1 mole of evolved H₂ gas should correspond to 1 mole of dissolved magnesium based on the stoichiometry of the electrochemical Mg dissolution reaction:



Our results are such that the total moles of released H₂ gas during the test was always 30–40% lower than the total moles of Mg dissolved. For instance, 1.8 mmol H₂ gas was collected during dissolution of ~3 mmol of Mg-0.3Sr-0.3Ca after 3 days immersion in SBF. Sources of experimental errors are related to the immersion test:

- i. underestimating the corrosion rate in terms of H₂ evolution due to the incomplete collection of H₂ bubbles. Some of the H₂ gas bubbles may stick to the sides of the funnel and cannot work their way up the burette, causing an error in gas volume reading. It is also possible that some of the H₂ gas bubbles escape from the funnel into the solution, leading to errors and less hydrogen readings;

- ii. overestimating the corrosion rate in terms of mass loss due to the physical separation of chunks into the solution, which leads to a higher than stoichiometric Mg mass loss (as discussed before).

Table 3. 1: Composition of SBF used for immersion test (Hank's solution)

Reagent	Amount (g/l)
NaCl	8.0
KCl	0.4
CaCl ₂	0.14
NaHCO ₃	0.35
C ₆ H ₆ O ₆	1.0
MgCl ₂ · 6H ₂ O	0.1
MgSO ₄ · 7H ₂ O	0.06
KH ₂ PO ₄ · H ₂ O	0.06
Na ₂ HPO ₄ · 7H ₂ O	0.06

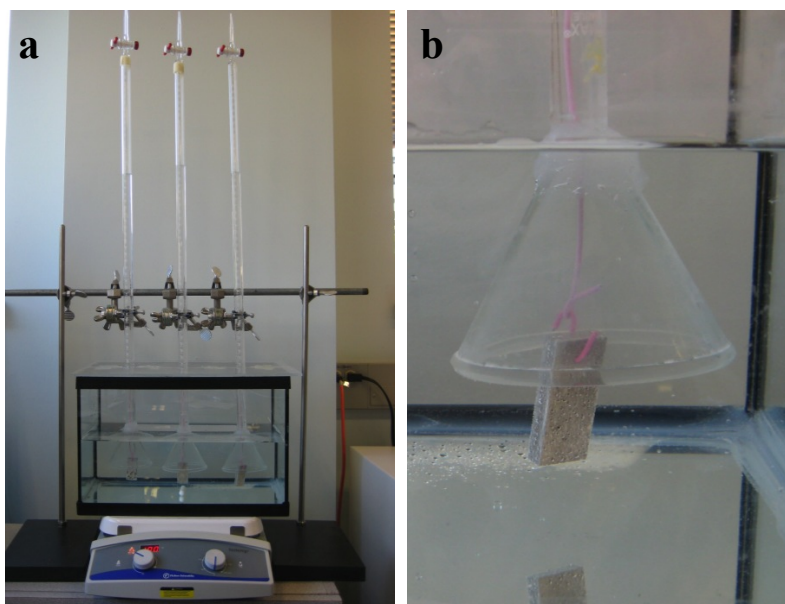


Fig. 3. 2. Experimental set-up for in vitro immersion test in SBF (a) and the close-up from the sample hung into the solution (b).

3. 3. Electrochemical test

The in vitro biocorrosion of Mg samples was also evaluated by potentiodynamic polarization tests using a three-electrode cell. Hank's solution was prepared using the same recipe as that of immersion test and used as an electrolyte. Saturated calomel electrode (SCE) and platinum were used as the reference electrode and the counter electrode respectively. The samples were polished down to 800 grit with SiC paper before soaking in Hank's solution. The three-electrode cell set-up had a fixed opening of 0.720 mm^2 to expose the solution to the surface of the sample (Fig. 3. 3). Such exposed area functioned as the working electrode. The current density was monitored as a function of open-circuit potential by using VersaSTAT3 (METEK). The samples were stabilized for 5 min in the solution and the test was conducted at $37 \text{ }^\circ\text{C}$ with a scan rate of 0.1666 mV/s for all the measurements. The corrosion current density of each specimen was derived by linear fit to the anodic and cathodic parts of the polarization curves.

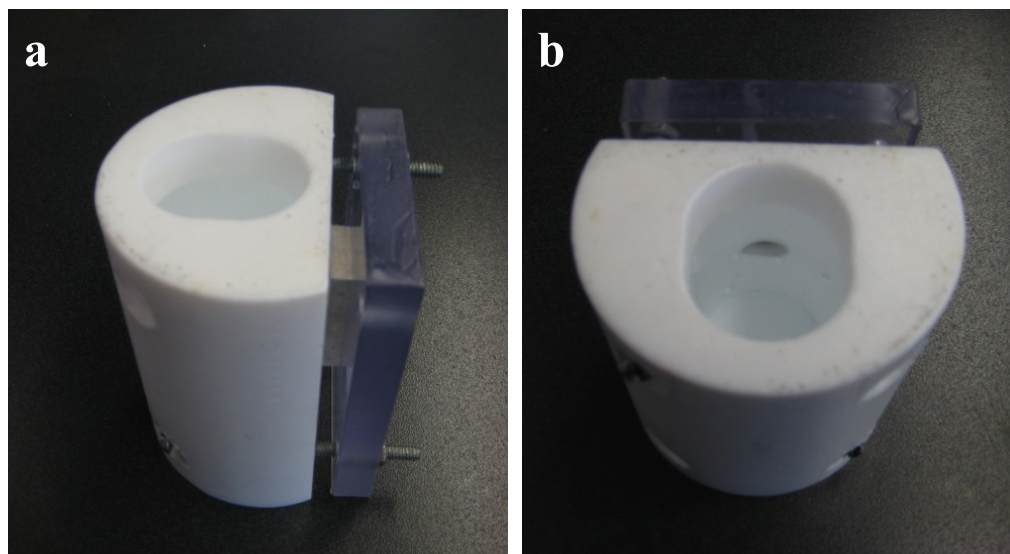


Fig. 3. 3. Side view (a) and top view (b) of the experimental set-up used for three-electrode cell electrochemical test in SBF.

3. 4. Optical microscopy

Samples were ground up with 1200 grit SiC papers then polished with 1μ diamond paste on low napped polishing cloths for a finer polish and to produce a smooth and mirror surface finish. Final polishing was done with colloidal silica. Further, the samples were etched with 5% Nital

for microstructural examination by optical microscopy. Samples were immersed in an etching solution for 3–5 seconds and then rinsed with running water and ethanol and dried using a drier.

Nikon Epiphot 200 optical microscopy and Olympus SZ40 Stereoscope with Clemex analysis software was used for microstructural examination. The cross-section of the samples was used to evaluate the microstructure before and after immersion tests and to analyze the depth of corrosion. Stereo microscopy was used to take images from the attacked surface of corroded samples.

3. 5. Scanning electron microscopy (SEM)

Hitachi S-4700 FE-SEM equipped with energy-disperse spectrometry (EDS) with a maximum resolution of 100 nm was used to evaluate the second phases in as-cast alloys and to analyze the surface products in corroded samples. An accelerating voltage of 5kV and secondary electron mode was used for examination. The samples for SEM were prepared with the same procedure as optical microscopy. The chemical composition of microstructural phases was evaluated using EDS point analysis. The distribution of the phases in the microstructure was evaluated using elemental mapping. FEI Quanta 450 Environmental Scanning Electron Microscope (FE-ESEM) was used to study the implant/tissue interface on the post implantation Mg stent samples. Elemental distribution was examined via point analysis as well as elemental mapping. Phenom G2 pure SEM was also used to analyze the fracture surface of Mg samples after tensile test.

3. 6. Transmission electron microscopy (TEM)

Philips CM 200 (Selected Area Electron Diffraction-SAED) and FEI Tecnai G2 (EDS line-scans) were used at 200kV to evaluate fine microstructural features and nano-sized particles in the Mg-0.3Sr-0.3Ca alloy. Plates of 1.0 mm thickness obtained from cross-section samples were ground down to 1200 grid to obtain 0.2 mm thickness. Discs, 3mm in diameter, were punched, polished down to 50 μ m and ion beam polished using a Gatan precision ion polishing system (PIPS) at an angle of 4° (top and bottom) using 3.8kV voltage. Composition of each phase in Mg-0.3Sr-0.3Ca alloy was identified using EDS analysis. The formation of globular Ca/Sr-rich phases was determined in the microstructure of this alloy.

3. 7. X-ray diffraction

The phases present in the as-cast samples were characterized by X-ray diffraction (XRD) using a Bruker D8 X-ray diffractometer with Cu K_{α} radiation ($\lambda = 1.544 \text{ \AA}$) at 40 kV and 40 mA. The oscillation of 2 mm was selected for the scan on the cross-section surface of the samples. The data was collected in the 2θ range between 10° and 95° using general area detector diffraction system (GADDS) software. XRD analysis was also conducted on the corrosion products collected from the surface of corroded Mg samples.

3. 8. X-ray photoelectron spectroscopy (XPS)

Corroded samples were removed from SBF after a certain time and dried for further surface analysis. The surface chemistry of the corrosion products was immediately analyzed using Thermo Scientific XPS K-alpha. Special care was taken to ensure that the samples are not exposed and contaminated by the environment because this is important for determination of corrosion products that specifically form during the SBF immersion test. All the measurements were conducted under ultra-high vacuum conditions ($< 10^{-7} \text{ Pa}$). The information was collected from the first 3–10 nm top layers of the sample. An X-ray source of Al- $K\alpha$ (1486.6 eV) with a spot size of 400 μm diameter was used for all the experiments. The energy resolution was 0.1 and 1 eV for the high resolution and survey scan, respectively. Although the Mg sample is conductive, the corrosion products on the surface are non-conductive, which can lead to changes in the binding energy. To prevent this charging effect, spectra were collected using a flood gun. The composition of layers underneath the surface was studied using an ion source (Ar^{+} ions) to bombard the surface and remove the outermost surface atoms. Depth profile analysis was carried out by etching the sample and collecting successive XPS spectra at each etch cycle. The Ar beam was generated using a potential and a current that would remove 0.3 nm/s from the reference material Ta_2O_5 (a much harder material than our alloys).

XPS was used to identify the elemental composition and chemical state of the atoms present on the surface of the corroded samples, as well as to quantify the atomic percentage of some elements, such as C, Sr, Ca, P, Mg and O, on the outermost surface layer and beneath, during depth profile. Quantitative values were based on averages of at least ten points.

3. 9. Mechanical testing

The mechanical properties of Mg samples were characterized with uni-axial tensile, compression and three point bending tests at room temperature. The tensile samples were machined according to ASTM-E8-04. The tensile tests were carried out using MTS Alliance RF/200 Instron testing machine with a displacement rate of 0.12 mm min^{-1} until fracture. The tensile yield strength (TYS), ultimate tensile strength (UTS) and elongation to failure were calculated based on the average values of at least three tests.

The compression samples were machined according to ASTM-E9-09. The compressive test was conducted at the constant speed of 0.12 mm min^{-1} ($0.005 \text{ in/ min}^{-1}$) using Instron 5885H. The compressive yield strength (CYS), ultimate compressive strength (UCS) and compressive strain were calculated from the true stress-true strain curves based on the average values of three tests.

The three-point bending tests were conducted using a Tinius Olsen H25K-S testing machine. Beam-shaped specimens with dimensions of $6 \times 6 \times 70 \text{ mm}^3$ were machined from thin plate samples. All the samples were polished down to 800 grit using SiC paper before testing. Strength and ductility of the samples were evaluated from the force-displacement curve.

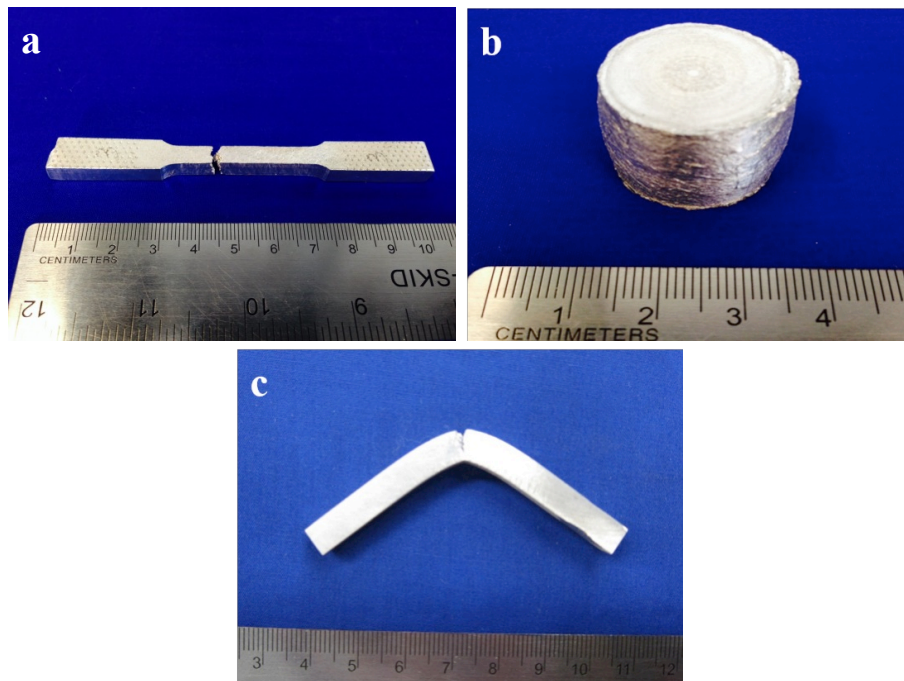


Fig. 3. 4. Tensile (a), compression (b) and bending (c) samples tested at room temperature.

3. 10. Cytocompatibility assay

To evaluate the cytocompatibility of Mg samples for cardiovascular application, we used human umbilical vascular endothelial cells (HUVECs). We purchased the HUVEC line from Cedarlane Laboratories (ATCC CRL-1730). To subculture the cells, they were maintained in F-12K medium supplemented with 2 mM L-glutamine (Invitrogen, Carlsbad, CA), 10% Newborn Calf Serum (NBCS, HyClone Laboratories Inc., Logan, UT) and 1% Penicillin Streptomycin antibiotic (Invitrogen, Carlsbad, CA) at 37°C in humidified atmosphere at of 5% CO₂. Heparin (0.1 mg/ml) and endothelial cell growth supplement (ECGS; 0.05 mg/ml) were used to grow the cells on a gelatin coated (0.2%) culture flasks.

Indirect assay was used to evaluate the cytocompatibility of Mg samples in which we conducted the following steps:

1. Ion extraction: Ion extract was obtained from $1 \times 1 \times 0.5 \text{ cm}^3$ of the sample by incubating in 10 ml of F-12K medium for 72 hrs in a humidified atmosphere containing 5% CO₂ and 95% air at 37 °C. The extracted medium was used in 100%, 50% and 10% concentration using F-12K medium. F-12K medium supplement was used as a positive control for cell growth.
2. Cell seeding: HUVEC were counted using a hemocytometer. Then, HUVECs were seeded onto 96-well cell culture plates at 5×10^3 cells/100 µl medium in each well and incubated overnight in order to ensure attachment to the well.
3. Cell exposure to extracted ions: The medium in each well was replaced with 100 µl of extraction medium and incubated in a humidified atmosphere with 5% CO₂ at 37°C for several time points. During the experiment, the cells were treated every three days with a fresh extraction medium containing heparin and ECGS.
4. Viability measurement: At the end of each time point, indicator Alamar blue (5% in F-12K medium with growth supplements) was added to each well and further incubated at 37 °C for 4 hrs. Finally, fluorescence emission of the solution was measured at 595 nm using 560 nm excitation. After background subtraction, fluorescence intensity was analyzed relative to the control medium.

Three wells were seeded for each alloy composition and each medium concentration for various assay time points. The average value was calculated and reported as the viability of the cells at each specific condition.

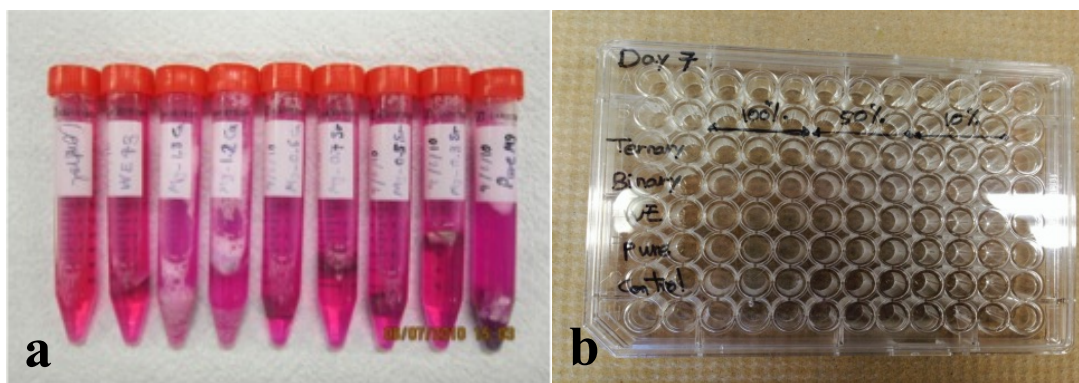


Fig. 3. 5. Indirect cytotoxicity assay: (a) extracting ions from Mg samples and (b) cell seeding onto 96-well cell culture plates.

3. 11. Animal study and histological evaluation

The biological performance of candidate Mg alloys were further evaluated by animal study. Samples were cast into rods and machined into perforated tubes with 2.4 mm diameter, 10 mm length and 0.25 mm wall thickness in order to implant into the right and left femoral artery of dog. The tubes were slit and folded over to provide flexibility during implantation. All animals received humane care in compliance with the “Guide to the Care and Use of Experimental Animals” of the Canadian Council on Animal Care. After pre-medication with 45 mg/kg of intraperitoneal methohexital sodium to establish an intravenous line through the ear vein, the animal was subjected to general anesthesia and endotracheal intubation for mechanical ventilation. Under sterile condition, the femoral arteries were exposed bilaterally. After proximal and distal control, an arteriotomy was carried out. One tubular stent was then inserted in each side and the arteriotomy sites were repaired with 7-0 prolene suture. The status and patency of the femoral stent was confirmed by the presence of palpable pulses in the distal femoral artery and by doppler ultrasound. The animal was then extubated and post-implantation studies were conducted by sacrificing the animal after a few days, depending on the degradation rate of the stent. Following an overdose of sodium pentobarbital, the femoral arteries were removed after in vivo fixation with 10% buffered formaldehyde solution perfused at 100 mm Hg for 15 min. Each artery was cut in consecutive slices of 2 mm from the proximal to the distal end and embedded in paraffin. Sections of the treated arteries (10 μ m thick sections cut 50 μ m apart) were examined for the presence of acute or organized thrombosis, fibrosis and endothelial damage or defects.

Explanted stents, including the surrounding tissues, were cut in a few sections for various post-implantation analyses. One section of the sample was dehydrated with ethanol to remove all the moisture (Fig. 3. 6a).

SEM was employed to investigate the surface morphology and the changes in the dimension of the Mg stents. Another section of the sample was used for histological analysis, which was carried out at the Centre for Bone and Periodontal Research. First, samples were fixed in 3.7% commercial formalin. Then they were embedded and sectioned (5 μm per section) with paraffin. Samples were cut perpendicular to their length for cross-sectional observation (Fig. 3. 6b). Finally the samples were stained using hematoxylin and eosin (H&E). We conducted at least three histological staining by H&E for each stent sample and its surrounding tissue (Fig. 3. 6c). The rest of explanted stents were embedded in epoxy for further microscopic analysis on the interface of the implant and surrounding tissues.

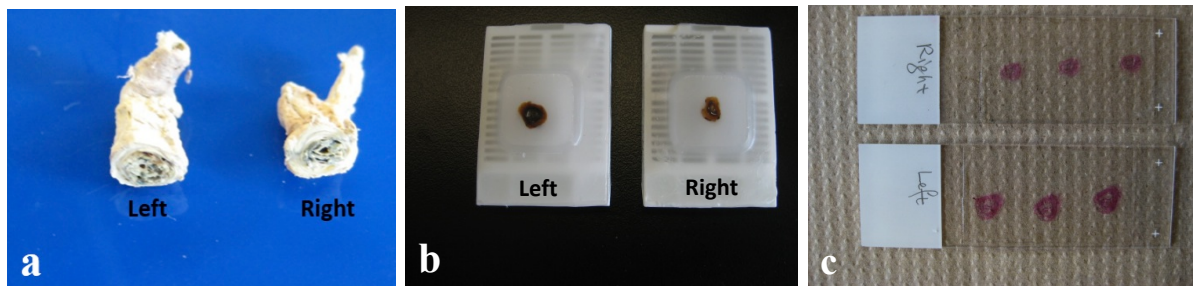


Fig. 3. 6. Post-implantation analysis on retrieved Mg stent samples: (a) cut and dehydrated for microscopic observation, (b) embedded and sectioned for histology and (c) stained using H&E.

CHAPTER 4

BIODEGRADATION BEHAVIOR AND BIOCOMPATIBILITY OF Mg-Sr ALLOYS AS TEMPORARY BIOMATERIALS

This chapter is comprised of one published journal manuscript. In this part of the study, the focus is to investigate the effect of Sr on the biodegradation behavior of Mg, to determine the best compositions among Mg-Sr binary alloys for temporary cardiovascular applications and to understand how these alloys biodegrade and the role of Sr in physiological conditions.

First, Mg-Sr alloys (with Sr in the range of 0.3–2.5%) were cast and the biodegradation rate in SBF was analyzed with in vitro corrosion tests to select the candidate alloy with the slower degradation rate. Then, the microstructural characterization was carried out using optical microscopy and SEM. In addition, surface characterization was performed on the corroded samples after the immersion test using EDS, XRD and XPS. Microstructural and surface analysis was used to understand the effect of Sr on the biodegradation mechanism of Mg samples. Following this, the cytocompatibility of the candidate Mg-Sr alloy was examined via indirect viability assay for HUVECs at three different time points: 1, 4 and 7 days. Finally, the in vivo biocompatibility of the Mg-Sr candidate alloy was examined via animal study by implantation of a tubular stent sample into the dog femoral artery for 3 weeks.

4. 0. Biocompatibility and biodegradability of Mg-Sr alloys: The formation of Sr-substituted hydroxyapatite

This section has been published as: M. Bornapour, N. Muja, D. Shum-Tim, M. Cerruti, M. Pekguleryuz, Biocompatibility and biodegradability of Mg-Sr alloys: The formation of Sr-substituted hydroxyapatite, *Acta Biomaterialia* 9 (2013) 5319-5330.

4. 1. ABSTRACT

Magnesium is an attractive material for use in biodegradable implants due to its low density, non-toxicity and mechanical properties similar to those of human tissue such as bone. Its biocompatibility makes it amenable for use in a wide range of applications from bone to cardiovascular implants. Here we investigated the corrosion rate in simulated body fluid (SBF) of a series of Mg-Sr alloys, with Sr in the range of 0.3–2.5%, and found that the Mg-0.5Sr alloy showed the slowest corrosion rate. The degradation rate from this alloy indicated that the daily Sr intake from a typical stent would be 0.01– 0.02 mg/day which is well below the maximum daily Sr intake levels of 4 mg/day. Indirect cytotoxicity assays using HUVECs indicated that Mg-0.5Sr extraction medium did not cause any toxicity and detrimental effect on the viability of the cells. Finally, a tubular Mg-0.5Sr stent sample along with a WE43 control stent, were implanted into the right and left dog femoral artery. No thrombosis effect was observed in the Mg-0.5Sr stent after 3 weeks of implantation while the WE43 stent thrombosed. X-ray diffraction (XRD) demonstrated the formation of hydroxyapatite and Mg(OH)₂ as a result of the degradation of Mg-0.5Sr alloy after 3 days in SBF. X-Ray photoelectron spectroscopy (XPS) further showed the possibility of formation of hydroxyapatite Sr-substituted layer that present as a thin layer at the interface between the Mg-0.5Sr alloy and the corrosion products. We believe that this interfacial layer stabilizes the surface of the Mg-0.5Sr alloy, and slows down its degradation rate over time.

4. 2. INTRODUCTION

Magnesium, being biocompatible and biodegradable, is seeing growing interest as a temporary implant material. Key application areas are temporary intravascular stents and orthopedic implants [1-8]. Metallic stents, usually stainless steel, Nitinol or cobalt-chromium alloys, cause restenosis due to the irritation of the endothelium and the resulting hyperplasia [9]. The shortcomings are the large differences in the mechanical behavior of the stented and the non-stented vessel areas, inability to adapt to growth in the case of pediatric patients, and non-permissive or disadvantageous characteristics for later surgical revascularization which makes it difficult or impossible to perform subsequent angioplasty or bypass graft surgery [6, 9, 10]. The complications include thrombogenicity, permanent physical irritation, long term endothelial dysfunction, and chronic inflammatory local reactions [10]. Sometimes a polymer-coated drug needs to be incorporated into the stent to reduce these problems.

Magnesium biomaterials are emerging as important candidates for bio-resorbable implant applications [11]. Because magnesium biodegrades via corrosion by the body fluids, the stimulus for hyperplasia is removed and the tendency to restenosis is minimized [9, 12], while the substrate for local tissue irritation is eliminated. Magnesium has an advantage over biodegradable polymeric stents in that it can have smaller mass for equal mechanical performance [10] and can be better visualized in CT scans. Biodegradable stents have been successfully used in pediatric patients with congenital heart disease [13] and other clinical trials with magnesium alloys have been undertaken [14-16].

The main shortcomings of magnesium alloys as a temporary implant material are (i) the fast corrosion rate of pure Mg, (ii) the high rate of hydrogen gas evolution during biodegradation which is detrimental to the surrounding tissue [17-20] and (iii) the toxicity of some of the alloying elements. While magnesium is biocompatible, not all alloying elements are. For example aluminum alloyed into magnesium may slow down the biodegradation rate of magnesium but is toxic to the human body [21, 22]. Certain magnesium alloys such as WE43 and LAE442 with rare-earth elements (cerium, neodymium, etc) have been developed [1, 9]. These may not pose substantial toxicity problems unless they contain aluminum but since rare-earths (REs) are not part of the human chemistry they may give rise to cell proliferation and high rate of neo-intima formation in stented vessels leading to potential risks of thrombosis [22, 23]. The effective application of magnesium requires the development of alloys with slow

biodegradation rate (i.e. low mass loss and low rate of hydrogen evolution), without compromising biocompatibility (i.e. low toxicity and low neointima). Because of this, considerable effort has focused on controlling the degradation rate of Mg via alloying and surface modification techniques [24-26].

Strontium (Sr) has been determined as a potential element for use in medical applications [27]. Sr can improve the mechanical properties and increase the corrosion resistance of certain Mg alloys [28]. Sr is a component of human bone and has been known to promote the growth of osteoblasts and prevent bone resorption [29-33]. The biological role of strontium in bone, muscles and heart has been demonstrated [34]. Strontium is known as a grain refiner for magnesium and it is also expected that the addition of strontium would improve the corrosion resistance of magnesium by altering its surface, due to its surface active nature [35, 36].

Mg-Sr alloys have been recently evaluated as potential materials for biodegradable implants [27, 37]. Brar et al [37] have investigated the mechanical properties of heat-treated Mg-Sr and Mg-Sr-Zn alloys as well as their biodegradation rate in SBF immersion tests and found the Mg-2Zn-0.5Sr alloy to have the lowest biodegradation rate but only moderate mechanical properties. Among the as-cast binary Mg-Sr alloys, Mg-0.5Sr showed the slowest degradation rate in immersion tests. Gu et al [27] conducted in vitro and in vivo studies on Mg alloys with 1–4 wt.% Sr for bone implantations. They found the Mg-2 wt.% Sr alloy in the as-rolled condition showed the highest strength and the slowest corrosion rate. Its cytotoxicity was evaluated as Grade 1 and the alloy showed acceptable host response during a 4-week implantation period. These examples show that there is considerable variation in the literature as to the optimal Sr level in Mg-Sr alloys. Furthermore, the exact mechanism by which Mg-Sr alloys degrade is still unknown. Understanding this mechanism is important, since it may explain, for example, why Mg-Sr alloys can be applied in a wide range of implants, while Mg-Ca alloys are suitable for bone implants but not for cardiovascular implants [5, 27, 38-40]. The focus of our study is thus to determine the best compositions among Mg-Sr alloys for cardiovascular and other orthopedic applications and to understand how these alloys biodegrade in physiological conditions.

4. 3. EXPERIMENTAL PROCEDURE

4. 3. 1. Alloy Synthesis and Plate Casting

Eight (8) thin plates of Mg-Sr with nominal strontium range varying from 0.3% to 2.5% were prepared by melting down pure Mg (99.9 wt.%) and pure Sr (99.99 wt.%), both supplied by Applied Magnesium (Formerly Timminco), in a Lindberg/Blue M Crucible Furnace. CO₂ with 0.5% SF₆ was used at a flow rate of 1.1 L/min as protective gas to prevent burning during melting and casting. A K-type (Chromel–Alumel) thermocouple was used with a digital thermometer to monitor the melt temperature. Steel die with a plate cavity coated with boron nitride release coating was heated to 400 °C before plates were cast. The actual chemical composition of each alloy analyzed by inductively coupled plasma (ICP) is shown in Table 4. 1; the samples also contain ppm level impurities which are commonly found in Mg alloys. WE43 containing 3.48 wt.% yttrium, 2 wt.% neodymium, 0.5 wt.% gadolinium and 0.15 wt.% praseodymium was also cast using the same procedure.

Table 4. 1: The chemical composition of the alloys

Alloy	Chemical composition (wt.%)					
	Sr	Al	Si	Fe	Mn	Mg
Mg-0.3Sr	0.28	0.012	0.006	0.036	0.003	Balance
Mg- 0.5Sr	0.57	0.011	0.004	0.038	0.003	Balance
Mg- 0.7Sr	0.74	0.014	0.003	0.036	0.003	Balance
Mg- 1Sr	1.12	0.011	0.004	0.039	0.003	Balance
Mg- 1.2Sr	1.30	0.010	0.004	0.046	0.003	Balance
Mg- 1.5Sr	1.56	0.011	0.003	0.034	0.002	Balance
Mg- 2Sr	1.96	0.009	0.003	0.035	0.003	Balance
Mg- 2.5Sr	2.62	0.007	0.003	0.036	0.003	Balance

4. 3. 2. Immersion Experiments

Corrosion experiments were carried out in simulated body fluid (SBF) using Hank's solution. Samples used in the experiment were cut from thin plates of 6 mm thickness into 2 × 4 cm² sections and were polished down to 800 grit with silicon-carbide paper. They were then cleaned, dried, and weighed. The pH value of Hank's solution (8.0 g/l NaCl, 0.4 g/l KCl, 0.14 g/l CaCl₂, 0.35 g/l NaHCO₃, 1.0 g/l C₆H₆O₆ (glucose), 0.1 g/l MgCl₂ · 6H₂O, 0.06 g/l MgSO₄ · 7H₂O, 0.06 g/l KH₂PO₄ · H₂O, 0.06 g/l Na₂HPO₄ · 7H₂O) was adjusted to 7.4 and the temperature

was maintained at 37 °C using a hot plate during immersion testing. The samples were removed from SBF after a certain time, cleaned off of corrosion residues and dried. Each sample was attached to a funnel covered by an inverted silicon caulked burette full of Hank's solution. All the hydrogen bubbles released from corroded samples were collected and transferred to the burette. The volume of hydrogen gas evolved was measured from the change of Hank's solution level before and after the corrosion test. The weight change of samples and the volume of hydrogen gas released as corrosion product were measured for each sample. The average value of corrosion rate in terms of both mass loss and hydrogen evolution were calculated as average values of triplicate corrosion tests. The Mg-Sr samples containing more than 1 wt.% Sr had rapid degradation rate which is not desirable for most stent applications. Therefore, only the evaluation and characterization results from Mg-Sr alloys containing less than 1 wt.%Sr are presented in this paper. Interrupted corrosion tests were also carried out to understand the in-vitro biodegradation mechanism and the evolution of the corrosion process. The Mg-0.5Sr samples were removed from SBF after 1, 2 and 3 days of immersion, cleaned, and evaluated via surface characterization methods.

4. 3. 3. Electro-Polarization Test

The polarization curve of the specimens was obtained by using three-electrode cell. Saturated calomel electrode (SCE) was used as the reference electrode and platinum as the counter electrode. Each specimen was immersed in Hank's solution at 37 °C. The setup had a fixed opening so as to expose to the solution a surface area of 0.720 mm² of the sample (working electrode). The current density was monitored as a function of open-circuit potential by using VersaSTAT3 (METEK). The samples were stabilized for 5 minutes in the solution and test was conducted with the scan rate of 0.1666mV/s for all the measurements. The corrosion current density was obtained by linear fit to the anodic and cathodic parts of the polarization curves.

4. 3. 4. Microstructure and Surface Analysis

The surface morphology and microstructure of each specimen was characterized via optical microscopy (OM) using a Nikon Epiphot 200 and stereo microscopy (SM) with Olympus SZ40 before and after corrosion testing. X-ray diffraction (XRD) was performed on the corroded surface of specimens using Bruker D8 X-Ray diffractometer CuK_α. Scanning electron microscopy (SEM, Hitachi S-4700 FE-SEM) equipped with energy-disperse spectrometry (EDS)

was employed to study the corrosion mechanism of Mg-0.5Sr alloy. The surface morphology of corroded samples was characterized by X-ray photoelectron spectroscopy (XPS, K-Alpha, Thermo Scientific) using an X-ray source of Al-K α (1486.6 eV) with a spot size of 400 μ m diameter. The energy resolution was 0.1 and 1 eV for the high resolution and survey scan, respectively. To prevent charging, spectra were collected using a flood gun. Samples were etched with Ar ions in-situ, in the XPS analysis chamber, to remove surface contamination and to measure compositional depth profiles.

4. 3. 5. Cytotoxicity Evaluation

Human umbilical vascular endothelial cells (HUVEC) purchased from Cedarlane Laboratories (ATCC CRL-1730) were employed in cell viability evaluation. HUVEC was maintained in F-12K medium supplemented with 2 mM L-glutamine (Invitrogen, Carlsbad, CA), 10% Newborn Calf Serum (NBCS, HyClone Laboratories Inc., Logan, UT) and 1% Penicillin Streptomycin antibiotic (Invitrogen, Carlsbad, CA) at 37 °C in humidified atmosphere at of 5% CO₂. Heparin (0.1 mg/ml) and endothelial cell growth supplement (ECGS; 0.05 mg/ml) were used to grow the cells on gelatin coated (0.2%) culture flasks.

The biocompatibility of the Mg-0.5Sr alloy was evaluated by indirect cell viability assay. First, an ion extract was obtained from 1 × 1 × 0.5 cm³ of Mg-0.5Sr specimen by incubating in 10 ml of F-12K medium for 72 hrs in humidified atmosphere containing 5% CO₂ and 95% air at 37 °C. The extracted medium was diluted to 10% concentration using F-12K medium with supplements in preparation for cell viability assays. The concentration of magnesium ions in the extracted medium measured by Varian AA 240 FS Atomic Absorption Spectrometer (AAS) was 0.5796 ± 0.002 mg/l. This value contains the amount of magnesium ions exist in F-12K components in addition to those extracted from the metallic sample. Table 4. 2 shows the concentration of inorganic salts in F-12K which has been used in this study. F-12K medium supplement was used as positive control for cell growth. Then, HUVECs were seeded onto 96-well cell culture plates at 5 × 10³ cells/100 μ l medium in each well and incubated overnight in order to ensure attachment to the well. Three wells were seeded for each alloy and each assay time point. Next, the medium in each well was replaced with 100 μ l of extract and again incubated in a humidified atmosphere with 5% CO₂ at 37 °C for 1, 4 and 7 days. During the experiment, the cells were treated every three days with fresh medium containing heparin and

ECGS. At the end of each test, indicator Alamar blue (5% in F-12K medium with growth supplements) was added to each well and further incubated at 37 °C for 4 hrs. Finally, fluorescence emission of the solution was measured at 595 nm using 560 nm excitation (Berthold Mithras LB 940 Instrument). After background subtraction, fluorescence intensity was analyzed relative to the control (F-12K medium). The cytotoxicity evaluation was also performed using WE43 as a commercial control sample. All three steps of ion extraction, cell seeding and exposure to extraction medium were exactly the same for two alloy compositions.

Table 4. 2: The concentration of inorganic salts in F-12K formulation

Inorganic salts	Concentration (mg/L)
Calcium Chloride (CaCl ₂) (anhyd.)	102
Cupric sulfate (CuSO ₄ ·5H ₂ O)	0.002
Ferric sulfate (FeSO ₄ ·7H ₂ O)	0.8
Magnesium Chloride (anhydrous)	49.7
Magnesium Sulfate (MgSO ₄) (anhyd.)	192
Potassium Chloride (KCl)	285
Sodium Bicarbonate (NaHCO ₃)	2500
Sodium Chloride (NaCl)	7530
Sodium Phosphate dibasic (Na ₂ HPO ₄) anhydrous	115.5
Sodium Phosphate monobasic (NaH ₂ PO ₄) anhydrous	59
Zinc sulfate (ZnSO ₄ ·7H ₂ O)	0.144

4. 3. 6. Animal Implantation

(a) Prototype stent fabrication: The Mg-0.5Sr alloy was cast into rods and machined into perforated tubes with 2.4 mm diameter, 10 mm length and 0.27 mm wall thickness in order to implant into the right femoral artery. WE43 was also fabricated with the same size and implanted as control sample into the left femoral artery of animal.

(b) Animal experiments: The performance of the new alloy stents was tested using established animal model (8.7 kg dog). All animals received humane care in compliance with the “Guide to the Care and Use of Experimental Animals” of the Canadian Council on Animal Care. After pre-medication with 45mg/kg of intraperitoneal methohexital sodium to establish an intravenous line through the ear vein, the animal was subjected to general anaesthesia and endotracheal intubation

for mechanical ventilation. Under sterile condition, the femoral arteries were exposed bilaterally as previously described [41, 42]. After proximal and distal control, an arteriotomy was carried out. A stent prepared with different designed Mg alloys were then inserted in each side (Right: Mg-0.5Sr; Left: WE 43) and the arteriotomy sites were repaired with 7-0 prolene suture. The status and patency of the femoral stent was confirmed by the presence of palpable pulses in the distal femoral artery and by doppler ultrasound. The animal was then extubated and survived for three weeks for further analysis. Post-implantation studies were conducted at three weeks by sacrificing the animal. Following an overdose of sodium pentobarbital, the femoral arteries were removed after in-vivo fixation with 10% buffered formaldehyde solution perfused at 100 mm Hg for 15 min. Each artery is cut in consecutive slices of 2 mm from the proximal to the distal end, and embedded in paraffin. Sections of the treated arteries (10 μm thick sections cut 50 μm apart) are examined for the presence acute or organized thrombosis, fibrosis and endothelial damage or defects. Two post-implanted stents were fixed and dehydrated with ethanol to remove all moisture. SEM was employed to investigate the surface morphology and the changes in the dimension of Mg stents.

4. 4. RESULTS AND DISCUSSIONS

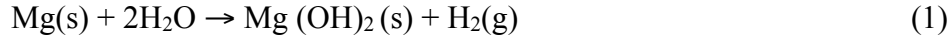
4. 4. 1. The Degradation Behavior in SBF

4. 4. 1. 1. Rate of Degradation

The degradation rates of Mg-Sr samples calculated in terms of mass loss and H_2 evolution (Fig. 4. 1) show that the Mg-Sr alloys containing Sr < 1 wt.% have slower degradation rate in SBF than pure Mg or Mg-Sr alloys of higher Sr content. Here the Mg-0.5Sr shows the lowest degradation rate. The addition of Sr > 1 wt.% accelerates the degradation rate under the same environmental condition. These results agree with Brar et al [37] but seem to deviate from the results of Gu et al [27] who found Mg-2 Sr to be better than Mg-1Sr.

The average corrosion rate of Mg-0.5Sr observed in our study is $\sim 2 \text{ mg /day/cm}^2$. Taking (i) the typical stent surface-area range to be 45–100 mm^2 , and (ii) the weight of Sr lost to be 0.5 wt.% of the alloy weight loss during the bio-corrosion of the stent, the average maximum daily Sr intake from the Mg-0.5Sr is estimated to be 0.01 mg/day which is well below the maximum average daily Sr intake of 4 mg/day.

As known, the amount of hydrogen evolved from magnesium is an important point in its application as a biomaterial in the human body, especially when it is used as a vascular stent [43, 44]. Large amounts of H₂ produced at the early stages of immersion or implantation were recorded in previous in-vitro and in-vivo studies [45-48]. Fig. 4. 2a presents the corrosion rate of Mg-0.5Sr in terms of both mass loss and H₂ release versus immersion time. According to the stoichiometry of the electrochemical Mg dissolution reaction:



1 mole of H₂ gas evolved should correspond to 1 mole of magnesium dissolved [45]. However, we can notice a higher volume of H₂ released at the beginning, which then slows down after 2–3 days. This observation is in agreement with previous reports of H₂ release during the bio-corrosion of Mg alloys [11]. The larger number of moles of Mg dissolved compared to the moles of H₂ evolved observed after 3 days should be related to the disintegration of some particles of the alloy, which leads to a higher than stoichiometric Mg mass loss. Overall, the average mass loss (M) is continuously higher than the amount of hydrogen (H₂) released and the relationship can be expressed as $\text{H}_2 = -1.3 \text{M}^2 + 3.8 \text{M}$ ($R^2 = 0.88$) (Fig 2b).

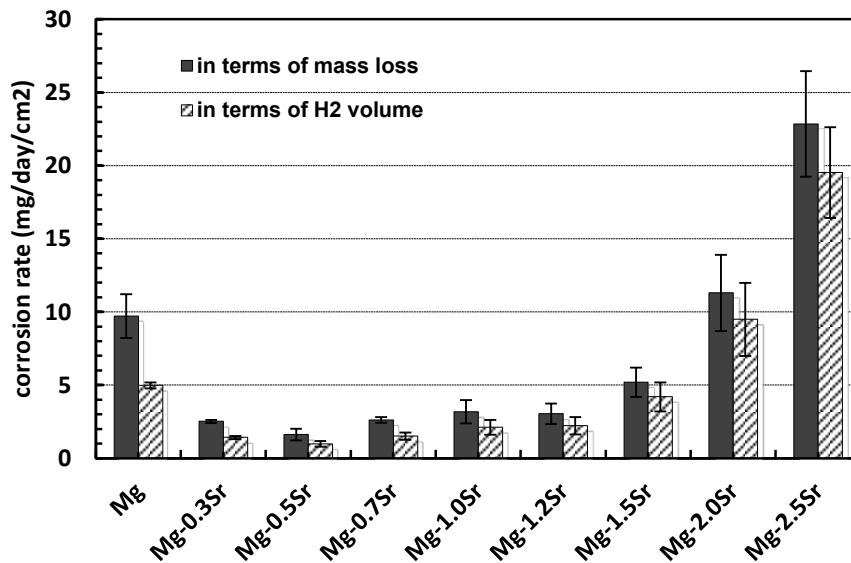
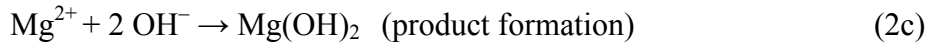
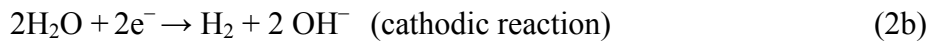
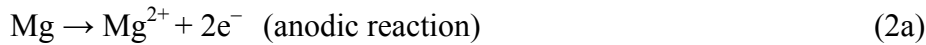


Fig. 4. 1 . The average corrosion rate (mg/day/cm²) in terms of mass loss and hydrogen evolution for Mg-Sr samples with various Sr content after immersion in SBF at 37°C.

The interrupted test is also useful in understanding the bio-degradation behavior of Mg-Sr alloys (using the values in Fig. 4. 2a). The total amount of H₂ released after 3 days of immersion corresponding to 1.63 mg/day/cm² (1.48 ml/day/cm²) is ~0.64 ml/cm² or an average daily release of 0.21 ml/day/cm² in the initial 3 days. The Mg-0.5Sr alloy after 1 day of immersion exhibits a hydrogen release rate which is higher than the average, which then decreases following the relationship $H_2 = 4.05 e^{(-0.314t)}$ where H₂ is in ml/day/cm² and t is in days. After 3 weeks, the H₂ release rate is estimated to be 0.0014 ml/day/cm². As commonly observed during the bio-degradation of Mg alloys, both the degradation rate and hydrogen evolution decrease with immersion time and they are not linearly related, indicating that a complex corrosion behavior is involved in the bio-degradation of the Mg-Sr alloy in SBF. This can be associated with the change in pH in the SBF solution, the micro-galvanic corrosion and the gradual formation of a surface barrier to corrosion.

Fig. 4. 3 shows that the pH value of SBF containing the Mg-0.5Sr specimen also increases very rapidly in the initial stages of degradation and then more slowly reaching a value of ~10 in about 3 days. In fact the corrosion of Mg in aqueous solution (equation (1) above) can be subdivided in three reactions [49]:



Continuous Mg dissolution in the initial stages of reaction consumes H⁺ ions and increases OH⁻ ions, shifting the pH value to basic level [43]. It is known that the corrosion of Mg alloys hardly takes place when the pH is above 11.4 and the corrosion is most severe at neutral conditions. The SBF test uses non-flow conditions so the increase in pH is not likely to simulate the human body where blood flow would alter the pH value [11].

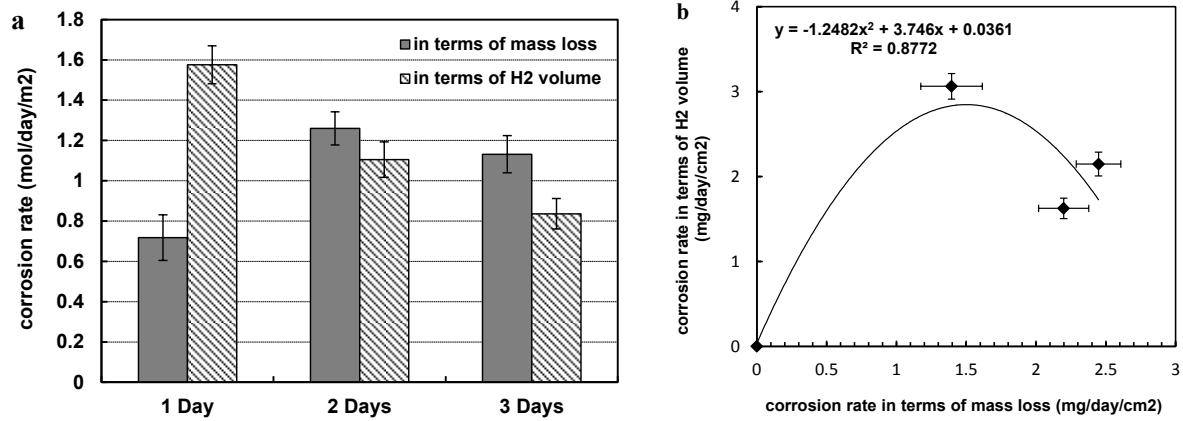


Fig. 4. 2. (a) The average corrosion rate of Mg-0.5Sr in terms of mass loss (M) and hydrogen evolution (H₂) after immersion in SBF for different times. (b) The relationship between mass loss (M) and hydrogen evolution (H₂) in SBF immersion fitted as $H_2 \approx -1.3 M^2 + 3.8 M$

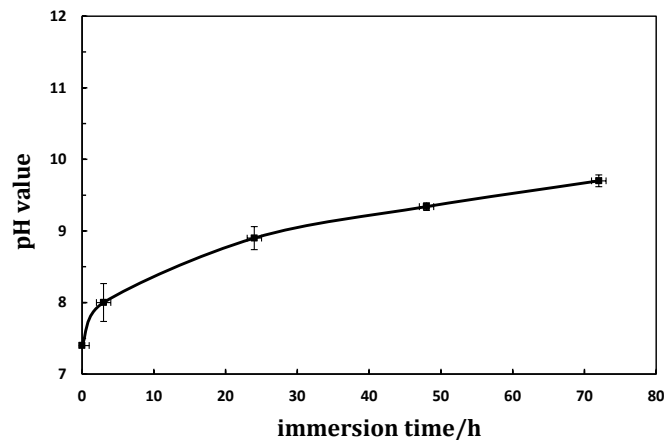


Fig. 4. 3. Change in pH of SBF during the immersion of the Mg-0.5Sr alloy as a function of immersion time.

Fig. 4. 4 represents the electrochemical polarization curves of Mg-0.5Sr compared to pure Mg. The potential has shifted to more noble values with the addition of 0.5wt.%Sr and the current density, indicating the rate of corrosion, has decreased. The values of the corrosion potential and the corrosion-current density of each specimen are shown in Table 4. 3. The cathodic polarization curve that corresponds to the hydrogen evolution reaction [38, 50] tends to increase in pure Mg. Hence, the cathodic hydrogen reaction proceeds more easily on pure Mg. One can conclude that the cathodic hydrogen-evolution reaction was retarded with the addition

of the alloying element. The anodic polarization curve of the Mg-0.5Sr exhibits a current plateau higher than that of pure Mg. This result shows again that the addition of a small amount of Sr can inhibit the dissolution of Mg, which agrees with the results observed in the immersion tests (Fig. 4. 1).

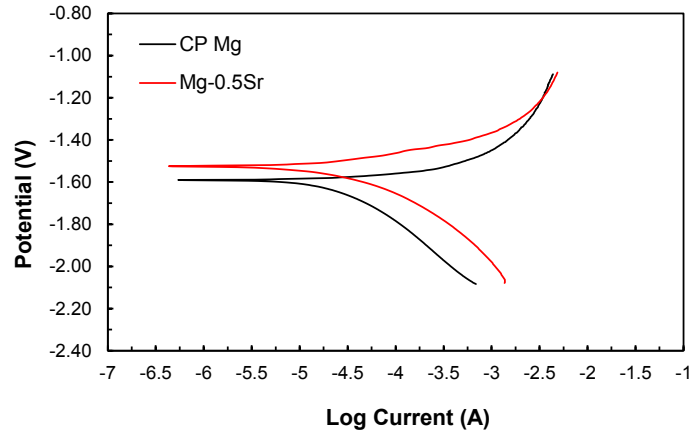


Fig. 4. 4. Polarization curves of as-cast pure Mg (CP Mg) and Mg-0.5Sr in Hank's solution.

Table 4. 3: Corrosion potential and corrosion current density of Mg alloys in SBF obtained by linear fitting on both cathodic and anodic parts of polarization curves

Alloys	I_{corr} (A/cm ²)	E_{corr} (V)
Mg-0.5Sr	5.011 E-06	-1.58
CP Mg	1.259 E-05	-1.6

4. 4. 1. 2. Surface Characterization

Images showing typical macroscopic appearance of Mg-0.5Sr surfaces cleaned after immersion in SBF for different time intervals are presented in Fig. 4. 5a-c. Notably, areas that are free of corrosion damage can be observed on the surface of Mg-0.5Sr even after 3 days of immersion. On the contrary, severe corrosion attack is observed even after just 1 day of immersion in SBF for pure Mg (Fig. 4. 5d). These highly localized areas of corrosion are usually attributed to small amounts of impurities in the chemical composition of commercially pure magnesium. Fig. 4. 6 shows the optical images from the cross-section of Mg-0.5Sr after immersion in SBF for different times showing the increasing area of attack and depth penetration with time. It can be seen that the depth of attack increased from $\sim 150 \mu\text{m}$ after 1 day of immersion to more than $\sim 300 \mu\text{m}$ after 3 days of immersion.

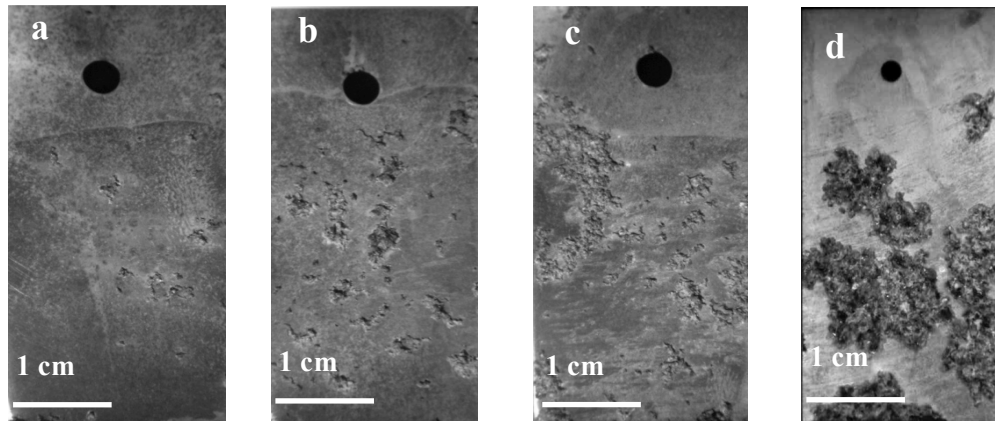


Fig. 4. 5. The surface appearance of as-cast Mg-0.5Sr removed from SBF after (a) 1 day, (b) 2 days (c) 3 days, and (d) pure Mg after 1 day of immersion at 37°C. A significant amount of the surface of pure Mg exhibits extensive corrosion even after one day of immersion.

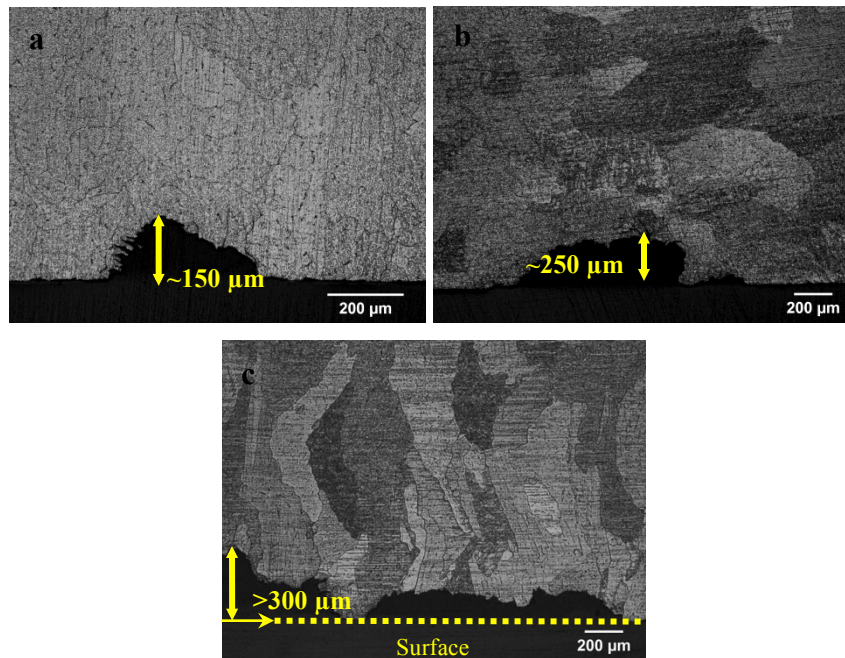


Fig. 4. 6. Optical micrograph from cross-section of as cast Mg-0.5Sr after immersion in SBF for (a) 1 day, (b) 2 days, and (c) 3 days showing the depth corrosion on the sample surface.

The binary Mg-Sr phase diagram indicates the presence of α -Mg matrix and secondary phases of $Mg_{17}Sr_2$ (β) at room temperature for alloys in the range that we investigated [51]. The

EDS analysis shows that the grain boundaries are decorated with Sr-compounds (Fig. 4. 7); based on the thermodynamic phase diagram, these would be $Mg_{17}Sr_2$ [51]. It is known that Mg intermetallic compounds have different corrosion potential than pure Mg which leads to the formation of micro galvanic couples [11]. Thus, the grain boundaries and interdendritic areas (in the as-cast structure) become regions of local corrosion. The microgalvanic couple results in large interdendritic or intergranular depressions where cathodic particles are removed and dissolved in the solution. This phenomenon would increase the apparent corrosion rate in terms of mass loss in this step, which is not only due to the electrochemical reaction. The rapid corrosion of the Mg-Sr alloys with Sr greater than 1 wt.% and higher amounts of $Mg_{17}Sr_2$ (as is known from the phase diagram and EDS analyses) thus is attributed to the formation of many galvanic cells on the surface where the amount of $Mg_{17}Sr_2$ increases with increasing Sr.

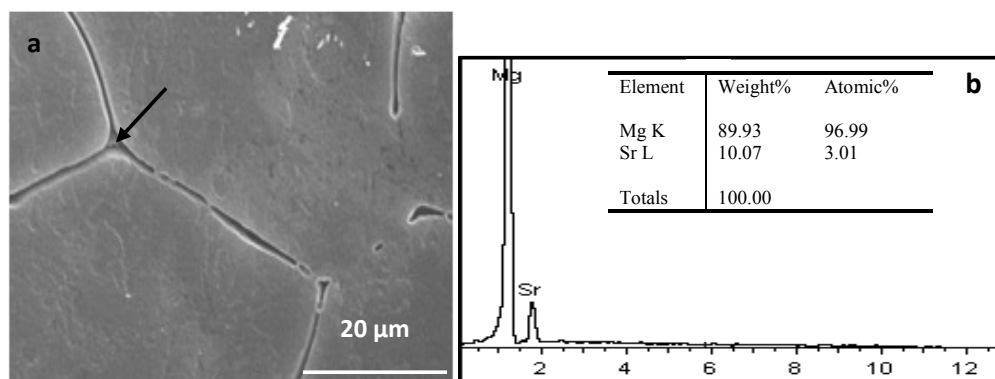


Fig. 4. 7. (a) Secondary electron images from cross-section of Mg-0.5Sr after immersion in SBF for 1 day and, (b) EDS spectroscopy from the gain boundary region marked with an arrow.

4. 4. 1. 3. Analysis of the Surface Layer

The typical electrochemical reaction of Mg in alkaline solution is the dissolution of Mg and the formation of $Mg(OH)_2$ on the surface. However, $Mg(OH)_2$ is highly soluble in the presence of Cl^- anions and transforms to $MgCl_2$ on the surface. Fig. 4. 8 a & b present the SEM cross-sectional images of the Mg-0.5Sr samples immersed in SBF for different times. Fig. 4. 8a shows that a thin surface-scale has formed and that relatively shallow depressions ($<3 \mu m$) have appeared. In Fig. 4. 8b, three days after immersion, the surface scale has increased in thickness and the depth of the depressions ($10-12 \mu m$) and the roughness of the surface have magnified. However, the depressions are rather shallow and with time a thin protective layer forms on the surface in parallel to the decelerating degradation rate. Although this layer may have an

inhibitory effect depending on its nature and serve as a barrier, the ions that exist in the solution may still pass through it and attack fresh Mg beneath this surface layer and continue the degradation process as observed by Li et al on Mg-Ca alloys [38].

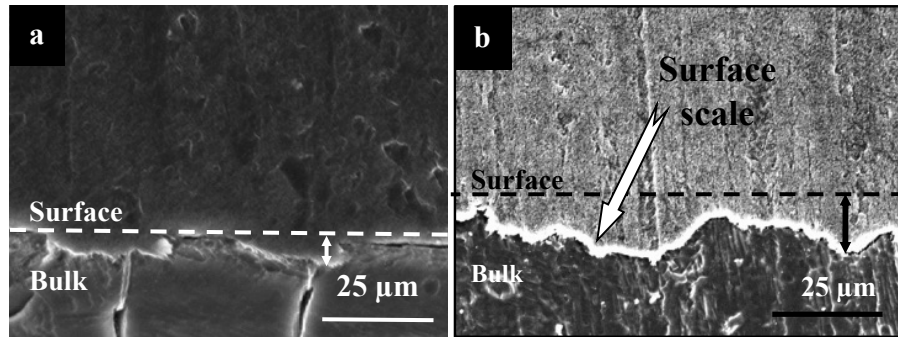


Fig. 4. 8. Secondary electron images from the cross-section of Mg-0.5Sr after immersion in SBF for (a) 1 day, and (b) 3 days showing the white surface scale on the sample.

The layers on the surface of Mg-0.5Sr and pure Mg were investigated via SEM (Fig. 4. 9). It can be seen that the morphology of the surface scale varies from globular in Mg-0.5Sr to needle-like in pure Mg. EDS analyses on both surfaces indicate the presence of Ca, P, O and Mg. The Ca/P ratio found on Mg-0.5Sr and pure Mg is ~ 1.6 and ~ 1.8 respectively. Fig. 4. 10 presents the XRD spectrum from the corroded surface of Mg-0.5Sr after 3 days of immersion in SBF. The major phase in the surface layer is $\text{Mg}(\text{OH})_2$, however, the XRD spectra also shows that hydroxyapatite (HA) has formed on the surface of Mg-Sr alloy after immersion. These results do not agree with the findings of Brar et al [37] who have found only $\text{Mg}(\text{OH})_2$ on the surface of Mg-Sr alloys after 7 days of immersion. The formation of HA is promoted by alkaline conditions, which is time-dependent during the bio-corrosion of Mg. Since after 7 days the pH would be higher than after 3 days, the time difference cannot explain such different behavior, which might instead be related to differences in the microstructure and surface conditions of the samples. XRD could not be successfully obtained on the non-adherent surface scale of pure Mg. Due to the difficulty of in-situ formation of an adherent and stable HA on pure Mg and on various Mg alloys, ex-situ electro-deposition of HA has been adopted [52, 53]. Wang et al [54] have associated the needle shaped crystal clusters with MgCl_2 rather than magnesium hydroxide or hydroxyapatite while Geng et al [55] saw a flake-like morphology and a Ca:P ratio of 1.54 on the β -TCP (β -tricalcium phosphate) coating on pure Mg; β -TCP is a precursor of HA.

XPS characterization was carried out on post-immersion surfaces of pure Mg and Mg-0.5Sr. Ca and P were found on both Mg-0.5Sr and pure Mg samples after immersion in SBF. In both samples, high resolution XPS spectra from corrosion products showed that the P_{2p} peak was centered at 133.6 eV, as expected for phosphate groups, and $Ca_{2p_{1/2}}$ at 351.3 eV as expected for Ca^{2+} in $Ca_{10}(PO_4)_6(OH)_2$ [56-59]. Compositional depth profiles were measured on these samples using argon sputtering cycles of 50 sec each. Table 4. 4 presents the C, Ca and P atomic % found on each layer on the two samples, along with the calculated Ca/P ratio. While the C atomic % decreased, indicating the amount of surface C was due to contamination, the Ca/P ratio increased as deeper levels were analyzed, and reached a value of approximately 1.6. This confirmed the formation of hydroxyapatite as part of the corrosion products of both Mg and Mg-Sr alloys [60-62]. Lower Ca/P ratios on the top layers can be attributed to defective, Ca-deficient hydroxyapatite at the surface [63-65]. The higher Ca/P ratio found from EDS on pure Mg is to be related to the deeper volume analyzed with EDS compared to XPS.

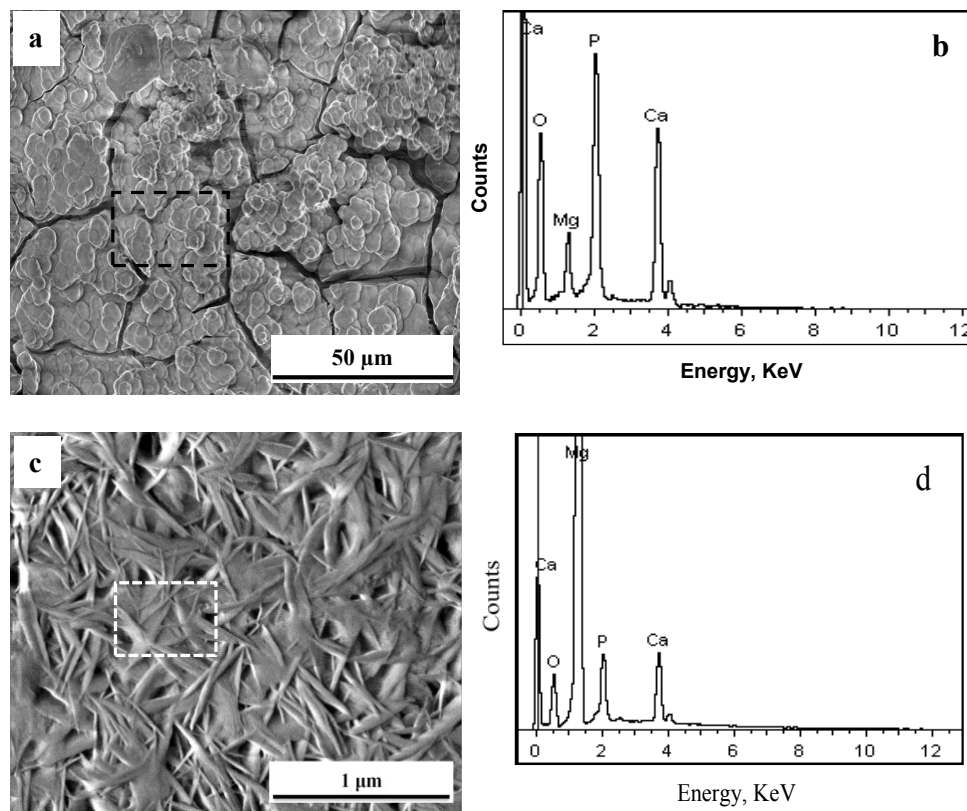


Fig. 4. 9. Secondary electron image and EDS analysis from the surface of (a & b) Mg-0.5Sr and (c & d) pure Mg after immersion in SBF. Thin layer of containing Ca, P, Mg and O formed on the surface.

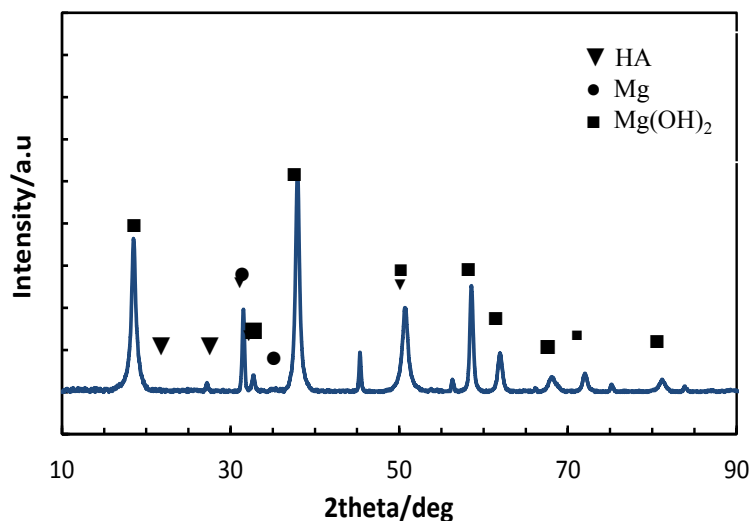


Fig. 4. 10. X-ray diffraction patterns correspond to corrosion products formed on the surface of Mg-0.5Sr after 3 days immersion in SBF. Hydroxyapatite was detected in the 2theta range 15-35°.

Table 4. 4: Atomic concentration found by XPS from the surface of Mg-0.5Sr and pure Mg before and after sputtering with Ar ions for successive 50 second cycles.

Sample	Etching level	Ca	P	C	Ca/P
Pure Mg	0	16.46	13.74	9.4	1.197
	1	20.9	14.17	0.56	1.474
	2	21.4	14.09	0.69	1.518
	3	22.13	13.37	0.67	1.655
Mg-0.5Sr	0	16.17	13.87	13.9	1.165
	1	20.97	16.17	0.83	1.296
	2	23.26	15.77	0.64	1.474
	3	24.45	14.89	0.62	1.654

SEM and XPS were conducted on the post-immersion surfaces of Mg-Sr and pure Mg after removing the corrosion products. Fig. 4. 11 shows the SEM image of the samples after the removal of corrosion products. While the Mg surface was quite homogeneous (Fig. 4. 11b), the Mg-Sr alloy surface clearly showed two different regions, marked as A and B in Fig. 11a. XPS analysis conducted on these samples showed that while Ca and P were barely found on pure Mg,

they could be detected on both regions “A” and “B” of Mg-Sr sample (Table 4. 5). The Ca atomic % is very high on the Mg-Sr especially on the region “B”. Small amounts of Sr (~ 0.8 %) were found on the surface of Mg-Sr after removing the corrosion products. Around 5% C was detected on the surface of Mg-Sr after removing the corrosion products. Around 5% C was detected on the surface of Mg-Sr sample, the presence of which can be related to the formation of carbonates rather than hydrocarbons since the latter forming due to the contamination were removed from the surface by few seconds etching before obtaining the XPS spectra.

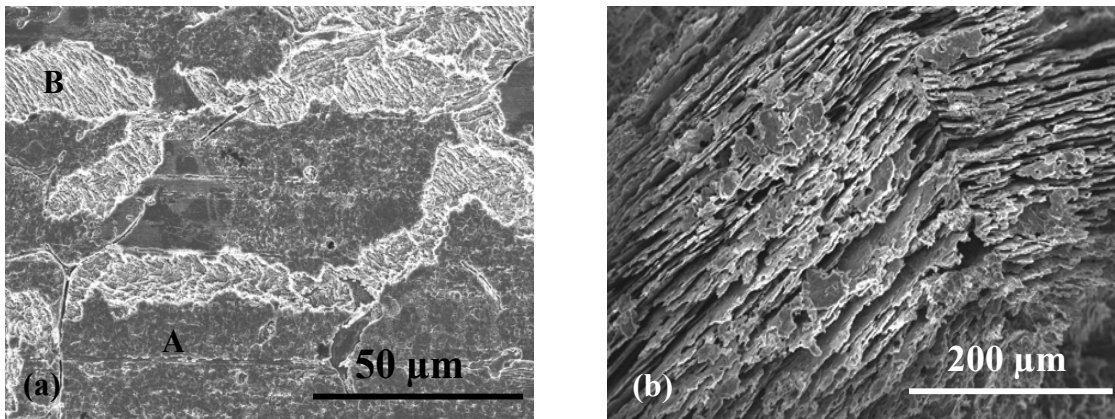


Fig. 4. 11. Secondary electron image from the surface of (a) Mg-0.5Sr and (b) pure Mg after removing the corrosion products.

Table 4. 5: XPS analysis from the surface of Mg-0.5Sr and pure Mg after removing the corrosion products and after a few seconds of etching with Ar ions.

Region	Elemental composition (At.%)					
	Mg	O	Ca	P	Sr	C
A (Mg-0.5Sr)	48.5	31.5	12.1	1.6	0.8	5.5
B (Mg-0.5Sr)	43.7	26.3	20.7	1.9	0.8	5.7
Pure Mg	64.7	33.5	1.6	0.1	-	0.1

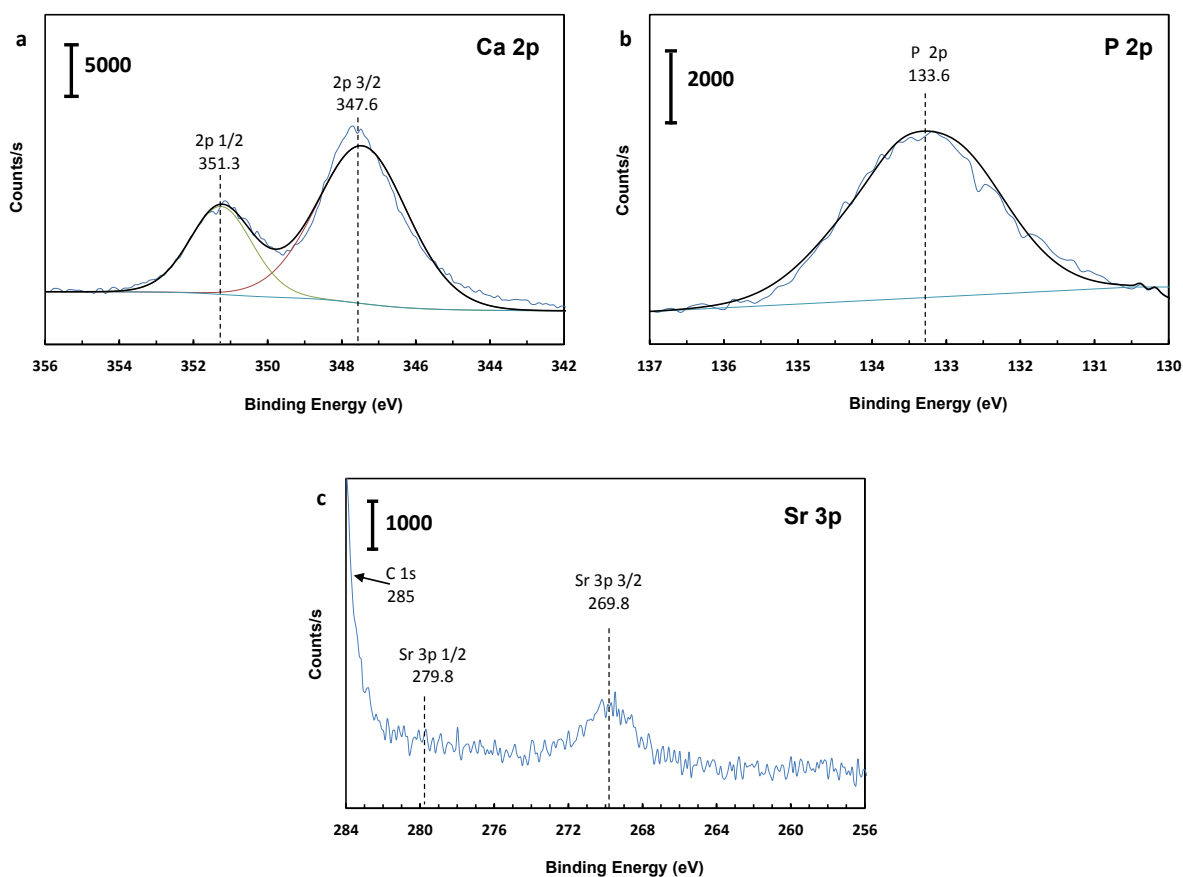


Fig. 4. 12. High resolution XPS spectra of Ca_{2p}, P_{2p} and Sr_{3p} on the surface of Mg-0.5Sr after 1 day immersion test and removing the corrosion products.

These results indicate that after immersion in SBF, a Ca-rich layer containing small amounts of P and Sr formed on the Mg-Sr alloy surface, which could be detected after cleaning the corrosion products. The high resolution spectra for Ca_{2p}, P_{2p} and Sr_{3p} on this sample are shown in Fig. 4. 12. The P_{2p} peak was centered at 133.6 eV and the Ca_{2p3/2} at 347.6 eV, which correspond to Ca²⁺ and PO₄³⁻ ions. The peak of Sr_{3p3/2} is centered at 269.8 eV, indicative of Sr²⁺ rather than metallic Sr [58, 66, 67]. These results suggest that part of the Ca detected on Mg-Sr alloys after the removal of the corrosion products is bound to PO₄³⁻ ions; the simultaneous presence of Sr²⁺ on the surface of these samples point at the formation of a Sr-substituted HA. Most likely the rest of the Ca detected is present in the form of CaCO₃ as discussed before.

These results provide an important indication: while on pure Mg the corrosion products can be removed by cleaning and leave only insignificant amounts of Ca and P on the surface, the

products are more strongly bound on the Mg-Sr alloys, particularly in certain regions (here called regions “B”, showing higher atomic % of Ca and P). This may be related to the formation of a Sr-substituted HA phase on this sample, formed due to the dissolution of Sr^{2+} ions from the alloy and their precipitation as Sr-HA. The Sr substitution into HA may be responsible for change in the morphology of the corrosion products (Fig. 4. 9). Sr-containing HA coatings have been found to improve the bioactivity and bio-corrosion resistance of titanium alloys as well [68, 69]. Sr-HA is known to have better biocompatibility, thermal stability and surface reactivity than pure HA [35, 70]. This preliminary analysis thus suggests that the formation of Sr-HA is a key advantage in the use Mg-Sr alloys as materials for bio-implants.

4. 4. 2. Cytotoxicity Evaluation

Mg-Sr implant materials are intended for use in various bio-implants ranging from bone to cardiovascular applications. In this study, the cytotoxicity of Mg-0.5Sr specimen was examined by evaluating the viability of the HUVECs (commonly used to evaluate stent materials) in contact with ions extracted from the alloy. WE43, which has been recently examined as a bioresorbable Mg stent, was selected as control sample for in vitro and in vivo evaluation [9, 15, 16, 40]. Fig. 4. 13 presents the cell viability after exposure for 1, 4 and 7 days to medium extracted from Mg-0.5Sr sample. The viability of the cells cultured in Mg-0.5Sr extraction medium containing $0.5796 \pm 0.002 \text{ mg/l Mg}^{2+}$ ions is close to the control in 24h after exposure. Furthermore, the viability of the cells was higher with longer exposure to the alloy extract, which indicates that the extracted cations promoted healthy growth of the cells. The lower viability at the first day of exposure can be attributed to the high rate of corrosion in the initial stages. This result demonstrates that Mg-0.5Sr alloy extraction medium has a positive influence on the viability and growth of the HUVECs. These results agree with the previous observation of Li et al [48] who recorded no inhibitory effect of alkali-heat-treated magnesium (with $\text{NaHCO}_3\text{-MgCO}_3$) on marrow-cell growth. Li et al [38] reported that abundant magnesium ions released from the Mg-1Ca specimen to the culture medium can enhance the cell attachment and promote the proliferation and growth of the L-929 cells. The adhesion and growth of human bone-derived cell (HBDC) was observed to be improved on magnesium modified Al_2O_3 substrate [19].

Fig. 4. 13 also shows results from cytotoxicity evaluation of WE43 extracts. Also in this case, HUVAC cells have more viability in contact with WE43 ions extract compared with control. However, there is no specific trend since the viability significantly increased after 4 days

but then decreased after 7 days of exposure. We can conclude that Mg-0.5Sr increases cell viability more than WE43 over longer exposure times.

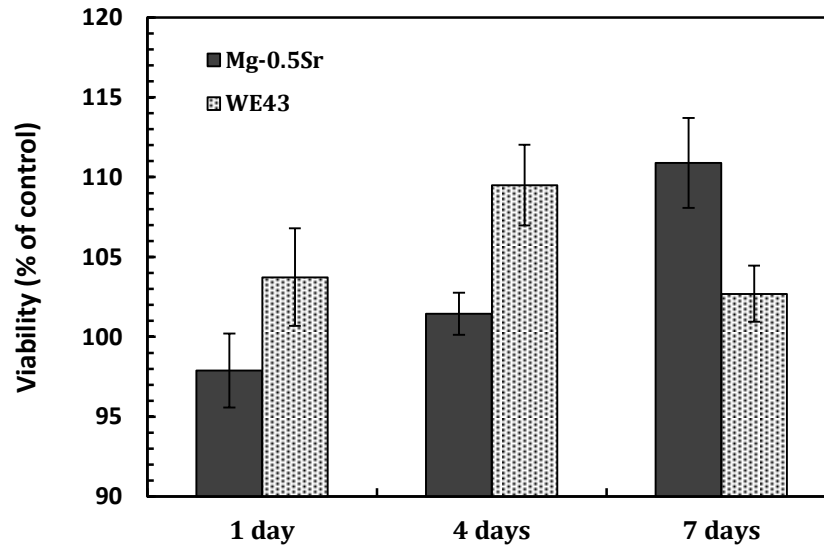


Fig. 4. 13. Cell viability expressed as a percentage of the viability of cells in the control (F-12K) after 1, 4 and 7 days of exposure to the extraction of Mg-0.5Sr and WE43 alloys.

4. 4. 3. Implantation and Post-Implantation Analysis

We examined the effect of Mg-0.5Sr and WE43 alloy stents implanted in medium animal (dog) arteries. WE43 alloy stents thrombosed after 3 weeks of implantation, and aggregates covered the surface and the inside of the stents. The Mg-0.Sr alloy, instead, accumulated only a small amount of residues, and did not thrombose.

Fig. 4. 14 a & b show the tubular Mg-0.5 Sr stent before and after implantation into the femoral artery, and Fig. 4. 15 illustrates the SEM images from longitudinal cross section of retrieved tubular shape stents of Mg-0.5Sr and WE43 harvested after three weeks of implantation. Both implants kept their tubular shape after 3 weeks implantation. However, WE43 stent maintained its initial dimension and its wall thickness did not change significantly whereas the post-operative Mg-0.5Sr tube lost about half of its initial wall thickness (0.27 mm). The wall surface of retrieved Mg-0.5Sr tube contained some pits caused by localized corrosion. The results indicated that the main volume of Mg-0.5Sr implant was gradually decreased over time. The WE43 stent on the other hand did not show considerable degradation during three weeks (Table 4. 6).

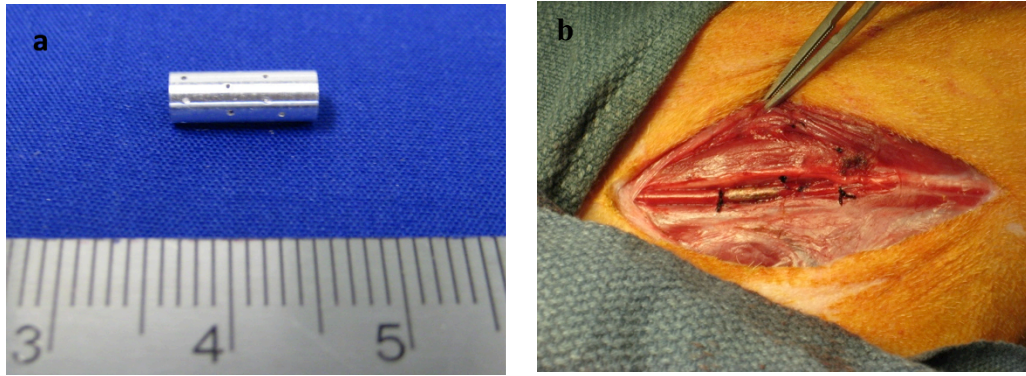


Fig. 4. 14. The Tubular Mg-0.5Sr stent (a) before and (b) after 3 weeks implantation into the right femoral artery of the animal.

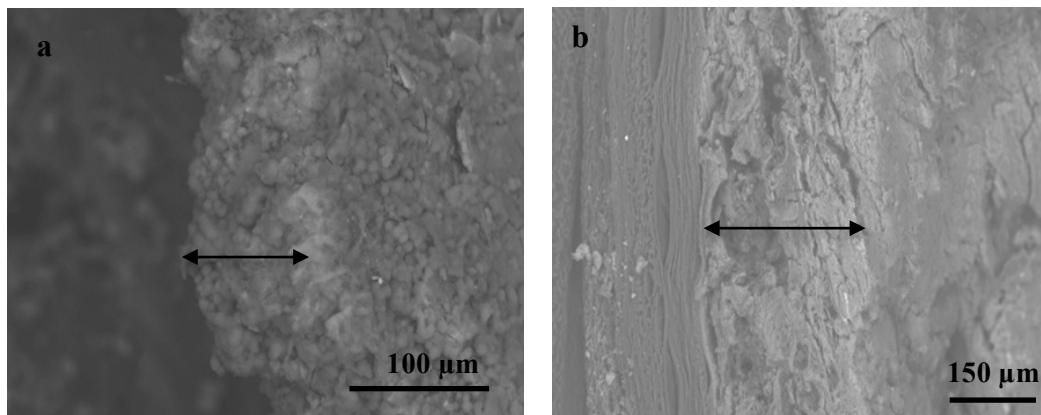


Fig. 4. 15. SEM images from the longitudinal cross section of (a) Mg-0.5Sr and (b) WE43 implanted in the right and left femoral artery of a dog respectively. Both samples were retrieved 3 weeks after operation. The wall thicknesses of retrieved Mg stents were marked with arrow. The initial wall thickness of the stents was 0.27 mm.

From the data shown in Table 4. 6, we can estimate the in vivo average biodegradation of the Mg-0.5Sr alloy. The stent wall in our in vivo study decreased to $\sim 1/2$ its initial dimension in 21 days. The total mass loss in 21 days is 0.063 g (or 3 mg/day of mass loss from the stent). Since the stent contains 0.5wt.% Sr, this implies a Sr release of 0.015 mg of Sr/day. This value is well below the allowed limits of 4–5 mg/day [71-73]. It is also comparable to the in vitro corrosion rate of 0.01 mg/day found in this study.

Table 4. 6: Initial Dimension, volume and mass of Mg-0.5Sr and WE43 stents before and after implantation

	Initial Dimension of the Stents			Final wall thickness (mm)	Initial Volume (mm ³)	Initial Mass (gr)	Final Volume (mm ³)	Final Mass (gr)
	Diameter (mm)	Length (mm)	Wall thickness (mm)					
Mg-0.5Sr	2.4	10	0.27	0.13	72.232	0.125	36.116	0.062
WE43	2.4	10	0.27	0.27	72.232	0.132	72.232	0.132

This study did not evaluate the time required for complete stent degradation; since the degradation is high in the initial stages the average rate calculated here does not allow the estimation of how long the stent would last when implanted. In vivo studies [27] on Mg-2Sr alloy gave an in vivo biodegradation rate of 1 mm/year. This alloy has shown 5 times higher rate of degradation than the Mg-0.5Sr in our study (Fig. 4. 1). Our ongoing research, which will be detailed in a forthcoming paper, shows that the biodegradation rate of Mg-0.5Sr is usually similar to Mg-Ca alloys with Ca level less than 1 wt.%. The bio-degradation rate of Mg-0.8Ca was found to be ~0.4 mm/year [27]; hence, the in vivo degradation rate of Mg-0.5Sr stent can be envisaged at ~0.2–0.4 mm/year. With a wall thickness 0.27 mm, the stent in this study is estimated to last 35–38 weeks.

The fact that the Mg-Sr alloy did not thrombose while the WE43 did is interesting even though the results do not have statistical significance because only a limited number of stents were evaluated in vivo. Mg and Sr are recognized as “familiar” ions by the body; hence cell proliferation is likely to be lower at the Mg-Sr stent. Instead, the rare earth ions present in WE43 are “foreign” to the make-up of the human body; this could therefore lead to enhanced cell proliferation at the WE43 stent, increasing the thrombosis risks. Recently, the cytocompatibility of rare earth elements has been evaluated by indirect cytotoxicity assays; Yttrium in WE43 has been found to have positive effects on cell viability. The cell viability test of this study also shows that both WE43 and the Mg-Sr alloy enhance cell viability creating an environment where cells would thrive enhancing endothelialization; however, since WE43 contains rare-earth elements, it could also increase the proliferation of cells such as smooth muscle cells (SMC) which can lead to the more significant formation of neo-intima on this stent. Mg and Sr in the Mg-0.5Sr stent would create a viable environment for endothelialization without the increased risk of SMC proliferation and thick neo-intimal growth. The results of this study suggests that a

stent fabricated via machining from as-cast Mg-0.5Sr alloy has the potential to offer an optimum combination of properties of acceptable degradation rate, good bio-compatibility, and low risk of thrombosis.

4. 5. CONCLUSIONS

The corrosion rate of pure Mg in SBF was tailored by addition of small amount of Sr. Mg alloys with low concentration of Sr such as the Mg-0.5Sr have slow degradation rate with decelerating hydrogen evolution after one day. Sr in excess of 1 wt.% alloyed to Mg leads to high biodegradation rate which is attributed to micro galvanic corrosion between the Mg-matrix and Mg₁₇Sr₂ intermetallic phase.

In vitro and in vivo tests show that Mg-0.5Sr has the potential to be used as temporary vascular implant since it did not lead to thrombosis during three weeks of implantation.

An important finding is the formation of Sr-substituted HA layer on Mg-0.5Sr during bio-corrosion in SBF. The formation of this modified layer slows down the degradation of this alloy in physiological conditions. Moreover, since Sr-substituted HA is known to enhance cell growth and proliferation and healing around bone implants, we can conclude that the Mg-0.5Sr alloy is a promising candidate for orthopedic applications.

4. 6. REFERENCES

- [1] Staiger MP, Pietak AM, Huadmai J, Dias G. Magnesium and its alloys as orthopedic biomaterials: A review. *Biomaterials*. 2006;27:1728-34.
- [2] Kannan MB, Raman RKS. In vitro degradation and mechanical integrity of calcium-containing magnesium alloys in modified-simulated body fluid. *Biomaterials*. 2008;29:2306-14.
- [3] Witte F, Fischer J, Nellesen J, Crostack HA, Kaese V, Pisch A, et al. In vitro and in vivo corrosion measurements of magnesium alloys. *Biomaterials*. 2006;27:1013-8.
- [4] Witte F, Feyerabend F, Maier P, Fischer J, Stoermer M, Blawert C, et al. Biodegradable magnesium-hydroxyapatite metal matrix composites. *Biomaterials*. 2007;28:2163-74.
- [5] Moravej M, Mantovani D. Biodegradable Metals for Cardiovascular Stent Application: Interests and New Opportunities. *International Journal of Molecular Sciences*. 2011;12:4250-70.
- [6] Witte F. The history of biodegradable magnesium implants: A review. *Acta Biomaterialia*. 2010;6:1680-92.

- [7] Kirkland NT, Birbilis N, Staiger MP. Assessing the corrosion of biodegradable magnesium implants: a critical review of current methodologies and their limitations. *Acta biomaterialia*. 2012;8:925-36.
- [8] Kraus T, Fischerauer SF, Haenzi AC, Uggowitz PJ, Loeffler JF, Weinberg AM. Magnesium alloys for temporary implants in osteosynthesis: In vivo studies of their degradation and interaction with bone. *Acta Biomaterialia*. 2012;8:1230-8.
- [9] Gu XN, Zhou WR, Zheng YF, Cheng Y, Wei SC, Zhong SP, et al. Corrosion fatigue behaviors of two biomedical Mg alloys-AZ91D and WE43-In simulated body fluid. *Acta Biomaterialia*. 2010;6:4605-13.
- [10] Heublein B, Rohde R, Kaese V, Niemeyer M, Hartung W, Haverich A. Biocorrosion of magnesium alloys: a new principle in cardiovascular implant technology? *Heart*. 2003;89:651-6.
- [11] Zeng R, Dietzel W, Witte F, Hort N, Blawert C. Progress and challenge for magnesium alloys as biomaterials. *Advanced Engineering Materials*. 2008;10:B3-B14.
- [12] Waksman R, Pakala R, Kuchulakanti PK, Baffour R, Hellinga D, Seabron R, et al. Safety and efficacy of bioabsorbable magnesium alloy stents in porcine coronary arteries. *Catheterization and Cardiovascular Interventions*. 2006;68:607-17.
- [13] Zartner P, Cesnjevar R, Singer H, Weyand M. First successful implantation of a biodegradable metal stent into the left pulmonary artery of a preterm baby. *Catheterization and Cardiovascular Interventions*. 2005;66:590-4.
- [14] Paul Erne MS, Therese J. Resink. The Road to Bioabsorbable Stents: Reaching Clinical Reality? *Cardiovasc Intervent Radiol*. 2006;29:5.
- [15] Erbel R, Di Mario C, Bartunek J, Bonnier J, de Bruyne B, Eberli FR, et al. Temporary scaffolding of coronary arteries with bioabsorbable magnesium stents: a prospective, non-randomised multicentre trial. *Lancet*. 2007;369:1869-75.
- [16] Di Mario C, Griffiths H, Goktekin O, Peeters N, Verbist J, Bosiers M, et al. Drug-eluting bioabsorbable magnesium stent. *Journal of interventional cardiology*. 2004;17:391-5.
- [17] McBride ED. Absorbable metal in bone surgery - A further report on the use of magnesium alloys. *Journal of the American Medical Association*. 1938;111:2464-6.
- [18] Song Y, Shan D, Chen R, Zhang F, Han E-H. Biodegradable behaviors of AZ31 magnesium alloy in simulated body fluid. *Materials Science & Engineering C-Biomimetic and Supramolecular Systems*. 2009;29:1039-45.

- [19] Zreiqat H, Howlett CR, Zannettino A, Evans P, Schulze-Tanzil G, Knabe C, et al. Mechanisms of magnesium-stimulated adhesion of osteoblastic cells to commonly used orthopaedic implants. *Journal of Biomedical Materials Research*. 2002;62:175-84.
- [20] Yun Y, Dong Z, Yang D, Schulz MJ, Shanov VN, Yarmolenko S, et al. Biodegradable Mg corrosion and osteoblast cell culture studies. *Materials Science & Engineering C-Materials for Biological Applications*. 2009;29:1814-21.
- [21] Gu X, Zheng Y, Cheng Y, Zhong S, Xi T. In vitro corrosion and biocompatibility of binary magnesium alloys. *Biomaterials*. 2009;30:484-98.
- [22] Witte F, Hort N, Vogt C, Cohen S, Kainer KU, Willumeit R, et al. Degradable biomaterials based on magnesium corrosion. *Current Opinion in Solid State & Materials Science*. 2008;12:63-72.
- [23] Rettig R, Virtanen S. Time-dependent electrochemical characterization of the corrosion of a magnesium rare-earth alloy in simulated body fluids. *Journal of Biomedical Materials Research Part A*. 2008;85A:167-75.
- [24] Gu XN, Zheng W, Cheng Y, Zheng YF. A study on alkaline heat treated Mg-Ca alloy for the control of the biocorrosion rate. *Acta Biomaterialia*. 2009;5:2790-9.
- [25] Zhang S, Zhang X, Zhao C, Li J, Song Y, Xie C, et al. Research on an Mg-Zn alloy as a degradable biomaterial. *Acta Biomaterialia*. 2010;6:626-40.
- [26] Wang HX, Guan SK, Wang X, Ren CX, Wang LG. In vitro degradation and mechanical integrity of Mg-Zn-Ca alloy coated with Ca-deficient hydroxyapatite by the pulse electrodeposition process. *Acta Biomaterialia*. 2010;6:1743-8.
- [27] Gu XN, Xie XH, Li N, Zheng YF, Qin L. In vitro and in vivo studies on a Mg-Sr binary alloy system developed 3 as a new kind of biodegradable metal. *Acta Biomaterialia*. 2012.
- [28] Fan Y, Wu G, Zhai C. Effect of strontium on mechanical properties and corrosion resistance of AZ91D. 2007. p. 567-70.
- [29] Dahl SG, Allain P, Marie PJ, Mauras Y, Boivin G, Ammann P, et al. Incorporation and distribution of strontium in bone. *Bone*. 2001;28:446-53.
- [30] Marie PJ. Strontium ranelate: a novel mode of action optimizing bone formation and resorption. *Osteoporosis International*. 2005;16:S7-S10.
- [31] Taylor A. Therapeutic uses of trace-elements. *Clinics in Endocrinology and Metabolism*. 1985;14:703-24.

- [32] Zhang W, Shen Y, Pan H, Lin K, Liu X, Darvell BW, et al. Effects of strontium in modified biomaterials. *Acta Biomaterialia*. 2011;7:800-8.
- [33] Bigi A, Boanini E, Capuccini C, Gazzano M. Strontium-substituted hydroxyapatite nanocrystals. *Inorganica Chimica Acta*. 2007;360:1009-16.
- [34] Nielsen SP. The biological role of strontium. *Bone*. 2004;35:583-8.
- [35] Suganthi RV, Elayaraja K, Joshy MIA, Chandra VS, Girija EK, Kalkura SN. Fibrous growth of strontium substituted hydroxyapatite and its drug release. *Materials Science & Engineering C-Materials for Biological Applications*. 2011;31:593-9.
- [36] Zeng XQ, Wang YX, Ding WJ, Luo AA, Sachdev AK. Effect of strontium on the microstructure, mechanical properties, and fracture behavior of AZ31 magnesium alloy. *Metallurgical and Materials Transactions a-Physical Metallurgy and Materials Science*. 2006;37A:1333-41.
- [37] Brar HS, Wong J, Manuel MV. Investigation of the mechanical and degradation properties of Mg-Sr and Mg-Zn-Sr alloys for use as potential biodegradable implant materials. *Journal of the mechanical behavior of biomedical materials*. 2012;7:87-95.
- [38] Li Z, Gu X, Lou S, Zheng Y. The development of binary Mg-Ca alloys for use as biodegradable materials within bone. *Biomaterials*. 2008;29:1329-44.
- [39] Wan Y, Xiong G, Luo H, He F, Huang Y, Zhou X. Preparation and characterization of a new biomedical magnesium-calcium alloy. *Materials & Design*. 2008;29:2034-7.
- [40] Hermawan H, Dube D, Mantovani D. Developments in metallic biodegradable stents. *Acta Biomaterialia*. 2010;6:1693-7.
- [41] Barth KH, Virmani R, Froelich J, Takeda T, Lossef SV, Newsome J, et al. Paired comparison of vascular wall reactions to Palmaz stents, Strecker tantalum stents, and Wallstents in canine iliac and femoral arteries. *Circulation*. 1996;93:2161-9.
- [42] Salam TA, Taylor B, Suggs WD, Hanson SR, Lumsden AB. Reaction to injury following balloon angioplasty and intravascular stent placement in the canine femoral-artery. *American Surgeon*. 1994;60:353-7.
- [43] Song G, Song S. Magnesium as a possible degradable bio-compatible material. In: Pekguleryuz M, Mackenzie L, editors. 45th Annual Conference of Metallurgists of CIM. Montreal: Magnesium Technology in the Global Age; 2006. p. 359.

- [44] Hassel T, Bach F-W, Golovko A, Krause C. Investigation of the mechanical properties and the corrosion behavior of low alloyed magnesium-calcium-alloys for use as absorbable biomaterial in the implant technique. In: Pekguleryuz M, Mackenzie L, editors. 45th Annual Conference of Metallurgists of CIM. Montreal: Magnesium Technology in the Global Age; 2006. p. 359.
- [45] Song G. Control of biodegradation of biocompatible magnesium alloys. *Corrosion Science*. 2007;49:1696-701.
- [46] Witte F, Kaese V, Haferkamp H, Switzer E, Meyer-Lindenberg A, Wirth CJ, et al. In vivo corrosion of four magnesium alloys and the associated bone response. *Biomaterials*. 2005;26:3557-63.
- [47] Ren Y, Huang J, Zhang B, Yang K. Preliminary study of biodegradation of AZ31B magnesium alloy. *Mater Sci*. 2007;1:3.
- [48] Li LC, Gao JC, Wang Y. Evaluation of cyto-toxicity and corrosion behavior of alkali-heat-treated magnesium in simulated body fluid. *Surface & Coatings Technology*. 2004;185:92-8.
- [49] Song GL, Atrens A. Corrosion mechanisms of magnesium alloys. *Advanced Engineering Materials*. 1999;1:11-33.
- [50] Takenaka T, Ono T, Narazaki Y, Naka Y, Kawakami M. Improvement of corrosion resistance of magnesium metal by rare earth elements. *Electrochimica Acta*. 2007;53:117-21.
- [51] Aljarrah M, Medraj M. Thermodynamic modelling of the Mg-Ca, Mg-Sr, Ca-Sr and Mg-Ca-Sr systems using the modified quasichemical model. *Calphad-Computer Coupling of Phase Diagrams and Thermochemistry*. 2008;32:240-51.
- [52] Song YW, Shan DY, Han EH. Electrodeposition of hydroxyapatite coating on AZ91D magnesium alloy for biomaterial application. *Materials Letters*. 2008;62:3276-9.
- [53] Song Y, Zhang S, Li J, Zhao C, Zhang X. Electrodeposition of Ca-P coatings on biodegradable Mg alloy: In vitro biomineralization behavior. *Acta Biomaterialia*. 2010;6:1736-42.
- [54] Wang Y, Wei M, Gao J, Hu J, Zhang Y. Corrosion process of pure magnesium in simulated body fluid. *Materials Letters*. 2008;62:2181-4.
- [55] Geng F, Tan LL, Jin XX, Yang JY, Yang K. The preparation, cytocompatibility, and in vitro biodegradation study of pure beta-TCP on magnesium. *Journal of Materials Science-Materials in Medicine*. 2009;20:1149-57.

- [56] Xu L, Pan F, Yu G, Yang L, Zhang E, Yang K. In vitro and in vivo evaluation of the surface bioactivity of a calcium phosphate coated magnesium alloy. *Biomaterials*. 2009;30:1512-23.
- [57] Landis W, Martin J. X-ray photoelectron spectroscopy applied to gold-decorated mineral standards of biological interest. *J Vac Sci Technol A*. 1984;2:4.
- [58] Han Y, Zhou J, Zhang L, Xu K. A multi-scaled hybrid orthopedic implant: bone ECM-shaped Sr-HA nanofibers on the microporous walls of a macroporous titanium scaffold. *Nanotechnology*. 2011;22.
- [59] Pereiro I, Rodríguez-Valencia C, Serra C, Solla EL, Serra J, González P. Pulsed laser deposition of strontium-substituted hydroxyapatite coatings. *Applied Surface Science*. 2012;6.
- [60] Kalita SJ, Bhardwaj A, Bhatt HA. Nanocrystalline calcium phosphate ceramics in biomedical engineering. *Materials Science & Engineering C-Biomimetic and Supramolecular Systems*. 2007;27:441-9.
- [61] Hanawa T, Ducheyne P, Nancollas GH, Legros RZ, Lemons JE, Kasemo B. Titanium and its oxide film - a substrate for formation of apatite. *Bone-Biomaterial Interface*. 1991;49-61.
- [62] Demri B, Muster D. XPS study of some calcium compounds. *Journal of Materials Processing Technology*. 1995;55:311-4.
- [63] Wang H, Guan S, Wang Y, Liu H, Wang H, Wang L, et al. In vivo degradation behavior of Ca-deficient hydroxyapatite coated Mg-Zn-Ca alloy for bone implant application. *Colloids and Surfaces B-Biointerfaces*. 2011;88:254-9.
- [64] Guo H, Su J, Wei J, Kong H, Liu C. Biocompatibility and osteogenicity of degradable Ca-deficient hydroxyapatite scaffolds from calcium phosphate cement for bone tissue engineering. *Acta Biomaterialia*. 2009;5:268-78.
- [65] Blumenthal NC, Betts F, Posner AS. Formation and structure of ca-deficient hydroxyapatite. *Calcified Tissue International*. 1981;33:111-7.
- [66] Vandoveren H, Verhoeven JAT. Xps spectra of ca, sr, ba and their oxides. *Journal of Electron Spectroscopy and Related Phenomena*. 1980;21:265-73.
- [67] Seyama H, Soma M. X-RAY photoelectron spectroscopic study of montmorillonite containing exchangeable divalent-cations. *Journal of the Chemical Society-Faraday Transactions I*. 1984;80:237-48.

- [68] Kung K-C, Lee T-M, Lui T-S. Bioactivity and corrosion properties of novel coatings containing strontium by micro-arc oxidation. *Journal of Alloys and Compounds*. 2010;508:384-90.
- [69] Pramatarova L, Pecheva E, Presker R, Pham MT, Maitz MF, Stutzmann M. Hydroxyapatite growth induced by native extracellular matrix deposition on solid surfaces. *European cells & materials*. 2005;9:9-12.
- [70] Gu Y, Liao D, Zhou Z. The experimental study of Sr-HAP on reconstructing mandibular bone defect. *Zhonghua kou qiang yi xue za zhi = Zhonghua kouqiang yixue zazhi = Chinese journal of stomatology*. 2001;36:262-5.
- [71] <http://www.lenntech.com/periodic/water/strontium/strontium-and-water.htm>.
- [72] Kabata-Pendai A, Mukherjee AB. Trace elements from soil to human. Berlin: Springer; 2007.
- [73] Kirkland NT, Staiger MP, Nisbet D, Davies CHJ, Birbilis N. Performance-driven design of Biocompatible Mg alloys. *Jom*. 2011;63:28-34.

CHAPTER 5

COMBINED ADDITION OF Sr AND Ca ON BIOCORROSION, MICROSTRUCTURE AND MECHANICAL PROPERTIES OF Mg

After determining the beneficial effect of Sr on the corrosion resistivity and biocompatibility of biodegradable Mg implants, the study continued towards investigating the combined addition of Sr with Ca. These results have been published as two journal articles. The Mg-Ca system has been previously identified in the literature and within our research group as a promising biodegradable alloy with a controlled degradation rate and acceptable biocompatibility. However, Ca is not desirable at high levels in the cardiovascular system. Our results presented in Chapter 4 showed that Sr has similar effects. The idea of using both Ca and Sr in Mg comes out from what is known as the “third element effect” for the corrosion and oxidation of alloys: the addition of even a minor level of a third element may decrease the levels of other alloying elements required to improve the corrosion or oxidation resistance of the final alloy. This decrease in the overall corrosion rate is obtained because the third element may change the activity of the other elements or form a barrier surface layer through its initial preferential corrosion.

In this chapter, the results on the effect of the combined addition of Sr and Ca on properties of Mg are discussed in view of its application in biodegradable implants. The chapter comprises two sections; each section is a published journal manuscript. Section 5.1 compares the effect of the combined addition of low levels of Sr and Ca to the single addition of each element. The effect of Sr and Ca addition on the *in vitro* corrosion rate in the physiological environment and the mechanical properties were examined compared to those of binary Mg-Sr and Mg-Ca alloys. In-depth microstructural evaluation was performed using optical microscopy, SEM, EPMA and

TEM to understand the effect of the alloying elements. The corrosion rate of the Mg-Sr-Ca alloy was correlated to the microstructural features and explained in terms of the third element effect. The microstructural investigation identified the presence of a new intermetallic finely dispersed in the as-cast alloy that was found to have beneficial effects both on the bio-corrosion resistance and on mechanical properties. Section 5.2 describes the effect of thermal exposure on the in vitro degradation and mechanical properties of Mg-Sr-Ca and Mg-Sr alloys. The corrosion behavior and mechanical behavior of these samples was investigated in the as-cast state as well as after thermal treatment at 400 °C for 8 h and 24 h. The metallurgical stability of the new phase identified in the first part of the work (Section 5.1) was evaluated. The optimum conditions and appropriate manufacturing process for the candidate alloys to maintain their beneficial mechanical properties during implantation and in-service mechanical performance were discussed.

5. 1. Magnesium implant alloy with low levels of strontium and calcium: the third element effect and phase selection improve bio-corrosion resistance and mechanical performance

This section has been published as: M. Bornapour, M. Celikin, M. Cerruti, M. Pekguleryuz, Magnesium implant alloy with low levels of strontium and calcium: the third element effect and phase selection improve bio-corrosion resistance and mechanical performance, *Materials Science & Engineering C-Materials for Biological Applications* 35 (2014), 267-282.

5. 1. 1. ABSTRACT

Low density, non-toxicity, biodegradability and mechanical properties similar to human tissues such as bone make magnesium (Mg) alloys attractive for biomedical applications ranging from bone to cardiovascular implants. The most important challenge that still prevents the widespread use of Mg implants is their rapid degradation rate. In this study we investigate the combined effect of calcium (Ca) and strontium (Sr) on the corrosion behavior of Mg via in vitro immersion and electrochemical tests in simulated body fluid (SBF), and analyze changes in mechanical properties. We show that the combined addition of 0.3wt.% Sr and 0.3wt.% Ca decreases the corrosion rate of Mg both in terms of mass loss and hydrogen evolution more effectively than the single addition of either alloying element. We investigate the microstructure of as-cast specimens and the morphology of the corrosion products using optical microscopy, scanning electron microscopy, electron probe micro-analysis, X-ray diffraction, and X-Ray photoelectron spectroscopy. Tensile and three point bending tests reveal that the ternary alloy Mg-0.3Sr-0.3Ca has a good combination of mechanical properties and corrosion resistance with hydrogen evolution rates of 0.01 mL/cm²/h in SBF. Higher concentrations of Sr and Ca alter the resulting microstructure leading to increased corrosion rates in SBF by promoting the micro-galvanic corrosion between the α -Mg matrix and intermetallic phases of Mg₁₇Sr₂ and Mg₂Ca along the grain boundaries. These results indicate that the combined addition of optimal amounts of Ca and Sr is a promising approach to decrease the high degradation rate of Mg implants in physiological conditions, as well as attaining high ductility in the alloy. The better properties of the Mg-0.3Sr-0.3Ca alloy are related to the new intermetallic phases found in this sample. The optimum composition is attributed to the “third element effect”, as seen in the corrosion behavior of metallic alloys.

5. 1. 2. INTRODUCTION

In recent years, biodegradable Mg alloys have been the subject of much research due to their low density (1.74 g/cm^3), Young's modulus close to that of natural bone [1-6] and their biocompatibility. Mg is one of the essential elements for human metabolism [7, 8]; it is known to stimulate the growth of bone cells and accelerate bone tissue healing process [3, 9]. When used in vivo, Mg forms a soluble and non-toxic oxide that can be eliminated in the urine [10].

Despite these advantages, the use of pure Mg is rather limited due to its poor mechanical strength and corrosion resistance [4, 11, 12]. The high corrosion rate of Mg in physiological condition is the major drawback to its use in biomedical implants [2]. Orthopedic and cardiovascular implants require adequate strength, ductility and fatigue resistance. Since alloying elements can improve the mechanical properties and decrease the corrosion rate of Mg, several Mg alloys have been tested as biomedical implant materials, such as AZ91 (Mg-9Al-1Zn), AZ31 (Mg-3Al-1Zn), LAE442 (Mg-4Li-4Al-1RE, where RE=rare earth element), WE43 (Mg-4Y-3RE), Mg-Zr and Mg-Zn [2, 6, 13-24] (all alloy compositions in this paper are in weight percent unless otherwise specified). The choice of alloying elements is limited, since only a few elements can be used in the body without harmful effects [25]. Aluminum can decrease the degradation rate of Mg but it is known to be neurotoxic to humans [13, 14, 26]. Zinc is highly cytotoxic and at high levels causes genotoxicity [27, 28]. Mg alloys containing REs such as WE43 and LAE442 enhanced the osteoblastic response in the guinea pig femur [3], and extruded Mg-Zn-Y-Nd alloy was identified as a good candidate for degradable vascular stents [29]. However, while REs may not be toxic, they may increase the risk of cell proliferation and thrombosis after implantation since they are not naturally present in the body [13-15, 26, 30]. Nakamura et al [30] reported severe hepatotoxicity after administration of yttrium, praseodymium and cerium. Our previous study showed that while WE43 did not negatively affect the viability of HUVECs in the short term, in the long run it led to the formation of a thick neo-intima layer and thrombosis after in vivo implantation [31].

The addition of Ca to Mg for biomedical applications has been studied as well [32-35]. Ca, with a density of 1.55 g/cm^3 is an alkaline-earth element like Mg. It is a major component of bone and an essential element for cell chemical signaling [36]. Several studies have analyzed Ca and Mg interactions in vivo and in vitro. Ca seems to better incorporate into bones in the presence of Mg ions [37]. Optimal amounts of Ca improve the mechanical properties and

increase the corrosion resistance of Mg [38]. Kannan et al [6] observed that the general and pitting corrosion of AZ91 in SBF decreased with Ca additions. Two different groups of authors showed that among different Mg-Ca alloys, Mg-0.6Ca exhibits the best mechanical and corrosion behavior [38, 39], while others reported Mg-1Ca as the alloy with the best corrosion resistance and acceptable biocompatibility [32]. The degradation rate of Mg-Ca alloys, while slower than pure Mg, is still not optimal. For example, a 10×2.5 mm Mg-1Ca pin completely degraded after 3 months of implantation in rabbits [32]—too fast compared to bone healing, which takes approximately 12 months [2].

Strontium (Sr) was recently tested for its use in medical applications [40]. Sr is a component of human bones, and its role in bone, heart and muscle function was shown in the 1950's and 1960's [41]. Sr is known to promote the growth of osteoblasts and prevent bone resorption [42-46]. Notably, if Sr is incorporated within synthetic hydroxyapatite (HA), it improves osteoblast function and bone formation [47-49]. As a grain refiner for Mg, Sr can improve the mechanical properties of some Mg alloys [50], as well as improve the corrosion resistance of Mg by altering its surface [51, 52]. Gu et al [40] studied Mg-Sr binary samples with 1 to 4 wt.% Sr and observed the best combination of corrosion resistance and high strength in as-rolled Mg-2Sr alloy; while Brar et al [53], in their investigation of Mg-Sr alloys with wt.% Sr varying between 0.5 and 1.5, found the lowest biodegradation rate in the Mg-0.5Sr alloy. We have shown that the addition of Sr in amounts lower than 1 wt.% retards the degradation rate of Mg [31]; specifically, we observed the lowest degradation rate for Mg-0.5Sr, among as-cast binary Mg-Sr alloys with Sr wt.% varying between 0.3 and 2.5. We detected a layer of Sr-modified HA on the surface of this alloy when immersed in SBF. This alloy also showed acceptable biocompatibility and enhanced the viability of HUVECs compared to pure Mg.

In this paper, we analyze the combined effect of Ca and Sr on the mechanical properties and degradation of Mg, in view of its application in biodegradable implants. The idea of using both Ca and Sr in Mg stems from what is known as the “third element effect” for the corrosion and oxidation of alloys: the addition of even a minor level of a third element may decrease the levels of other alloying elements required to improve the corrosion or oxidation resistance of the final alloy. This decrease in the overall corrosion rate is obtained because the third element may change the activity of the other elements or form a barrier surface layer through its initial preferential corrosion [54-56]. At the same time, though, the addition of extra elements can alter

the phase selection and the microstructure of the alloy, thereby altering its mechanical properties. The third element effect is described in detail by Wagner [57] for Cu-Al and Fe-Al alloys with Zn and Cr additions, respectively. In this study we correlate the corrosion rate of Mg-Sr-Ca as-cast alloys to their microstructural features, and compare the mechanical properties of the ternary alloys to those of binary Mg-Sr and Mg-Ca alloys.

5. 1. 3. EXPERIMENTAL PROCEDURE

5. 1. 3. 1. Alloy synthesis and sample preparation

Mg alloys were synthesized by melting down pure Mg (99.9 wt.%), pure Sr (99.99 wt.%) and Mg-30Ca master alloy all supplied by Applied Magnesium (Formerly Timminco) in a Lindberg/Blue M Crucible Furnace. CO₂ with 0.5% SF₆ was used at a flow rate of 1.1 L/min as a protective gas to prevent burning during melting and casting. K-type (Chromel-Alumel) thermocouple was used with a digital thermometer to monitor the melt temperature. Thin plates were cast using a steel die coated with boron-nitride release coating and pre-heated to 400°C. The chemical analysis of the alloys was obtained by inductively coupled plasma atomic emission spectroscopy (ICP-AES). Two binary samples of Mg-0.5Sr and Mg-0.6Ca were selected as base alloys, since they are known as good candidates for biodegradable implants. Two ternary alloys with nominal compositions of Mg-0.3Sr-0.3Ca and Mg-0.5Sr-0.6Ca were designed. Table 5. 1 lists the nominal and analyzed chemical compositions of the alloys. Commercially pure Mg was also cast into the thin plate mold as a control sample.

Table 5. 1: The actual chemical composition of the alloys

Alloy	Chemical composition (wt. %)						
	Sr	Ca	Al	Si	Fe	Mn	Mg
Mg-0.5Sr	0.51	–	0.011	0.004	0.038	0.003	Balance
Mg-0.6Ca	–	0.73	0.016	0.004	0.036	0.003	Balance
Mg-0.5Sr-0.6Ca	0.53	0.79	0.010	0.004	0.037	0.003	Balance
Mg-0.3Sr-0.3Ca	0.31	0.39	0.011	0.005	0.044	0.003	Balance

5. 1. 3. 2. Immersion test

Corrosion experiments were conducted at $37\pm 1^\circ\text{C}$ in Hank's SBF, the composition of which is given in Table 5. 2. Rectangular samples, $2 \times 4 \text{ cm}^2$, were cut from the as-cast thin plates of 6 mm thickness for the in vitro degradation tests in SBF. Samples were polished, cleaned and sterilized in acetone before immersion in Hank's solution. The pH of the solution was fixed at 7.4 at the beginning of the immersion test. Each sample was suspended to the bottom of a funnel immersed in Hank's solution. The funnel was covered by an inverted silicon caulked burette evacuated and filled with Hank's solution. Hydrogen bubbles released from the corrosion reaction were collected by the funnel and transferred to the burette. The volume of hydrogen gas evolved was measured from the change in the level of Hank's solution during the corrosion test. The experiment was stopped when the amount of hydrogen gas could not be measured due to the limited volume of the burette. Samples were cleaned off of corrosion residues using chromium trioxide (CrO_3) according to ASTM G1-90 and air dried immediately after the immersion tests. The amount of mass loss, H_2 gas released and the pH of SBF were monitored during and at the end of each test. The corrosion rate was calculated in terms of mass loss and hydrogen evolution and an average value was reported for each composition from triplicate experiments.

Table 5. 2: Composition of Hank's simulated body fluid.

Reagent	Amount (g/l)
NaCl	8.0
KCl	0.4
CaCl_2	0.14
NaHCO_3	0.35
$\text{C}_6\text{H}_6\text{O}_6$	1.0
$\text{MgCl}_2 \cdot 6\text{H}_2\text{O}$	0.1
$\text{MgSO}_4 \cdot 7\text{H}_2\text{O}$	0.06
$\text{KH}_2\text{PO}_4 \cdot \text{H}_2\text{O}$	0.06
$\text{Na}_2\text{HPO}_4 \cdot 7\text{H}_2\text{O}$	0.06

5. 1. 3. 3. Electrochemical measurements

Potentiodynamic polarization tests were performed using a three-electrode cell. Saturated calomel electrode (SCE) and platinum were used as the reference electrode and the counter

electrode respectively. The samples were polished with SiC paper (down to 800 grit) before soaking in Hank's solution. The three-electrode cell set up had a fixed opening of 0.720 mm² to expose the solution to the surface of the sample. Such exposed area functioned as the working electrode. The current density was monitored as function of open-circuit potential by using VersaSTAT3 (METEK). The samples were stabilized for 5 min in the solution and the test was conducted at 37°C with a scan rate of 0.1666 mV/s for all the measurements. The corrosion current density of each specimen was derived by linear fit to the anodic and cathodic parts of the polarization curves.

5. 1. 3. 4. Microstructural and surface characterization

Optical microscopy (OM) was carried out to observe the microstructure of each sample before and after the immersion tests. The cross-sections of post-immersion specimens were ground, polished with 1 μm diamond paste and etched in 5% Nital. The microstructure of the alloys was characterized using an electron probe micro-analysis (EPMA, JEOL 8900). Field emission gun/scanning electron microscopy (FEG-SEM, Hitachi S-4700) equipped with energy-dispersive spectrometry (EDS) was conducted in secondary electron mode to examine the microstructure of the samples and the corrosion morphology after immersion. The phases present in the as-cast samples were also characterized by X-ray diffraction (XRD) with a Bruker D8 X-ray diffractometer using Cu K_α radiation.

Plates of 1.0 mm thickness obtained from cross-section samples were ground down to 1200 grid to obtain 0.2 mm thickness for transmission electron microscopy (TEM). Disks, 3mm in diameter, were punched, polished down to 50μm and ion beam polished (PIPS, GATAN 691 Precision Ion Polishing) at an angle of 4° (top and bottom) using 3.8kV voltage. Scanning Transmission Electron Microscopy (S/TEM) analysis was conducted using both Philips CM 200 (Selected Area Electron Diffraction-SAED) and FEI Tecnai G2 (EDS line-scans) at 200kV. To facilitate the SAED analysis, diffraction patterns were also drawn via crystallography software (Carine Crystallography) and compared with the actual diffraction patterns obtained via TEM analysis.

The surface morphology of the corroded samples was characterized by X-ray photoelectron spectroscopy (XPS, K-Alpha, Thermo Scientific) using an X-ray source of Al-K_α (1486.6 eV) with a spot size with 400μm diameter. The energy resolution for the high resolution and survey scan was 0.1 and 1 eV respectively. Since the corrosion products were not conductive, spectra

were collected using a flood gun to prevent charging the sample. The surface of the sample was etched with Ar ions in-situ while collecting XPS spectra to remove surface contamination and to measure compositional depth profiles.

5. 1. 3. 5. Mechanical properties

Standard tensile samples of as-cast Mg alloys were machined according to ASTM-E8-04. The tensile tests were carried out at a displacement rate of 0.12 mm min^{-1} using an MTS Alliance RF/200 Instron testing machine. The average values of yield strength (YS), ultimate tensile strength (UTS), and elongation for each alloy composition were obtained from three measurements. Fractography was performed using scanning electron microscopy (SEM, Phenom G2 pure) on the fracture surface of the tensile-tested samples. Beam-shaped samples with dimensions of $6 \times 6 \times 70 \text{ mm}^3$ were prepared for three-point bending tests. All the samples were polished down to 800 grit using SiC paper before testing. The three-point bending tests were conducted using a Tinius Olsen H25K-S testing machine.

5. 1. 4. RESULTS AND DISCUSSION

5. 1. 4. 1. As-cast microstructure and phase analysis

Fig. 5. 1-3 present the optical microstructures, XRD and the SEM analyses of the binary and the ternary alloys. Fig 4 gives the EPMA mapping of the ternary alloys.

Binary Alloys: The as-cast microstructures of Mg-0.5Sr and Mg-0.6Ca are presented in Fig. 5. 1a and b. The microstructures of Mg binary alloys contain an α -Mg matrix and an α -Mg + β -eutectic micro constituent [58]. According to the thermodynamic phase diagrams, the Mg-0.5Sr has the $\text{Mg}_{17}\text{Sr}_2$ equilibrium phase and the Mg-0.6Ca alloy contains the Mg_2Ca equilibrium intermetallic phase at room temperature [58]. Fig. 5. 2 shows the XRD spectra from the cross-sections of as-cast binary and ternary alloys confirming the presence of $\text{Mg}_{17}\text{Sr}_2$ and Mg_2Ca in the alloys. In the binary samples, the β phase has formed along the grain boundaries; continuous brittle phases such as this are usually detrimental to tensile properties since cracks that initiate can easily propagate large distances along these phases. Fig. 5. 3a-d presents the SEM-secondary electron images (SEM-SEI) recorded on the cross-section of Mg alloys. The corresponding EDS analyses (Table 5. 3) reconfirm the presence of Mg and Sr or Mg and Ca in the second phases at

the grain boundaries of binary samples (region B), but no solid solubility of Sr and/or Ca is observed in the Mg matrix (region A).

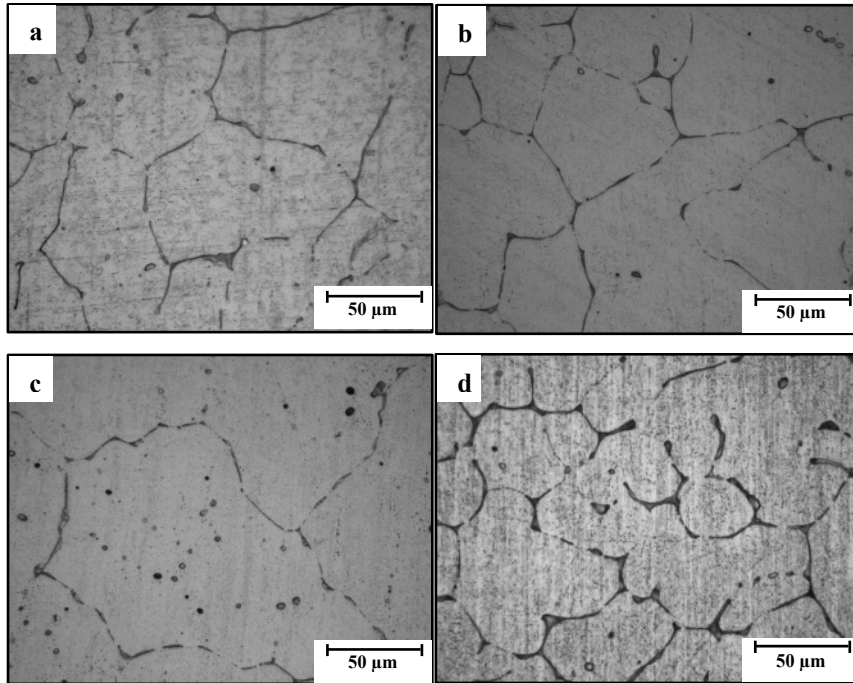


Fig. 5. 1. Optical micrograph from cross-sections of as-cast (a) Mg-0.5Sr, (b) Mg-0.6Ca, (c) Mg-0.3Sr-0.3Ca, and (d) Mg-0.5Sr-0.6Ca.

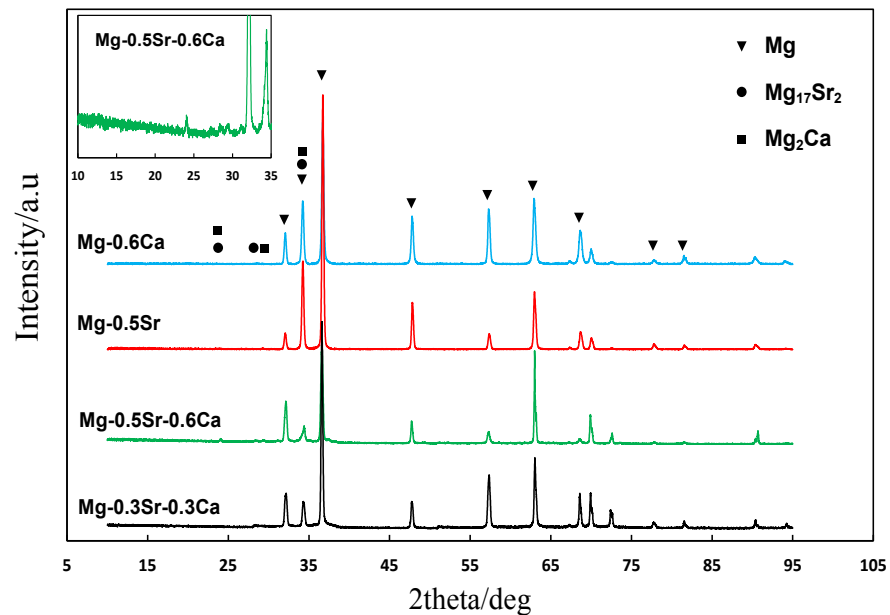


Fig. 5. 2. X-ray diffraction patterns of (a) Mg-0.5Sr, (b) Mg-0.6Ca, (c) Mg-0.3Sr-0.3Ca, and (d) Mg-0.5Sr-0.6Ca. α -Mg, $Mg_{17}Sr_2$ and Mg_2Ca were detected.

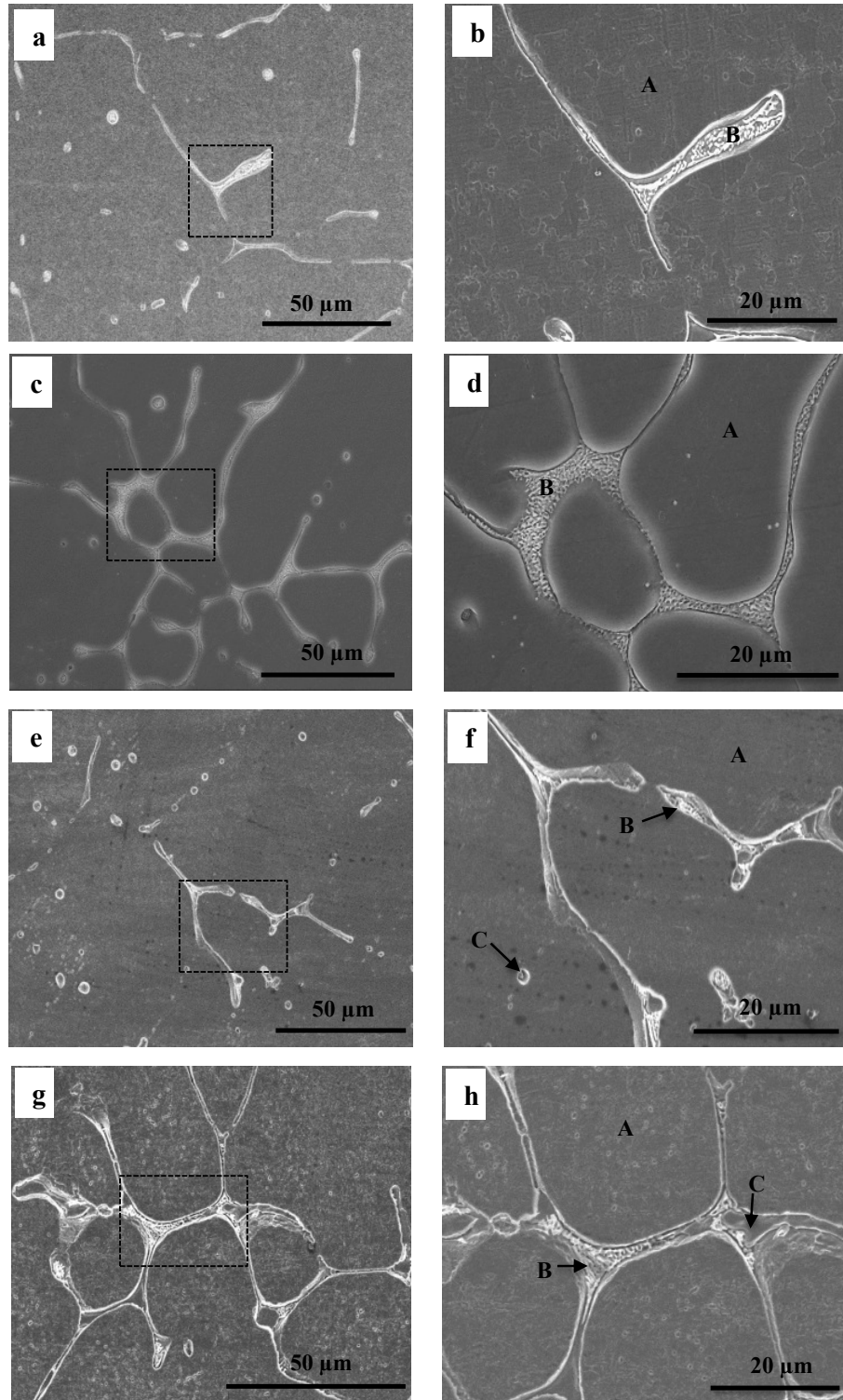


Fig. 5. 3. Secondary electron images from the longitudinal cross sections of (a & b) Mg-0.5Sr, (c & d) Mg-0.6Ca, (e & f) Mg-0.3Sr-0.3Ca and (g & h) Mg-0.5Sr-0.6Ca. Regions marked as A, B and C on the high-magnification images correspond to areas where EDS was performed (see Table 5. 3).

Ternary Alloys: Fig. 5. 1c and d shows the as-cast microstructures of Mg-0.3Sr-0.3Ca and Mg-0.5Sr-0.6Ca. The Mg-0.5Sr-0.6Ca alloy shows a higher volume fraction of the intermetallic phase. Compared to Mg-0.5Sr-0.6Ca, the Mg-0.3Sr-0.3Ca alloy has a coarser dendritic structure and as expected a lower amount of intermetallics. The XRD spectrum of the Mg-0.5Sr-0.6Ca alloy exhibits higher intensities of second phases (Fig. 5. 2). It is known that the amount of second phase plays an important role on the corrosion performance of these alloys; while low levels of Sr or Ca have been found to decrease the corrosion rate of Mg in SBF [32, 38, 59], higher levels lead to the formation of a large amount of second phases, which act as micro galvanic cells and accelerate the corrosion rate of Mg alloys [1, 59].

Table 5. 3: Composition of different regions of the as-cast microstructure of Mg binary and ternary alloys in wt.% (marked as A, B and C in Fig. 3) obtained by EDS.

Alloy	Region A			Region B			Region C		
	Mg	Sr	Ca	Mg	Sr	Ca	Mg	Sr	Ca
Mg-0.5Sr	~100	–	–	92.61	7.39	–	–	–	–
Mg-0.6Ca	~100	–	–	96.99	–	3.01	–	–	–
Mg-0.3Sr-0.3Ca	~100	–	–	91.71	4.67	3.63	90.41	4.29	5.30
Mg-0.5Sr-0.6Ca	~100	–	–	94.01	5.99	–	90.05	–	9.95

The eutectic microconstituent in the ternary alloys (regions B and C in Fig. 5. 3e-h) has a flaky morphology rather than the fibrous morphology seen in the binary alloys. Small globular phases (region C) are also seen dispersed in the microstructure of the ternary alloys. The Sr and Ca levels in the second phases of the ternary alloy vary (Table 5. 3). EDS analyses of Mg-0.3Sr-0.3Ca indicate that the network phases (region B in Fig. 5. 3f) are rich in both Sr and Ca and the small globular particles (region C in Fig. 5. 3f) contain more Ca than Sr. Fig. 5. 4 presents EPMA maps and the elemental distribution of each sample, thus confirming the presence of Sr- and Ca-enriched interdendritic phases and their compositional variations.

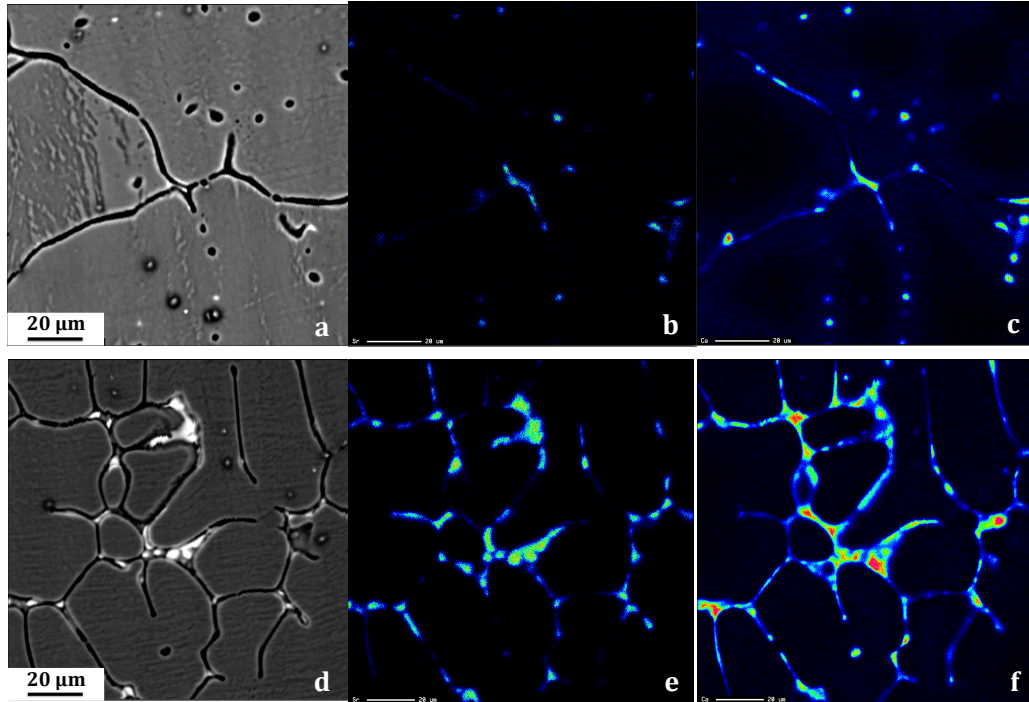


Fig. 5. 4. EPMA micrographs of as-cast Mg-0.3Sr-0.3Ca (a) and Mg-0.5Sr-0.6Ca (d), and their corresponding Sr (b & e) and Ca (c & f) elemental maps.

While thermodynamic studies reveal no intermetallic phase formation between Sr and Ca [58], Pearson [60] indicates the formation of a few Sr-Ca compounds (Table 5. 4). We analyzed the presence of intermetallic phases on Mg-0.3Sr-0.3Ca by TEM analysis, and found three types of second phases in the ternary alloy (Figs. 5-7): (i) interdendritic phase; (ii) globular phase; (iii) needle-shaped phase associated with fine nano-scale globular phase.

Table 5. 4: Crystal structure of the intermetallic compounds

Phase	Prototype	Space group	Pearson symbol	Comments	Ref
Ca-Sr	Cu	cF4	$Fm\bar{3}m$	$Ca_{(1-x)}Sr_x$, $x=0-1$ at 298K	[60]
Ca-Sr	Mg	hP2	$P6_3/mmc$	$Ca_{(1-x)}Sr_x$, $x=0-1$ at 698K	[60]
Ca-Sr	W	cI2	$Im\bar{3}m$	$Ca_{(1-x)}Sr_x$, $x=0-1$ at 903K	[60]
Interdendritic Mg_2 (Ca, Sr)	MgZn ₂ (C14-laves)	hP12	$P6_3/mmc$	$a= 6.212, c= 10.050$	[61]
				$a= 6.36, c= 10.01$ Ca/Sr = 1/ 6	This study
Globular Ca-Sr (Mg)	—	—		hcp ($a=6.42, c= 9.44$) Ca/Sr = 3/2	This study

(i) *Interdendritic phase*: The TEM image (Fig. 5. 5a) of the interdendritic region shows the eutectic morphology with the intermetallic phase surrounding islands of α -Mg. The interdendritic phase was determined to have hexagonal closed packed-hcp structure with lattice parameters $a = 6.36\text{\AA}$ and $c = 10.01\text{\AA}$ by SAED analysis (Fig. 5. 5b). Similar lattice parameters ($a = 6.212\text{\AA}$ and $c = 10.050\text{\AA}$) are reported for the $\text{Mg}_2(\text{Ca}, \text{Sr})$ intermetallic compound (Table 5. 4) in the Ca-Mg-Sr ternary system [61]. EDS shows high levels of Sr and Mg and a small amount of Ca, with an average Ca/ Sr ratio of $\sim 1/6$ (Fig. 5. 5c).

(ii) *Globular phase*: The TEM image shows globular phases 1.5-2.0 μm in size (Fig. 5. 6a); the crystal structure of these globular phase was determined to be hcp with lattice parameters $a = 6.42\text{\AA}$ and $c = 9.44\text{\AA}$ by SAED analysis. Diffraction pattern obtained at $B=[\bar{1}2\bar{1}3]$ and the reciprocal lattice drawn using the same lattice parameters via the crystallography software (Carine Crystallography) are shown in Fig. 5. 6b. The EDS analysis (Fig. 5. 6c) gives a Ca/Sr ratio of 3/2; the high Mg signal likely has a matrix contribution. This is a new phase designated a Ca-Sr(Mg); its crystal structure is different from the binary $\text{Mg}_{17}\text{Sr}_2$ or Mg_2Ca found in the binary alloys and the Ca-Sr compounds listed by Pearson (Table 5. 4).

(iii) *Needle-shaped phase associated with nano-scale globular phase*: This phase is shown in the TEM image of Fig. 5. 7a and is closely associated with a nano-scale globular phase, different from the micron-scale globular phase described above. The line scan across the two phases, globular and needle-shaped, confirms that both phases are Ca-rich and contain a lower amount of Sr; however, the globular phase contains higher level of Ca than the needle-shaped phase (Fig. 5. 7b). The latter also has high levels of Mg indicating it to be $\text{Mg}_2(\text{Ca}, \text{Sr})$. The fine nano-scale globular phase has very low Mg (likely a matrix signal given the small size of the phase), and is basically a binary Ca-Sr intermetallic compound. This phase is similar to the Ca-Sr(Mg) globular phase discussed above but it can also be one of the binary Ca-Sr phases mentioned by Pearson (Table 5. 4).

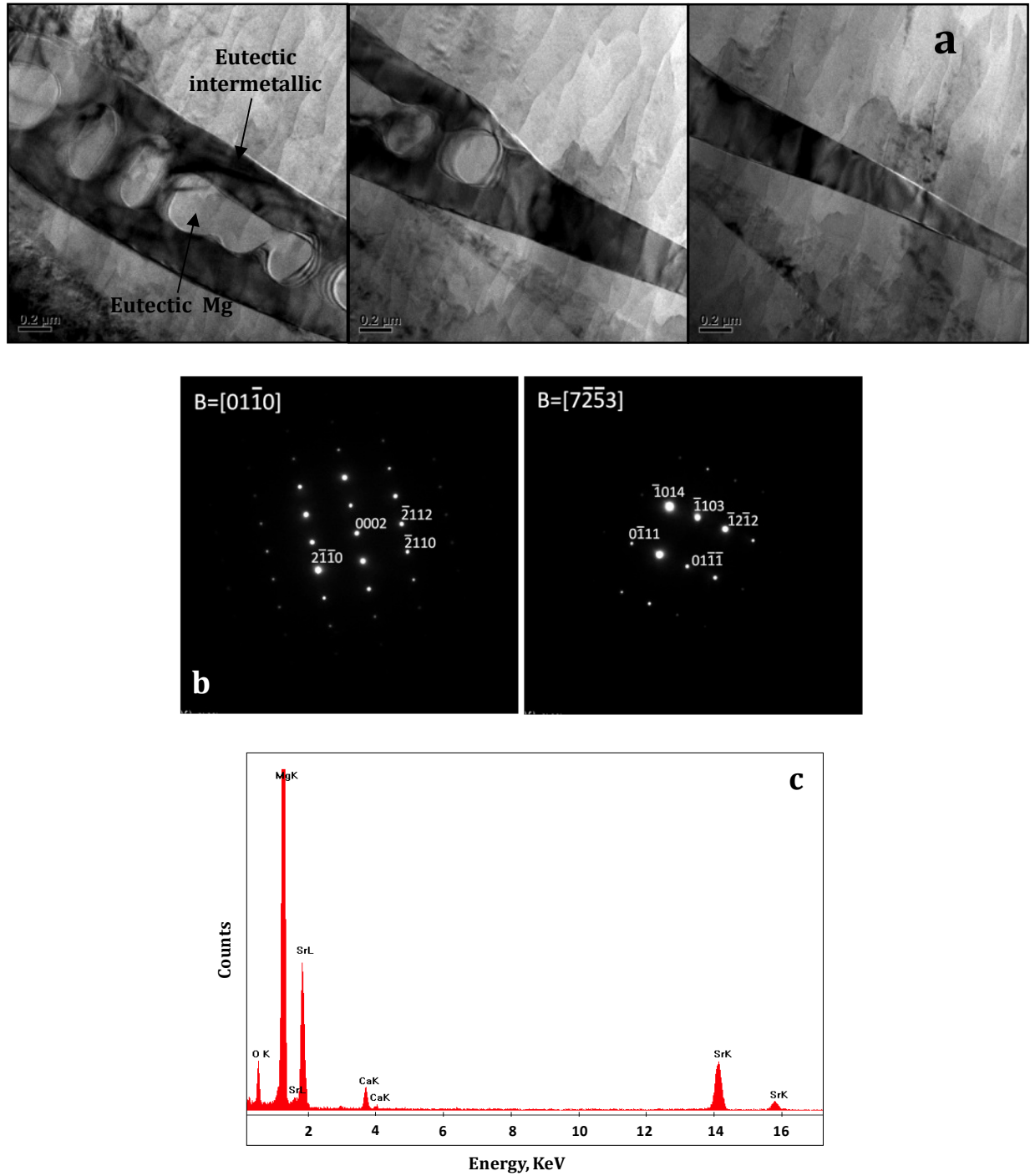


Fig. 5. 5. (a) TEM image showing the intermetallic/Mg phases in the interdendritic eutectic phase in Mg-0.3Sr-0.3Ca; (b) SAED patterns obtained from interdendritic phase at $B = [0\bar{1}\bar{1}0]$ and $B = [7\bar{2}\bar{5}3]$; (c) EDS analysis from the interdendritic phase.

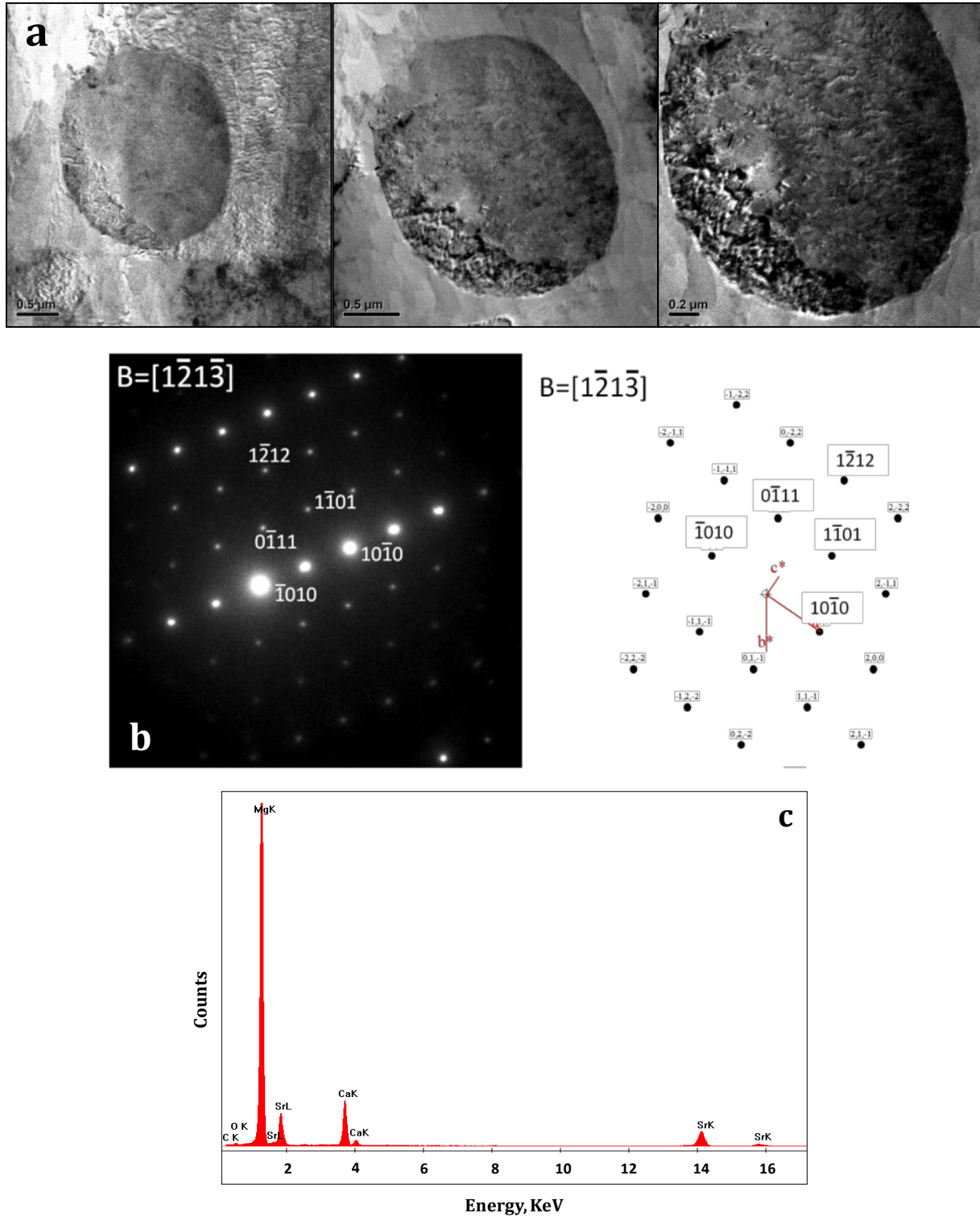


Fig. 5. 6. (a) TEM image of the globular phase in Mg-0.3Sr-0.3Ca at different magnifications; (b, left) SAED pattern obtained from globular phase at $B=[\bar{1}\bar{2}\bar{1}\bar{3}]$ and (b, right) reciprocal lattice drawn using same lattice parameters; (c) EDS analysis from the globular phase.

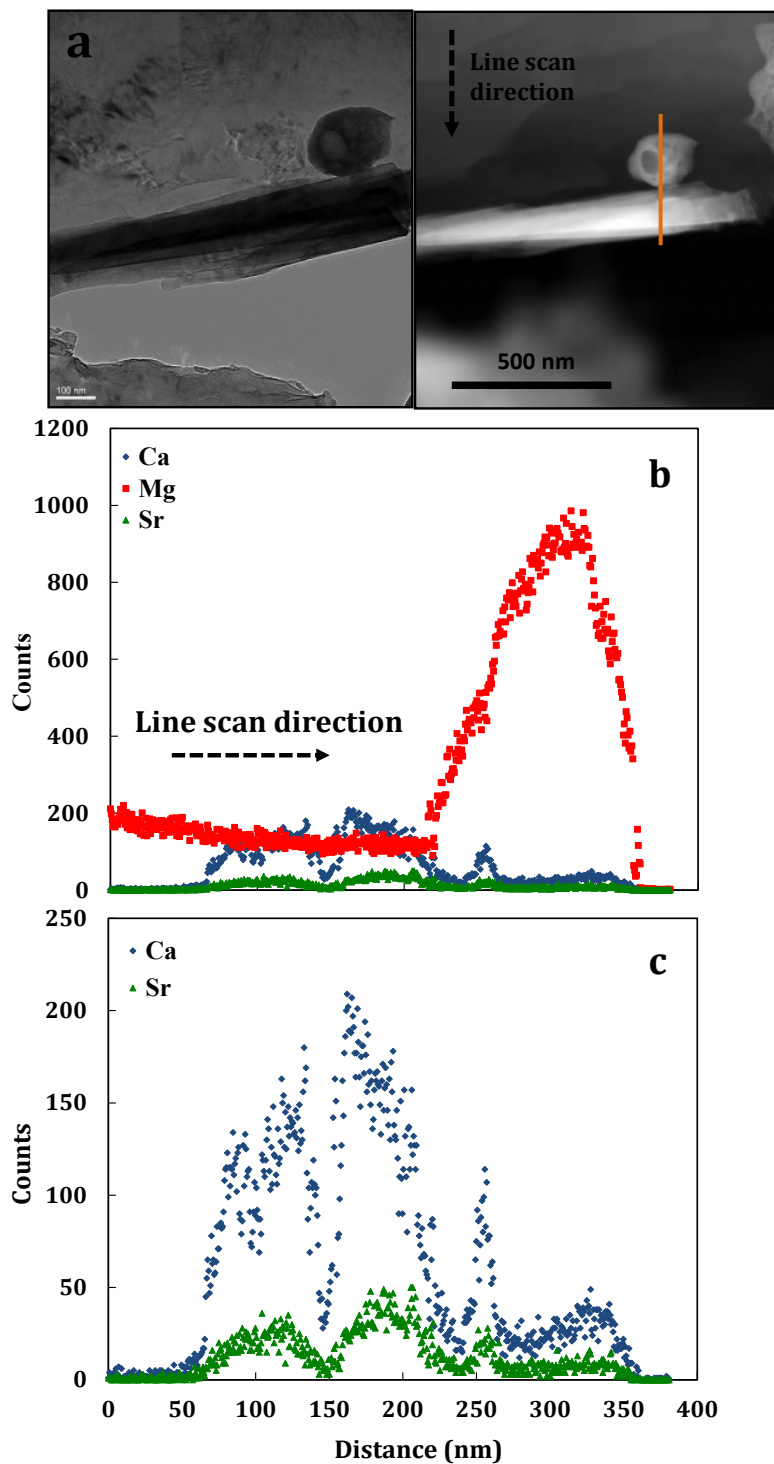


Fig. 5. 7. (a) TEM dark field and bright field image of the needle-shaped phase near a nano-scale globular phase in Mg-0.3Sr-0.3Ca; (b) Line scan across the nano-scale globular phase and needle-shaped phases along the direction shown with an arrow in (a) for Ca (blue), Mg (red) and Sr (green); (c) high resolution line scan of Ca and Sr in (b) without Mg.

5. 1. 4. 2. Corrosion tests in SBF

5.1.4.2.1. Degradation rate

The degradation rates of Mg alloys in SBF calculated in terms of mass loss and H₂ evolution are shown in Fig. 5. 8. The ternary Mg-0.5Sr-0.6Ca alloy degrades faster than the binary alloys, and the ternary Mg-0.3Sr-0.3Ca shows a lower degradation rate than the binaries. The higher degradation rate in the Mg-0.6Sr-0.6Ca can be attributed to the higher amount of micro-galvanic second phase in the alloy, which was also seen in binary alloys [59]. The rate of degradation is lower with the combined ~0.6 wt.% addition of Sr and Ca compared to the single additions of 0.5-0.6 wt.% Ca or Sr (Fig. 5. 8).

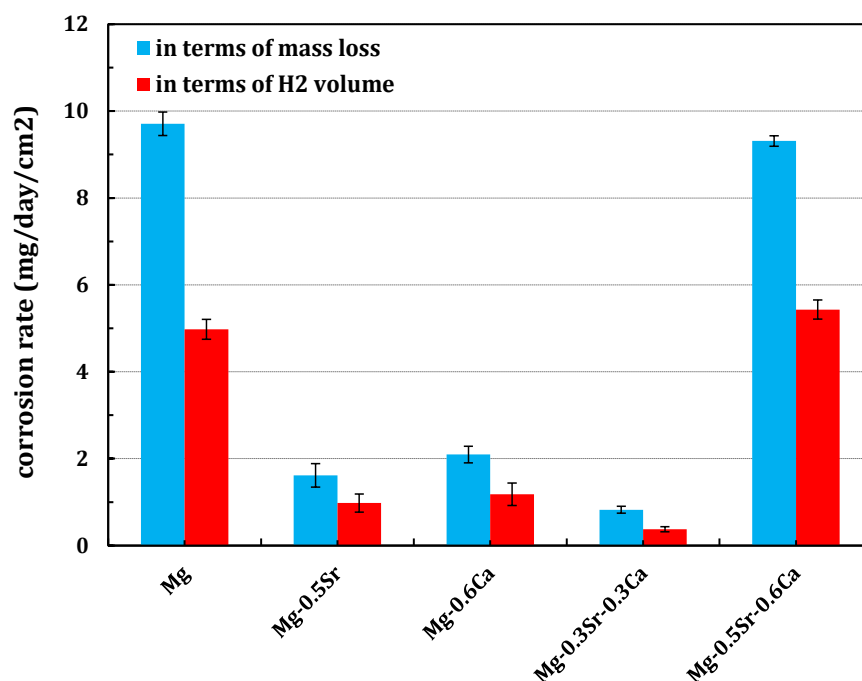


Fig. 5. 8. The average corrosion rate (mg/day/cm²) in terms of mass loss and hydrogen evolution for pure Mg and Mg binary and ternary alloys after immersion in SBF at 37°C.

Fig. 5. 9a shows the pH variation of SBF containing different Mg alloys compared to commercially pure Mg. In the presence of pure Mg, the pH increases very rapidly early in the test. An even faster increase in pH is observed in the presence of Mg-0.5Sr-0.6Ca. In the case of Mg-0.5Sr and Mg-0.6Ca, as observed previously [38, 39, 59], the pH increases rapidly in the first day of immersion; after one day, the pH increase slows down, and it reaches a value of ~9.5 in about 3 days. The test was stopped after 3 days due to the limited volume of the burette to

collect hydrogen gas. The slowest increase in pH is observed for Mg-0.3Sr-0.3Ca: after an initial increase, the pH measured in the presence of this sample reaches a plateau of ~ 9.2 .

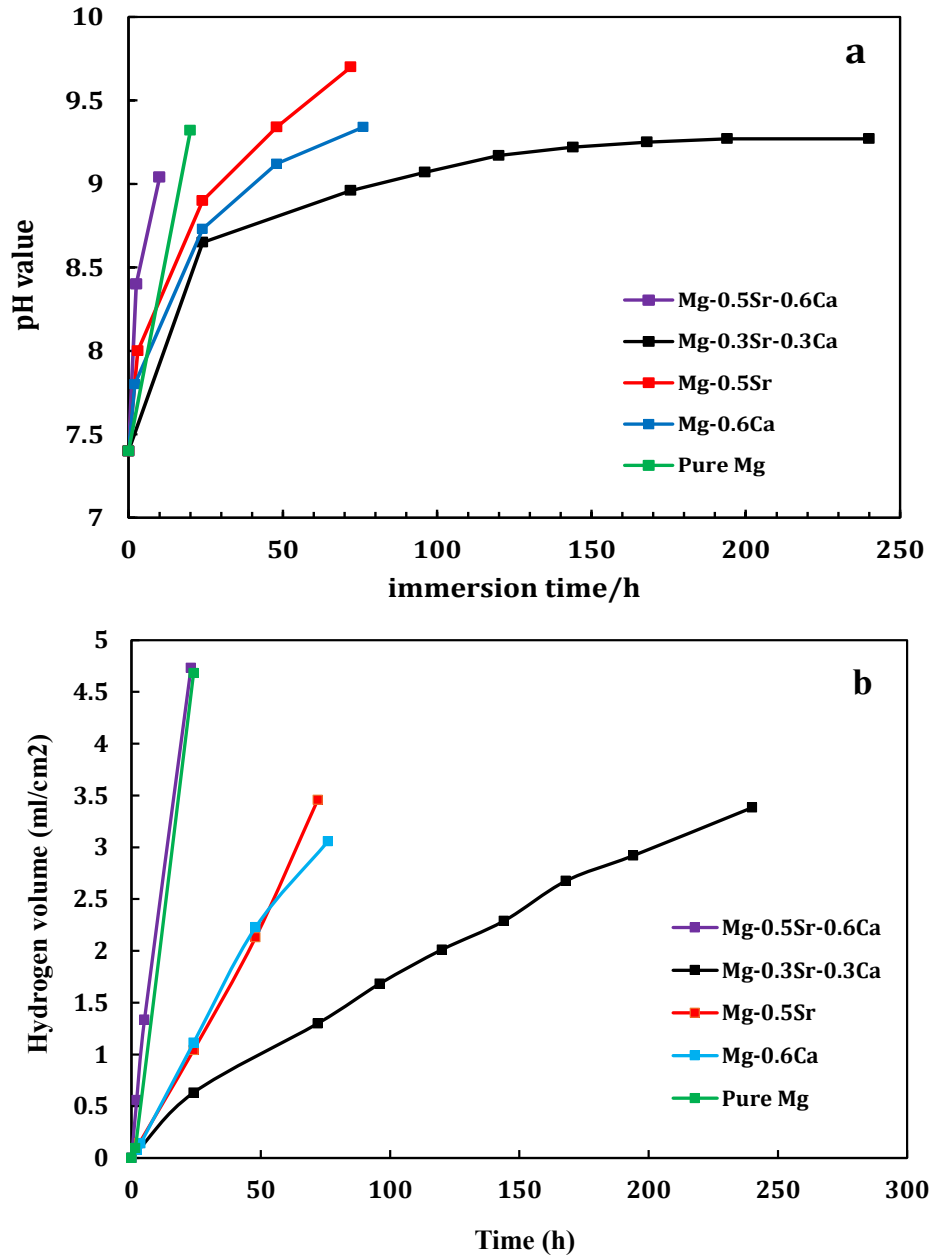
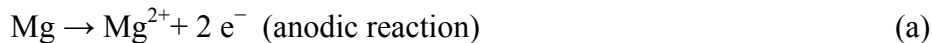


Fig. 5. 9. (a) pH measured in SBF and (b) hydrogen volume released from different Mg samples during the immersion test as a function of immersion time.

The pH increase for all samples can be explained by considering the reactions involved in Mg corrosion in water [62]:



Thus the initial increase in pH is due to the continuous dissolution of Mg and the increase in OH^{-} ions in the solution [63]. A layer of corrosion products forms on the surface which restricts/slows down the diffusion of all ionic species in the solution with time of immersion if this layer remains on the surface. The diffusion of ions and the formation of a protective layer reach a dynamic equilibrium when the pH plateaus [17, 64]. The increase in pH measured in our in vitro tests may be larger than what would be observed in physiological conditions, where blood flow would dilute the OH^{-} ions produced [1].

The volume of hydrogen generated at different immersion times is shown in Fig. 5. 9b. The lowest hydrogen evolution rate ($\sim 0.01 \text{ ml cm}^{-2} \text{ h}^{-1}$) is obtained in the presence of Mg-0.3Sr-0.3Ca, while an intermediate value ($\sim 0.04 \text{ ml cm}^{-2} \text{ h}^{-1}$) is observed for binary alloys, and the highest values ($\sim 0.2 \text{ ml cm}^{-2} \text{ h}^{-1}$) for pure Mg and Mg-0.5Sr-0.6Ca. This correlates with the pH changes and the degradation rates discussed before.

Fig. 5. 10 shows the electrochemical polarization curves measured in SBF for Mg alloys and pure Mg. The corrosion potential (E_{corr}) and the current density (I_{corr}) of each specimen are extrapolated from the curves (Table 5. 5). The addition of both 0.3 wt.% Sr and 0.3 wt.% Ca shifts the corrosion potential to more noble values. The corrosion potential in Mg-0.3Sr-0.3Ca is lower than Mg-0.6Ca and higher than Mg-0.5Sr.

The anodic and cathodic polarization curves of Mg-0.3Sr-0.3Ca show similar trends to the binary alloys. The corrosion current density is lowered with the combined addition of both 0.3 wt.%Sr and 0.3 wt.%Ca in comparison to that of pure Mg. The corrosion potential and corrosion current density of Mg-0.5Sr-0.6Ca, however, are even higher than pure Mg. The cathodic polarization curve of Mg-0.5Sr-0.6Ca changes sharply at a current density $6.3\text{E}-05 \text{ A/cm}^2$ ($\text{Log } I = -4.2$ in Fig. 5. 10) and the corrosion potential increases quickly; these data are in agreement with the high hydrogen evolution rate of this alloy (Fig. 5. 5) since the curve corresponds to hydrogen evolution [32, 65, 66]. The anodic polarization curve of Mg-0.5Sr-0.6Ca follows a similar trend to pure Mg, however, the curve becomes unsmooth after $2.8\text{E}-03 \text{ A/cm}^2$ ($\text{Log } I =$

–255 in Fig. 5. 10) which suggests the formation of an unstable film on the surface of Mg-0.5Sr-0.6Ca, which partially protects the alloy until it breaks and falls off [67]. These results agree with the in vitro immersion experiments.

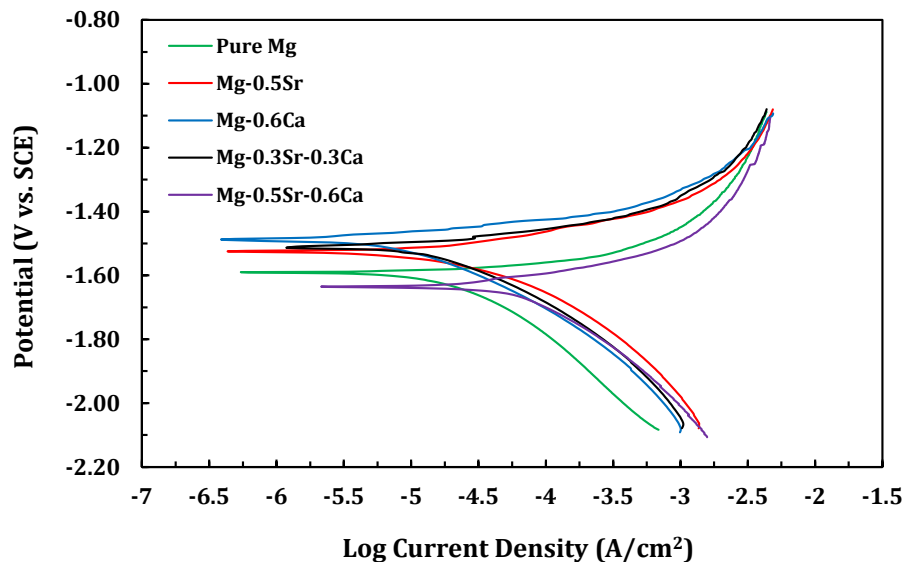


Fig. 5. 10. Polarization curves of pure Mg and binary and ternary Mg alloys in SBF.

Table 5. 5: Corrosion current density (I_{corr}) and corrosion potential (E_{corr}) of Mg alloys in SBF derived from the polarization curves.

Alloys	I_{corr} (A/cm^2)	E_{corr} (V)
CP Mg	1.259 E-05	-1.6
Mg-0.5Sr	5.011 E-06	-1.58
Mg-0.6Ca	4.015 E-06	-1.55
Mg-0.3Sr-0.3Ca	6.300 E-06	-1.57
Mg-0.5Sr-0.6Ca	5.622 E-05	-1.65

The effect of the combined addition of alloying elements on the corrosion resistance of Mg alloys has been reported for some elements. Chen et al [66] found that the simultaneous addition of Sr and Y to AZ31 is more effective than the addition of Sr alone; the β phase in AZ31 alloyed with Y and Sr exhibits an altered morphology leading to improved corrosion resistance. Niu et al reported that the combined addition of Sr and RE to AZ91D enhances the corrosion resistance by providing a more stable protective surface film and depressing the micro-galvanic couples [67].

The third element effect has also been seen in Mg alloys containing Y and Ce: the addition of Y at 10 wt.% is effective at improving the oxidation and ignition resistance; however, added together with 0.8 wt.%Ca, Y becomes effective at 3.5 wt.% only [54-56]. The addition of Ca as a third element promotes the preferential formation of CaO over the molten alloy, resulting in a change in the activity of the Y and stabilizing the formation of Y_2O_3 at lower concentrations.

5.1.4.2.2. Analysis of the corroded surface

Fig. 5. 11 shows the SEM morphology and EDS chemical composition of the surface of Mg alloys after 24 h of immersion in SBF at 37 °C. Ca and P are detected in the corrosion products formed on the surface of both binary alloys; indeed, formation of calcium phosphate compounds was previously reported on the surface of Mg-0.5Sr and Mg-0.6Ca after immersion in SBF [32, 59]. The corrosion products formed on the surface of Mg-0.3Sr-0.3Ca contain P and significant amounts of Ca. The Ca/P ratio measured on Mg-0.5Sr samples is ~1.6. Such a value is close to the Ca/P ratio for HA. The Ca/P ratio measured on the surface of Mg-0.6Ca and Mg-0.3Sr-0.3Ca is ~1.8, which is higher than Ca/P ratio for HA. This can be related to the large sample volume analyzed by EDS, which includes Ca from the material bulk and not only from the corroded surface layer. The corrosion products on the surface of Mg-0.5Sr-0.6Ca contained mainly magnesium oxide, and no Ca or P was detected on this sample.

The corroded alloys show different surface morphology. The corrosion product on the surface of Mg-0.5Sr is compact and globular, and has cracks (Fig. 5. 11a). Mg-0.6Ca has a compact scale with faceted topography and has no cracks (Fig. 5. 11b). The surface of the ternary alloy Mg-0.3Sr-0.3Ca is very dense and compact (Fig. 5. 11c). In our previous study, we showed that the formation of Sr-substituted HA on the surface of Mg-0.5Sr changes the morphology of the corrosion products and leads to the formation of a more stable and protective scale on the surface. Also here, the formation of a fine and compact corrosion layer as seen in Fig. 5. 11c can be indicative of the presence of Sr-substituted HA on the surface of Mg-0.3Sr-0.3Ca [31, 49]. Severe corrosion has occurred on Mg-0.5Sr-0.6Ca and a large amount of product layer accumulation is seen on the entire surface (Fig. 5. 11d); this layer is non-adherent and easily detaches from the surface. The needle-like morphology of the surface scale of Mg-0.5Sr-0.6Ca is similar to that observed on the surface scale of pure Mg after immersion tests performed in the same conditions [59]. The non-adherent, non-protective nature of the surface scale is another indication of the high degradation rate of this alloy.

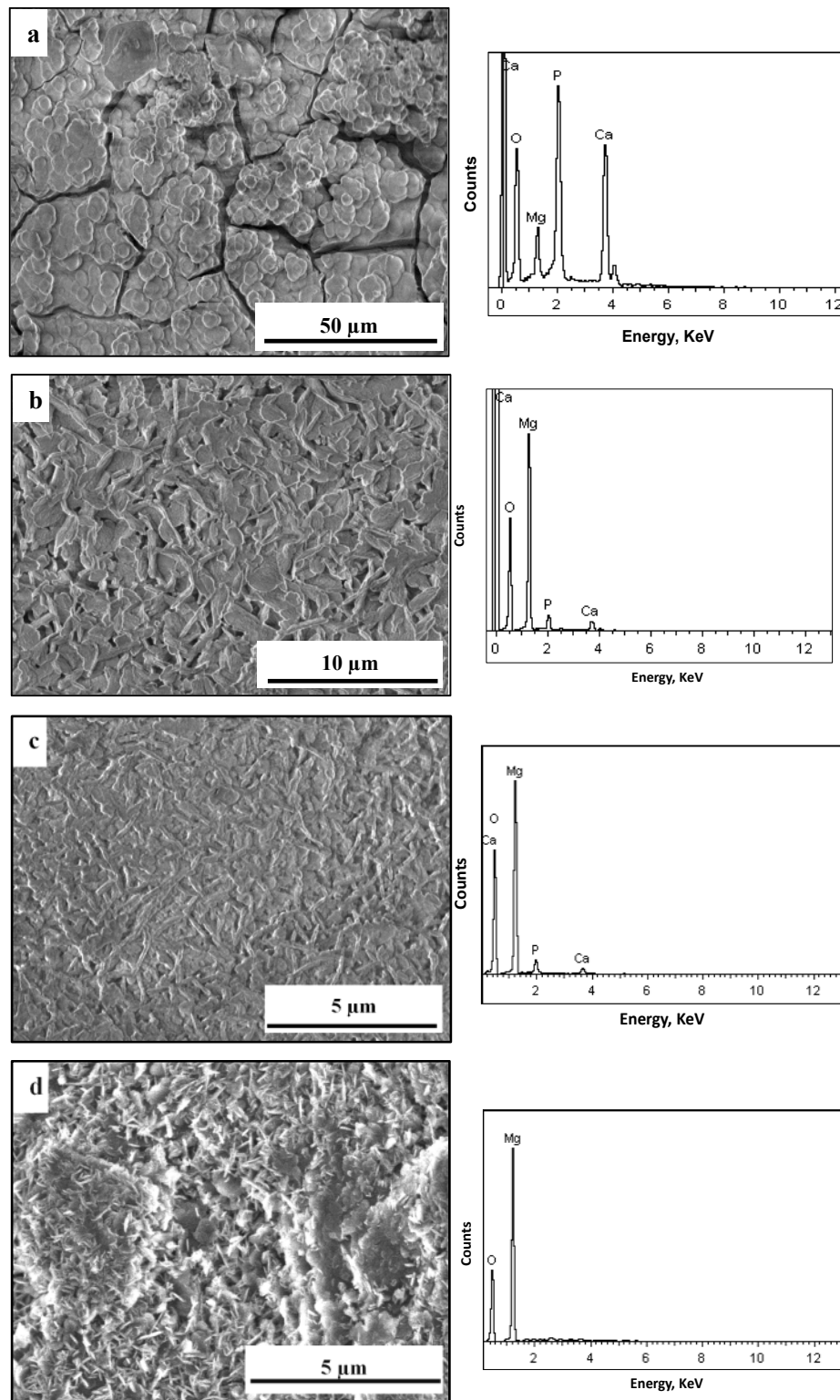


Fig. 5. 11. SEM and EDS of the surface of corroded (a) Mg-0.5Sr, (b) Mg-0.6Ca, (c) Mg-0.3Sr-0.3Ca and (d) Mg-0.5Sr-0.6Ca after 1 day immersion in SBF at 37 °C.

We analyzed by XPS the surface composition of Mg-0.5Sr, Mg-0.6Ca and Mg-0.3Sr-0.3Ca after 1 day of immersion in SBF. Table 5. 6 summarizes the atomic composition of the three samples on their surface and after 200 s of argon sputtering, corresponding to layers present more than 60 nm under the surface (Ta_2O_5 , a much harder material than our alloys, is removed at 0.3 nm/s as a reference). XPS analysis confirmed the presence of Ca and P on the surface of all samples after immersion in SBF. A significant amount of C was detected on the surface of all samples. The C atomic % decreased after 200 s of sputtering, indicating that the C detected on the surface layer is due to the contamination. The Ca/P ratio is 1.2 on the top surface of Mg-0.5Sr and increases to 1.7 after 200 s of sputtering. This indicates the formation of a HA layer covered by a calcium phosphate layer that contains less Ca than HA [59]. The Ca/P ratio changes from 1.5 to 1.8 on the surface of Mg-0.6Ca after 200 s of sputtering. In this case, such increase in Ca/P ratio can be related to either the high amount of Ca detected from the layers underneath the surface, or to the formation of other calcium phosphate compounds such as TTCP (tetracalcium phosphate, $\text{Ca}_4\text{P}_2\text{O}_9$, which has a Ca/P ratio of 2) on the surface of Mg-0.6Ca [68]. On the ternary sample, the Ca/P ratio is close to that of HA both at the very top layer and as deep as at least 60 nm. This shows that the formation of HA is promoted by this alloy composition.

Table 5. 6: Atomic percent composition and Ca/P ratio measured by XPS before (0 s etching time) and after (200 s etching time) removing the top layer from the surface of Mg-0.5Sr, Mg-0.6Ca and MG-0.3Sr-0.3Ca immersed for 1 day in SBF.

Alloy	Etching time (s)	Ca %	P %	C %	Ca/P
Mg-0.5Sr	0	16.2 ± 0.6	13.9 ± 0.4	13.9 ± 0.6	1.2 ± 0.1
	200	24.5 ± 0.4	14.8 ± 0.3	0.6 ± 0.0	1.6 ± 0.0
Mg-0.6Ca	0	10.1 ± 0.5	6.7 ± 0.4	13.4 ± 0.5	1.5 ± 0.1
	200	11.2 ± 0.3	6.2 ± 0.2	2.3 ± 0.1	1.8 ± 0.0
Mg-0.3Sr-0.3Ca	0	9.8 ± 0.5	6.1 ± 0.4	16.3 ± 0.8	1.6 ± 0.1
	200	13.7 ± 0.5	8.1 ± 0.3	2.7 ± 0.5	1.6 ± 0.0

We focused on Mg-0.3Sr-0.3Ca and studied deeper layers of this sample. Table 5. 7 presents the elemental composition measured at different depths on the surface of Mg-0.3Sr-0.3Ca after immersion in SBF. A high amount of C (~ 16%) is present at the surface, and decreases as deeper layers are analyzed. This is clearly related to the presence of surface hydrocarbon contamination, which can be easily removed after 100 s ion sputtering. The Ca/P ratio increased after 100 s etching and reached the value of ~1.6, thus confirming the formation of HA on the surface of Mg-0.3Sr-0.3Ca immersed in SBF. The Mg/O ratio increased after the very top surface layer was sputtered away, which indicates that some of the O present on the surface was related to contamination. After removing the contamination from the surface layer, the Mg/O ratio decreased during the following sputtering cycles, which can be attributed to the formation of Mg-substituted HA at the outermost layers of the surface. The Mg/Ca ratio shows a large variation on the surface layer, indicative of a non-homogenous coverage, and then overall decreases during sputtering. This can be related to the formation of a substituted HA on the outermost layers, in which Mg substitutes some of the Ca ions.

Table 5. 7: Atomic percent composition and Ca/P, Mg/O and Mg/Ca ratios obtained by XPS from the surface of Mg-0.3Sr-0.3Ca immersed for 1 day in SBF, before and after sputtering with Ar ions. Every 100 s etching is corresponds to at least 30 nm sputtering.

Etching time (s)	Elemental composition (At.%)			
	C %	Ca/P	Mg/O	Mg/Ca
0	16.3 ± 0.8	1.6 ± 0.1	0.3 ± 0.1	1.5 ± 0.2
100	2.8 ± 0.6	1.6 ± 0.0	0.5 ± 0.0	1.9 ± 0.0
200	2.7 ± 0.5	1.6 ± 0.0	0.5 ± 0.0	1.8 ± 0.0
300	2.6 ± 0.3	1.6 ± 0.0	0.5 ± 0.0	1.5 ± 0.0
400	2.0 ± 0.3	1.6 ± 0.0	0.4 ± 0.0	1.4 ± 0.0
500	1.9 ± 0.2	1.6 ± 0.0	0.4 ± 0.0	1.4 ± 0.0

We performed a compositional depth profile on Mg-0.3Sr-0.3Ca using argon sputtering cycles of 100 sec each, corresponding to more than 30 nm/cycle. Fig. 5. 12 shows the high resolution XPS spectra of Ca_{2p}, P_{2p}, C_{1s}, Mg_{2p}, and O_{1s} obtained before and after 100 s sputtering of the corroded surface of Mg-0.3Sr-0.3Ca. The Ca_{2p_{1/2}} peak remained centered at 351.3 eV at all depths (Fig. 5. 12a), while the P_{2p} peak shifted from 133.4 eV at the surface to 133.6 eV after sputtering (Fig. 5. 12b). Binding energies of 351.3 eV for Ca_{2p_{1/2}} and of 133.6 eV for P_{2p} are typically found for calcium and phosphate ions in HA [69]; the initially lower binding energy for P_{2p} can be attributed to the formation of Mg-substituted HA on the outer layer of the surface scale [70]. The C_{1s} peak has three components on the surface layer (Fig. 5. 12c). The high intensity peak centered at 285 eV indicates the presence of C-C/C-H groups. This component is observed on the surface of all metals at room temperature, and is related to contamination. Indeed, the intensity of this peak diminishes by sputtering. The C_{1s} peak centered at ~290 eV can be attributed to the formation of magnesium carbonate (MgCO₃), which is explained by diffusion of CO₂ from the environment and reaction with the air-formed film [71]. A less intense peak located at ~288 eV is associated with the presence of C=O; these species are also related to environmental surface contamination, and in fact they disappear after 100 s sputtering. The Mg_{2p} peak centered at ~50 eV is usually observed for Mg²⁺, in the form of MgO or Mg(OH)₂ (at 50.5 eV) and MgCO₃ (at 50.9 eV). In our case (Fig. 5. 12d), the MgO/Mg(OH)₂ component is much more pronounced than the MgCO₃ component; within the MgO/Mg(OH)₂ peak, although impossible to discriminate by XPS, we can hypothesize that Mg(OH)₂ is more abundant, since it is the main corrosion product identified by XRD (see Fig. 5. 13 below) [72]. The peak relative to metallic Mg, located at 49.5 eV, is not detected on the surface layer [72]. The extra peak shown in Fig. 5. 12d centered at 44.3 eV is to be attributed to Ca_{3s}. The O_{1s} peak (Fig. 5. 12e) is centered at 531.5 eV on the surface; this peak can be attributed to both Mg(OH)₂ and MgCO₃, and possibly some phosphates. After 100 s sputtering a new component appears at ~529 eV, corresponding to MgO [72, 73].

The XRD spectrum measured on the corroded surface of Mg-0.3Sr-0.3Ca after 1 day of immersion in SBF (Fig. 5. 13) shows the main peaks of HA in the 2θ range between 15° and 35°, and indicates the presence of Mg(OH)₂ too. This confirms the results obtained with XPS and EDS.

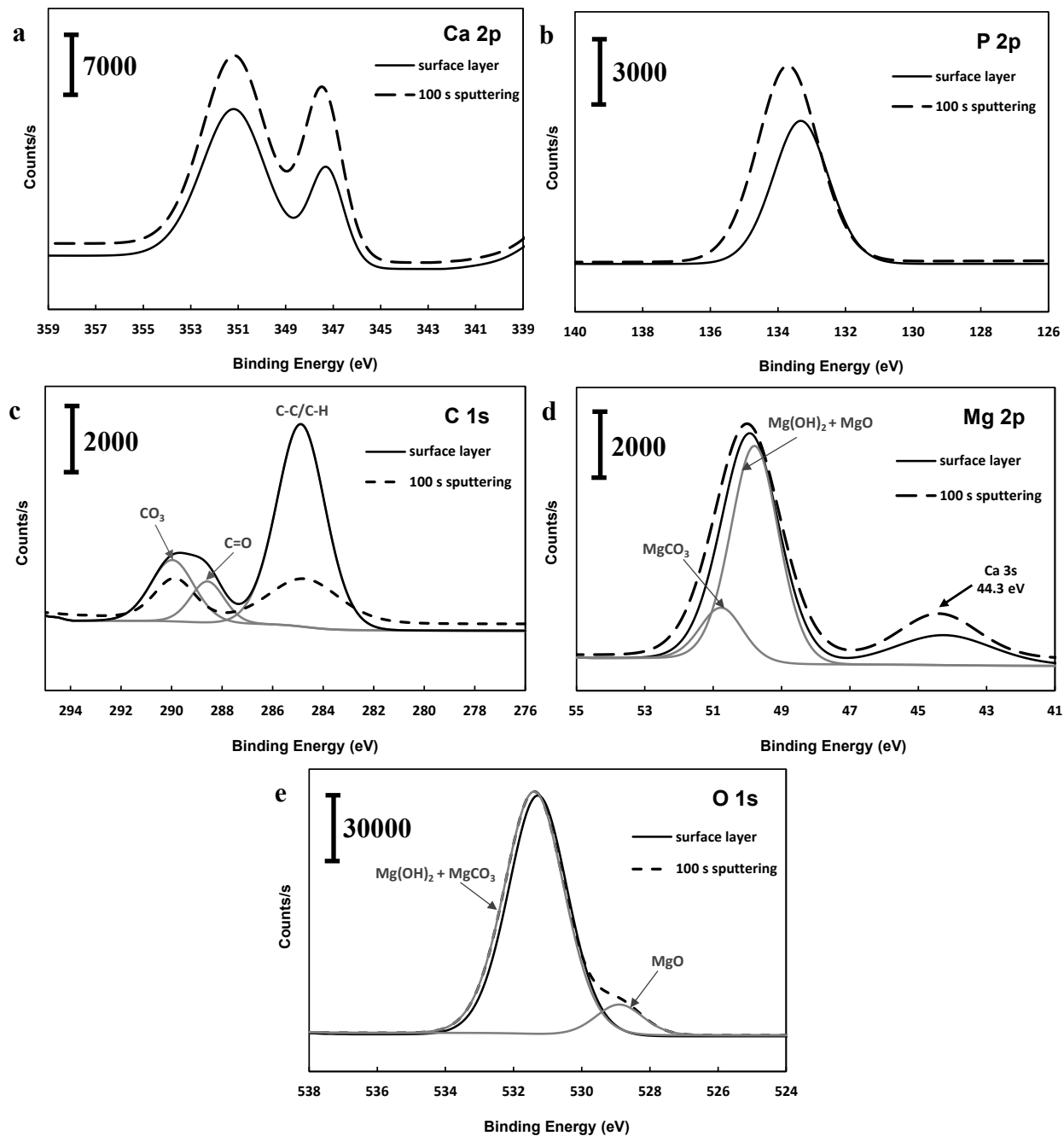


Fig. 5. 12. High resolution XPS spectra of (a) Ca_{2p}, (b) P_{2p}, (c) C_{1s}, (d) O_{1s} and (e) Mg_{2p} measured on the surface of Mg-0.3Sr-0.3Ca after 1 day immersion in SBF at 37 °C. Surface layer represents the XPS spectra on the surface before sputtering, whereas 100 s sputtering corresponds to the at least 30 nm of sputtering. Figs. (c) and (d) show the fits corresponding to the peak components of the surface layer spectra. Fig. (e) shows the peak fittings on the spectrum obtained after 100 s sputtering.

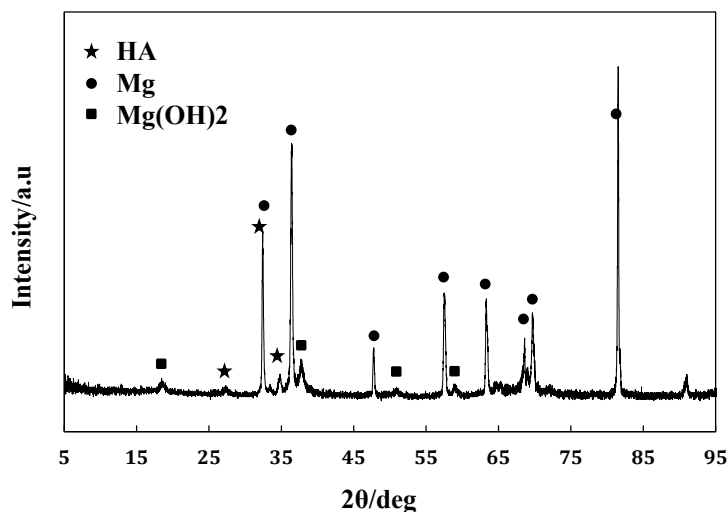


Fig. 5. 13. X-ray diffraction pattern of the corrosion products formed on the surface of Mg-0.3Sr-0.3Ca after 1 day immersion in SBF at 37°C.

5. 1. 4. 3. Mechanical Properties

Mechanical properties of the implant materials are important for the in-service performance as well as during the fabrication and deployment of the implant. For bone applications, mechanical properties close to bone are required especially to avoid stress shielding, which results in the reduction of bone density and prevents bone remodeling due to the removal of normal stress from the bone by the implant [74, 75]. Stress shielding is significant if the implant material's modulus of elasticity is much higher than that of bone. For cardiovascular implants, both the fabrication and the deployment in the cardiovascular vessel require adequate ductility and bendability; additionally, sufficient strength is needed for in-service performance.

We excluded Mg-0.5Sr-0.6Ca from further characterization since it degraded rapidly in SBF and showed low corrosion resistance, and we performed tensile tests on pure Mg, binary alloys and Mg-0.3Sr-0.3Ca (Table 5. 8, Fig. 5. 14). Pure Mg shows the highest elongation (9.6%), but the lowest yield strength (24MPa). The results are both higher than those reported on sand-cast Mg (Table 5. 8, [76]); this is expected, since we used permanent-mold cast instead of sand-cast metals. The binary alloys exhibit low elongation values (4-5%), and consequently the ultimate tensile strength is lower than pure Mg; however, their yield strengths are higher due to second-phase strengthening. The fracture surfaces of pure Mg and of the binary alloys are shown in Fig. 5. 15. Despite the 9.6% elongation, Mg shows cleavage cracks (Fig. 5. 15a). Such a brittle

fracture is seen in tensile testing of pure Mg and some of its alloys, and it is twin-induced [77]. Mg-0.6Ca alloy exhibits mixed brittle / ductile fracture with cleavage planes as well as dimples (Fig. 5. 15b). The mixed fracture mode of Mg-0.6Ca can be attributed to multiple factors: the reduction in twinning, which decreases the extent of twin-induced cleavage; the increase in slip deformation; and the presence of brittle second phase particles of Mg_2Ca , which crack in regions of strain accumulation. The fracture surface of Mg-0.5Sr (Fig. 5. 15c) does not show cleavage planes; however, the fracture surface shows intergranular cracking, decorated with second phases ($Mg_{17}Sr_2$). The lack of cleavage planes implies that twinning is suppressed, and easy glide has led to dislocation pile up at the interdendritic phases causing cracking.

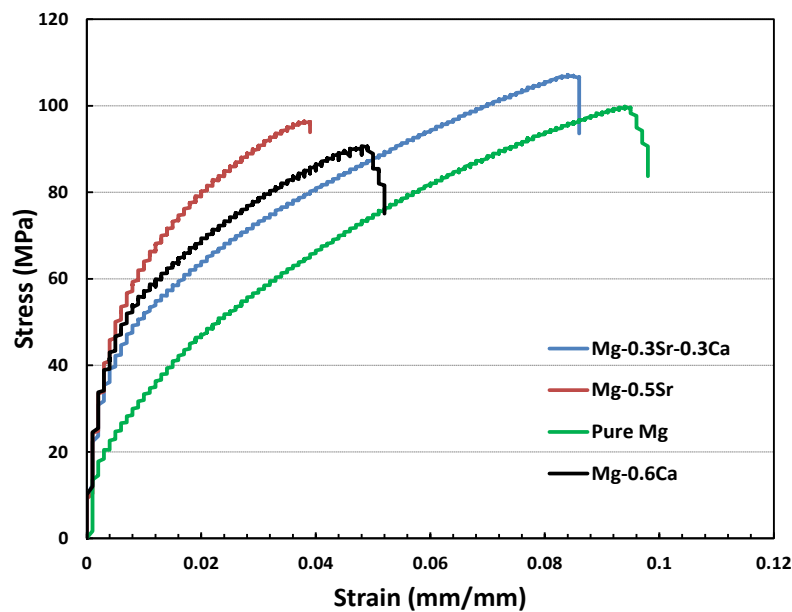


Fig. 5. 14. Tensile stress-strain curved of as-cast Mg-0.5Sr, Mg-0.6Ca, Mg-0.3Sr-0.3Ca and pure Mg generated at room temperature.

The combined addition of Sr and Ca improves both strength and elongation. Mg-0.3Sr-0.3Ca shows higher ultimate tensile strength and higher elongation than both Mg-0.5Sr and Mg-0.6Ca and much higher strength than pure Mg (Table 5. 8). Its fracture mode is similar to that of Mg-0.5Sr, and the fracture surface is similarly decorated with second phases (Fig. 5. 15d). Intergranular cracking is present too. The difference between the ternary and the binary alloys seems to be in the amount of strain before cracking, as shown in Fig. 5. 14. Since the ternary alloy has micron size globular precipitates in the matrix, easy glide in the HCP Mg is slowed

down; dislocation pile-up at the interdendritic phases and eventual cracking are delayed. Furthermore, the nano-scale globular precipitates close to the interdendritic phases would also slow down dislocation motion and delay their pile-up and eventual crack propagation contributing to the improved ductility of the alloy.

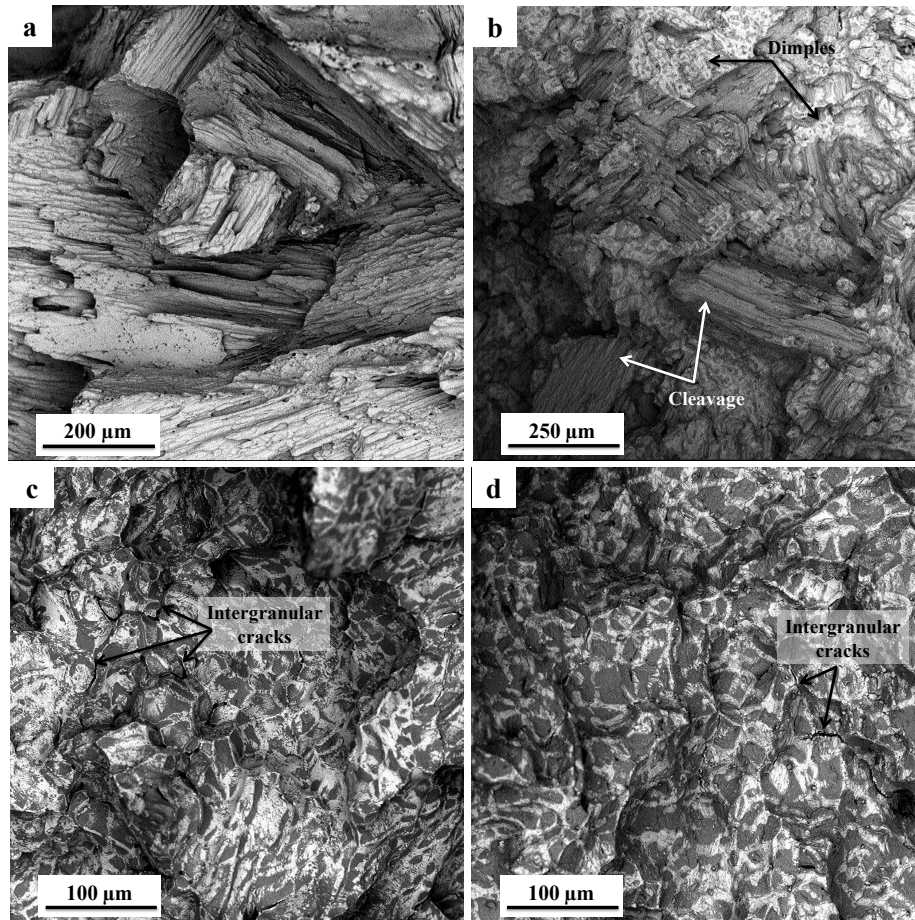


Fig. 5. 15. SEM fractographs of tensile tested (a) pure Mg, (b) Mg-0.6Ca, (c) Mg-0.5Sr and (d) Mg-0.3Sr-0.3Ca.

These results show that the addition of small amounts of Sr and Ca improves the mechanical properties of Mg and makes it more suitable for implant applications. Mg-0.3Sr-0.3Ca has higher mechanical strength compared to pure Mg, but lower than Ti and Co-Cr alloys. The modulus of elasticity of Mg alloys (~ 40-45 GPa) is much closer to that of natural bone (5-23 GPa for cortical bone, and 15-20 GPa for femur bone) [74, 78] than that of titanium alloys such as Ti-6Al-4V (116 GPa) [78], stainless steel (193 GPa) [78] and Co-Cr alloys (200 GPa) [79]. This significantly reduces the stress-shielding effect [2, 74, 78].

Table 5. 8: Tensile properties of as-cast Mg, Mg-0.5Sr, Mg-0.6Ca, and Mg-0.3Sr-0.3Ca.

Alloy	% Elongation	Ultimate tensile strength (MPa)	0.2% Yield strength (MPa)	Modulus of Elasticity (GPa)
Pure Mg	9.6	100	24	40-45 [2]
Mg-0.5Sr	4.0	98	44	
Mg-0.6Ca	5.0	91	51	
Mg-0.3Sr-0.3Ca	8.8	107	52	
Pure Mg sand cast [76]	2-6	90	21	
AZ91C (cast) [76]	1-3	110	68	
Cortical bone	1.07-2.10	35-283	104.9-114.3	5-23 [78]
Cancellous bone		1.5-38		0.01-1.57 [78]
Ti-6Al-4V (annealed)	10	860	795	116 [78]
Co-Cr alloy	10-35	480-1030		200 [79]
Stainless steel 360 L type (annealed)	40	490	190	193 [78]

Bending properties are also very important, especially during manufacturing and implantation of cardiovascular implants. Fig. 5. 16 shows the effect of Ca and Sr on the bending properties of Mg. The lowest bending strength is obtained for pure Mg, while the ultimate strength and yield strength increased with the addition of Sr and Ca. The largest increase is observed again with the combined addition of 0.3 wt.% Sr and 0.3 wt.% Ca. Most data relative to the bending properties reported in the literature refer to wrought Mg and not on cast alloys, so there is no comparative data. In wrought Mg alloys, the bending properties have similar trends to the tensile properties. The bending properties of the cast Mg alloys studied here also show the same compositional dependence as the tensile properties.

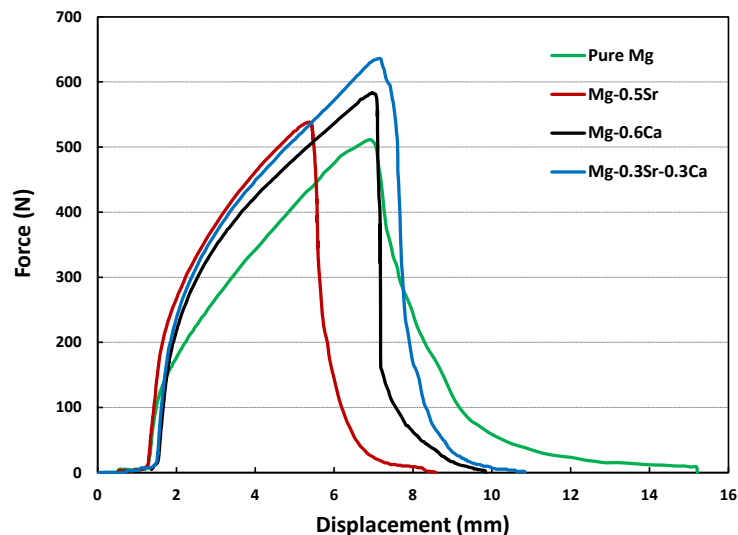


Fig. 5. 16. Force-displacement curve generated by three-point bending test of as-cast Mg-0.5Sr, Mg-0.6Ca, Mg-0.3Sr-0.6Ca and pure Mg at room temperature.

5. 1. 5. CONCLUSIONS

The fast corrosion rate of Mg is its main drawback that prevents it from being applied as an implant material. The addition of extra elements in Mg alloys is known to be able to solve this problem, but no alloy tested so far has shown enough reduction in corrosion while keeping good mechanical properties and maintaining the biocompatibility of the final material. Here we have studied the addition to Mg of two elements that are naturally present in our body, Sr and Ca. We show that the combined addition of both Sr and Ca in small amounts increases the corrosion resistance of Mg in physiological conditions more than the single additions of Sr or Ca. Specifically, the corrosion rate of Mg decreases by 90% when low amounts of Sr and Ca are added (0.3 wt.% Sr and 0.3 wt.% Ca). This is to be related to two factors: (i) the “third element effect”, which reduces the amount at which an element becomes effective in improving the corrosion resistance of an alloy; and (ii) the formation of globular Ca/Sr-rich phases in the microstructure of the alloy. These phases are observed both at the grain boundaries and in the grain interior, and are able to slow down the dissolution of the alloy by decreasing the difference in corrosion potential between the Mg matrix and the grain boundaries. In addition, HA and Mg(OH)₂ form on the surface of Mg-0.3Sr-0.3Ca after immersion in SBF for 1 day. The presence of small amount of Sr and Ca changes the morphology of the product to a very compact

layer with more stable HA on the surface. The formation of these corrosion products slows down further degradation of the alloy. On the contrary, high levels of Sr and Ca such as in the Mg-0.5Sr-0.6Ca alloy increase the corrosion rate of Mg due to significant micro galvanic effect: a non-adherent surface scale forms, which easily detaches and does not act as a barrier. The finer and modified ternary precipitates in the Mg-0.3Sr-0.3Ca alloy seem to minimize micro-galvanic corrosion in this alloy. Among the alloys studied, Mg-0.3Sr-0.3Ca also shows the highest tensile and bending properties, as well as higher ductility.

Overall, these results show that the combined addition of optimum amounts of Sr and Ca is a promising route towards developing Mg-based biodegradable implants. Our previous work on Mg-Sr alloys [31] in the range of 0.3 to 2.5 wt.% Sr shows that Mg-0.5Sr has higher corrosion resistance and mechanical strength than Mg-0.3Sr. Several groups studying Mg-Ca binary alloys up to 3 wt.% Ca found that Mg-0.6Ca [38, 39] showed the best combination of mechanical and corrosion resistance for biomedical applications. Our work shows that the combined addition can utilize lower levels of Ca and Sr in the ternary alloy and results in improved performance. The high strength, good bending properties and stiffness closer than Ti alloys to bone make these alloys promising materials for orthopedic implant applications, and the combination of high strength, ductility and bending properties makes them also suitable for cardiovascular stent fabrication, deployment and use.

5. 1. 6. REFERENCES

- [1] Zeng R, Dietzel W, Witte F, Hort N, Blawert C. Progress and challenge for magnesium alloys as biomaterials. *Advanced Engineering Materials*. 2008;10:B3-B14.
- [2] Staiger MP, Pietak AM, Huadmai J, Dias G. Magnesium and its alloys as orthopedic biomaterials: A review. *Biomaterials*. 2006;27:1728-34.
- [3] Witte F, Kaese V, Haferkamp H, Switzer E, Meyer-Lindenberg A, Wirth CJ, et al. In vivo corrosion of four magnesium alloys and the associated bone response. *Biomaterials*. 2005;26:3557-63.
- [4] Song G. Control of biodegradation of biocompatible magnesium alloys. *Corrosion Science*. 2007;49:1696-701.
- [5] Wang H, Estrin Y, Zuberova Z. Bio-corrosion of a magnesium alloy with different processing histories. *Materials Letters*. 2008;62:2476-9.

- [6] Kannan MB, Raman RKS. In vitro degradation and mechanical integrity of calcium-containing magnesium alloys in modified-simulated body fluid. *Biomaterials*. 2008;29:2306-14.
- [7] Hartwig A. Role of magnesium in genomic stability. *Mutation Research-Fundamental and Molecular Mechanisms of Mutagenesis*. 2001;475:113-21.
- [8] Vormann J. Magnesium: nutrition and metabolism. *Molecular aspects of medicine*. 2003;24:27-37.
- [9] Yun Y, Dong Z, Yang D, Schulz MJ, Shanov VN, Yarmolenko S, et al. Biodegradable Mg corrosion and osteoblast cell culture studies. *Materials Science & Engineering C-Materials for Biological Applications*. 2009;29:1814-21.
- [10] Saris NEL, Mervaala E, Karppanen H, Khawaja JA, Lewenstam A. Magnesium - An update on physiological, clinical and analytical aspects. *Clinica Chimica Acta*. 2000;294:1-26.
- [11] Kirkland NT, Birbilis N, Staiger MP. Assessing the corrosion of biodegradable magnesium implants: A critical review of current methodologies and their limitations. *Acta Biomaterialia*. 2012;8:925-36.
- [12] Xin Y, Hu T, Chu PK. In vitro studies of biomedical magnesium alloys in a simulated physiological environment: A review. *Acta Biomaterialia*. 2011;7:1452-9.
- [13] Gu X, Zheng Y, Cheng Y, Zhong S, Xi T. In vitro corrosion and biocompatibility of binary magnesium alloys. *Biomaterials*. 2009;30:484-98.
- [14] Witte F, Hort N, Vogt C, Cohen S, Kainer KU, Willumeit R, et al. Degradable biomaterials based on magnesium corrosion. *Current Opinion in Solid State & Materials Science*. 2008;12:63-72.
- [15] Rettig R, Virtanen S. Time-dependent electrochemical characterization of the corrosion of a magnesium rare-earth alloy in simulated body fluids. *Journal of Biomedical Materials Research Part A*. 2008;85A:167-75.
- [16] Zhang B, Hou Y, Wang X, Wang Y, Geng L. Mechanical properties, degradation performance and cytotoxicity of Mg-Zn-Ca biomedical alloys with different compositions. *Materials Science & Engineering C-Materials for Biological Applications*. 2011;31:1667-73.
- [17] Song Y, Shan D, Chen R, Zhang F, Han E-H. Biodegradable behaviors of AZ31 magnesium alloy in simulated body fluid. *Materials Science & Engineering C-Biomimetic and Supramolecular Systems*. 2009;29:1039-45.

- [18] Zhang E, Yang L. Microstructure, mechanical properties and bio-corrosion properties of Mg-Zn-Mn-Ca alloy for biomedical application. *Materials Science and Engineering a-Structural Materials Properties Microstructure and Processing*. 2008;497:111-8.
- [19] Li Y, Wen C, Mushahary D, Sravanthi R, Harishankar N, Pande G, et al. Mg-Zr-Sr alloys as biodegradable implant materials. *Acta biomaterialia*. 2012;8:3177-88.
- [20] Zhang X, Yuan G, Niu J, Fu P, Ding W. Microstructure, mechanical properties, biocorrosion behavior, and cytotoxicity of as-extruded Mg-Nd-Zn-Zr alloy with different extrusion ratios. *Journal of the Mechanical Behavior of Biomedical Materials*. 2012;9.
- [21] Gonzalez S, Pellicer E, Fornell J, Blanquer A, Barrios L, Ibanez E, et al. Improved mechanical performance and delayed corrosion phenomena in biodegradable Mg-Zn-Ca alloys through Pd-alloying. *Journal of the Mechanical Behavior of Biomedical Materials*. 2012;6.
- [22] Peng Q, Li X, Ma N, Liu R, Zhang H. Effects of backward extrusion on mechanical and degradation properties of Mg-Zn biomaterial. *Journal of the Mechanical Behavior of Biomedical Materials*. 2012;10:128-37.
- [23] Gastaldi D, Sassi V, Petrini L, Vedani M, Trasatti S, Migliavacca F. Continuum damage model for bioresorbable magnesium alloy devices - Application to coronary stents. *Journal of the Mechanical Behavior of Biomedical Materials*. 2011;4.
- [24] Grogan JA, Leen SB, McHugh PE. Comparing coronary stent material performance on a common geometric platform through simulated bench testing. *Journal of the Mechanical Behavior of Biomedical Materials*. 2012;12:129-38.
- [25] Kirkland NT, Staiger MP, Nisbet D, Davies CHJ, Birbilis N. Performance-driven design of Biocompatible Mg alloys. *Jom*. 2011;63:28-34.
- [26] Abd El-Rahman SS. Neuropathology of aluminum toxicity in rats (glutamate and GABA impairment). *Pharmacological Research*. 2003;47:189-94.
- [27] Fosmire GJ. ZINC TOXICITY. *American Journal of Clinical Nutrition*. 1990;51.
- [28] Wataha JC. Biocompatibility of dental casting alloys: A review. *Journal of Prosthetic Dentistry*. 2000;83.
- [29] Wu Q, Zhu S, Wang L, Liu Q, Yue G, Wang J, et al. The microstructure and properties of cyclic extrusion compression treated Mg-Zn-Y-Nd alloy for vascular stent application. *Journal of the Mechanical Behavior of Biomedical Materials*. 2012;8.

- [30] Nakamura Y, Tsumura Y, Tonogai Y, Shibata T, Ito Y. Differences in behavior among the chlorides of seven rare earth elements administered intravenously to rats. *Fundamental and Applied Toxicology*. 1997;37:106-16.
- [31] Bornapour M, Muja N, Shum-Tim P, Cerruti M, Pekguleryuz M. Biocompatibility and biodegradability of Mg-Sr alloys: The formation of Sr-substituted hydroxyapatite. *Acta Biomaterialia*. 2013;9:5319-30.
- [32] Li Z, Gu X, Lou S, Zheng Y. The development of binary Mg-Ca alloys for use as biodegradable materials within bone. *Biomaterials*. 2008;29:1329-44.
- [33] Gu XN, Zheng W, Cheng Y, Zheng YF. A study on alkaline heat treated Mg-Ca alloy for the control of the biocorrosion rate. *Acta Biomaterialia*. 2009;5:2790-9.
- [34] Wang HX, Guan SK, Wang X, Ren CX, Wang LG. In vitro degradation and mechanical integrity of Mg-Zn-Ca alloy coated with Ca-deficient hydroxyapatite by the pulse electrodeposition process. *Acta Biomaterialia*. 2010;6:1743-8.
- [35] Zhou P, Gong HR. Phase stability, mechanical property, and electronic structure of an Mg-Ca system. *Journal of the Mechanical Behavior of Biomedical Materials*. 2012;8:154-64.
- [36] Ilich JZ, Kerstetter JE. Nutrition in bone health revisited: A story beyond calcium. *Journal of the American College of Nutrition*. 2000;19.
- [37] Serre CM, Papillard M, Chavassieux P, Voegel JC, Boivin G. Influence of magnesium substitution on a collagen-apatite biomaterial on the production of a calcifying matrix by human osteoblasts. *Journal of Biomedical Materials Research*. 1998;42:626-33.
- [38] Wan Y, Xiong G, Luo H, He F, Huang Y, Zhou X. Preparation and characterization of a new biomedical magnesium-calcium alloy. *Materials & Design*. 2008;29:2034-7.
- [39] Hassel T, Bach F-W, Golovko A, Krause C. Investigation of the mechanical properties and the corrosion behavior of low alloyed magnesium-calcium-alloys for use as absorbable biomaterial in the implant technique. In: Pekguleryuz M, Mackenzie L, editors. 45th Annual Conference of Metallurgists of CIM. Montreal: Magnesium Technology in the Global Age; 2006. p. 359.
- [40] Gu XN, Xie XH, Li N, Zheng YF, Qin L. In vitro and in vivo studies on a Mg–Sr binary alloy system developed 3 as a new kind of biodegradable metal. *Acta Biomaterialia*. 2012.
- [41] Nielsen SP. The biological role of strontium. *Bone*. 2004;35:583-8.

- [42] Dahl SG, Allain P, Marie PJ, Mauras Y, Boivin G, Ammann P, et al. Incorporation and distribution of strontium in bone. *Bone*. 2001;28:446-53.
- [43] Marie PJ. Strontium ranelate: a novel mode of action optimizing bone formation and resorption. *Osteoporosis International*. 2005;16:S7-S10.
- [44] Taylor A. THERAPEUTIC USES OF TRACE-ELEMENTS. *Clinics in Endocrinology and Metabolism*. 1985;14:703-24.
- [45] Zhang W, Shen Y, Pan H, Lin K, Liu X, Darvell BW, et al. Effects of strontium in modified biomaterials. *Acta Biomaterialia*. 2011;7:800-8.
- [46] Bigi A, Boanini E, Capuccini C, Gazzano M. Strontium-substituted hydroxyapatite nanocrystals. *Inorganica Chimica Acta*. 2007;360:1009-16.
- [47] Kung K-C, Lee T-M, Lui T-S. Bioactivity and corrosion properties of novel coatings containing strontium by micro-arc oxidation. *Journal of Alloys and Compounds*. 2010;508:384-90.
- [48] Pramatarova L, Pecheva E, Presker R, Pham MT, Maitz MF, Stutzmann M. Hydroxyapatite growth induced by native extracellular matrix deposition on solid surfaces. *European cells & materials*. 2005;9:9-12.
- [49] Boanini E, Gazzano M, Bigi A. Ionic substitutions in calcium phosphates synthesized at low temperature. *Acta Biomaterialia*. 2010;6:1882-94.
- [50] Fan Y, Wu G, Zhai C. Effect of strontium on mechanical properties and corrosion resistance of AZ91D. 2007. p. 567-70.
- [51] Suganthi RV, Elayaraja K, Joshy MIA, Chandra VS, Girija EK, Kalkura SN. Fibrous growth of strontium substituted hydroxyapatite and its drug release. *Materials Science & Engineering C-Materials for Biological Applications*. 2011;31:593-9.
- [52] Zeng XQ, Wang YX, Ding WJ, Luo AA, Sachdev AK. Effect of strontium on the microstructure, mechanical properties, and fracture behavior of AZ31 magnesium alloy. *Metallurgical and Materials Transactions a-Physical Metallurgy and Materials Science*. 2006;37A:1333-41.
- [53] Brar HS, Wong J, Manuel MV. Investigation of the mechanical and degradation properties of Mg-Sr and Mg-Zn-Sr alloys for use as potential biodegradable implant materials. *Journal of the mechanical behavior of biomedical materials*. 2012;7:87-95.

- [54] Fan JF, Yang GC, Chen SL, Xie H, Wang M, Zhou YH. Effect of rare earths (Y, Ce) additions on the ignition points of magnesium alloys. *Journal of Materials Science*. 2004;39:6375-7.
- [55] Fan JF, Yang GC, Cheng SL, Xie H, Hao WX, Wang M, et al. Surface oxidation behavior of Mg-Y-Ce alloys at high temperature. *Metallurgical and Materials Transactions a-Physical Metallurgy and Materials Science*. 2005;36A:235-9.
- [56] Fan JF, Yang GC, Zhou YH, Wei YH, Xu BS. Selective Oxidation and the Third-Element Effect on the Oxidation of Mg-Y Alloys at High Temperatures. *Metallurgical and Materials Transactions a-Physical Metallurgy and Materials Science*. 2009;40A:2184-9.
- [57] Wagner C. Passivity and inhibition during the oxidation of metals at elevated temperatures. *Corrosion Science*. 1965;5:23.
- [58] Aljarrah M, Medraj M. Thermodynamic modelling of the Mg-Ca, Mg-Sr, Ca-Sr and Mg-Ca-Sr systems using the modified quasichemical model. *Calphad-Computer Coupling of Phase Diagrams and Thermochemistry*. 2008;32:240-51.
- [59] Bornapour M, Muja N, Shum-Tim D, Cerruti M, Pekguleryuz M. Biocompatibility and biodegradability of Mg-Sr alloys: the formation of Sr-substituted hydroxyapatite. *Acta Biomaterialia*. 2012.
- [60] Villars P, Calvert LD. *Pearson's Handbook of Crystallographic Data for Intermetallic Phases* 1985.
- [61] Zhong Y. Investigation in Mg-Al-Ca-Sr-Zn System by Computational Thermodynamics Approach Coupled With First-Principles Energetics and Experiments: The Pennsylvania State University; 2005.
- [62] Song GL, Atrens A. Corrosion mechanisms of magnesium alloys. *Advanced Engineering Materials*. 1999;1:11-33.
- [63] Song G, Song S. Magnesium as a possible degradable bio-compatible material. In: Pekguleryuz M, Mackenzie L, editors. 45th Annual Conference of Metallurgists of CIM. Montreal: Magnesium Technology in the Global Age; 2006. p. 359.
- [64] Yang L, Zhang E. Biocorrosion behavior of magnesium alloy in different simulated fluids for biomedical application. *Materials Science & Engineering C-Biomimetic and Supramolecular Systems*. 2009;29.

- [65] Takenaka T, Ono T, Narazaki Y, Naka Y, Kawakami M. Improvement of corrosion resistance of magnesium metal by rare earth elements. *Electrochimica Acta*. 2007;53:117-21.
- [66] Chen G, Peng X-d, Fan P-g, Xie W-d, Wei Q-y, Ma H, et al. Effects of Sr and Y on microstructure and corrosion resistance of AZ31 magnesium alloy. *Transactions of Nonferrous Metals Society of China*. 2011;21:725-31.
- [67] Niu J-x, Chen Q-r, Xu N-x, Wei Z-l. Effect of combinative addition of strontium and rare earth elements on corrosion resistance of AZ91D magnesium alloy. *Transactions of Nonferrous Metals Society of China*. 2008;18:1058-64.
- [68] Kalita SJ, Bhardwaj A, Bhatt HA. Nanocrystalline calcium phosphate ceramics in biomedical engineering. *Materials Science & Engineering C-Biomimetic and Supramolecular Systems*. 2007;27:441-9.
- [69] Xu L, Pan F, Yu G, Yang L, Zhang E, Yang K. In vitro and in vivo evaluation of the surface bioactivity of a calcium phosphate coated magnesium alloy. *Biomaterials*. 2009;30:1512-23.
- [70] Pereiro I, Rodríguez-Valencia C, Serra C, Solla EL, Serra J, González P. Pulsed laser deposition of strontium-substituted hydroxyapatite coatings. *Applied Surface Science*. 2012;258:6.
- [71] Feliu S, Jr., Merino MC, Arrabal R, Coy AE, Matykina E. XPS study of the effect of aluminium on the atmospheric corrosion of the AZ31 magnesium alloy. *Surface and Interface Analysis*. 2009;41:143-50.
- [72] Wang L, Shinohara T, Zhang B-P. XPS study of the surface chemistry on AZ31 and AZ91 magnesium alloys in dilute NaCl solution. *Applied Surface Science*. 2010;256:5807-12.
- [73] Brar HS, Ball JP, Berglund IS, Allen JB, Manuel MV. A study of a biodegradable Mg-3Sc-3Y alloy and the effect of self-passivation on the in vitro degradation. *Acta Biomaterialia*. 2013;9:5331-40.
- [74] Zhang S, Zhang X, Zhao C, Li J, Song Y, Xie C, et al. Research on an Mg-Zn alloy as a degradable biomaterial. *Acta Biomaterialia*. 2010;6:626-40.
- [75] Zhang E, Yin D, Xu L, Yang L, Yang K. Microstructure, mechanical and corrosion properties and biocompatibility of Mg-Zn-Mn alloys for biomedical application. *Materials Science & Engineering C-Biomimetic and Supramolecular Systems*. 2009;29.

[76] Friedrich H, Mordike B. Melting, Alloying, Refining. In: Pekguleryuz M, editor. Magnesium Technology: Metallurgy, Design Data, Automotive Applications: Springer Verlag; 2006. p. 147.

[77] Staroselsky A. Advances in Fatigue, Fracture and Damage Assessment of Materials: WITPress; 2005.

[78] Kubasek J, Vojtech D, Lipov J, Ruml T. Structure, mechanical properties, corrosion behavior and cytotoxicity of biodegradable Mg-X (X=Sn, Ga, In) alloys. Materials science & engineering C, Materials for biological applications. 2013;33:2421-32.

[79] Hanawa T. Materials for metallic stents. Journal of Artificial Organs. 2009;12:73-9.

5. 2. Thermal exposure effects on the in vitro degradation and mechanical properties of Mg-Sr and Mg-Ca-Sr biodegradable implant alloys and the role of the microstructure

This section has been published as: M. Bornapour, M. Celikin, M. Pekguleryuz, Thermal exposure effects on the in vitro degradation and mechanical properties of Mg-Sr and Mg-Ca-Sr biodegradable implant alloys and the role of the microstructure, *Materials Science & Engineering C-Materials for Biological Applications* 46 (2015), 16-24.

5. 2. 1. ABSTRACT

Magnesium is an attractive biodegradable material for medical applications due to its non-toxicity, low density and good mechanical properties. The fast degradation rate of magnesium can be tailored with alloy design. The combined addition of Sr and Ca results in a good combination of mechanical and corrosion properties, the most performant alloy compositions being Mg-0.5Sr and Mg-0.3Sr-0.3Ca. In this study, we investigated an important effect, namely thermal treatment (at 400 °C) on alloy properties. The bio-corrosion of the alloys was analyzed via in vitro corrosion tests in simulated body fluid (SBF); the mechanical properties were studied through tensile, compression and three-point bending tests in two alloy conditions, as-cast and heat-treated. We showed that 8 h of heat treatment increases the corrosion rate of Mg-0.5Sr very rapidly and decreases its mechanical strength. The same treatment does not significantly change the properties of Mg-0.3Sr-0.3Ca. In-depth microstructural investigation via transmission electron microscopy, scanning electron microscopy, electron probe micro-analysis and X-ray diffraction elucidated the effects of the thermal exposure. Microstructural characterization revealed that Mg-0.3Sr-0.3Ca has a new intermetallic phase which is stable after 8 h of thermal treatment. Longer thermal exposure (24 h) leads to the dissolution of this phase and to its gradual transformation to the equilibrium phase $Mg_{17}Sr_2$, as well as to loss of mechanical and corrosion properties. The ternary alloy shows better thermal stability than the binary alloy, but the manufacturing processes should aim at not exceeding exposure to high temperatures (400 °C) for prolonged periods (over 24 h).

5. 2. 2. INTRODUCTION

Magnesium (Mg) alloys are drawing attention as attractive candidate materials for the next generation of medical implants and devices as it naturally exists in the human body and has an essential role in many biological reactions [1, 2]. Studies showed that the osteoblast adhesion increases on the surface of hydroxyapatite (HA) when it is incorporated with Mg ions [3, 4]. Mg ions can substitute into the crystal lattice of apatite and increase cell adhesion leading to an acceleration in the growth of bone tissues [5, 6]. In addition to its unique biological properties, Mg has mechanical properties comparable to those of natural bone. Mg has a low density of 1.74 g/cm³ which is very close to that of human bone, 1.8-2.1 g/cm³ [7]. The modulus of elasticity of Mg (40–45 GPa) is also much closer to natural bone (3–23 GPa for cortical bone) when compared with titanium alloys (110–117 GPa), stainless steel (193GPa) and cobalt-chromium alloys (200 GPa) [7, 8]. The close matching of the moduli significantly decreases the stress-shielding effect in the surrounding bone tissue.

Despite these important advantages, major challenges remain for Mg as biodegradable implant material; these are its low mechanical strength and high degradation rate under physiological environment where the presence of ions accelerate the degradation and the loss of mechanical integrity before the healing process is completed [7]. Rapid degradation of the implant can also lead to Mg ion accumulation and a high rate of hydrogen evolution, which can increase the local pH and can deteriorate for the surrounding tissues [9, 10]. Since alloying can improve the mechanical properties and corrosion resistance, several Mg alloy systems have been recently evaluated as biomedical implant material; among these, AZ31 (Mg-3Al-1Zn), AZ91 (Mg-9Al-1Zn), WE43 (Mg-4Y-3RE), Mg-Zn-Sr and Mg-Sr-Ca alloys [9, 11-16] can be cited.

Alloying elements that can be used in the body without any harmful effects are very limited. Two of the attractive candidates to use as alloying elements are Ca and Sr because they are naturally found in the human body and their role to enhance the growth of osteoblasts has been observed [17-20]. We have shown that the addition of Sr in amounts < 1 wt.% reduces the degradation rate of Mg. Among as-cast binary Mg-Sr alloys with Sr wt.% varying between 0.3 and 2.5, the lowest degradation rate belonged to Mg-0.5Sr, [15, 16, 21]. In our recent investigation we have also shown that the combined addition of low levels of Sr and Ca improves the mechanical properties and decreases the corrosion rate by 90% in the physiological solution [14].

Mechanical performance is an important requirement for new implant materials with respect to the choice of fabrication processes and in-service functioning. Researchers use several techniques in addition to alloying to enhance the mechanical properties of biodegradable materials; heat treatment is one such approach. Lui et al [22] observed that heat treatment decreases the amount of MgZn particles and the Zn content in Zn-rich segregation in Mg-3Zn. Chang et al [23] reported that Mg-3Nd-0.2Zn-0.4Zr has better corrosion resistance in the solution treated state compared to the as-cast and aged conditions because solutionizing leads to the dissolution of cathodic compounds and increases the dissolved Nd in the matrix. However, it was also observed that the hydrogen evolution reaction increases after the solution and aging treatments. Fan et al [24] observed that 10 h heat treatment of Mg-1.5Y-1.2Zn-0.44Zr at 450 °C leads to an increase in the mechanical strength and ductility of the sample and to slower biodegradation.

The corrosion behavior of Mg-0.5Sr and Mg-0.3Sr-0.3Ca alloys has been recently studied by the authors in the as-cast state [14, 21]. We observed that a globular Ca/Sr-rich phase in the microstructure of Mg-0.3Sr-0.3Ca reduces the difference in the corrosion potential and decelerates the degradation rate in the solution. Mg-0.3Sr-0.3Ca also showed higher ductility and strength, and better bending properties compared to the binary Mg-Sr, Mg-Ca and other Mg-Sr-Ca alloys with higher concentration of additional elements. Since the fabrication of implants usually takes place at temperatures higher than room temperature, as-cast Mg alloys go through several mechanical processing at high temperatures. Elevated temperatures can alter the microstructures, phases and the resultant properties of metallic alloys. In this paper, the effect of thermal exposure on the microstructure, mechanical properties and corrosion behavior of Mg-0.5Sr and Mg-0.3Sr-0.3Ca is comprehensively studied in order to determine the optimum conditions for the candidate alloys.

5. 2. 3. EXPERIMENTAL PROCEDURE

5. 2. 3. 1. Alloy synthesis and sample preparation

Thin plates of binary Mg-0.5Sr and ternary Mg-0.3Sr-0.3Ca alloys were synthesized by melting down pure Mg (99.9 wt.%), pure Sr (99.99 wt.%) and Mg-30Ca master alloy all supplied by Applied Magnesium (Formerly Timminco) in a Lindberg/Blue M Crucible Furnace. CO₂ with

0.5% SF₆ was used at a flow rate of 1.1 L/min as a protective gas. A K-type (Chromel-Alumel) thermocouple was used with a digital thermometer to monitor the melt temperature. Samples were cast using a steel die coated with boron-nitride release coating and pre-heated to 400°C. Half of the thin plates were homogenized at 400 °C for 8 h and 24 h (heat-treated condition) using an electrically heated air-circulating chamber furnace (Lindberg Blue M). The actual chemical analysis of the alloys was obtained by inductively coupled plasma atomic emission spectroscopy (ICP-AES). Table 5. 9 lists the nominal and analyzed chemical compositions of the alloys.

Table 5. 9: The actual chemical composition of the alloys

Alloy	Chemical composition (wt. %)						
	Sr	Ca	Al	Si	Fe	Mn	Mg
Mg-0.5Sr	0.51	-	0.011	0.004	0.038	0.003	Balance
Mg-0.3Sr-0.3Ca	0.31	0.39	0.011	0.005	0.044	0.003	Balance

5. 2. 3. 2. Immersion test

Corrosion experiments were carried out at 37±1 °C in simulated body fluid (SBF) using Hank's buffered saline solution (HBSS) with the composition of 8.0 g/l NaCl, 0.4 g/l KCl, 0.14 g/l CaCl₂, 0.35 g/l NaHCO₃, 1.0 g/l C₆H₆O₆ (glucose), 0.1 g/l MgCl₂ · 6H₂O, 0.06 g/l MgSO₄ · 7H₂O, 0.06 g/l KH₂PO₄ · H₂O, 0.06 g/l Na₂HPO₄ · 7H₂O. The pH of the solution was fixed at 7.4 at the beginning of the immersion test. Rectangular samples, 2 × 4 cm², were cut from the as-cast thin plates of 6 mm thickness for the in vitro degradation tests in SBF. Samples were prepared, sterilized and tested in Hank's solution as described in our previous work [14]. Samples were cleaned off of corrosion residues and dried immediately after the immersion tests. The amount of mass loss, H₂ gas released and the pH of SBF were monitored during and at the end of each test. The corrosion rate was calculated in terms of mass loss and hydrogen evolution and an average value was reported for each composition from triplicate experiments.

5. 2. 3. 3. Electrochemical measurements

Three-electrode cell was used to conduct potentiodynamic polarization tests. Saturated calomel electrode (SCE) and platinum were used as the reference electrode and the counter electrode respectively. The samples were polished and cleaned before testing in Hank's solution. The

exposed area on the surface of the sample functioned as the working electrode. The experimental procedure and testing parameters were set as described in our previous work [14]. The current density was monitored as function of open-circuit potential by using VersaSTAT3 (METEK). The corrosion current density of each specimen was derived by linear fit to the anodic and cathodic parts of the polarization curves.

5. 2. 3. 4. Microstructural and surface characterization

The microstructures of as-cast and heat-treated binary and ternary samples were studied via scanning electron microscopy (Philips XL30 SEM) and field emission gun/scanning electron microscopy (FE-SEM, Hitachi SU-70) equipped with energy-dispersive spectrometry (EDS) in secondary electron mode. The cross-sections of post-immersion specimens were ground, polished with 1 μm diamond paste and etched in 5% Nital. The microstructure of the alloys was characterized using an electron probe microanalysis-wavelength dispersive spectroscopy (EPMA-WDS, JEOL 8900) after polishing.

Plates of 1.0 mm thickness obtained from the cross-section of the samples were ground down to 1200 grid to obtain 0.2 mm thickness for transmission electron microscopy (TEM). Discs, 3 mm in diameter, were punched, polished down to 50 μm and ion beam polished (PIPS, GATAN 691 Precision Ion Polishing) at an angle of 4° (top and bottom) using 3.8kV voltage. Scanning Transmission Electron Microscopy (S/TEM) analysis was conducted using Philips CM 200 (Selected Area Electron Diffraction-SAED) at 200kV. To facilitate the SAED analysis, diffraction patterns were also drawn via crystallography software (Carine Crystallography) and compared with the actual diffraction patterns obtained via TEM analysis.

5. 2. 3. 5. Mechanical properties

Standard specimens of as-cast and heat-treated Mg alloys were machined as per ASTM-E8-04 for tensile testing and ASTM-E9-09 for compression testing. The tensile test specimens had the gage area of 6 \times 6 mm² and the cylindrical compression specimens were 20 mm diameter \times 30 mm length. The tensile tests were carried out at a displacement rate of 0.12 mm min⁻¹ using an MTS Alliance RF/200 Instron testing machine. The compressive test was conducted at the speed of 0.12 mm min⁻¹ (0.005 in/ min⁻¹) using Instron 5885H. Stress-strain curves of tensile and compressive tests were obtained at room temperature for as-cast and heat-treated conditions. The average values of yield strength, ultimate compressive and tensile strength, and % elongation and

compressive strain (%) for each sample were taken from at least five measurements. Fractography was performed using scanning electron microscopy (SEM, Phenom G2 pure) on the fracture surface of the tensile-tested samples. Beam-shaped specimens with dimensions of $6 \times 6 \times 70 \text{ mm}^3$ were prepared for three-point bending tests. All the samples were polished down to 800 grit using SiC paper before testing. The three-point bending tests were conducted using a Tinius Olsen H25K-S testing machine.

5. 2. 4. RESULTS AND DISCUSSION

5. 2. 4. 1. Corrosion tests in SBF

The degradation rates of as-cast and heat-treated Mg-0.5Sr and Mg-0.3Sr-0.3Ca alloys in SBF calculated in terms of mass loss and H_2 evolution are shown in Fig. 5. 17. The degradation rate of Mg-0.5Sr increased after the heat treatment; the degradation rate of Mg-0.5Sr (8 h heat-treated) in term of mass loss (5.37 mg/day/cm^2) is more than two times the rate of as-cast Mg-0.5Sr (1.91 mg/day/cm^2); in terms of hydrogen evolution (3.51 mg/day/cm^2); it is ~twice the value for as-cast Mg-0.5Sr (1.63 mg/day/cm^2). The degradation rate of this sample increases further but with a slower rate when heat treated for 24 h at the same temperature. The volume of hydrogen gas released from Mg-0.5Sr after heat treatment for 24 h (3.51 mg/day/cm^2) is still lower than that of pure Mg (4.98 mg/day/cm^2) [21]. The ternary Mg-0.3Sr-0.3Ca shows slower degradation rate than the binary Mg-0.5Sr in both the as-cast and heat-treated conditions. The degradation rate of the ternary sample both in terms of mass loss and hydrogen evolution remains in the same range after 8 h heat treatment; $\sim 0.8 \text{ mg/day/cm}^2$ in terms of mass loss and $\sim 0.4 \text{ mg/day/cm}^2$ in terms of hydrogen evolution. Longer heat treatment (24 h), however, leads to an increase in the degradation rate; 1.73 mg/day/cm^2 in terms of mass loss and $\sim 0.62 \text{ mg/day/cm}^2$ in terms of hydrogen evolution.

Fig. 5. 18 shows the variation of the pH value of the SBF containing the as-cast and the heat-treated Mg-0.5Sr and Mg-0.3Sr-0.3Ca specimens. In the case of the as-cast Mg-0.5Sr, the pH value increases rapidly in the first day of immersion. The pH increase slows down and tends to a value of ~ 9.5 . In this case, the test was stopped after 3 days of immersion due to the volume limitation of the burette to collect hydrogen gas. The pH value of the solution containing the heat-treated Mg-0.5Sr increases at a faster rate and the test was stopped after 2 days due to the

large volume of gas collected in the burette. The variation of pH value is much slower in the solution containing Mg-0.3Sr-0.3Ca and the test was continued for 2 weeks due to the small amount of hydrogen gas released during the immersion. Both the as-cast and heat-treated Mg-0.3Sr-0.3Ca show similar trends; after an initial increase, the pH value measured in the presence of these samples increases very slowly until the curve reaches a plateau of ~ 9.2 .

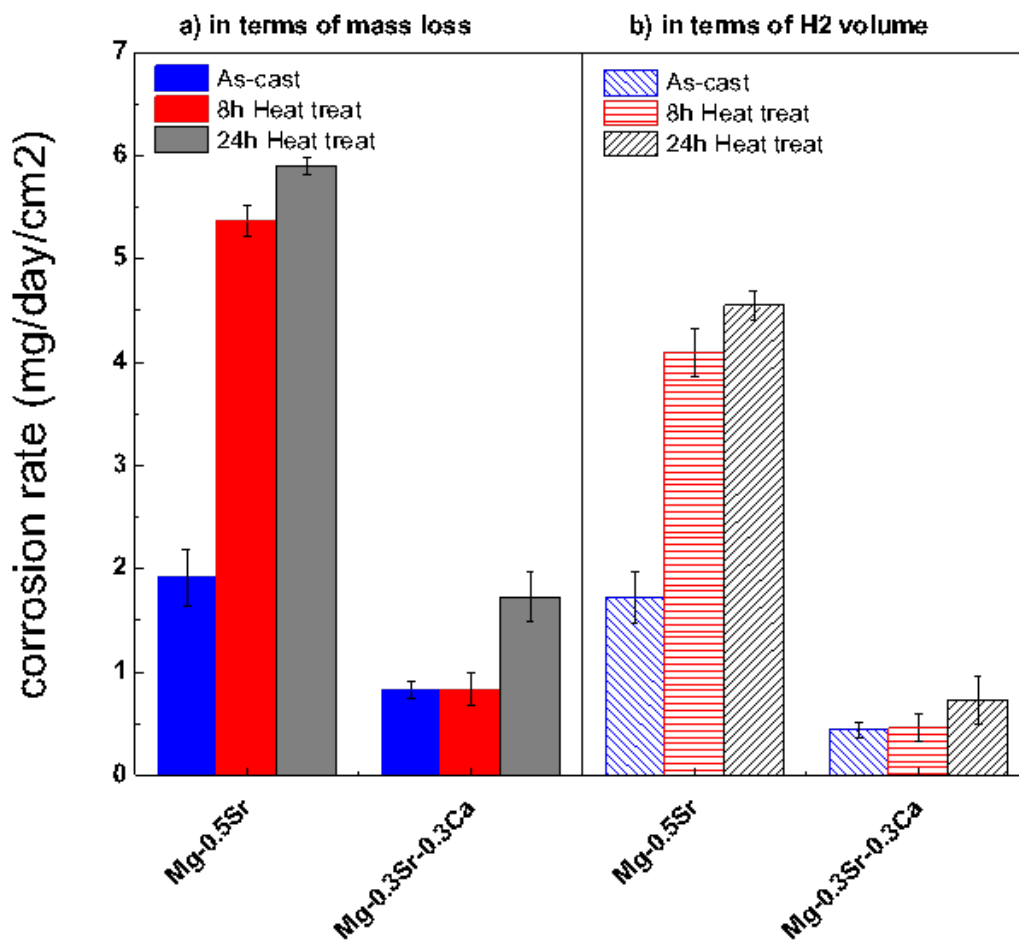


Fig. 5. 17. The average corrosion rate (mg/day/cm^2) in terms of mass loss and hydrogen evolution for as-cast and heat-treated Mg-0.5Sr and Mg-0.3Sr-0.3Ca after immersion in SBF at 37°C .

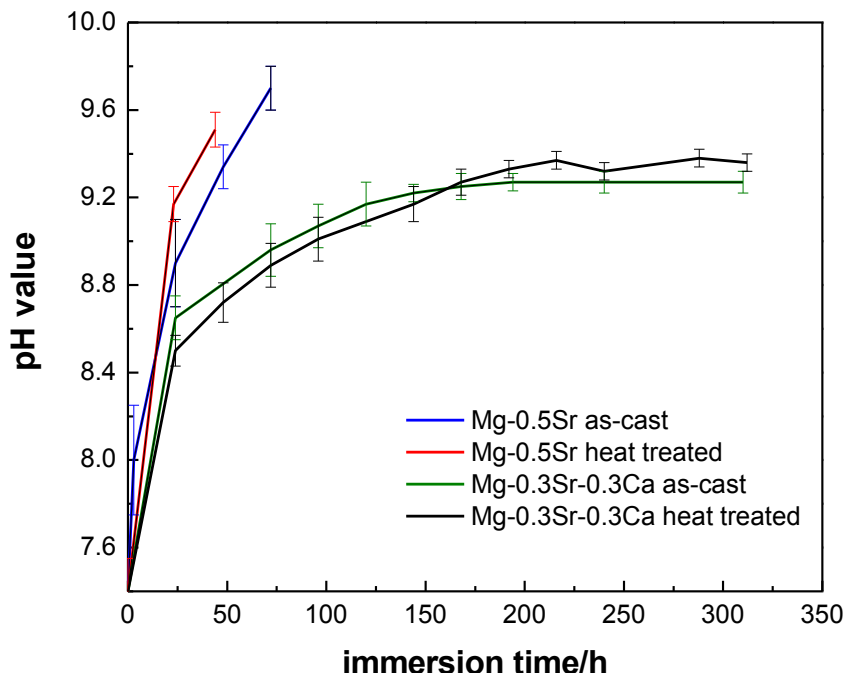
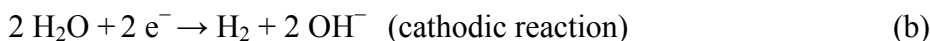
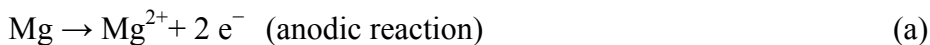


Fig. 5. 18. pH measured in SBF containing as-cast and 8 h heat-treated Mg-0.5Sr and Mg-0.3Sr-0.3Ca samples during the immersion test as a function of immersion time.

The corrosion of Mg in aqueous environment is considered in three reactions:



The initial increase of the pH value is due to the dissolution of Mg that increases the concentration of OH^{-} ions in the solution and shifts the pH value to basic levels. It is known that the formation of protective layer on the surface can restrict or decelerate the diffusion of ionic species at the material/solution interface and eventually slows down the degradation of the material. There is a dynamic balance between the diffusion of the ions from or into the interface of the material when the pH tends to a plateau.

Alloying Mg with surface active elements such as Ca, Sr can slow down the kinetics of Mg oxidation by changing the surface scale of Mg [25-27]. These surface-active elements occupy the surface layer and change the properties of the surface oxide film making it more resistant to corrosion. Even though the corrosion of Mg in aqueous environments is different from its oxidation in air, the surface active elements seem to exert positive influence on bio-corrosion resistance as well [28]. In our previous studies, we have seen that the presence of Sr on the

surface can modify the surface scale and leads to the formation of Sr-substituted hydroxyapatite (Sr-HA) which slows down the degradation rate of as-cast Mg-0.5Sr [21]. Thermal treatment is not likely to change the surface activity which is not a bulk effect and which is related to the decrease of the surface energy with the incorporation of the surface active element, hence, it is deemed that the main reasons for the change in the corrosion resistance with thermal treatment are related to certain changes in the metastable solidification microstructure (phase transformation, change in the composition and/or the amount of the phases, elimination of coring). The segregation of eutectic alloying elements to the interdendritic regions is a common condition in solidification structures. Unlike the long thermal treatment, the shorter treatment of 8 h at 400 °C does not change the corrosion rate of Mg-0.3Sr-0.3Ca significantly; this supports the fact that the underlying mechanism is diffusion-controlled. Thermal treatment could also alter the grain size which can play a role in corrosion, however, 400 °C is a little under the limit for grain growth in Mg alloys.

Fig. 5. 19 represents the electrochemical polarization curves of Mg-0.3Sr-0.3Ca alloy before and after 8 h heat treatment at 400 °C. The values of the corrosion potential (E_{corr}) and the corrosion-current density (I_{corr}) of each specimen are shown in Table 5. 10. The potential has shifted to more negative values and the current density, which represents the corrosion rate of sample, has increased after heat treatment process. The cathodic polarization curve, corresponding the hydrogen evolution reaction [29] increases very slowly in the case of as-cast sample while cathodic polarization curve of heat-treated sample changes very sharply at $2.5\text{E}-05 \text{ A/cm}^2$ ($\text{Log } I = -4.6$ in Fig. 5. 19) and the corrosion potential rapidly increases. Hence, the hydrogen evolution reaction takes place easier on the surface of this sample in comparison to as-cast sample. We can conclude that the cathodic hydrogen-evolution reaction was accelerated with the thermal exposure. The anodic polarization curves of both samples are smooth and show similar trend up to a current density of 0.001 A/cm^2 ($\text{Log } I = -3$ in Fig. 5. 19). Beyond this point, the anodic polarization curve of heat-treated sample changes more rapidly. The curve also becomes unsmooth at the end that suggests the formation of an unstable film on the surface of heat-treated sample, which partially protects the alloy until it breaks and falls off. This result shows again that the heat treatment process can facilitate the biodegradation of Mg-0.3Sr-0.3Ca.

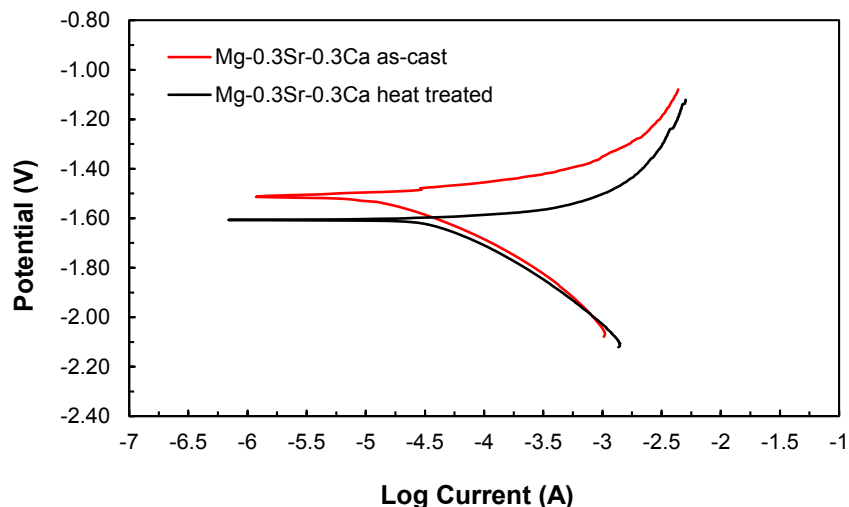


Fig. 5. 19. Polarization curves of as-cast and 8 h heat-treated Mg-0.3Sr-0.3Ca in Hank's solution.

Table 5. 10: Corrosion potential and corrosion current density of as-cast and heat-treated Mg-0.3Sr-0.3Ca in SBF obtained by linear fitting on both cathodic and anodic parts of polarization curves.

Alloys	I_{corr} (A/cm ²)	E_{corr} (V)
As-cast Mg-0.3Sr-0.3Ca	6.3 E-06	-1.5
Heat-treated Mg-0.3Sr-0.3Ca	7.9 E-05	-1.6

5. 2. 4. 2. Microstructure and phase analysis

The microstructural analyses were conducted to shed light onto the effects of thermal exposure on the alloys. Fig. 5. 20a-d present the SEM cross-sectional images of the as-cast and heat-treated Mg-0.5Sr and Mg-0.3Sr-0.3Ca. The microstructure of as-cast Mg-0.5Sr exhibits dispersed intermetallic phases within the grains and at the grain boundaries (Fig. 5. 20a). After the heat treatment, the microstructure is more homogeneous and the intermetallic phases cannot be detected within the grains (Fig. 5. 20b); they are seen mostly at the grain boundaries. The amount of intermetallic network at the grain boundaries increases after heat treatment in this sample. The heat treatment has also led to a morphological change in the interdendritic network which appears to be thinner. EPMA-WDS analysis from various regions (marked as A and B in Fig. 5. 20a & b) confirms that the matrix of as-cast Mg-0.5Sr contains a small amount of Sr (~0.04 wt.%) whereas no Sr is detected in the matrix of this alloy after 8 h heat treatment (Table

5. 11). Such compositional transformation in the microstructure of Mg-0.5Sr can be explained as follows: (i) the thermal treatment draws the microstructure to equilibrium where the α -Mg matrix supersaturated in Sr attains the equilibrium value of negligible solid solubility, (ii) the amount of the intermetallic phase at the grain boundaries increases to reach the equilibrium amount.

In the case of Mg-0.3Sr-0.3Ca, our previous work had shown the formation of globular Ca/Sr-rich phases both at the grain boundaries and in the grain interior (Fig. 5. 20c), which were found to slow down the dissolution of the alloy by decreasing the difference in corrosion potential between the Mg matrix and the grain boundaries [14]. Fig. 5. 20d reveals that these phases are still dispersed in the microstructure of the Mg-0.3Sr-0.3Ca with the same configuration after 8 h heat treatment process at 400 °C. Fig. 5. 21 shows the EPMA mapping of the Mg-0.3Sr-0.3Ca before and after heat treatment which confirms the presence of Ca and Sr in the grain boundaries and globular phases dispersed in the microstructure. Some coarsening of the intermetallics is detectable after the heat treatment.

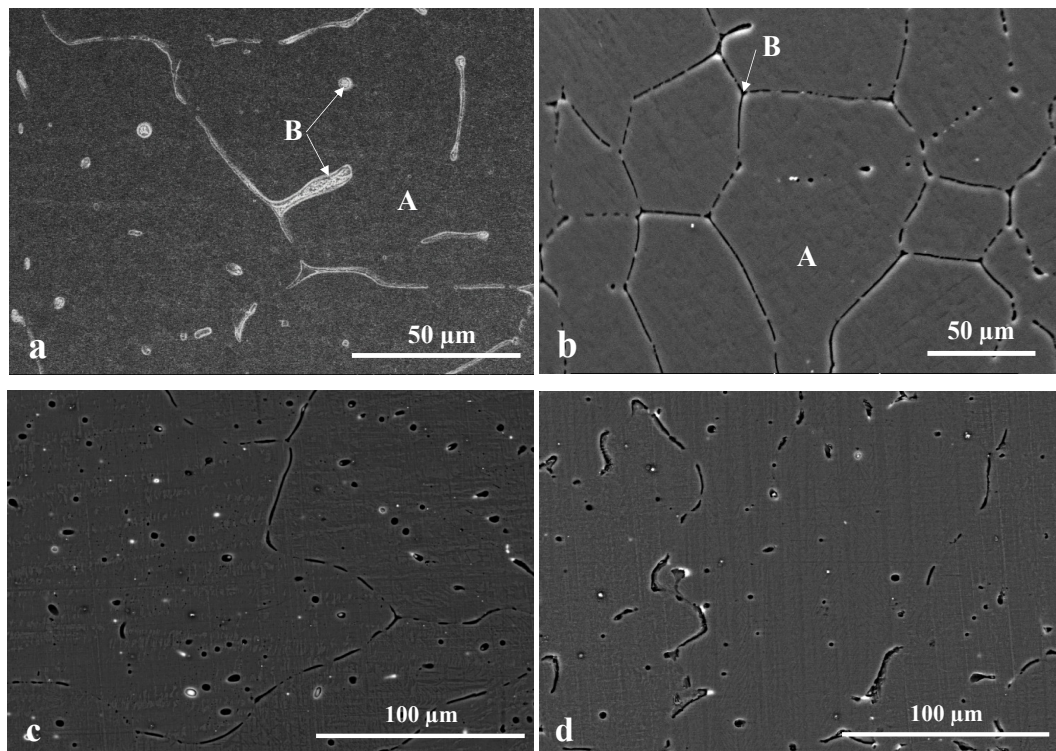


Fig. 5. 20. Secondary electron images from the longitudinal cross sections of as-cast and 8 h heat-treated (a & b) Mg-0.5Sr and (c & d) Mg-0.3Sr-0.3Ca.

Table 5. 11: Composition of different regions of the as-cast and heat-treated microstructure of Mg-0.5Sr in wt.% (marked as A and B regions in Fig. 5. 20a & b) obtained by EPMA-WDS.

Alloy	Region A		Region B	
	Mg	Sr	Mg	Sr
As-cast Mg-0.5Sr	~99.96	~0.04	≤80.7	≥19.3
Heat-treated Mg-0.5Sr	~100	-	≤76.5	≥23.5

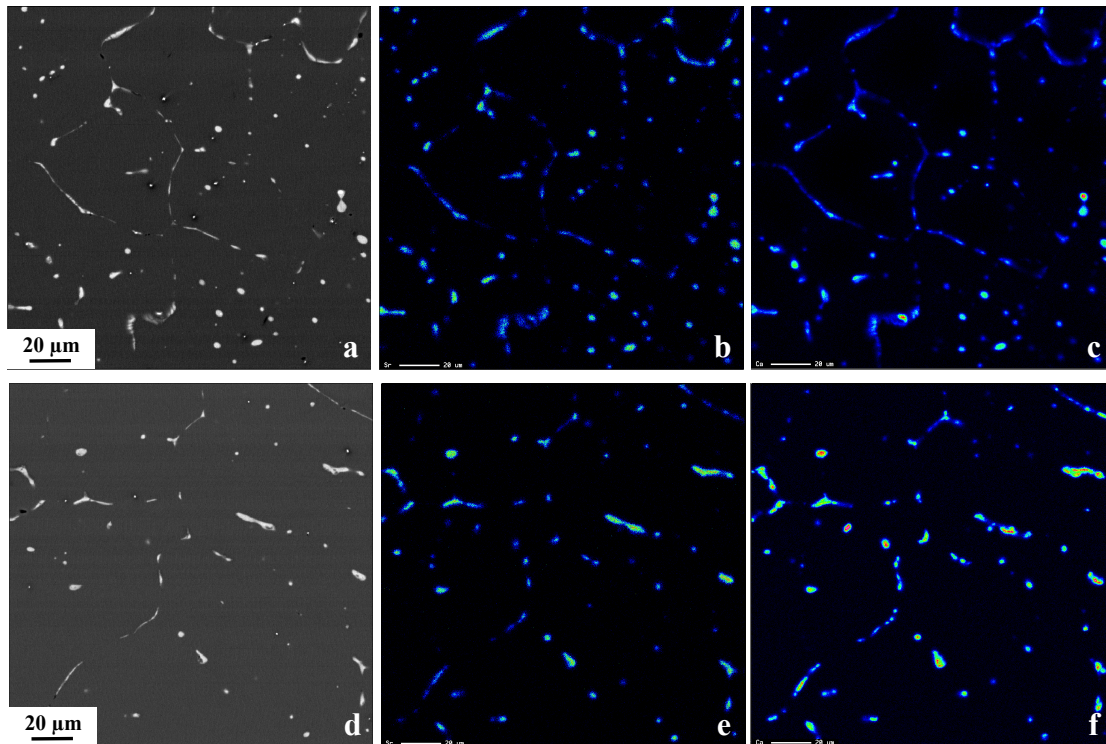
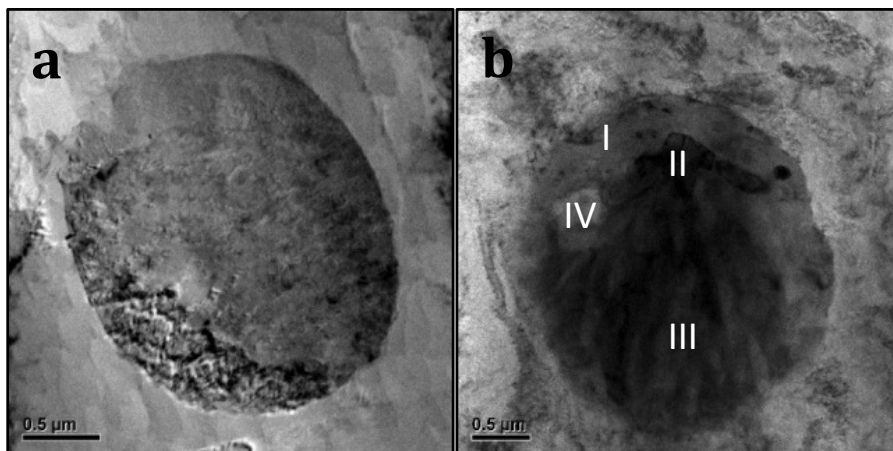


Fig. 5. 21. EPMA micrographs of (a) as-cast and (d) 8 h heat-treated Mg-0.3Sr-0.3Ca samples, and their corresponding Sr (b & e) and Ca (c & f) elemental maps.

To further investigate if the globular phases in the microstructure of Mg-0.3Sr-0.3Ca have changed after 8 h heat treatment, TEM analysis was conducted on the heat-treated alloy. In our recent study [14], TEM characterization on globular phases of as-cast Mg-0.3Sr-0.3Ca had revealed the following: (i) the phase is 1.5–2.0 μm in size (Fig. 5. 22a) with hcp crystal structure (lattice parameters $a = 6.42\text{\AA}$ and $c = 9.44\text{\AA}$) (ii) EDS results determine a Ca/Sr ratio of 3/2 with a crystal structure different from $\text{Mg}_{17}\text{Sr}_2$ or Mg_2Ca phases found in binary Mg-Sr and Mg-Ca alloys. The presence of same globular phase is still seen in the microstructure after 8 h heat

treatment (Fig. 5. 22b). Similar crystal structure and lattice parameters are observed in some parts of the phase. However, compositional change is detected in different points of a majority of the globular phases. These regions can be seen with varying contrast (darker and brighter) inside the globular phase. Fig. 5. 22c-f shows EDS analysis from different points inside globular phase shown in Fig. 5. 22b. The amount of Ca/Sr ratio changes from region to region inside this phase as listed in Table 5. 12. These compositional changes are due to the dissolution of Sr and Ca into the Mg matrix and phase transformation towards more stable phases. Fig. 5. 22g shows the diffraction pattern obtained from brighter regions of the globular phase after heat treatment (region 4). The crystal structure of these region was determined to be hcp with lattice parameters $a = 10.64\text{\AA}$ and $c = 10.40\text{\AA}$ by SAED analysis. Diffraction pattern obtained at $B=[\bar{1}2\bar{1}3]$ and the reciprocal lattice drawn using the same lattice parameters via the crystallography software (Carine Crystallography) are shown in Fig. 5. 22g. Similar lattice parameters ($a = 10.533\text{\AA}$, $c = 10.342\text{\AA}$) are reported in the diffraction pattern of the equilibrium phase $\text{Mg}_{17}\text{Sr}_2$ [14, 15]. The slight degradation in bio-corrosion resistance is clearly due to the loss of the Ca/Sr globular phase and the increase in the amount of the stable phase such as $\text{Mg}_{17}\text{Sr}_2$. However, the microstructural transformation seems to be slow which explains the fact that the increase in the bio-corrosion rate becomes more pronounced only with prolonged (24 h) thermal treatment.



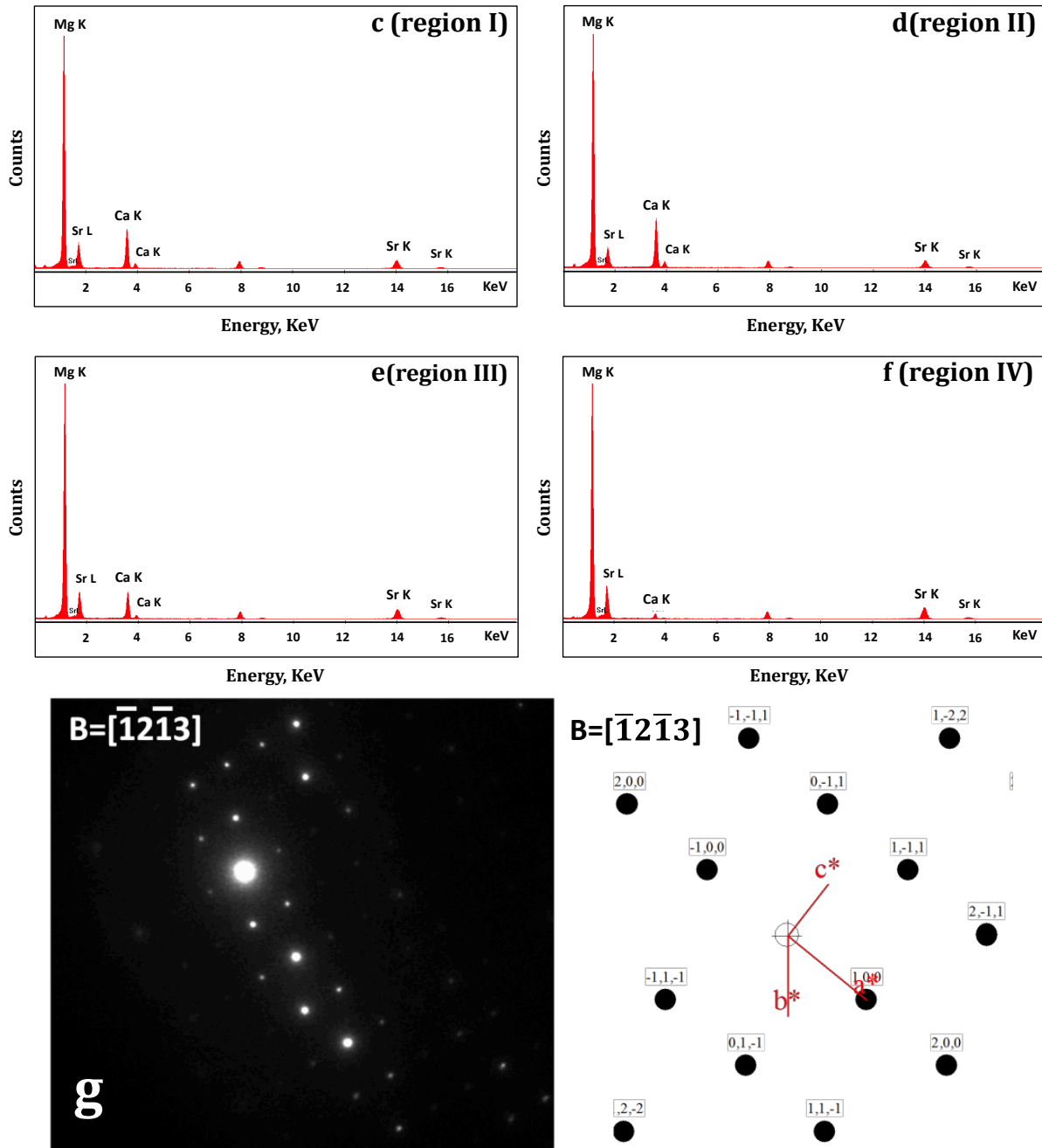


Fig. 5. 22. TEM image of the globular phase in (a) as-cast and (b) heat-treated Mg-0.3Sr-0.3Ca. (c-f) EDS analysis from various regions with different contrast within the globular phase (marked as I-IV in b) after 8 h heat treatment at 400 °C shows the variation of Ca/Sr ratio as listed in Table 5. 12. (g, left) SAED pattern obtained from the brighter regions in the globular phase after heat treatment at $B=[\bar{1}2\bar{1}3]$ and (g, right) reciprocal lattice drawn using same lattice parameters.

Table 5. 12: Variation of Ca/Sr ratio obtained by EDS analysis from different regions of globular Ca-Sr (Mg) phase in Mg-0.3Sr-0.3Ca after 8 h heat treatment at 400 °C.

	Region I	Region II	Region III	Region IV
Ca/Sr ratio	3/2	2	1	1/6

5. 2. 4. 3. Mechanical properties

The mechanical properties of biomedical materials are important for fabrication and deployment as well as for in-service performance. In the case of bone implants, mechanical properties similar to bone are desired to avoid stress shielding effect. If the implant material has a modulus of elasticity much higher than that of bone, stress shielding effect leads to the transfer of normal stress from the bone to the implant; the consequences are a reduction in bone density and lack of bone remodeling [30]. In the case of cardiovascular implants, sufficient ductility and bendability are required during fabrication and the implantation of the stent. Stent materials also need to have adequate strength to keep the mechanical integrity for the entire healing process in the body [31, 32].

Tensile and Compressive Properties

We performed tensile and compression tests on as-cast and 8 h heat-treated Mg samples (Fig. 5. 23). Mg-0.3Sr-0.3Ca shows higher ultimate tensile strength and higher elongation than Mg-0.5Sr.

Tensile Properties and Fractography: The ultimate tensile strength of the ternary alloy decreases slightly after thermal exposure. However, the percent elongation before fracture does not change significantly and remains at around ~9%. These results are in line with the microstructural change that was observed; the globular phases remain in the matrix but undergo a slow transformation, which could only slightly alter their dislocation pinning ability during deformation. In the case of the binary sample, the thermal treatment slightly decreases its ultimate tensile strength and increases the elongation from 4% to 5% (Fig. 5. 23a). Tensile yield strength of ternary sample remains in the same range (~50 MPa) with a small decrease after heat treatment whereas the tensile yield strength of binary sample drops from 44 MPa in as-cast condition to 34 MPa in the heat-treated condition (Fig. 5. 23b). Again the microstructural observations of the binary alloy support the loss of its tensile properties; the loss of Sr from the matrix and the increase in the Mg₁₇Sr₂ induce embrittlement in the binary alloy.

The fracture surfaces of as-cast and heat-treated binary and ternary alloys are shown in Fig. 8. The fracture surface of Mg-0.5Sr (Fig. 5. 24a) exhibits dimples and no cleavage planes, which is typical of a ductile fracture; the surface, is decorated with second phases ($Mg_{17}Sr_2$) and occasional intergranular cracking, indicating that the deformation has proceeded via easy gliding which led to dislocation pile up at the interdendritic phases causing cracking. The fracture surface of 8 h heat-treated Mg-0.5Sr (Fig. 5. 24b) shows mixed brittle / ductile fracture with cleavage planes and dimples. No second phase particles are seen in the fracture surface showing that the $Mg_{17}Sr_2$ precipitates and the interdendritic and the intergranular regions did not play a significant effect in the fracture. The cleavage planes are apparently trans-granular and the loss of Sr from the Mg matrix has led to the loss of ductility. Brittle fracture is seen in tensile testing pure Mg and certain Mg alloys, and it is twin-induced [33]. In our previous study [14], we have observed such twin-induced brittle cleavage cracking in certain Mg alloy compositions. Even low levels of solute in the α -Mg can change the twinning susceptibility and the twinning modes [34, 35]; it is interesting to see that as Sr is lost from the α -Mg matrix of the binary alloy through the thermal treatment, twin induced brittle fracture sets in.

Fracture mode of as-cast Mg-0.3Sr-0.3Ca is similar to that of as-cast Mg-0.5Sr, and the ductile fracture surface is similarly decorated with second phases (Fig. 5. 24c). Intergranular cracking is also present. The difference between the ternary and the binary alloys in the as-cast state seems to be in the amount of strain before cracking, which was also observed in our previous study [14]. The globular phases in the matrix would slow down easy glide delaying cracking. Fracture surface of 8 h heat-treated Mg-0.3Sr-0.3Ca (Fig. 5. 24d) shows ductile mode with larger dimples compared to the as-cast sample. Since no intermetallics are observed in the fracture surface, it can be concluded that easy glide is still delayed by the globular phases, which prevents the rapid pile up of dislocations at the interdendritic phases. The change in the globular phase has, however, facilitated transgranular deformation through the matrix and as the ductility of the alloy is exhausted it has failed in a ductile mode. Only a small amount of brittle cleavage is seen in the surface indicating that some Sr (and Ca) may have been lost from the matrix initiating twin-induced cracking.

In summary, we observe that 8 h heat treatment at 400 °C decreases both the ultimate and yield strength of ternary sample but it does not affect its ductility. In the case of Mg-0.5Sr,

ultimate and yield strength decrease after 8 h heat treatment as well as the ductility. The ternary alloy shows higher ultimate strength and yield strength than the as-cast Mg-0.5Sr.

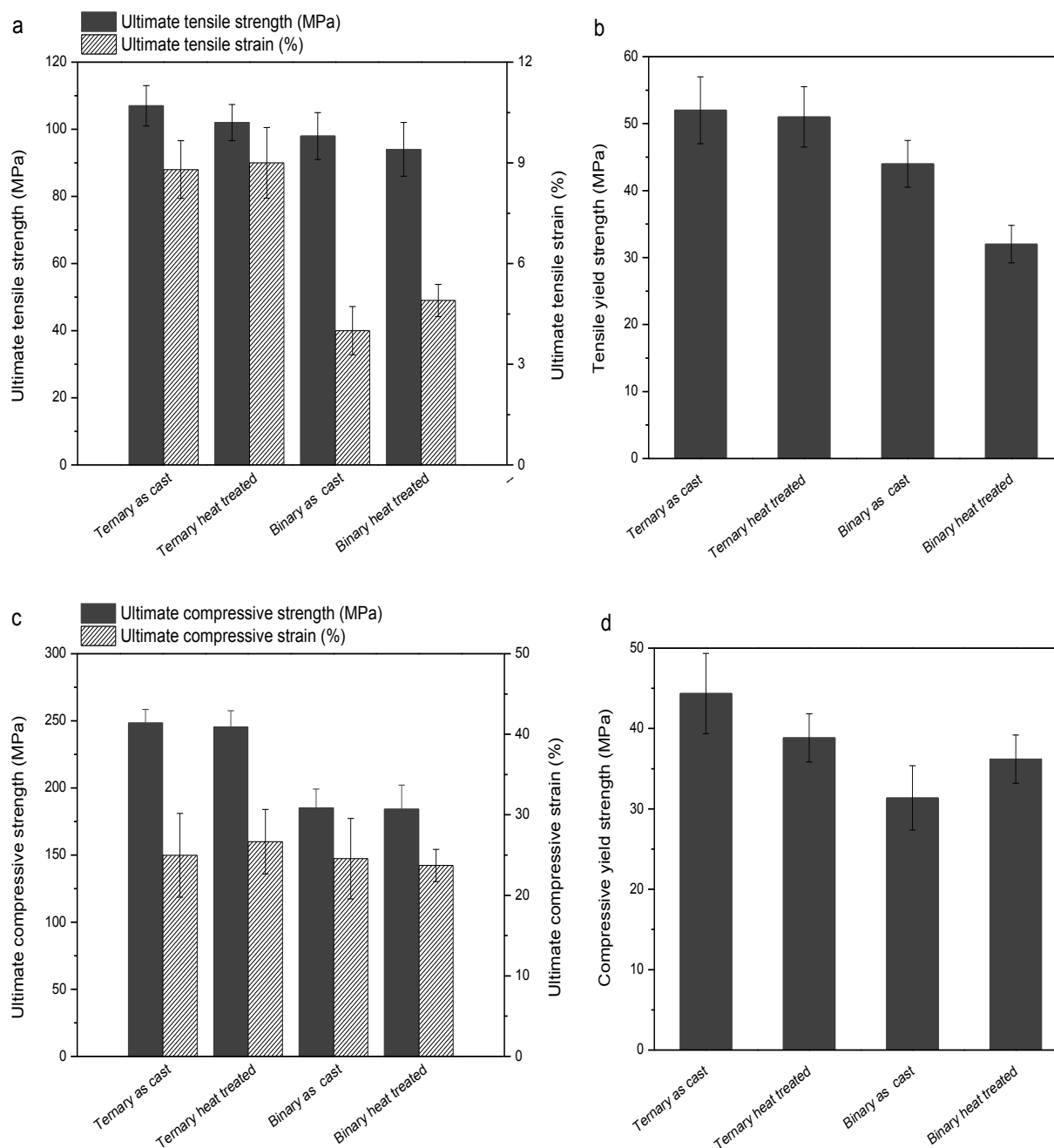


Fig. 5. 23. Mechanical properties of Mg-0.5Sr (binary) and Mg-0.3Sr-0.3Ca (ternary) samples before and after 8 h heat treatment at 400 °C; (a) Ultimate tensile strength and ultimate tensile strain (b) Tensile yield strength (c) Ultimate compressive strength and ultimate compressive strain (d) Compressive yield strength.

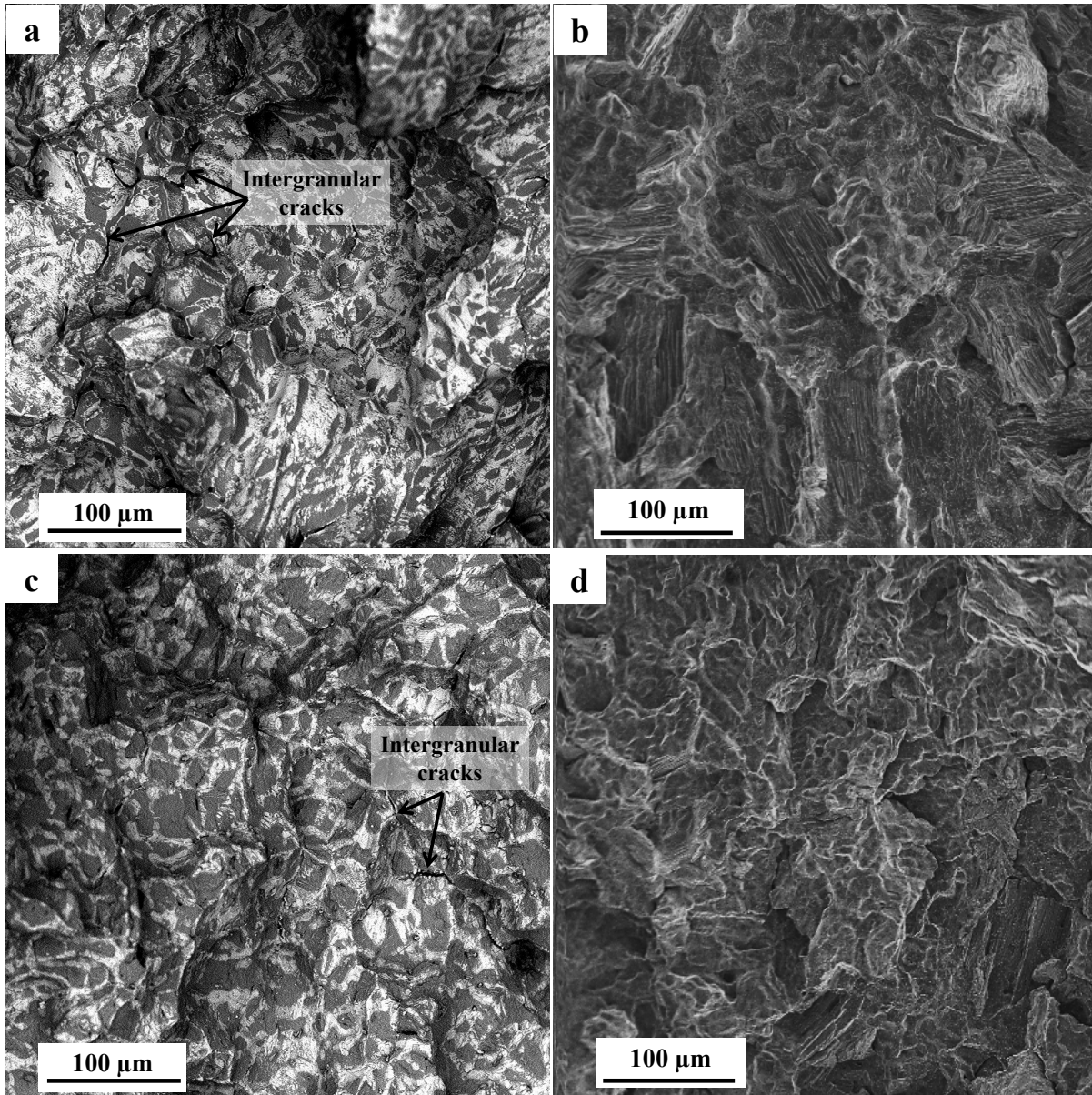


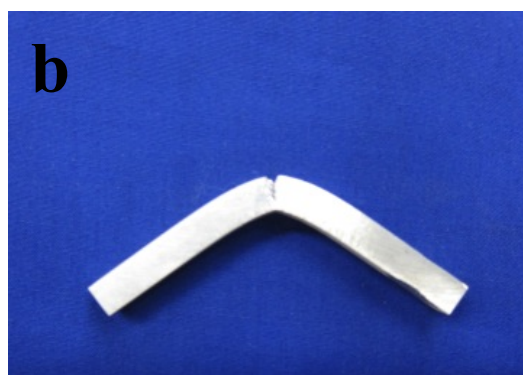
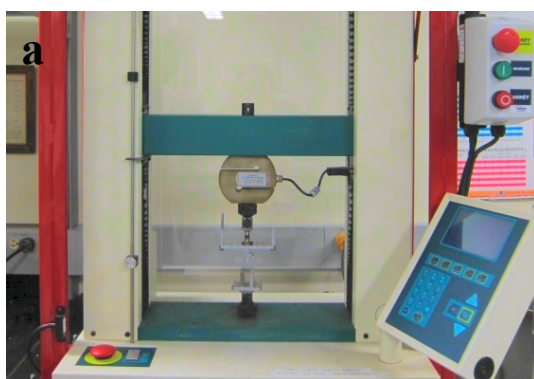
Fig. 5. 24. SEM fractographs of tensile tested samples of as-cast versus 8 h heat-treated at 400 °C of Mg-0.5Sr (a & b) and Mg-0.3Sr-0.3Ca (c & d). Tensile test was performed at room temperature.

Compression: The compression test results of Mg alloys demonstrate different behavior. Although the ternary alloy shows higher ultimate compressive strength than the binary alloy, the value of compressive strain (%) is always in the same range (~24-27 %) for both as-cast and heat-treated binary and ternary alloys. The final compressive strain of neither binary nor ternary

sample did change significantly after thermal exposure (Fig. 5. 23c). The compressive yield strength (CYS) of the ternary alloy decreases after the heat treatment from 44 MPa to 38 MPa, whereas the CYS of the binary sample increases from 32 MPa to 36 MPa after heat treatment (Fig. 5. 23 d). It can be seen that the compressive strengths (CS) of the binary and the ternary alloys equate after the heat-treatment as twinning becomes more prominent and the globular phase is lost from the ternary alloy. The slight gain in the CS of the binary alloy with heat-treatment is likely due to the crystallographic orientation change with the onset of twinning and the increase in the amount of the intermetallic phase. The loss of CS in the ternary alloy is due to the loss of the globular phase.

Bending Properties

Due to the importance of bending properties during manufacturing and implantation of biomaterial especially in the case of cardiovascular implants, we also evaluated Mg samples by performing three point bending test. Fig. 5. 25a & b show the bending set up used for this experiment and the Mg sample after test at room temperature. Fig. 5. 25c shows the effect of 8 h heat treatment on bending properties of Mg-0.5Sr and Mg-0.3Sr-0.3Ca. The highest bending strength is obtained for as-cast Mg-0.3Sr-0.3Ca. As reported in our previous work [14], the trend in the bending properties of the ternary and the binary alloy are similar to tensile properties with respect to compositional dependence and the effect of the thermal treatment.



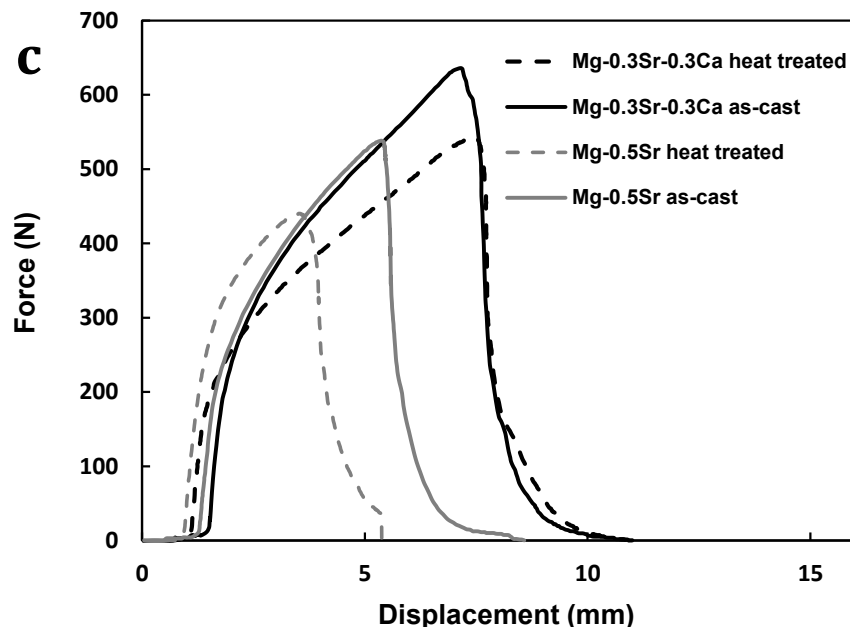


Fig. 5. 25. (a) Three-point bend tester used on Mg alloys; (b) Mg sample after bending experiment and (c) force-displacement curve generated by three-point bending test of as-cast and 8 h heat-treated samples of Mg-0.5Sr and Mg-0.3Sr-0.3Ca.

5. 2. 5. CONCLUSIONS

It has been observed that the single or combined addition of small amounts of Ca and Sr can improve the biodegradation resistance of Mg and its mechanical properties, which are microstructure related. In this work we studied the effect of thermal exposure to assess the stability of the microstructure and the retention of the properties during fabrication, processing and service required for implant (bone and vascular) applications.

- 1) The mechanical properties of Mg-0.5Sr and its corrosion resistance in SBF decrease drastically with thermal treatment.
- 2) Mg-0.3Sr-0.3Ca keeps its mechanical strength and slow degradation rate after 8 h heat treatment at 400 °C. Longer heat treatment at this temperature shows deteriorating effect on these properties.
- 3) The globular Ca/Sr-rich phase present in the as-cast condition of Mg-0.3Sr-0.3Ca transforms during thermal exposure at 400 °C. The globular phase starts to show compositional variation after 8 h heat treatment at 400 °C partially tending towards equilibrium phases.

4) The globular phase is known to reduce micro-galvanic corrosion in the ternary alloy and to improve mechanical strength. Its gradual transformation leads to some loss in the corrosion resistance and mechanical properties of the alloy. 8 h exposure at 400 °C exerts only a small influence on the properties while longer treatment (24 h) has a more pronounced effect. Fabrication processes should aim at using lower temperatures and shorter times to maintain the advantageous properties of the ternary alloy.

5. 2. 6. REFERENCES

- [1] Hartwig A. Role of magnesium in genomic stability. *Mutation Research-Fundamental and Molecular Mechanisms of Mutagenesis*. 2001;475:113-21.
- [2] Vormann J. Magnesium: nutrition and metabolism. *Molecular aspects of medicine*. 2003;24:27-37.
- [3] Yun Y, Dong Z, Yang D, Schulz MJ, Shanov VN, Yarmolenko S, et al. Biodegradable Mg corrosion and osteoblast cell culture studies. *Materials Science & Engineering C-Materials for Biological Applications*. 2009;29:1814-21.
- [4] Witte F, Kaese V, Haferkamp H, Switzer E, Meyer-Lindenberg A, Wirth CJ, et al. In vivo corrosion of four magnesium alloys and the associated bone response. *Biomaterials*. 2005;26:3557-63.
- [5] Serre CM, Papillard M, Chavassieux P, Voegel JC, Boivin G. Influence of magnesium substitution on a collagen-apatite biomaterial on the production of a calcifying matrix by human osteoblasts. *Journal of Biomedical Materials Research*. 1998;42:626-33.
- [6] Zreiqat H, Howlett CR, Zannettino A, Evans P, Schulze-Tanzil G, Knabe C, et al. Mechanisms of magnesium-stimulated adhesion of osteoblastic cells to commonly used orthopaedic implants. *Journal of Biomedical Materials Research*. 2002;62:175-84.
- [7] Staiger MP, Pietak AM, Huadmai J, Dias G. Magnesium and its alloys as orthopedic biomaterials: A review. *Biomaterials*. 2006;27:1728-34.
- [8] Kubasek J, Vojtech D, Lipov J, Ruml T. Structure, mechanical properties, corrosion behavior and cytotoxicity of biodegradable Mg-X (X = Sn, Ga, In) alloys. *Materials Science & Engineering C-Materials for Biological Applications*. 2013;33:2421-32.

- [9] Song Y, Shan D, Chen R, Zhang F, Han E-H. Biodegradable behaviors of AZ31 magnesium alloy in simulated body fluid. *Materials Science & Engineering C-Biomimetic and Supramolecular Systems*. 2009;29:1039-45.
- [10] McBride ED. Absorbable metal in bone surgery - A further report on the use of magnesium alloys. *Journal of the American Medical Association*. 1938;111:2464-6.
- [11] Guan R-G, Cipriano AF, Zhao Z-Y, Lock J, Tie D, Zhao T, et al. Development and evaluation of a magnesium-zinc-strontium alloy for biomedical applications - Alloy processing, microstructure, mechanical properties, and biodegradation. *Materials science & engineering C, Materials for biological applications*. 2013;33:3661-9.
- [12] Zong Y, Yuan G, Zhang X, Mao L, Niu J, Ding W. Comparison of biodegradable behaviors of AZ31 and Mg-Nd-Zn-Zr alloys in Hank's physiological solution. *Materials Science and Engineering B-Advanced Functional Solid-State Materials*. 2012;177:395-401.
- [13] Kannan MB, Raman RKS. In vitro degradation and mechanical integrity of calcium-containing magnesium alloys in modified-simulated body fluid. *Biomaterials*. 2008;29:2306-14.
- [14] Bornapour M, Celikin M, Cerruti M, Pekguleryuz M. Magnesium implant alloy with low levels of strontium and calcium: The third element effect and phase selection improve biocorrosion resistance and mechanical performance. *Materials Science & Engineering C-Materials for Biological Applications*. 2014;35:267-82.
- [15] Pekguleryuz M, Bornapour M. The effect of Sr and Ca on corrosion behavior of magnesium as biodegradable material. 9th International Conference on Magnesium Alloys & Applications. Vancouver, Canada 2012.
- [16] Bornapour M, Cerruti M, Shum-Tim D, Pekguleryuz M. Biocompatibility, bio-degradation and mechanical properties of Mg-0.5Sr alloy for use as temporary cardiovascular implants. The 4th International Symposium on Surface and Interface of Biomaterials. Roma, Italy: European Cells and Materials; 2013. p. 121.
- [17] Ilich JZ, Kerstetter JE. Nutrition in bone health revisited: A story beyond calcium. *Journal of the American College of Nutrition*. 2000;19.
- [18] Zhou P, Gong HR. Phase stability, mechanical property, and electronic structure of an Mg-Ca system. *Journal of the Mechanical Behavior of Biomedical Materials*. 2012;8:154-64.
- [19] Dahl SG, Allain P, Marie PJ, Mauras Y, Boivin G, Ammann P, et al. Incorporation and distribution of strontium in bone. *Bone*. 2001;28:446-53.

- [20] Marie PJ. Strontium ranelate: a novel mode of action optimizing bone formation and resorption. *Osteoporosis International*. 2005;16:S7-S10.
- [21] Bornapour M, Muja N, Shum-Tim P, Cerruti M, Pekguleryuz M. Biocompatibility and biodegradability of Mg-Sr alloys: The formation of Sr-substituted hydroxyapatite. *Acta Biomaterialia*. 2013;9:5319-30.
- [22] Liu X-b, Shan D-y, Song Y-w, Han E-h. Effects of heat treatment on corrosion behaviors of Mg-3Zn magnesium alloy. *Transactions of Nonferrous Metals Society of China*. 2010;20:1345-50.
- [23] Chang J-W, Guo X-W, Fu P-H, Peng L-M, Ding W-J. Effect of heat treatment on corrosion and electrochemical behaviour of Mg-3Nd-0.2Zn-0.4Zr (wt.%) alloy. *Electrochimica Acta*. 2007;52:3160-7.
- [24] Fan J, Qiu X, Niu X, Tian Z, Sun W, Liu X, et al. Microstructure, mechanical properties, in vitro degradation and cytotoxicity evaluations of Mg-1.5Y-1.2Zn-0.44Zr alloys for biodegradable metallic implants. *Materials science & engineering C, Materials for biological applications*. 2013;33:2345-52.
- [25] Pekguleryuz M. An overview of the effects of calcium and strontium on the properties of aluminum and magnesium alloys. IMMC (15th International Metallurgy and Materials Congress). Istanbul, Turkey 2010.
- [26] Pekguleryuz M, Kainer K, Kaya E. The alloying behaviour of magnesium. *Fundamentals of magnesium metallurgy*. Cambridge, UK: Woodhead; 2013.
- [27] Pekguleryuz M, Avedesian MM. Magnesium Alloying- Some Metallurgical Aspects. In: Mordike BL, Hehman F, editors. *Magnesium Alloys & their Applications*. Germany: DGM; 1992. p. 213-20.
- [28] Sahoo P, Debroy T, McNallan MJ. Surface-tension of binary metal - surface-active solute systems under conditions relevant to welding metallurgy. *Metallurgical Transactions B-Process Metallurgy*. 1988;19:483-91.
- [29] Li Z, Gu X, Lou S, Zheng Y. The development of binary Mg-Ca alloys for use as biodegradable materials within bone. *Biomaterials*. 2008;29:1329-44.
- [30] Zhang E, Yin D, Xu L, Yang L, Yang K. Microstructure, mechanical and corrosion properties and biocompatibility of Mg-Zn-Mn alloys for biomedical application. *Materials Science & Engineering C-Biomimetic and Supramolecular Systems*. 2009;29.

- [31] Fang G, Ai WJ, LeeFlang S, Duszczyc J, Zhou J. Multipass cold drawing of magnesium alloy minitubes for biodegradable vascular stents. *Materials Science & Engineering C-Materials for Biological Applications*. 2013;33:3481-8.
- [32] Schinhammer M, Steiger P, Moszner F, Loeffler JF, Uggowitzer PJ. Degradation performance of biodegradable Fe-Mn-C(-Pd) alloys. *Materials Science & Engineering C-Materials for Biological Applications*. 2013;33:1882-93.
- [33] Friedrich H, Mordike B. *Melting, Alloying, Refining. Magnesium Technology: Metallurgy, Design Data, Automotive Applications*: Springer Verlag; 2006. p. 147.
- [34] Pekguleryuz M, Celikin M, Hoseini M, Becerra A, Mackenzie L. Study on edge cracking and texture evolution during 150 degrees C rolling of magnesium alloys: The effects of axial ratio and grain size. *Journal of Alloys and Compounds*. 2012;510:15-25.
- [35] Pekguleryuz MO, Masoumi M, Becerra A. Texture evolution in Mg-Mn and Mg-Mn-Ce alloys and the effect of as-cast grain size. *Philosophical Magazine*. 2012;92:3766-79.

CHAPTER 6

DEGRADATION MECHANISM AND BIOCOMPATIBILITY OF Mg-0.3Sr-0.3Ca AS A TEMPORARY CARDIOVASCULAR STENT

This chapter contains one submitted manuscript, which is a comprehensive study on the best alloy, Mg-0.3Sr-0.3Ca, identified in our work (Chapters 4 & 5); it focuses on understanding the biodegradation behavior and biocompatibility of the Mg-0.3Sr-0.3Ca alloy. Several corrosion tests with and without SBF renewal and extensive surface characterization (XPS and Raman) were carried out to understand the role of Sr and its effect on the corrosion products that form on the surface. The corrosion mechanism of the Mg-0.3Sr-0.3Ca alloy in the biological environment was studied and a new reaction was added to those that were considered in previous studies on Mg alloy corrosion. In vitro cytocompatibility and in vivo biocompatibility evaluation on animal model were conducted to determine the interaction between Mg-0.3Sr-0.3Ca and its surrounding environment. It was found that the in-situ formation of Sr-substituted hydroxyapatite layer stabilizes the surface of the Mg-0.3Sr-0.3Ca alloy, acts as barrier between the biomaterial and its surrounding environment (SBF/tissue) and slows down its degradation rate over time.

6. 0. Biodegradable Mg-0.3Sr-0.3Ca alloy as temporary cardiovascular stent: Surface characterization, in vitro and in vivo biocompatibility evaluation

This section has been submitted as: M. Bornapour, H. Mahjoubi, H. Vali, D. Shum-Tim, M. Cerruti, M. Pekguleryuz, Biodegradable Mg-0.3Sr-0.3Ca alloy as temporary cardiovascular stent: Surface characterization, in vitro and in vivo biocompatibility evaluation, *Biomaterials*, December 2014.

6. 1. ABSTRACT

Magnesium-based alloys are an attractive material for medical applications. In our earlier work we have shown that Mg-Sr based alloys are good candidates for use in biodegradable implants due to slow corrosion rates. Specifically, we showed that Mg-0.3Sr-0.3Ca has the slowest degradation rate among all the binary Mg-Sr, Mg-Ca and ternary Mg-Sr-Ca alloys. We also showed that Mg-0.3Sr-0.3Ca forms a compact layer of corrosion products on the surface when immersed in simulated body fluid (SBF); we hypothesized this film to be a Sr-substituted hydroxyapatite. Here, we want to extend this study, and we have two main goals: (i) understand the mechanism of degradation of Mg-0.3Sr-0.3Ca and identify the exact nature of the protective layer that forms on its surface in physiological environments; and (ii) evaluate the in vitro and in vivo biocompatibility of the alloy. To achieve the first goal, we immersed the alloy in SBF and refreshed the SBF daily to better simulate the physiological environment. These experiments showed that the formation of a barrier on the surface of Mg-0.3Sr-0.3Ca is the main factor that reduces its degradation in SBF. Raman spectroscopy and X-Ray photoelectron spectroscopy (XPS) confirmed the formation of a thin, Sr-substituted, hydroxyapatite layer at the interface between the Mg-0.3Sr-0.3Ca alloy and the corrosion products. Another important factor is the biocompatibility of Mg-Ca-Sr ternary alloys for cardiovascular applications, which had not been studied before. To evaluate in vitro biocompatibility, we performed indirect cytotoxicity assays using HUVECs. The results showed that Mg-0.3Sr-0.3Ca extraction medium was not toxic or detrimental to cells. In fact, ions extracted from this sample increased the viability and proliferation of HUVECs after one week. In vivo tests were performed by implanting a tubular

Mg-0.3Sr-0.3Ca stent along with a WE43 control stent into the right and left femoral artery of a dog. Post implantation and histological analysis showed no thrombosis effect in the artery with Mg-0.3Sr-0.3Ca stent after 5 weeks of implantation while the artery implanted with WE43 stent was extensively occluded and thrombosed. Microscopic observation of the Mg-0.3Sr-0.3Ca implant-tissue interface confirmed the in situ formation of Sr-substituted hydroxyapatite on the surface during in vivo implantation. These results show that this interfacial layer protects the surface of the Mg-0.3Sr-0.3Ca alloy both in vitro and in vivo, contributes to the bio-corrosion resistance of the alloy.

6. 2. INTRODUCTION

In recent years, magnesium (Mg) and its alloys have been recognized as a novel class of materials for biodegradable metallic implants in different medical applications due to the low density ($\sim 1.74 \text{ g/cm}^3$), good mechanical properties and biocompatibility [1-7]. One of the application areas is temporary cardiovascular stent. Currently, metallic stents are made of stainless steel, Nitinol (Ni-Ti) and cobalt-chromium alloys [1]. Mg has superior advantages over these permanent metallic stents which may release toxic ions and particles through corrosion or wear and cause immune response in the body [1, 7]. Permanent metallic stents can also cause restenosis and hyperplasia due to the irritation of the endothelium [8]. They have much higher mechanical strength than natural tissues; the significant difference in the mechanical behavior of the stented and non-stented vessel areas can lead to growth restriction especially in the case of pediatric patients [4, 9, 10], necessitating a second surgery to remove the permanent metallic stent. This exposes patients to more surgical risks [11]. Other complications of permanent stents are thrombogenicity, permanent physical irritation, long-term endothelial dysfunction, and local chronic inflammatory reactions [9]. One of the advantages of Mg alloys over the traditional metals used for implants is that they are biodegradable [12-15]; their use as stents would thus eliminate the stimulus for hyperplasia and reduce the risk of restenosis [8, 16]. Mg alloys also have better visibility with high dimensional accuracy in CT scan compared to stainless steel biomaterials. Some clinical trials with Mg alloys have been undertaken for cardiovascular stent applications [17, 18].

Despite the first use of Mg in medical implants dates back to more than a century ago [4], its fast degradation rate has severely limited its applications [19]. During Mg degradation, high

volumes of H₂ gas are generated, which cannot be tolerated by the host tissue [20, 21]. Another complication is the loss of mechanical integrity before the healing process is complete [21]. This is a crucial problem for stent applications, since the main role of stents is to provide mechanical support for arterial walls and avoid early recoil while healing is in progress [22].

Thus, a considerable amount of research has focused on controlling the degradation rate of Mg by adding alloying elements [23-28]. Alloying elements should slow down the biodegradation without compromising the biocompatibility. Only a limited number of elements can be used in the body without causing toxicity or harmful effects on organs. Mg alloys containing rare earths (REs) such as WE43 (Mg-4Y-3RE) and LAE442 (Mg-4Li-4Al-2RE) have been evaluated for bio-implants [1]. Unless the alloys contain Al, substantial toxicity problems are not expected with REs; however, REs are not part of the human chemistry and they may cause undesired cell proliferation and high rate of neo-intima formation in stented vessels leading to potential risks of thrombosis [8, 29]. Animal studies using WE43 as cardiovascular stent have shown that the alloy had good mechanical integrity but caused the formation of thick neo-intima and thrombosis [30].

Strontium (Sr) and calcium (Ca) are naturally found in the human body [28, 31-35]. We previously reported that Mg-0.5Sr has a significantly lower degradation rate compared to pure Mg and other as-cast binary Mg-Sr alloys with Sr wt.% ranging from 0.3 to 2.5 [36]. We showed that Sr improves the corrosion resistance of Mg by altering its surface chemistry due to its surface active nature, and we detected a thin layer of Sr-modified hydroxyapatite on the surface of Mg-0.5Sr after immersion in SBF, which seemed to stabilize the surface and reduce the degradation rate [36]. Sr-containing HA coatings improved the bioactivity and bio-corrosion resistance of titanium alloys as well [37, 38]. Sr-HA is known to have better biocompatibility, thermal stability and surface reactivity than pure HA [39, 40].

In a subsequent study, the authors have found that the combined addition of both Sr and Ca in small amounts increases the corrosion resistance of Mg in physiological conditions more than the single addition of Sr or Ca; this was related to the third element effect [41]. An alloy containing low levels of Sr and Ca, Mg-0.3Sr-0.3Ca had the lowest degradation rate (~0.8 mg /day/cm² in terms of mass loss and ~0.4 mg /day/cm² in terms of H₂ evolution) among all the ternary Mg-Sr-Ca and the binary Mg-Sr and Mg-Ca alloys in SBF; it exhibited 90% slower degradation rate than pure Mg. The alloy produced a slow change in the pH of SBF and the H₂

evolution rate obtained was $\sim 0.01 \text{ ml cm}^{-2} \text{ h}^{-1}$, which is lower than that measured for Mg-Sr and Mg-Ca binary alloys ($\sim 0.04 \text{ ml cm}^{-2} \text{ h}^{-1}$) and significantly below that of pure Mg ($\sim 0.2 \text{ ml cm}^{-2} \text{ h}^{-1}$) [41].

Mg-0.3Sr-0.3Ca also showed the best mechanical and bending properties and thermal stability among any Mg-Sr and Mg-Ca binary alloys tested due to the formation of globular Ca/Sr-rich phases in the microstructure of Mg-0.3Sr-0.3Ca [41, 42]. The microstructure of this ternary Mg alloy contains α -Mg matrix and (α -Mg + β) eutectic micro constituents. The existence of the finely dispersed new Sr/Ca phase in the matrix slows down the corrosion rate by reducing micro-galvanic corrosion and improves the mechanical properties of the alloy.

After immersion of Mg-0.3Sr-0.3Ca in SBF, we observed the formation of a fine and compact scale containing hydroxyapatite (HA) on the alloy surface. The surface of a medical implant is the first region that the natural tissue comes in contact with. Thus, understanding the surface chemistry of an implant and its interactions with the physiological environment is crucial for biomaterials. Still, in our previous work we did not study the exact nature of the protective scale formed on the alloy surface, and its role in degradation. The present work is focused on a surface analysis of this scale and on the mechanism of alloy degradation. Also, previously the alloy degradation was tested in static conditions without changing the SBF solution, which did not simulate well the dynamic nature of the physiological environment with respect to the pH levels of the solution. Here, we improve the test by daily renewing the SBF solution in which the alloys are immersed. Finally, this work investigates the *in vitro* and *in vivo* biocompatibility of Mg-0.3Sr-0.3Ca, hitherto not evaluated, and its interactions with surrounding tissues for cardiovascular applications.

6. 3. EXPERIMENTAL PROCEDURE

6. 3. 1. Materials

A thin plate of Mg-0.3Sr-0.3Ca was prepared by melting down pure Mg (99.9 wt.%), pure Sr (99.99 wt.%) and Mg-30Ca master alloy all supplied by Applied Magnesium (Formerly Timminco) in a Lindberg/Blue M Crucible Furnace. CO_2 with 0.5% SF_6 was used at a flow rate of 1.1 L/min as protective gas to prevent burning during melting and casting. K-type (Chromel-Alumel) thermocouple was used with a digital thermometer to monitor the melt temperature. Steel die with a plate cavity coated with boron nitride release coating was heated to

400 °C before plates were cast. The chemical composition of alloy was analyzed by inductively coupled plasma atomic emission spectroscopy (ICP-AES) as listed in Table 6. 1. Pure Mg and WE43 containing of 3.48 wt.% yttrium, 2 wt.% neodymium, 0.5 wt.% gadolinium and 0.15 wt.% praseodymium was also cast using the same procedure.

Table 6. 1: The actual chemical composition of as-cast Mg-0.3Sr-0.3Ca obtained by ICP-AES

Alloy	Chemical composition (wt. %)						
	Sr	Ca	Al	Si	Fe	Mn	Mg
Mg-0.3Sr-0.3Ca	0.31	0.39	0.011	0.005	0.044	0.003	Balance

6. 3. 2. Immersion Test

Interrupted corrosion experiments was conducted in SBF using Hank's solution (8.0 g/l NaCl, 0.4 g/l KCl, 0.14 g/l CaCl₂, 0.35 g/l NaHCO₃, 1.0 g/l C₆H₆O₆ (glucose), 0.1 g/l MgCl₂ · 6H₂O, 0.06 g/l MgSO₄ · 7H₂O, 0.06 g/l KH₂PO₄ · H₂O, 0.06 g/l Na₂HPO₄ · 7H₂O). Samples used in the experiment were cut from thin plates of 6 mm thickness into 2 × 4 cm² sections and were polished down to 800 grit with silicon-carbide paper. They were then cleaned, dried, and weighed. Interrupted immersion test was carried out in static conditions (without SBF renewal). In this test, the pH value of Hank's solution was adjusted to 7.4 at the beginning and the temperature was maintained at 37 °C using a hot plate during immersion testing. The samples were removed from SBF after a certain time, cleaned off of corrosion residues and dried. The variation of pH, the weight change and the volume of H₂ gas released were measured. The average value of corrosion rate in terms of both mass loss and H₂ evolution were calculated as average values of triplicate corrosion tests. Some of the samples were only rinsed with ethanol and dried without cleaning the corrosion product for further surface characterization. Another set of immersion test was carried out using fresh solution (daily SBF renewal) to investigate the effect of pH change on the degradation of the sample. The solution was replaced every day with fresh SBF and the variation of pH value and the amount of different ions released from Mg-0.3Sr-0.3Ca into the solution was monitored during the time. The temperature was always maintained at 37 °C. The concentration of metallic ions in the SBF was measured by inductively coupled plasma mass spectrometry (ICP-MS) for both experimental conditions (with/without

SBF renewal). These values contain the amount of ions exist in Hank's solution components in addition to those dissolved from the metallic sample.

6. 3. 3. Surface Analysis

6. 3. 3. 1. Raman spectroscopy

Raman spectra were obtained from the corrosion product formed on the surface after 3 days of immersion in SBF using a Bruker Senterra confocal Raman microscope connected to a Bruker MultiRAM stand-alone FT-Raman spectrometer. The 1032 nm laser was used as excitation source. A fiber optic cable transferred the laser from the MultiRAM to the Senterra microscope. The spectra were collected using a 40x objective with 256 scans at 3.5 cm^{-1} resolution and were acquired in the range of $0 - 3600 \text{ cm}^{-1}$. Another fiber optic cable transferred the collected signal back to the MultiRAM detector.

6. 3. 3. 2. X-ray photoelectron spectroscopy (XPS)

The surface scale of corroded Mg-0.3Sr-0.3Ca was characterized by X-ray photoelectron spectroscopy (XPS, K-Alpha, Thermo Scientific) using an X-ray source of Al-K α (1486.6 eV) with a spot size of 400 μm diameter. The energy resolution was 0.1 and 1 eV for the high resolution and survey scan, respectively. To prevent charging, spectra were collected using a flood gun. Samples were etched with Ar ions in-situ, in the XPS analysis chamber, to remove surface contamination and to measure compositional depth profiles.

6. 3. 4. Cytotoxicity Evaluation

Human umbilical vascular endothelial cells (HUVEC) purchased from Cedarlane Laboratories (ATCC CRL-1730) were employed in cell viability evaluation. HUVEC was maintained in F-12K medium supplemented with 2 mM L-Glutamine (Invitrogen, Carlsbad, CA), 10% Newborn Calf Serum (NBCS, HyClone Laboratories Inc., Logan, UT) and 1% Penicillin Streptomycin antibiotic (Invitrogen, Carlsbad, CA) at 37 °C in humidified atmosphere at of 5% CO₂. Heparin (0.1 mg/ml) and endothelial cell growth supplement (ECGS; 0.05 mg/ml) were used to grow the cells on gelatin coated (0.2%) culture flasks.

The biocompatibility of the Mg-0.3Sr-0.3Ca alloy was evaluated by indirect cell viability assay. The cytotoxicity evaluation was also performed using pure Mg and WE43 as control samples. All the steps of the experiment were exactly the same for three alloy compositions.

An ion extract was obtained from $1 \times 1 \times 0.5 \text{ cm}^3$ of each alloy specimen by incubating in 10 ml of F-12K medium for 72 h in humidified atmosphere containing 5% CO_2 and 95% air at 37 °C. The extracted medium was diluted to 50% and 10% concentration using F-12K medium with supplements in preparation for cell viability assays. The concentration of Mg ions in the extracted medium was measured by ICP-MS for each alloy extraction. F-12K medium supplement was used as positive control for cell growth. HUVECs were then seeded onto 96-well cell culture plates at 5×10^3 cells/100 μl medium in each well and incubated overnight in order to ensure attachment to the well. Three wells were seeded for each alloy composition and each assay time point. Next, the medium in each well was replaced with 100 μl of extract and again incubated in a humidified atmosphere with 5% CO_2 at 37 °C for 1, 4 and 7 days. During the experiment, the cells were treated every three days with fresh medium containing heparin and ECGS. At the end of each test, indicator Alamar blue (5% in F-12K medium with growth supplements) was added to each well and further incubated at 37 °C for 4 h. Finally, fluorescence emission of the solution was measured at 595 nm using 560 nm excitation (Infinite 200, Tecan). After background subtraction, fluorescence intensity was analyzed relative to the control (F-12K medium).

6. 3. 5. Animal Implantation

(a) Prototype stent fabrication: The Mg-0.3Sr-0.3Ca alloy was cast into rods and machined into perforated stents with 2.4 mm diameter, 10 mm length and 0.25 mm wall thickness in order to implant into the femoral artery. The stents were slit longitudinally and folded over to reduce its diameter during implantation. Once inserted in place, the stent could be dilated with a balloon to fully expand it against the femoral artery. A WE43 stent was also fabricated with the same size, design, and implanted as control sample into the contralateral femoral artery of the same animal.

(b) Animal experiments: The performance of the new alloy stents was tested using established animal model (12 kg Beagle dog). All animals received humane care in compliance with the “Guide to the Care and Use of Experimental Animals” of the Canadian Council on Animal Care. After pre-medication with 45 mg/kg of intraperitoneal methohexital sodium to establish an intravenous line through the ear vein, the animal was subjected to general anesthesia and endotracheal intubation for mechanical ventilation. Under sterile condition, the femoral arteries were exposed bilaterally as previously described [43, 44]. After proximal and distal control, an

arteriotomy was carried out. A stent prepared with different Mg alloys were then inserted in each side (Right: Mg-0.3Sr-0.3Ca; Left: WE43) as described above. The arteriotomy sites were repaired with 7-0 prolene suture to re-establish arterial patency. The status and patency of the femoral stent was confirmed by the presence of palpable pulses in the distal femoral artery and by doppler ultrasound. The animal was then extubated and survived for five weeks for further analysis. Post-implantation studies were conducted at five weeks before sacrificing the animal. Following an overdose of sodium pentobarbital, the femoral arteries were removed after in vivo fixation with 10% buffered formaldehyde solution perfused at 100 mm Hg for 15 min. Each artery containing stent was excised and fixed in 4% commercial formalin for histological studies. To determine the presence of acute and/or organized thrombosis, fibrosis, endothelial damage or medial hypertrophy, two explanted stents within surrounding arteries were divided into two sections for various post-implantation analyses: (i) One section of each sample was used for histological analysis. Samples were embedded in paraffin and sectioned (5 μ m per section) using Leica RM2265 microtome; they were cut in the transverse direction for cross-sectional observation. They were stained using hematoxylin and eosin and mounted in Eukitt according to a standard procedure. For each stent sample and its surrounding tissue, we conducted at least three histological staining per hematoxylin and eosin. (ii) The second section of each sample was used to assess the morphological characteristics of the stent and the surrounding tissue. The section was exposed to 2.5% gluteraldehyde in 0.1M sodium cacodylate buffer and kept at 4 °C for 24 h to fix the tissue; it was then post-fixed with 1% aqueous OSO_3 + 1.5% aqueous potassium ferrocyanide for 2 h, and washed 3 times with washing buffer. The fixative solution was then carefully removed; the sample was washed three times for 10 min with 0.1M cacodylate washing buffer, and dehydrated with ethanol in increments of 10% from 30% up to 90%, allowing 5 min intervals between each increment. The specimens were then further dehydrated twice with 100% ethanol over 10 min intervals. Following dehydration, the specimens were infiltrated by adding increasing amounts of epon ethanol (from 1:1 to 3:1), allowing 30 min intervals between each subsequent addition. Pure epon, deaerated under vacuum (constant pressure <25 psi) was then added to the samples, and allowed to stand for 1 h under vacuum to remove ethanol residue and air bubbles in the epon. Finally, the samples containing wells were refilled with new epon and placed in an oven at 60 °C for 48 h to polymerize the epon. The epoxy block containing the stent and tissue were cross-sectioned using a diamond

knife. The cut surface were coated with C and analyzed in FEI Quanta 450 Environmental Scanning Electron Microscope (FE-ESEM) by backscatter imaging mode and EDS mapping to examine the implant/tissue interface.

6. 4. RESULTS AND DISCUSSIONS

6. 4. 1. Degradation behavior, role of immersion time and pH

6. 4. 1. 1. Interrupted test and the role of immersion time

We previously showed that alloying Mg with low levels of both Sr and Ca decreased the corrosion rate in SBF [41]. Indeed, Mg-0.3Sr-0.3Ca showed the lowest degradation rate and volume of H₂ released among all the ternary Mg-Sr-Ca and the binary Mg-Sr and Mg-Ca alloys in static immersion tests in SBF. Here we evaluate the degradation rate of the alloy using an interrupted immersion test, to monitor and understand the evolution of the biodegradation. Fig. 6. 1a presents the corrosion rate of Mg-0.3Sr-0.3Ca in terms of both mass loss and H₂ release obtained from interrupted test after 1, 2 and 3 days immersion in SBF. As commonly observed for Mg alloys, the degradation rate (both in terms of mass loss and of H₂ evolution) decreases with immersion time. The highest degradation rate is observed after 1 day. The degradation rate decreases very slowly after 1 day of immersion and the degradation rate is very similar at 2 and 3 days. This can be associated with a change in pH of the SBF solution and/or the gradual formation of a corrosion barrier on the surface of this sample.

6. 4. 1. 2. Daily SBF renewal and the role of pH

In our previous work the degradation was evaluated in static immersion tests [41]. To better simulate the physiological environment and keep the SBF pH more constant, here we evaluated the corrosion of Mg-0.3Sr-0.3Ca in a test where the immersion solution is replaced with fresh SBF every day. Fig. 6. 1b shows the pH variation after each 24 h cycle and before replacing the solution with fresh SBF. The pH value increases to ~8.7 after the 1st day of immersion before SBF replacement, and then drops to 8.1 after the 2nd day. The decreasing trend continues throughout the experiment, and after 7 days the pH reaches 7.8. The variation of pH measured during the immersion test without SBF renewal is also shown in this graph [41]. The pH value reaches to higher values (~9.2) in the absence of SBF renewal. Fig. 6. 1c shows the average degradation rate of Mg-0.3Sr-0.3Ca during the immersion test with and without daily SBF renewal. The degradation in these two experimental conditions is very close; in fact, there is no

significant difference either in terms of mass loss or H_2 evolution ($P > 0.05$). The insignificant difference in corrosion rate of the two conditions (with and without SBF renewal) shows the minor effect of the pH change on alloy corrosion. In both conditions, the initial increase in pH can be related to the continuous dissolution of Mg and the increase in OH^- ions in the solution [45]. Once a layer of corrosion products forms on the surface, the diffusion of ionic species is slowed down [20, 46], and a dynamic equilibrium is reached. This is shown by the achievement of a constant pH in solution. A plateau in pH is observed in both conditions, but the values are quite different: ~ 9.2 in the test without SBF renewal, and ~ 7.8 in the test with SBF renewal.

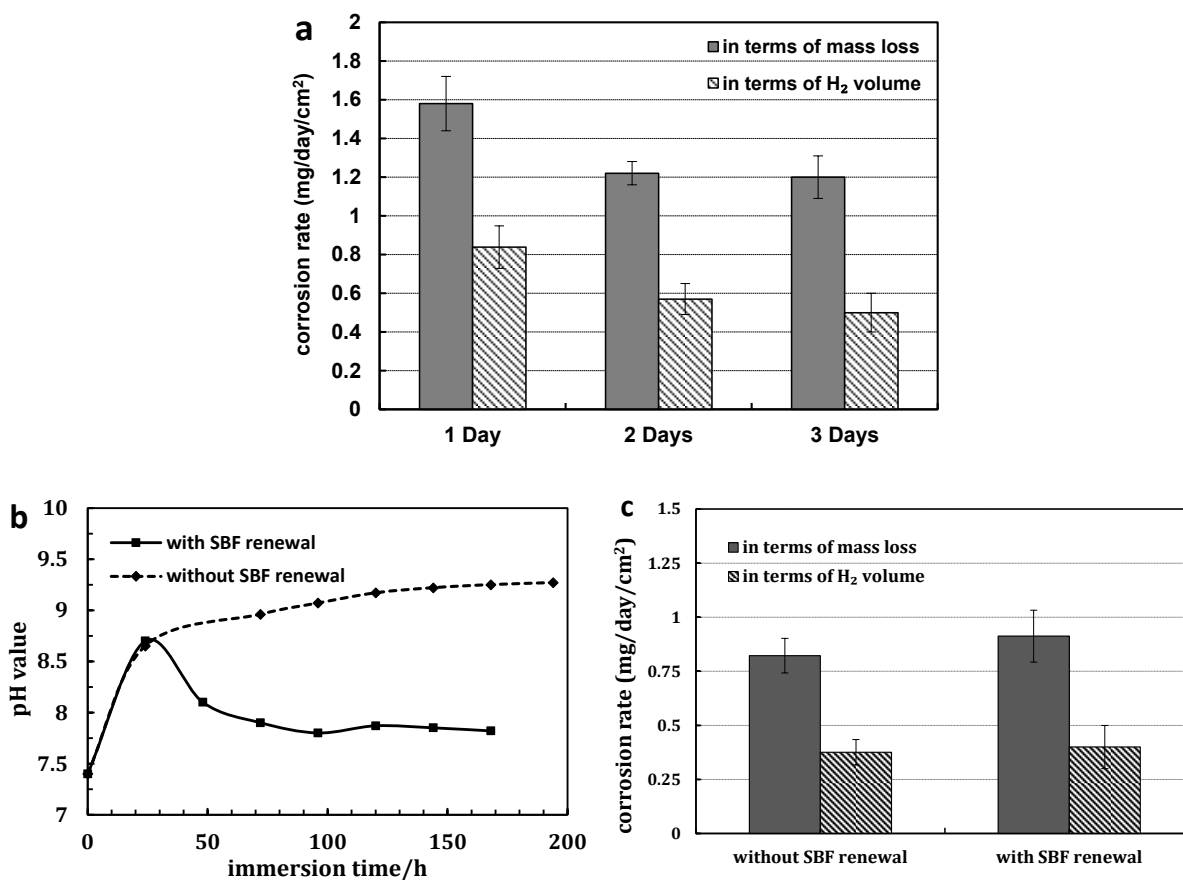


Fig. 6. 1. (a) Average corrosion rate (mg/day/cm²) of Mg-0.3Sr-0.3Ca in terms of mass loss and H₂ evolution during interrupted immersion test without SBF renewal. (b) Comparison of pH change of the solution containing Mg-0.3Sr-0.3Ca in experiments with and without SBF renewal. (c) Average corrosion rate (mg/day/cm²) of Mg-0.3Sr-0.3Ca in terms of mass loss and H₂ evolution after immersion tests with and without SBF renewal.

To complement the pH data, we analyzed the ions released in both immersion tests (with and without daily SBF renewal) by ICP. In agreement with the observed increase in pH, the results show the highest increase in concentration of Mg ions in SBF during the 1st day of immersion (Table 6. 2). In both test conditions (with and without SBF renewal) the amount of Mg ions in SBF increases during the tests compared to the original value in SBF (~37 mg/l); however, less Mg is released in the second and third day compared to the first day. Overall, more Mg is released in the test performed with SBF renewal, probably because of a larger concentration gradient caused by SBF renewal after days 2 and 3. The amount of Sr in both conditions is very small and cannot be detected with ICP. Both Ca and P ions decrease compared to the original values in SBF (~50 mg/l and ~28 mg/l, respectively). This confirms the formation of a Ca phosphate layer on the alloys. In the test without SBF renewal, the decrease in Ca and P increases after the first day, going from a decrease in Ca corresponding to 14 mg/l after the first day, to 22 mg/l after the second day, and then slows down to no further decrease after the third day. In the test performed with SBF renewal, the decrease is 14 mg/l after first day, 8 mg/l after second day and only 3 mg/l after third day. The higher decrease in Ca observed during the second day in the test performed without SBF renewal indicates a larger precipitation in this case; this may be related to the higher pH measured in the test performed without SBF renewal, since HA is less soluble at higher pH. These results also indicate that the sample degradation/reprecipitation reaches a steady state in 2nd day in the test performed without SBF renewal, whereas this takes longer in the tests performed with SBF renewal. This again agrees with the different time necessary to reach a plateau in pH in the two conditions (Fig. 6. 1b).

Table 6. 2: The concentration of metallic ions (mg/l) in the SBF measured by ICP after immersion of Mg-0.3Sr-0.3Ca in SBF, with and without daily renewal. Values include the ions pre-existing in Hank's solution. The amount of Sr was very low and not traceable.

Mg-0.3Sr-0.3Ca	With daily SBF renewal			Without daily SBF renewal		
	Mg	Ca	P	Mg	Ca	P
Day 1*	63.9 ± 0.6	36.0 ± 0.5	20.3 ± 0.3	63.9 ± 0.6	36.0 ± 0.5	20.3 ± 0.3
Day 2	52.3 ± 0.3	42.7 ± 0.6	26.5 ± 0.4	71.2 ± 0.4	14.4 ± 0.2	10.6 ± 0.2
Day 3	51.6 ± 0.5	46.9 ± 0.8	28.7 ± 0.7	74.4 ± 0.7	14.5 ± 0.4	10.5 ± 0.5

* The experimental condition at day 1 is the same in both tests with and without SBF renewal.

6. 4. 2. Analysis of the surface layer

We previously saw the formation of a highly compact corrosion layer on the surface of Mg-0.3Sr-0.3Ca after immersion in SBF at 37 °C; XPS compositional depth profile showed that this layer was mostly HA [41]. We hypothesized that such homogenous compact layer was due to the presence of a thin, Sr-substituted HA interface layer formed on the surface of Mg-0.3Sr-0.3Ca. Here we performed a more extensive surface analysis to determine the exact nature of this surface layer.

The powders collected from the corroded surface of Mg-0.3Sr-0.3Ca were analyzed with Raman spectroscopy, which can provide information on HA substitution degree [47] and crystallinity [48]. Fig. 6. 2 shows the spectra acquired from powders scratched off the alloy surface after 1 day of immersion in SBF, along with the spectra collected on HA powders as control sample. All four bands of phosphate ν_1 (962 cm^{-1}), ν_2 (420 cm^{-1}), ν_3 (1050 cm^{-1}), and ν_4 (580 cm^{-1}) are visible on the spectrum of the HA control. The ν_1 phosphate band maximum is at $\sim 959\text{ cm}^{-1}$ in the spectrum relative to the Mg alloy corrosion products, and the peak is much broader on this sample than on the control HA. O'Donnell et al [49] reported that the position of the Raman ν_1 phosphate band in HA shifts to lower values linearly depending on the amount of Sr in $(\text{Sr}_x\text{Ca}_{1-x})_5(\text{PO}_4)_3\text{OH}$, all the way down to 949 cm^{-1} at full Sr-substitution. Li et al [47] also reported a similar shift in the ν_1 phosphate band in Sr-substituted HA. They also observed that the peak becomes broader with increasing amount of incorporated Sr. This may also be related to a decrease in crystallinity [48]. Thus, the shift and the larger width observed for the ν_1 peak of the corrosion product spectrum can be an indication of the formation of a less crystalline, Sr-substituted HA on the alloy upon immersion in SBF.

To confirm this, we analyzed the surface of the alloy after removal of the corrosion products by XPS. Mg-0.3Sr-0.3Ca was cleaned off of corrosion products using chromic acid, rinsed with ethanol and dried. XPS analysis conducted on this sample showed that Ca and P could be detected on the surface of Mg-0.3Sr-0.3Ca after removing the corrosion products (Table 6. 3). We performed a similar experiment for pure Mg in the same conditions, but we did not detect any Ca or P [36]. The high amount of C ($\sim 16\%$) is due to environmental contamination, and it can be easily removed after few seconds of sputtering. The relative concentration of all the C and O decreases during the depth profile, thus showing that some O was also related to contamination. The amount of O decreases from $\sim 61\%$ to $\sim 39\%$ after only 50 s sputtering. The

concentration of O decreases down to ~17% after 250 s sputtering. After 200 s sputtering, the atomic percent of C is $\leq 0.5\%$, while Ca and P reach and stay at ~1.6% and ~0.7% respectively. The amount of C detected at lower etching levels may be related to the presence of small traces of carbonates. The Mg/O ratio increases during sputtering cycles indicating that we are removing MgO from the surface as we go deeper in the sample. Small amounts of Sr (~0.2%) were found after 100 s sputtering, corresponding to layers present more than 30 nm under the surface (Ta_2O_5 , a much harder material than our alloys, is removed at 0.3 nm/s as a reference).

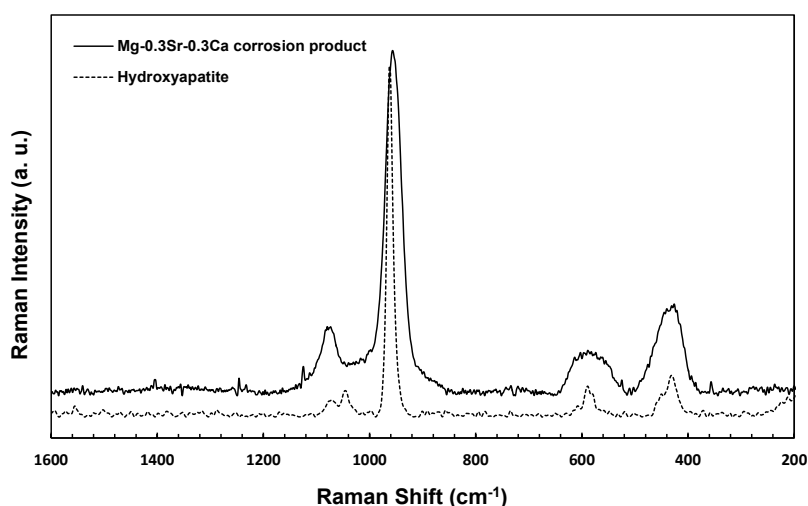


Fig. 6. 2. Raman spectra of corrosion product scratched off the surface of Mg-0.3Sr-0.3Ca after 1 day immersion in SBF compared with HA powders as control.

These results indicate that after immersion in SBF, a layer of calcium phosphate containing small amounts of Sr formed on the surface of Mg-0.3Sr-0.3Ca, which can be detected after cleaning the corrosion products and removing surface contamination. The Ca/P ratio found on the surface layers varies from 2.5 (top layer) to 2.3 (after 250 s sputtering). This value is somewhat higher than what expected for HA (1.67), and may indicate that some of the Ca may be bound to carbonates or other ions. The presence of Ca, P and Sr on these layers confirms the formation of Sr-substituted HA on the surface of Mg-0.3Sr-0.3Ca. This changes the morphology of the product layer and slows down the degradation, similar to what previously observed on binary Mg-0.5Sr alloys [36].

Table 6. 3: XPS analysis from the surface of Mg-0.3Sr-0.3Ca after removing the corrosion products and after sputtering with Ar ions for successive 50-second cycles.

Etching time (s)	Elemental composition (At.%)					
	Mg	O	Ca*	P	C	Sr
0	9.8 ± 0.3	61.3 ± 0.4	8.7 ± 0.5	3.4 ± 0.5	16.8 ± 0.3	–
50	53.9 ± 0.8	39.4 ± 0.4	3.6 ± 0.4	1.3 ± 0.1	1.7 ± 0.2	–
100	63.3 ± 0.7	32.5 ± 0.5	1.9 ± 0.2	1.0 ± 0.1	1.1 ± 0.1	0.2 ± 0.1
150	68.9 ± 0.7	28.1 ± 0.4	1.6 ± 0.2	0.7 ± 0.1	0.5 ± 0.1	0.2 ± 0.1
200	74.5 ± 1.0	22.4 ± 0.3	1.6 ± 0.2	0.7 ± 0.1	0.4 ± 0.1	0.4 ± 0.1
250	79.4 ± 0.8	17.5 ± 0.3	1.6 ± 0.2	0.7 ± 0.1	0.3 ± 0.1	0.5 ± 0.1

* The values for Ca are obtained from the Ca_{3s} peak due to the overlap between Ca_{2p} and Mg Auger peaks.

The high resolution spectra for Ca_{2p}, P_{2p}, Sr_{3p} and Mg_{2p} on this sample on the surface and after 250 s of argon sputtering are shown in Fig. 6. 3. The Mg_{2p} peak shows two components on the surface, one centered at ~49.5 eV, relative to metallic Mg, and another peak that can be due to either MgO (expected at 50.5 eV) or MgCO₃ (expected at 50.9 eV) [50]. This component strongly decreases upon etching, thus confirming the removal of MgO (and possibly carbonates) from the surface and the presence of more metallic Mg in the bulk. The P_{2p} peak was centered at 133.6 eV and did not change significantly upon etching. This value corresponds to the energy expected for PO₄³⁻ ions. The peak relative to Sr_{3p_{3/2}} shows up after 250 s etching, and is centered at 269.8 eV, indicative of Sr²⁺ rather than metallic Sr [51-53]. The intensity of the corresponding Sr_{3p_{1/2}} peak is so low that even after 250 s etching it cannot be detected.

The Ca_{2p} spectrum is harder to analyze due to the presence of Mg Auger peaks at the same binding energy. At the surface we see two components, one centered at 347.6 eV and one at 351.3 eV. These are related to Ca²⁺, and specifically the Ca_{2p_{3/2}} and Ca_{2p_{1/2}} peaks, respectively. However, one would expect a higher intensity for the Ca_{2p_{3/2}} component of the doublet, which is not the case for the surface spectrum. This can be attributed to the presence of a Mg Auger peak superimposed. After 250 s sputtering, another peak shows up at ~357.5 eV, which corresponds to another Mg Auger peak. Similar peak positions are observed at all sputtering levels after removing the surface layer (spectra not shown). Overall, the high resolution Ca_{2p} spectra show

that all Ca is in the form of Ca^{2+} , and no metallic Ca is ever observed [54]. Because of the superposition with Auger peaks, we have used the Ca_{3s} peaks to evaluate the total amount of Ca on these samples.

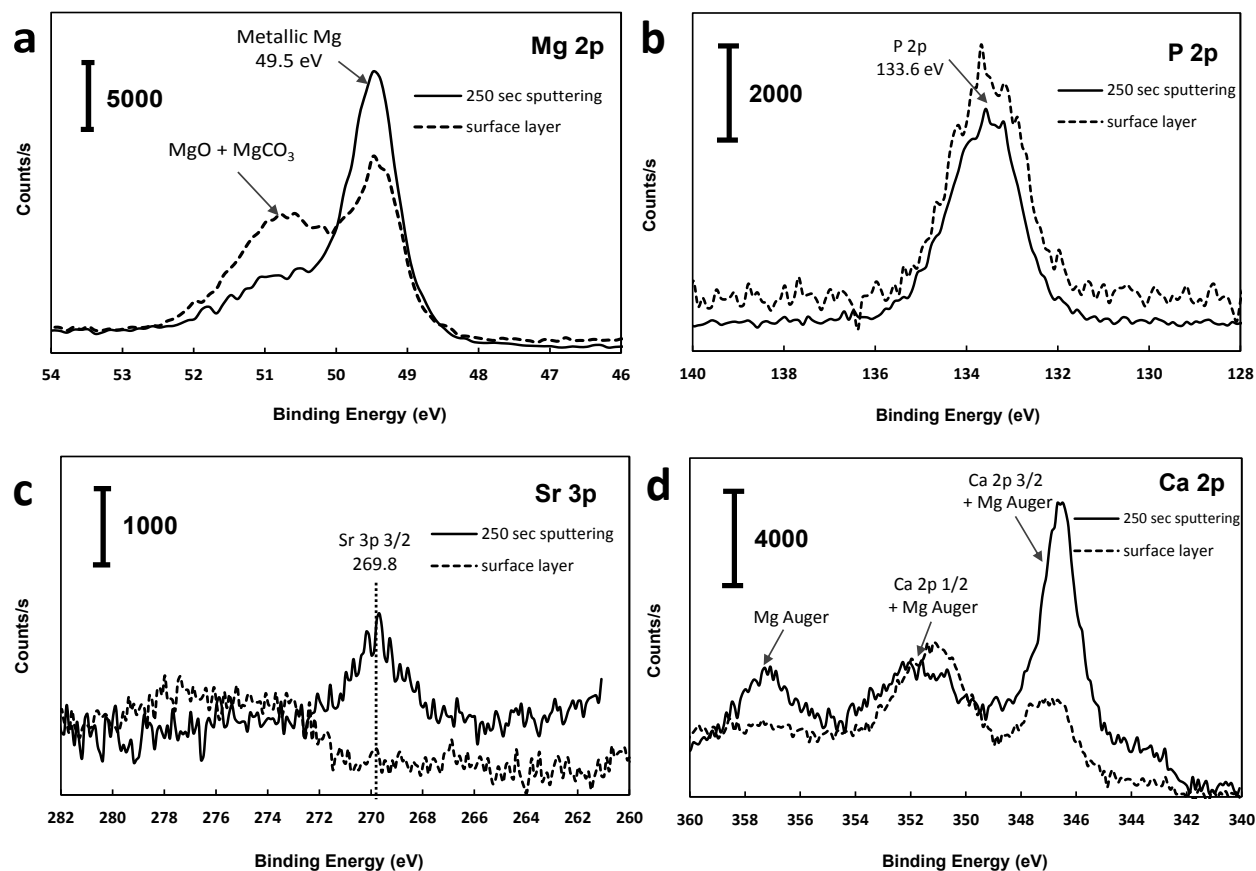


Fig. 6. 3. High resolution XPS spectra of Mg_{2p} , P_{2p} , Sr_{3p} and Ca_{2p} (superimposed with Mg Auger peak) on the surface of Mg-0.3Sr-0.3Ca after 1 day immersion test and removing the corrosion products.

6. 4. 3. Cytotoxicity evaluation

Mg-based materials are promising candidates as biodegradable implants ranging from bone to cardiovascular applications. In this work, we performed indirect cytotoxicity tests on Mg-0.3Sr-0.3Ca and compared with WE43 (previously evaluated as biodegradable Mg stent material in clinical trials [30]) and pure Mg. HUVECs were put in contact with ions extracted from the alloys and Mg after immersion in F-12K. Less Mg^{2+} was released from the alloys than from pure

Mg: the concentration of Mg^{2+} measured via ICP was 0.23 ± 0.05 mg/l in the extract from Mg-0.3Sr-0.3Ca, 0.15 ± 0.03 mg/l in the one from WE43 and 4.46 ± 0.34 mg/l from pure Mg extract, after subtracting the amount of Mg^{2+} present in F-12K [36]. The lower amount of Mg^{2+} released from WE43 could be related to its lower Mg content and/or its slower corrosion rate.

Fig. 6. 4 shows cell viability after exposure for 1, 4 and 7 days to different concentrations of the medium extracted from all the samples. The data is reported as a percentage of what was measured on F-12K, used as control. For all exposure periods, cell viability decreased with increasing extract concentration. This is in agreement with previous observations, which showed that high extraction concentration caused toxicity due to osmotic shock [55, 56]. A ten-fold extract dilution is recommended to evaluate the cytocompatibility of Mg alloys [55]. Severely reduced viability was observed only when cells were exposed to the extract from pure Mg. After 1 day of exposure to extraction medium at any dilution, cells cultured in the extracts from Mg-0.3Sr-0.3Ca and WE43 did not show any reduction in viability (Fig. 6. 4a). Based on the ISO protocol for cytotoxicity evaluation, an extract that allows for above 75% cell viability is considered as non-cytotoxic [12]. However, the viability of the cells cultured in pure Mg extract reduced to ~75% at extract dilutions as low as 50% and 10%. After 4 days (Fig. 6. 4b), the viability of the cells cultured in WE43 and Mg-0.3Sr-0.3Ca extractions was promoted to above 110% at 10% extraction concentration indicating the positive effect of released ions on cells viability and growth and there is no significant differences between them; whereas the viability of cells cultured in extracts from pure Mg dropped to ~60% at 10% concentration. After 7 days (Fig. 6. 4c), the viability of cells cultures in extract from pure Mg stays around 60% at 10% concentration. The viability of the cells cultured in WE43 and Mg-0.3Sr-0.3Ca are significantly higher than cells cultured in pure Mg. The viability of cells cultured in WE43 extractions decreased significantly after 7 days compared to those cultured in Mg-0.3Sr-0.3Ca. No significant differences in viability between 4 and 7 days of culture were observed for cells cultured in the extracts from Mg-0.3Sr-0.3Ca; instead, the viability decreased between 4 and 7 days for cells cultured in WE43 extracts (Fig. 6. 4d).

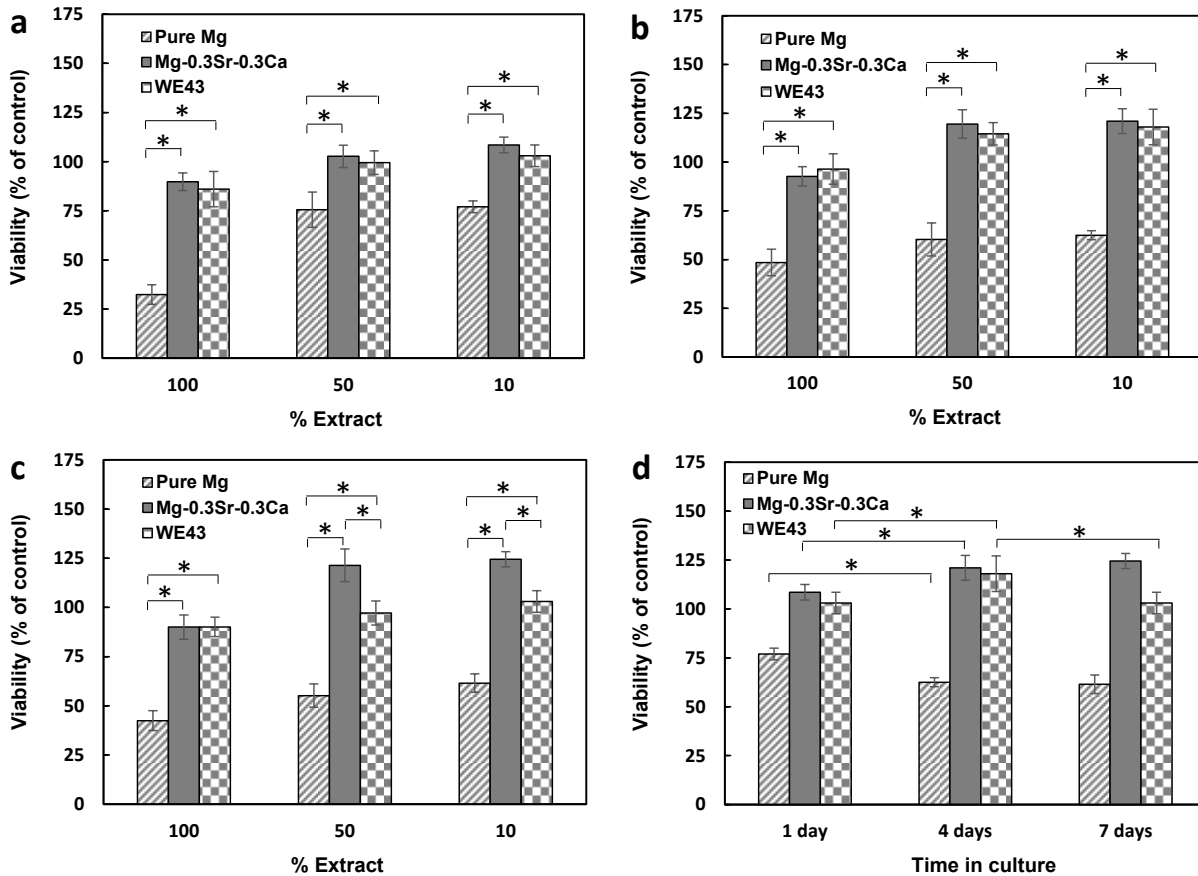


Fig. 6. 4. Cell viability expressed as a percentage of the viability of HUVECs in the control media (F-12K) after (a) 1 day, (b) 4 days and (c) 7 days of exposure to different concentration of extractions obtained from Mg-0.3Sr-0.3Ca, pure Mg and WE43 alloys (* $P < 0.05$). (d) Comparison of viability of HUVECs in contact with 10% extraction medium of Mg-0.3Sr-0.3Ca, pure Mg and WE43 with time of exposure (* $P < 0.05$).

The results show that although the viability of the cells in contact with pure Mg extracts is ~75% on day 1, continued exposure of the cells to this sample extract decreases the viability to 60% at 10% concentration on day 4. This can be attributed to the high concentration of ions released to the medium and increase in pH level resulting from the high degradation rate. The increase in cell viability over time for cells cultured in the extracts from WE43 and Mg-0.3Sr-0.3Ca shows that cells were able to proliferate and grow when in contact with these extract media. The better performance of cells exposed for 7 days to extracts from Mg-0.3Sr-0.3Ca compared to WE43 shows that our proposed alloy is more cytocompatible than WE43. These findings are in line with our recent observations showing the positive influence of low

concentrations of Mg and Sr ions on viability of HUVECs [36]. Li et al [34] observed that ions released from Mg-1Ca to the culture medium promoted cell attachment and increased the proliferation of L-929 cells.

6. 4. 4. Implantation and post-implantation analysis

We examined the performance of Mg-0.3Sr-0.3Ca and WE43 stents implanted in Beagle dog arteries. The femoral artery in which the WE43 stent was implanted became occluded within 5 weeks, whereas the contralateral femoral artery containing the Mg-0.3Sr-0.3Ca stent was completely patent over the same period; Mg-0.3Sr-0.3Ca stent did not cause any sign of occlusion. Fig. 6. 5a & b show the tubular Mg-0.3Sr-0.3Ca stent before and immediately after implantation into the femoral artery. The angiographic study in Fig. 6. 6 showed that WE43 sample thrombosed within 5 weeks of implantation. The stented area of the artery was marked by circle in both Fig. 6. 6a & b. Normal patent blood flow was visible through the stented area in Fig. 6. 6a but “string like” stenosed lumen was visualized in Fig. 6. 6b.

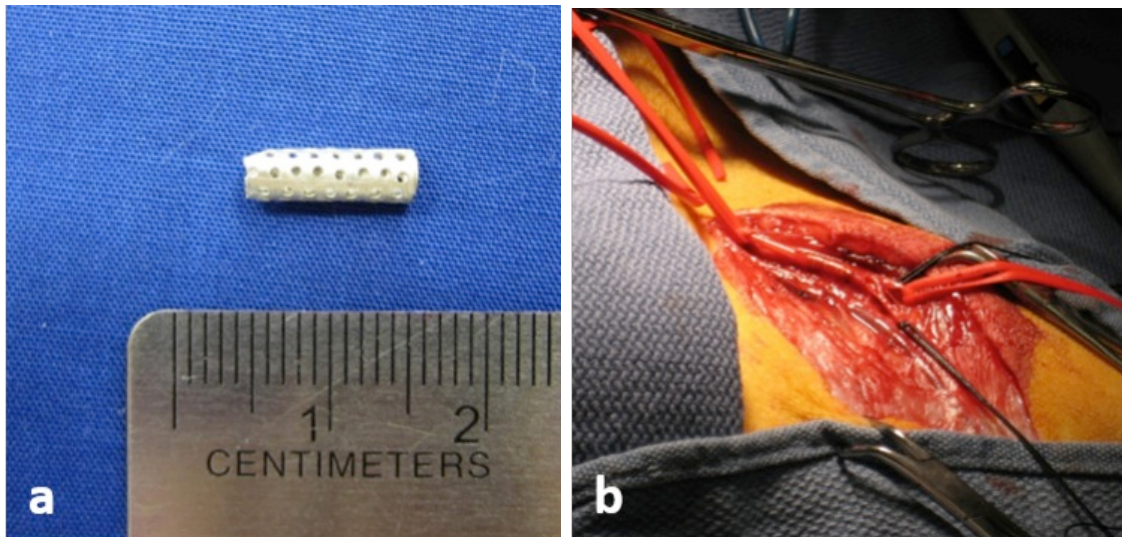


Fig. 6. 5. The tubular Mg-0.3Sr-0.3Ca stent (a) before and (b) after implantation into the right femoral artery of the animal.

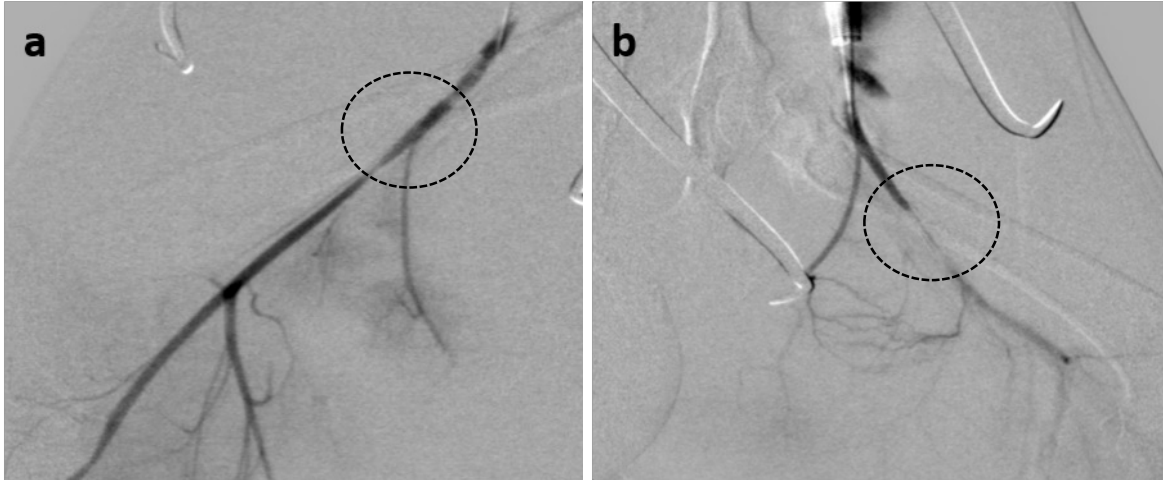


Fig. 6. 6. Artery condition after 5 weeks implantation of (a) Mg-0.3Sr-0.3Ca and (b) WE43 in the right and left femoral artery respectively. The stented area of the artery is marked in the figures. Blood flow is illustrated by epinephrine injection before sacrificing the animal.

Fig. 6. 7 shows the optical and histological images of the cross sections of tubular samples harvested from both femoral arteries implanted with the Mg-0.3Sr-0.3Ca and WE43 stents. Note the occluded lumen and the presence of thrombosis in WE43 (Fig. 6. 7c) versus patent lumen in the Mg-0.3Sr-0.3Ca group (Fig. 6. 7a). These residues are mostly generated during the preparation and staining for histology. The acidity of the stains causes reaction and degradation of thin sections of the metallic stents. The internal wall of Mg-0.3Sr-0.3Ca was covered with a thin layer of cells. These were most likely endothelial cells that prevented thrombosis and blockage of the artery. The non-circular shape of the lumen represented partial distortion inside the stented area generated during cutting and sectioning of the metallic stents. On the other hand, a significant amount of residues and cells was observed around and inside the WE43 stent, and the lumen in this case was mostly blocked. The high population of the cells generated inside the lumen can be attributed to the presence of rare earth elements in this sample that cause foreign body reaction that enhances the cell proliferation and increases the risk of thrombosis. Our cell viability test shows that both Mg-0.3Sr-0.3Ca and WE43 create an environment where HUVECs thrive enhancing endothelialization; however, since WE43 contains rare-earth elements, it is also important to consider the proliferation of cells such as smooth muscle cells (SMC), which can lead to more significant formation of neo-intima on this stent. Drynda et al [58] observed that rare-earth metals at low concentrations do not interfere the proliferation of SMC. However,

higher concentration of these elements induces the mRNA expression of IL-6, IL-8, and ICAM-1, which produces the upregulation of the inflammatory genes and increases the inflammatory processes. This can cause accumulation of leukocytes within the vascular tissue at the stent implantation site that can lead to restenosis and blockage of the stented vessel. Further evaluation on cell viability and gene expression is needed to elucidate the role of rare-earth elements in thrombosis of WE43 stent.

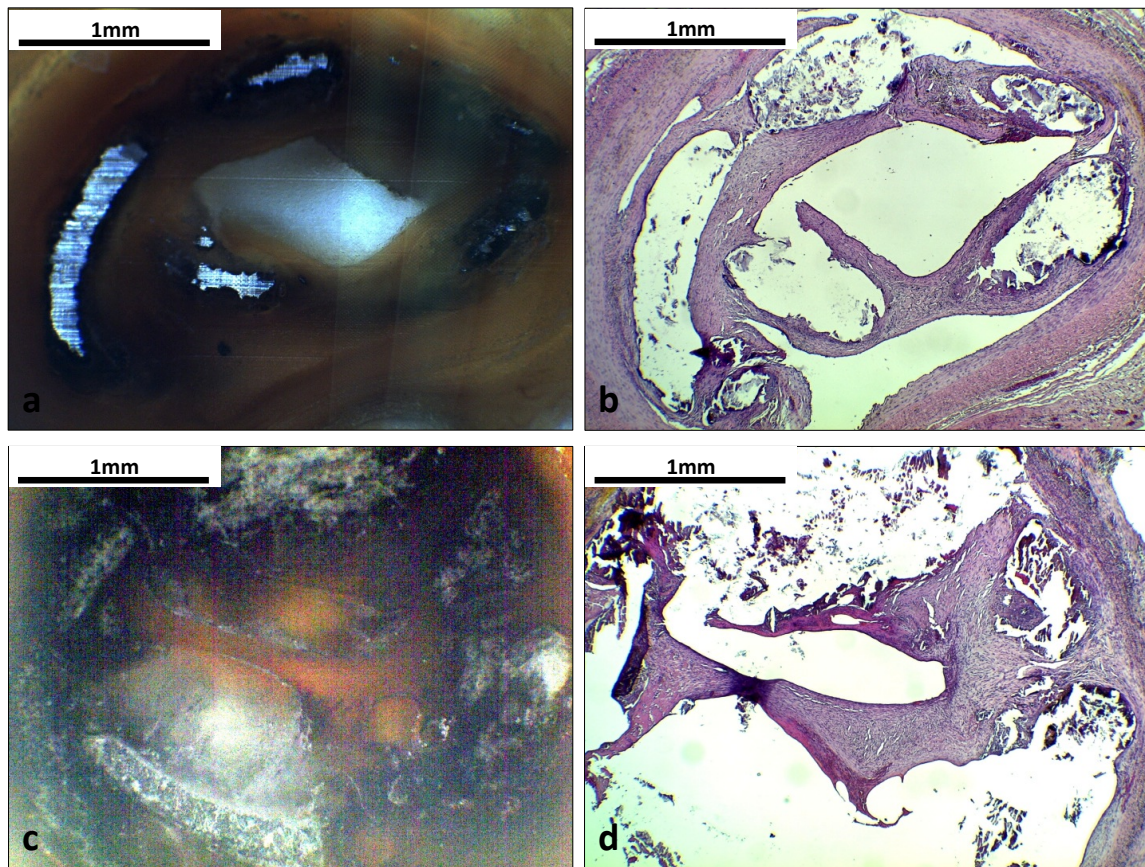


Fig. 6. 7. Optical and histology images (H&E staining) of vascular tissue surrounding (a & b) Mg-0.3Sr-0.3Ca and (c & d) WE43 tubular stent samples implanted in right and left femoral artery for 5 weeks.

Optical images also show that both samples still kept their initial tubular shape 5 weeks after implantation. WE43 stent maintained its initial dimensions and its wall thickness did not change significantly ($\sim 250 \mu\text{m}$) whereas post-implanted Mg-0.3Sr-0.3Ca stent lost part of its wall

thickness from 250 μm to ~ 200 μm . We have seen previously that the wall thickness of a Mg-0.5Sr tubular stent with the same design changed from 270 μm to 130 μm during 3 weeks of implantation, corresponding to a mass loss of 3 mg/day and Sr release of 0.015 mg of Sr/day. The degradation rate of Mg-0.3Sr-0.3Ca is much slower than that of Mg-0.5Sr. The total mass loss over 5 weeks was 0.025 g, corresponding to 0.7 mg/day. Since the stent contains 0.3wt.% Sr, this implies a Sr release of 0.002 mg of Sr/day, which is well below the average intake levels of 4-5 mg/day for Sr [58]. The results indicate that the volume of Mg-0.3Sr-0.3Ca implant has gradually decreased over time with a slow degradation rate. The WE43 stent on the other hand did not show considerable degradation during 5 weeks implantation. Fig. 6. 8 presents the SEM images and EDS elemental maps of Mg-0.3Sr-0.3Ca stent-tissue interface. A Ca-P rich layer just a few nanometers thick formed over the entire stent surface (Fig. 6. 8d & e, and point 3 in Table 6. 4). This scale, which is seen with brighter contrast in Fig. 6. 8a, contains a significant amount of Sr (~ 0.5 wt.%); the Ca+Sr/P ratio measured on point 3 was 1.58, which is very close to that of hydroxyapatite. These results show that also in vivo, Sr-substituted HA has formed at the surface of the stent, similarly to what observed by XPS in vitro. Point 1 was on the bulk of the stent, and the composition was what expected for the Mg-0.3Sr-0.3Ca alloy (Ca ~ 0.27 wt.% and Sr ~ 0.23 wt.%). MgO can be seen as reaction product commonly occurring when Mg is exposed to ambient atmosphere, which can take place before implantation. In fact, MgO was observed on the regions closer to the surface (Mg/O ratio ~ 1 shown by EDS in point 2). Higher amounts of Ca and Sr were detected at the region close to the surface of Mg-0.3Sr-0.3Ca (~ 0.8 wt.% Sr at point 2), which is in agreement with the results obtained by XPS, showing the surface-active nature of these elements. Points 4 and 5 are obtained from the tissue embedded in epoxy with significant amount of osmium (Os ~ 34 wt.%). Points 6 and 8 show high amount of Ca, P and O. This can be attributed to the presence of Ca-rich compounds such as $\text{Ca}(\text{OH})_2$ and HA. Point 7 shows high amount of Ca, P, Mg and O, which implies the presence of both MgO and HA.

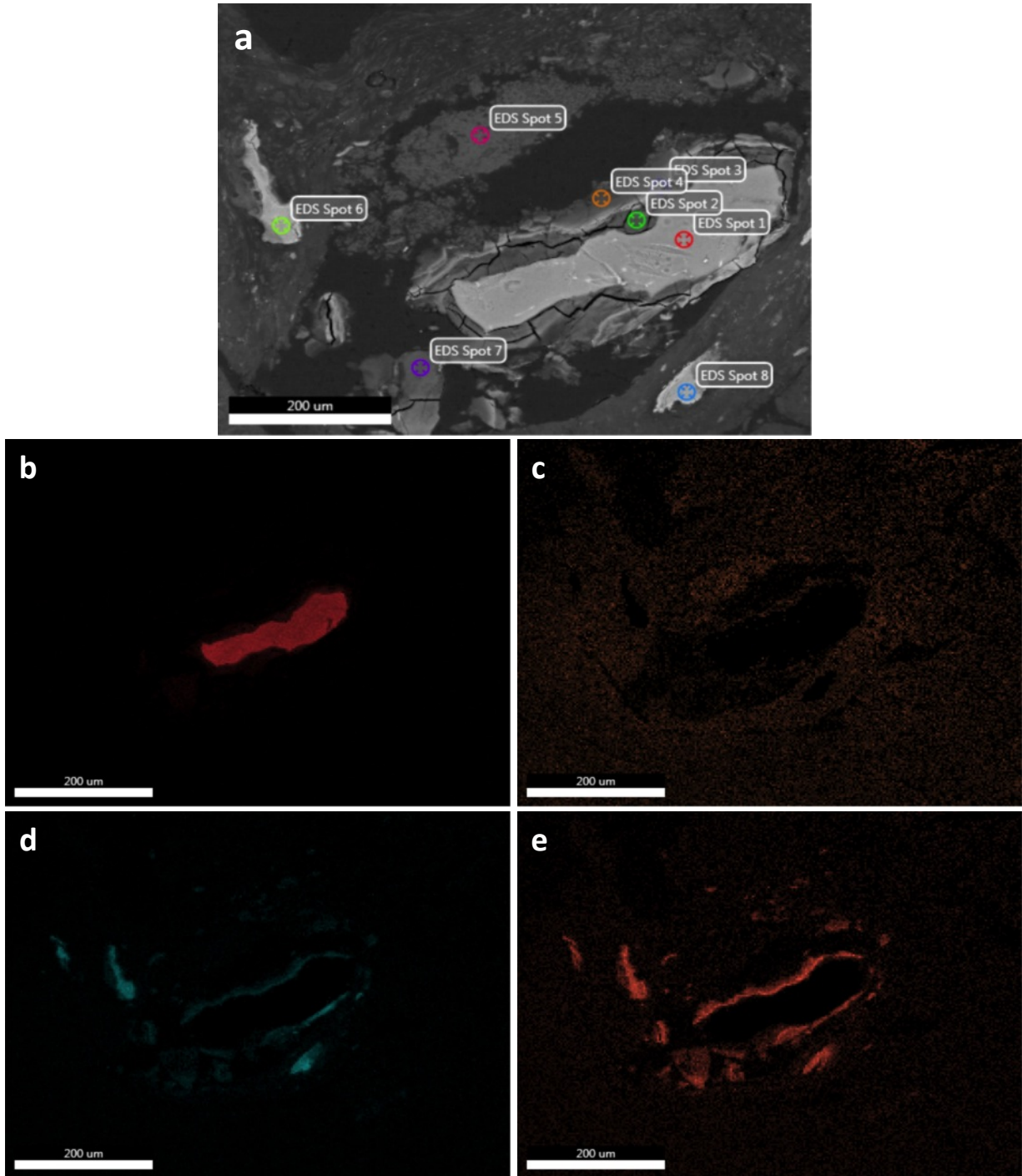


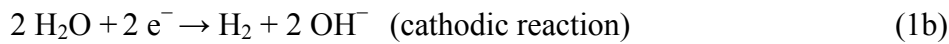
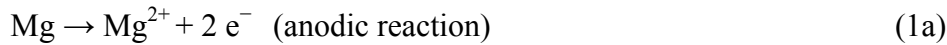
Fig. 6. 8. (a) SEM image and EDS mapping of elemental distribution for (b) Mg, (c) O, (d) Ca, and (e) P at the interface of Mg-0.3Sr-0.3Ca and its surrounding tissue after 5 weeks implantation (EDS compositional analysis obtained from different points is shown in Table 6. 4).

Table 6. 4: EDS compositional analysis obtained from of different regions at the interface of the tubular Mg-0.3Sr-0.3Ca stent and its surrounding tissue after 5 weeks implantation at right femoral artery (spots marked from 1 to 8 in Fig. 6. 8)

Mg-0.3Sr-0.3Ca EDS spots	Chemical composition (wt. %)						
	C	O	Mg	P	Ca	Sr	Os
Spot 1	0.89	18.01	76.44	0.0	0.27	0.23	0.19
Spot 2	1.43	42.34	40.79	1.12	3.54	0.80	1.63
Spot 3	0.0	47.4	18.12	12.04	18.26	0.53	0.33
Spot 4	1.83	3.56	1.02	8.34	9.37	1.90	33.64
Spot 5	0.02	3.31	0.25	6.98	5.99	1.97	33.86
Spot 6	0.0	28.47	1.45	13.19	52.73	0.38	0.38
Spot 7	0.0	23.56	15.44	8.87	17.36	1.07	5.43
Spot 8	0.0	24.74	0.0	6.55	65.30	0.61	0.83

6. 5. BIOCORROSION MECHANISM

The equations that are used to explain the corrosion reaction of pure Mg are the following [45, 59]:



These three reactions can be summarized as following electrochemical reaction:



Here, we also refer to these reactions since Mg is the main component in Mg-0.3Sr-0.3Ca alloy. However, we propose a more complete mechanism of degradation of Mg-0.3Sr-0.3Ca upon immersion in SBF based on the current in vitro and in vivo observations (Fig. 6. 9):

- a) Since Sr is surface active in Mg, a significant amount of Sr exists on the surface of the alloy before immersion. When the surface of the alloy is exposed to aqueous solutions, microgalvanic corrosion accrues and Mg dissolution starts (Fig. 6. 9a), releasing both Mg^{2+} and H_2 and increasing OH^{-} concentration in the solution. At the same time some Sr^{2+} is released in solution.

- b) At the same time, the continuous dissolution of Mg and the increase in OH^- ions in solution leads to the formation of $\text{Mg}(\text{OH})_2$ on the surface, which can partially protect it (Fig. 6. 9b). A dissolution-precipitation mechanism is involved in the growth of $\text{Mg}(\text{OH})_2$ layer in aqueous solution [60].
- c) The presence of Cl^- in physiological environments changes the equilibrium of this mechanism by reacting with Mg^{2+} and producing MgCl_2 , which is highly soluble in water. This implies that the $\text{Mg}(\text{OH})_2$ scale is not protective in physiological environment and the degradation continues. This exposes fresh Mg sample to SBF and shifts the corrosion reaction interphase inward (Fig. 6. 9c).
- d) The formation of $\text{Mg}(\text{OH})_2$ on the alloy surface (Fig. 6. 9b) and their re-dissolution (Fig. 6. 9c) continue as dynamic process until a protective layer is formed (Fig. 6. 9d). The increase in pH leads to supersaturation of the solution with respect to HA [61]. The $\text{Mg}(\text{OH})_2$ layer formed on the surface can act as nucleation site for HA [62]. The presence of Sr on the surface of the alloy and in solution leads to the formation of a thin Sr-substituted HA layer on the surface of Mg-0.3Sr-0.3Ca, which is strongly bound to the surface (Fig. 6. 9d, and see Fig. 6. 3 and Table 6. 3).
- e) HA continues to grow consuming Ca^{2+} and PO_4^{3-} ions from the solution. A compact layer is formed, which uniformly covers the surface, due to the presence of the interfacial layer of Sr-substituted HA. This compact and protective scale slows down the diffusion of ionic species to and from the alloy, thus slowing down its degradation (Fig. 6. 9e).

In Mg alloys with a two-phase structure, as the degradation continues, chunks and residues can disintegrate from the bulk and be released into the surrounding environment due to the microgalvanic corrosion between the α -Mg matrix and second phases in the grain boundaries [34]. However, this is not observed for the Mg-0.3Sr-0.3Ca alloy, most likely because of the fine, homogenous and intragranular distribution of the Ca-Sr phase. This phase forms at the expense of the coarse intergranular Mg_2Ca and $\text{Mg}_{17}\text{Sr}_2$ phases; its presence in the microstructure minimizes microgalvanic corrosion and reduces particle separation from the bulk. This is reflected in the lower mass loss of the Mg-0.3Sr-0.3Ca alloy compared to Mg-Sr and Mg-Ca binary alloys possessing coarse intermetallic phases.

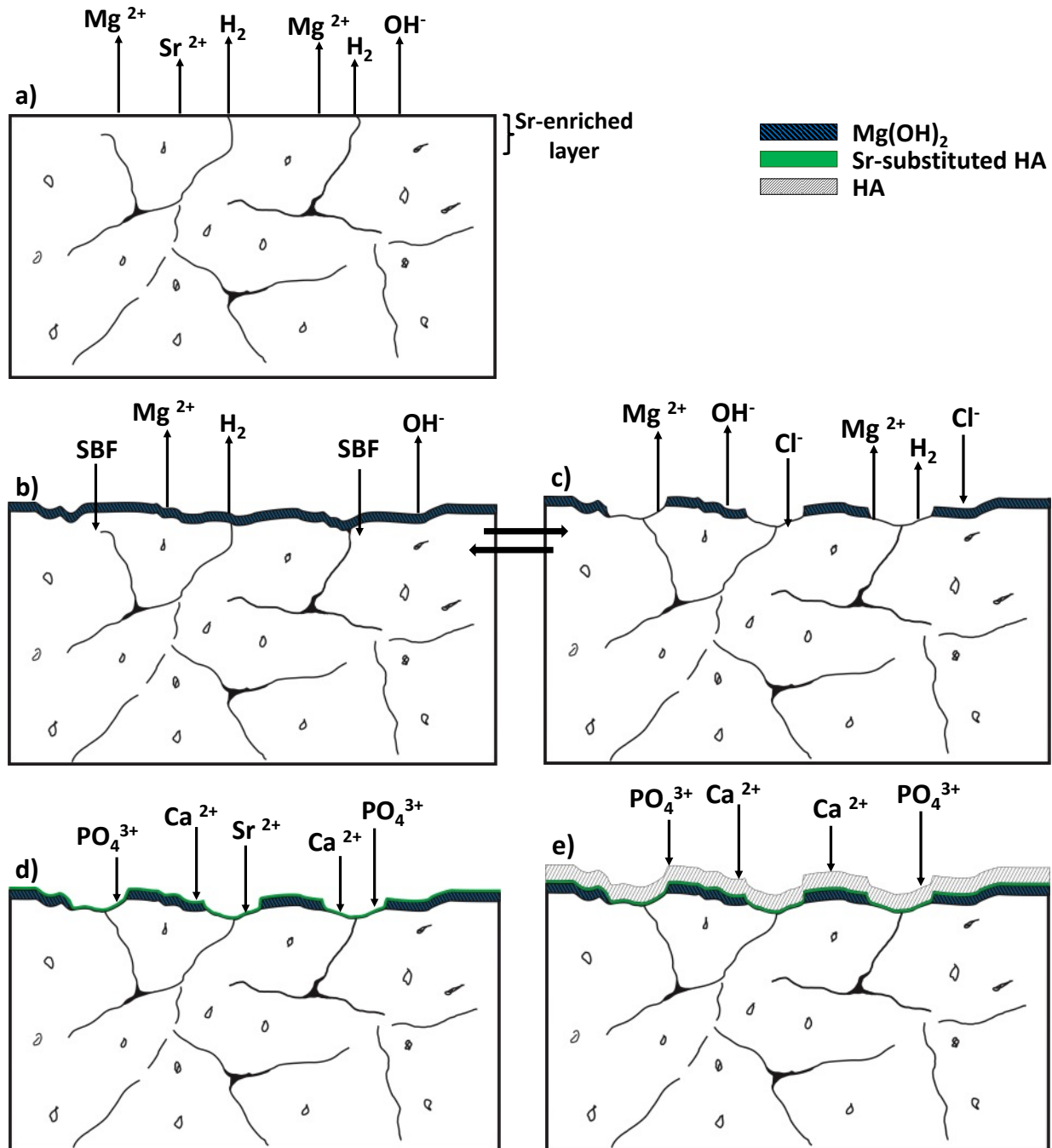


Fig. 6. 9. Schematic presentation of the Mg-0.3Sr-0.3Ca alloy biocorrosion interface in physiological environment: a) galvanic corrosion and Mg dissolution; b) formation of partially protective layer of $Mg(OH)_2$; c) diffusion of Cl^- ions and inward shift of corrosion interface, thus creating a dynamic scale formation/dissolution equilibrium with b); d) Sr-substituted HA formation; and e) formation of a compact and homogenous layer of HA on the surface. The thickness of the layers is exaggerated to better visualize the mechanism.

6. 6. CONCLUSIONS

We have studied the degradation mechanism of Mg-0.3Sr-0.3Ca via interrupted corrosion tests in SBF and immersion tests with daily SBF renewal to prevent an artificial increase in pH. We studied the nature of the protective scale formed on the alloy upon immersion in SBF by Raman and XPS, and evaluated its *in vitro* and *in vivo* biocompatibility of the alloy to test its applicability in temporary cardiovascular implants.

The results provide important insights:

1. The degradation rate of Mg-0.3Sr-0.3Ca did not significantly change with or without daily SBF renewal. This confirms the minor effect of pH increase on the alloy degradation, and the protective role of the scale formed on the surface of this alloy upon immersion in SBF, which acts as barrier and slows down degradation.
2. The corrosion products on the surface of Mg-0.3Sr-0.3Ca are strongly bound to the surface and provide a compact and homogeneous layer that stabilizes the alloy. This is due to the formation of a Sr-substituted HA on this sample. The formation of Sr-HA is a key advantage in the use of Sr-containing Mg alloys as materials for biodegradable implants due to the surface active nature of Sr.
3. Both *in vitro* cytocompatibility tests and *in vivo* implantation show that Mg-0.3Sr-0.3Ca is biocompatible: the ions released by the alloy actually improve the viability of HUVECs after 7 days of exposure, and a tubular stent made of Mg-0.3Sr-0.3Ca does not cause any thrombosis after 5 weeks of implantation in the femoral artery of a dog, allowing for healthy blood flow.
4. A Sr-HA scale is found on the surface of the stent after removing it from the dog artery. This finding shows that the protective Sr-HA layer is formed not only *in vitro*, but also *in vivo*.

6. 7. REFERENCES

- [1] Staiger MP, Pietak AM, Huadmai J, Dias G. Magnesium and its alloys as orthopedic biomaterials: A review. *Biomaterials*. 2006;27:1728-34.
- [2] Kannan MB, Raman RKS. In vitro degradation and mechanical integrity of calcium-containing magnesium alloys in modified-simulated body fluid. *Biomaterials*. 2008;29:2306-14.
- [3] Witte F, Fischer J, Nellesen J, Crostack HA, Kaese V, Pisch A, et al. In vitro and in vivo corrosion measurements of magnesium alloys. *Biomaterials*. 2006;27:1013-8.
- [4] Witte F. The history of biodegradable magnesium implants: A review. *Acta Biomaterialia*. 2010;6:1680-92.
- [5] Kirkland NT, Birbilis N, Staiger MP. Assessing the corrosion of biodegradable magnesium implants: A critical review of current methodologies and their limitations. *Acta Biomaterialia*. 2012;8:925-36.
- [6] Kraus T, Fischerauer SF, Haenzi AC, Uggowitzer PJ, Loeffler JF, Weinberg AM. Magnesium alloys for temporary implants in osteosynthesis: In vivo studies of their degradation and interaction with bone. *Acta Biomaterialia*. 2012;8:1230-8.
- [7] Zeng R, Dietzel W, Witte F, Hort N, Blawert C. Progress and challenge for magnesium alloys as biomaterials. *Advanced Engineering Materials*. 2008;10:B3-B14.
- [8] Gu XN, Zhou WR, Zheng YF, Cheng Y, Wei SC, Zhong SP, et al. Corrosion fatigue behaviors of two biomedical Mg alloys-AZ91D and WE43-In simulated body fluid. *Acta Biomaterialia*. 2010;6:4605-13.
- [9] Heublein B, Rohde R, Kaese V, Niemeyer M, Hartung W, Haverich A. Biocorrosion of magnesium alloys: a new principle in cardiovascular implant technology? *Heart*. 2003;89:651-6.
- [10] Yaremchuk MJ, Fiala TGS, Barker F, Ragland R. The effects of rigid fixation on craniofacial growth of rhesus-monkeys. *Plastic and Reconstructive Surgery*. 1994;93:1-10.
- [11] Gilardino MS, Chen E, Bartlett SP. Choice of internal rigid fixation materials in the treatment of facial fractures. *Craniofacial trauma & reconstruction*. 2009;2:49-60.
- [12] Hong D, Saha P, Chou D-T, Lee B, Collins BE, Tan Z, et al. In vitro degradation and cytotoxicity response of Mg-4% Zn-0.5% Zr (ZK40) alloy as a potential biodegradable material. *Acta Biomaterialia*. 2013;9:8534-47.

- [13] Kuhlmann J, Bartsch I, Willbold E, Schuchardt S, Holz O, Hort N, et al. Fast escape of hydrogen from gas cavities around corroding magnesium implants. *Acta Biomaterialia*. 2013;9:8714-21.
- [14] Brar HS, Ball JP, Berglund IS, Allen JB, Manuel MV. A study of a biodegradable Mg-3Sc-3Y alloy and the effect of self-passivation on the in vitro degradation. *Acta Biomaterialia*. 2013;9:5331-40.
- [15] Haenzi AC, Gerber I, Schinhammer M, Loeffler JF, Uggowitzer PJ. On the in vitro and in vivo degradation performance and biological response of new biodegradable Mg-Y-Zn alloys. *Acta Biomaterialia*. 2010;6.
- [16] Waksman R, Pakala R, Kuchulakanti PK, Baffour R, Hellinga D, Seabron R, et al. Safety and efficacy of bioabsorbable magnesium alloy stents in porcine coronary arteries. *Catheterization and Cardiovascular Interventions*. 2006;68:607-17.
- [17] Zartner P, Cesnjevar R, Singer H, Weyand M. First successful implantation of a biodegradable metal stent into the left pulmonary artery of a preterm baby. *Catheterization and Cardiovascular Interventions*. 2005;66:590-4.
- [18] Erne P, Schier M, Resink TJ. The road to bioabsorbable stents: Reaching clinical reality? *Cardiovascular and Interventional Radiology*. 2006;29:11-6.
- [19] Witte F, Kaese V, Haferkamp H, Switzer E, Meyer-Lindenberg A, Wirth CJ, et al. In vivo corrosion of four magnesium alloys and the associated bone response. *Biomaterials*. 2005;26:3557-63.
- [20] Song Y, Shan D, Chen R, Zhang F, Han E-H. Biodegradable behaviors of AZ31 magnesium alloy in simulated body fluid. *Materials Science & Engineering C-Biomimetic and Supramolecular Systems*. 2009;29:1039-45.
- [21] Hassel T, Bach F-W, Golovko A, Krause C. Investigation of the mechanical properties and the corrosion behavior of low alloyed magnesium-calcium-alloys for use as absorbable biomaterial in the implant technique. In: Pegguleryuz M, Mackenzie L, editors. 45th Annual Conference of Metallurgists of CIM. Montreal: Magnesium Technology in the Global Age; 2006. p. 359.
- [22] Moravej M, Mantovani D. Biodegradable Metals for Cardiovascular Stent Application: Interests and New Opportunities. *International Journal of Molecular Sciences*. 2011;12:4250-70.

- [23] Yang L, Huang Y, Feyerabend F, Willumeit R, Mendis C, Kainer KU, et al. Microstructure, mechanical and corrosion properties of Mg-Dy-Gd-Zr alloys for medical applications. *Acta Biomaterialia*. 2013;9:8499-508.
- [24] Hort N, Huang Y, Fechner D, Stoermer M, Blawert C, Witte F, et al. Magnesium alloys as implant materials - Principles of property design for Mg-RE alloys. *Acta Biomaterialia*. 2010;6:1714-25.
- [25] Li Y, Wen C, Mushahary D, Sravanthi R, Harishankar N, Pande G, et al. Mg-Zr-Sr alloys as biodegradable implant materials. *Acta biomaterialia*. 2012;8:3177-88.
- [26] Zhang S, Zhang X, Zhao C, Li J, Song Y, Xie C, et al. Research on an Mg-Zn alloy as a degradable biomaterial. *Acta Biomaterialia*. 2010;6:626-40.
- [27] Gu XN, Zheng W, Cheng Y, Zheng YF. A study on alkaline heat treated Mg-Ca alloy for the control of the biocorrosion rate. *Acta Biomaterialia*. 2009;5:2790-9.
- [28] Gu XN, Xie XH, Li N, Zheng YF, Qin L. In vitro and in vivo studies on a Mg-Sr binary alloy system developed as a new kind of biodegradable metal. *Acta Biomaterialia*. 2012;8:14.
- [29] Witte F, Hort N, Vogt C, Cohen S, Kainer KU, Willumeit R, et al. Degradable biomaterials based on magnesium corrosion. *Current Opinion in Solid State & Materials Science*. 2008;12:63-72.
- [30] Peuster M, Beerbaum P, Bach FW, Hauser H. Are resorbable implants about to become a reality? *Cardiology in the Young*. 2006;16:107-16.
- [31] Nielsen SP. The biological role of strontium. *Bone*. 2004;35:583-8.
- [32] Ilich JZ, Kerstetter JE. Nutrition in bone health revisited: A story beyond calcium. *Journal of the American College of Nutrition*. 2000;19.
- [33] Serre CM, Papillard M, Chavassieux P, Voegel JC, Boivin G. Influence of magnesium substitution on a collagen-apatite biomaterial on the production of a calcifying matrix by human osteoblasts. *Journal of Biomedical Materials Research*. 1998;42:626-33.
- [34] Li Z, Gu X, Lou S, Zheng Y. The development of binary Mg-Ca alloys for use as biodegradable materials within bone. *Biomaterials*. 2008;29:1329-44.
- [35] Wang J, Wang L, Guan S, Zhu S, Ren C, Hou S. Microstructure and corrosion properties of as sub-rapid solidification Mg-Zn-Y-Nd alloy in dynamic simulated body fluid for vascular stent application. *Journal of Materials Science-Materials in Medicine*. 2010;21:2001-8.

- [36] Bornapour M, Muja N, Shum-Tim P, Cerruti M, Pekguleryuz M. Biocompatibility and biodegradability of Mg-Sr alloys: The formation of Sr-substituted hydroxyapatite. *Acta Biomaterialia*. 2013;9:5319-30.
- [37] Kung K-C, Lee T-M, Lui T-S. Bioactivity and corrosion properties of novel coatings containing strontium by micro-arc oxidation. *Journal of Alloys and Compounds*. 2010;508:384-90.
- [38] Pramatarova L, Pecheva E, Presker R, Pham MT, Maitz MF, Stutzmann M. Hydroxyapatite growth induced by native extracellular matrix deposition on solid surfaces. *European cells & materials*. 2005;9:9-12.
- [39] Gu Y, Liao D, Zhou Z. The experimental study of Sr-HAP on reconstructing mandibular bone defect. *Zhonghua kou qiang yi xue za zhi = Zhonghua kouqiang yixue zazhi = Chinese journal of stomatology*. 2001;36:262-5.
- [40] Suganthi RV, Elayaraja K, Joshy MIA, Chandra VS, Girija EK, Kalkura SN. Fibrous growth of strontium substituted hydroxyapatite and its drug release. *Materials Science & Engineering C-Materials for Biological Applications*. 2011;31:593-9.
- [41] Bornapour M, Celikin M, Cerruti M, Pekguleryuz M. Magnesium implant alloy with low levels of strontium and calcium: The third element effect and phase selection improve bio-corrosion resistance and mechanical performance. *Materials Science & Engineering C-Materials for Biological Applications*. 2014;35:267-82.
- [42] Bornapour M, Celikin M, Pekguleryuz M. Thermal exposure effects on the in-vitro degradation and mechanical properties of Mg-Sr and Mg-Ca-Sr biodegradable implant alloys and the role of the microstructure. *Materials Science & Engineering C-Materials for Biological Applications*. 2014.
- [43] Barth KH, Virmani R, Froelich J, Takeda T, Lossef SV, Newsome J, et al. Paired comparison of vascular wall reactions to Palmaz stents, Strecker tantalum stents, and Wallstents in canine iliac and femoral arteries. *Circulation*. 1996;93:2161-9.
- [44] Salam TA, Taylor B, Suggs WD, Hanson SR, Lumsden AB. Reaction to injury following balloon angioplasty and intravascular stent placement in the canine femoral-artery. *American Surgeon*. 1994;60:353-7.

- [45] Song G, Song S. Magnesium as a possible degradable bio-compatible material. In: Pekguleryuz M, Mackenzie L, editors. 45th Annual Conference of Metallurgists of CIM. Montreal: Magnesium Technology in the Global Age; 2006. p. 359.
- [46] Yang L, Zhang E. Biocorrosion behavior of magnesium alloy in different simulated fluids for biomedical application. *Materials Science & Engineering C-Biomimetic and Supramolecular Systems*. 2009;29.
- [47] Li ZY, Lam WM, Yang C, Xu B, Ni GX, Abbah SA, et al. Chemical composition, crystal size and lattice structural changes after incorporation of strontium into biomimetic apatite. *Biomaterials*. 2007;28:1452-60.
- [48] Eimar H, Siciliano R, Abdallah M-N, Nader SA, Amin WM, Martinez P-P, et al. Hydrogen peroxide whitens teeth by oxidizing the organic structure. *Journal of Dentistry*. 2012;40:E25-E33.
- [49] O'Donnell MD, Fredholm Y, de Rouffignac A, Hill RG. Structural analysis of a series of strontium-substituted apatites. *Acta Biomaterialia*. 2008;4:1455-64.
- [50] Wang L, Shinohara T, Zhang B-P. XPS study of the surface chemistry on AZ31 and AZ91 magnesium alloys in dilute NaCl solution. *Applied Surface Science*. 2010;256:5807-12.
- [51] Han Y, Zhou J, Zhang L, Xu K. A multi-scaled hybrid orthopedic implant: bone ECM-shaped Sr-HA nanofibers on the microporous walls of a macroporous titanium scaffold. *Nanotechnology*. 2011;22.
- [52] Vandoveren H, Verhoeven JAT. XPS spectra of Ca, Sr, Ba and their oxides. *Journal of Electron Spectroscopy and Related Phenomena*. 1980;21:265-73.
- [53] Seyama H, Soma M. X-ray photoelectron spectroscopic study of montmorillonite containing exchangeable divalent-cations. *Journal of the Chemical Society-Faraday Transactions I*. 1984;80:237-48.
- [54] Sosulnikov MI, Teterin YA. X-ray photoelectron studies of Ca, Sr and Ba and their oxides and carbonates. *Journal of Electron Spectroscopy and Related Phenomena*. 1992;59:111-26.
- [55] Fischer J, Proefrock D, Hort N, Willumeit R, Feyerabend F. Improved cytotoxicity testing of magnesium materials. *Materials Science and Engineering B-Advanced Functional Solid-State Materials*. 2011;176:830-4.

- [56] Chou D-T, Hong D, Saha P, Ferrero J, Lee B, Tan Z, et al. In vitro and in vivo corrosion, cytocompatibility and mechanical properties of biodegradable Mg-Y-Ca-Zr alloys as implant materials. *Acta Biomaterialia*. 2013;9:8518-33.
- [57] Drynda A, Deinet N, Braun N, Peuster M. Rare earth metals used in biodegradable magnesium-based stents do not interfere with proliferation of smooth muscle cells but do induce the upregulation of inflammatory genes. *Journal of Biomedical Materials Research Part A*. 2009;91A:360-9.
- [58] Kirkland NT, Staiger MP, Nisbet D, Davies CHJ, Birbilis N. Performance-driven design of Biocompatible Mg alloys. *Jom*. 2011;63:28-34.
- [59] Song G. Control of biodegradation of biocompatible magnesium alloys. *Corrosion Science*. 2007;49:1696-701.
- [60] Nordlien JH, Ono S, Masuko N, Nisancioglu K. A TEM investigation of naturally formed oxide films on pure magnesium. *Corrosion Science*. 1997;39:1397-414.
- [61] Jonasova L, Muller FA, Helebrant A, Strnad J, Greil P. Biomimetic apatite formation on chemically treated titanium. *Biomaterials*. 2004;25:1187-94.
- [62] Kokubo T. Formation of biologically active bone-like apatite on metals and polymers by a biomimetic process. *Thermochimica Acta*. 1996;280:479-90.

CHAPTER 7

CONCLUSIONS AND RECOMMENDATIONS FOR FUTURE WORK

The objective of this PhD study was to develop a new biodegradable Mg alloy to be used as a temporary cardiovascular stent. It also aimed to understand the effect of Sr addition on the corrosion mechanism of Mg alloy in physiological condition. The degradation behavior of Mg, Mg-Sr and Mg-Ca-Sr alloys was investigated by in vitro corrosion tests. The study also evaluated the mechanical properties of the candidate alloys. The role of Sr was investigated and the biocompatibility of candidate Mg-Sr and Mg-Ca-Sr alloys was evaluated via cell viability in in vitro tests and in vivo animal studies. The key conclusions of this doctoral study are presented in Section 7.1. Additionally, Section 7.2 gives suggestions for future work.

7. 1. CONCLUSIONS

A. Biodegradation, microstructure and biocompatibility of Mg-Sr alloys

This study contained the synthesis of Mg-Sr binary alloys via casting and the corrosion evaluation in physiological condition. Following this, microstructural analysis and surface characterization were carried out to understand the corrosion mechanism and the effect of Sr on the degradation behavior of Mg implants.

1. Among the Mg-(0.3-2.5 wt.%) Sr binary alloys, those containing less than 1 wt.% Sr have slower degradation rate in simulated body fluid (SBF) than pure Mg. Mg-0.5Sr shows the lowest degradation rate in this range of composition. The addition of more than 1 wt.% Sr accelerates the degradation rate under the same environmental condition.
2. The binary Mg-Sr phase diagram indicates the presence of α -Mg matrix and secondary phases of $\text{Mg}_{17}\text{Sr}_2$ (β) at room temperature for alloys in this range of composition. The difference between corrosion potential of these regions leads to the formation of micro-galvanic couples and increases the corrosion rate. The rapid corrosion of the Mg-Sr alloys

with more than 1 wt.% Sr and substantial amounts of $Mg_{17}Sr_2$ is attributed to the formation of a large amount of anodic regions for galvanic cells.

3. Corrosion products on the surface of Mg-0.5Sr are more adherent and compact compared to that of pure Mg. The morphology of the corrosion product varies from needle-like in pure Mg to globular in Mg-0.5Sr. $Mg(OH)_2$ and hydroxyapatite forms on the surface of Mg-0.5Sr after immersion in SBF.
4. A Sr-substituted HA layer forms on the surface of Mg-0.5Sr during bio-corrosion in SBF. This is due to the dissolution of Sr^{2+} ions from the alloy and their precipitation as Sr-HA. The formation of this modified layer slows down the degradation of this alloy in physiological conditions.
5. Mg-0.5Sr extraction media do not cause any toxicity and detrimental effects on the viability of HUVECs after 7 days of exposure.
6. Mg-0.5Sr does not cause any thrombosis after 3 weeks of implantation into the femoral artery of an animal.
7. The amount of Sr release from Mg-0.5Sr during in vitro corrosion test is 0.01mg/day. The stent sample made of this alloy has a Sr release of 0.015mg/day during 3 weeks implantation, which is well below the allowed limits of 4–5mg/day.

B. Effect of combined addition of Sr and Ca on bio-corrosion, microstructure and mechanical properties of Mg

Two binary samples of Mg-0.5Sr and Mg-0.6Ca were selected as base alloys and two ternary alloys of Mg-0.3Sr-0.3Ca and Mg-0.5Sr-0.6Ca were designed and synthesized via casting. The combined effect of Ca and Sr on the corrosion behavior of Mg was studied via in vitro immersion and electrochemical tests in SBF. The microstructure, surface and mechanical properties of alloys were analyzed to study the effect of the simultaneous addition of Sr and Ca on the biodegradation of Mg. In addition, the effect of thermal exposure was investigated to assess the stability of the microstructure and the retention of the properties during fabrication and service required for implant applications.

8. The combined addition of Sr and Ca in small amounts increases the corrosion resistance of Mg in physiological conditions more than the single additions of Sr or Ca. The degradation

rate of Mg-0.3Sr-0.3Ca in SBF is 90% lower than that of pure Mg, and the pH value of SBF containing the Mg-0.3Sr-0.3Ca increases very slowly compared to the other alloys.

9. High levels of Sr and Ca in Mg-0.5Sr-0.6Ca alloy increase the corrosion rate of Mg due to a significant micro-galvanic effect. A non-adherent surface scale forms on the surface of this alloy, which easily detaches and does not act as a barrier layer.
10. The “third element (i.e., Sr) effect” reduces the amount at which Ca becomes effective in improving the corrosion resistance of Mg-Ca-Sr (0.3 wt.%Ca in the ternary Mg-Sr-Ca system versus 0.6 wt.% in binary Mg-Ca system).
11. A new binary Ca/Sr phase is observed in the Mg-0.5Sr-0.6Ca alloy in the as-cast condition; TEM analysis shows that this phase has a hexagonal close-packed structure.
12. The slow degradation rate of Mg-0.3Sr-0.3Ca is attributed to two factors:
 - (i) The formation of globular Ca/Sr phases in the microstructure of the alloy. These phases are observed both at the grain boundaries and in the grain interior, and are able to slow down the dissolution of the alloy by decreasing the difference in corrosion potential between the Mg matrix and the grain boundaries;
 - (ii) The formation of a very compact layer of corrosion product consisting of hydroxyapatite and Mg(OH)₂ on the surface after 1 day immersion in SBF.
13. Mg-0.3Sr-0.3Ca also shows the highest tensile and bending properties, as well as higher ductility among binary and ternary samples tested in this study, due to the presence of the new Ca/Sr phase.
14. Mg-0.3Sr-0.3Ca keeps its mechanical strength and slow degradation rate after 8h heat treatment at 400 °C as opposed to Mg-0.5Sr. Longer heat treatment at this temperature transforms the globular Ca/Sr-rich phase present in the as-cast condition of Mg-0.3Sr-0.3Ca towards equilibrium phases, which leads to some loss in the corrosion resistance and mechanical properties of the alloy.
15. Processing that can be achieved at lower temperatures and in shorter times would largely maintain the advantageous properties of Mg-0.3Sr-0.3Ca alloy and make it a good candidate for biodegradable implant applications. Longer heat treatment processes increase the degradation rate of this alloy and care should be taken to optimize the time and temperature of the processing to achieve the desired properties.

C. Understanding the surface scale that forms on the Mg-0.3Sr-0.3Ca alloy under physiological conditions

The degradation behavior of Mg-0.3Sr-0.3Ca in simulated body fluid (SBF) was studied via immersion tests with and without SBF renewal to evaluate the effect of pH increase and corrosion product formation on the degradation rate of this sample. Following this, in-depth surface characterization (XPS and Raman) was carried out to investigate the role of Sr addition on the biodegradation behavior of Mg-0.3Sr-0.3Ca.

16. The pH value of SBF containing Mg-0.3Sr-0.3Ca increases in the initial stages of degradation due to the dissolution of Mg and the increase in OH⁻ ions in the solution. This value increases very slowly until it reaches the plateau ~ 9.2 in immersion test without SBF renewal. The largest increase in pH value and volume of H₂ released occurs during the initial stage of immersion (day 1).
17. The average degradation rate obtained from the immersion test with daily SBF renewal is slightly higher than the test without SBF renewal. Thus, the high concentration of OH⁻ ions and alkaline pH value in surrounding SBF slightly retards the corrosion of the sample in the test without SBF renewal compared to the test which replenishes the SBF.
18. A product layer consisting of hydroxyapatite and Mg(OH)₂ forms on the surface of Mg-0.3Sr-0.3Ca after 1 day immersion in SBF, which acts as a barrier to further corrosion and leads to a slow biodegradation rate. The formation of this layer is the main reason for slower degradation rate of this sample.
19. The amount of increase in pH value decreases with time of immersion during the immersion test with daily SBF renewal, showing that the product layer that forms on the surface of Mg-0.3Sr-0.3Ca acts as barrier to further corrosion and higher increase in pH value.
20. The Sr-substituted HA phase forms on the alloys due to the dissolution of Sr²⁺ ions from the alloy and their precipitation as Sr-HA on the surface. Corrosion products are more stable and strongly bound on the Mg alloys containing small amounts of Sr (in our study: Mg-0.5Sr and Mg-0.3Sr-0.3Ca).

D. In vitro and in vivo biocompatibility evaluation of Mg-0.3Sr-0.3Ca alloy

The biocompatibility of Mg-0.3Sr-0.3Ca was evaluated as a candidate for cardiovascular stent applications via cytotoxicity assays and 5 weeks implantation in femoral artery of dog, using

WE43 (Mg-4Y-3RE) alloy, previously evaluated as biodegradable Mg stent material in clinical trials, as a control.

21. The viability of the HUVECs cultured in Mg-0.3Sr-0.3Ca increases with exposure to the alloy extracts, implying proliferation and growth of the cells. Mg-0.3Sr-0.3Ca provides better cytocompatibility and promotes viability over longer exposure time (7 days) compared to WE43.
22. The Mg-0.3Sr-0.3Ca stent sample causes no thrombosis and inflammation effect after 5 weeks implantation into the femoral artery. The artery stented with this alloy has completely open lumen with healthy blood flow after the second surgery, whereas WE43 stent thromboses under the same condition and aggregates a huge volume of residues inside the vessel. The artery stented with WE43 was heavily occluded.
23. Microstructural analysis on the material-tissue interface confirms the surface-active effect of Sr that leads to the formation of Sr-substituted hydroxyapatite on the surface of this stent, which is a key advantage in the use of Sr-containing Mg alloys as materials for biodegradable implants.

7. 2. RECOMMENDATIONS FOR FUTURE WORK

1. Strontium surface activity:

- a) It would be a worthwhile endeavor to characterize and quantify Sr-surface activity in Sr-based Mg alloys by analyzing the surface layers of the bulk alloy via XPS.
- b) The surface activity of an element is related to the Wiegner-Seitz Ratio (WSR) of an element with respect to the WSR of the host metal (table below). A surface active element has higher WSR than the host metal. Solute elements are surface active (they concentrate on surface defects) because they decrease the surface or the interface energy of the host metal. When an element is surface active, it can lower the surface tension of the host metal. It is known that among the elements that lower the surface activity of Mg, Sr is the most effective element due to the higher WSR compared to that of Mg. A future study can examine the effects of other elements with WSR larger than Mg_{WSR} , especially Se, which is potentially biocompatible.

Al	Mg	Sr	Ca	Ce	Ni	Nd	Si	Sb	Sn	Se	Fe	Te	Mn	Li
0.15	0.18	0.23	0.21	0.20	0.14	0.20	0.16	0.11	0.19	0.19	0.14	0.21	0.14	0.17

2. The effect of other alloying elements (such as Zn and Mn) can be evaluated on biodegradation behavior of Mg for biomedical applications. Although these elements are not surface active in Mg, however they are biocompatible and may tailor the bio-corrosion of Mg through other mechanisms.

3. Studies on bio-corrosion resistance

A modified set-up can be designed for in vitro immersion capture of all the hydrogen generation.

4. Studies on mechanical properties

Full analysis of the mechanical properties of Mg-0.3Sr-0.3Ca can be undertaken to evaluate the resistance of material to pulsatile radial compression force as well as its bending fatigue.

5. In vivo studies on the bio-compatibility of the Mg-0.3Sr-0.3Ca

Various stent designs can be investigated to test, in animal model, the effects of stent design and to identify optimum stent designs. Long-term in vivo biocompatibility of Mg-0.3Sr-0.3Ca should also be evaluated.

6. Applications

- (i) The use of Mg biodegradable stents is medically important for pediatric patients. Application development activities should be undertaken with pediatric clinics to develop effective devices.
- (ii) Both Ca and Sr are components of human bone. The applications of the alloys can also be extended to orthopedic implants.

CHAPTER 8

CONTRIBUTIONS TO ORIGINAL KNOWLEDGE

This doctoral study gives new perspective into the development of biodegradable alloys with slow corrosion rate, optimal mechanical properties and improved biological performance to be used for temporary cardiovascular implant. Systematic investigations were used to elucidate the role of Sr as a key alloying element in the corrosion mechanism, microstructural evolution, mechanical properties and biological performance of Mg implant. The feasibility of using Sr additional alloying for cardiovascular applications was first evaluated through Mg-Sr binary alloy system. Combined addition of Sr and Ca (another well know element for biodegradable implant applications) was then evaluated in Mg-Sr-Ca ternary system. Mg-0.3Sr-0.3Ca showed better bio-corrosion resistance, mechanical properties and biological performance compared to all other ternary Mg-Sr-Ca and binary Mg-Sr and Mg-Ca alloys. The main contributions of this study are:

Mg-Sr alloys

Bio-corrosion resistance

1. The notion of the surface activity of Sr in Mg was utilized to develop bio-corrosion resistant Mg alloys. *The positive outcome of this study opens a new direction in Mg alloy development; specifically, the use of effective surface active elements (Sr and others) can contribute to a wide range of research related to developing corrosion resistant Mg alloys.*
2. The compositional dependence of the bio-corrosion resistance of Mg-Sr alloys was determined. The micro-galvanic effect of the Mg₁₇Sr₂ second phase was identified as a limiting factor for the Sr addition level. *Such microstructure and phase dependence will provide important insight for the development of bio-corrosion resistant Mg alloys.*

3. The in-situ generation of a Sr-modified hydroxyapatite during contact with body fluid was discovered for the first time. Its beneficial effect on bio-corrosion resistance was observed. *This finding is of profound importance for the development of bio-corrosion resistant Mg alloys. It underlines the advantage of incorporating Sr additions in Mg alloys to generate a bio-corrosion resistant coating.*

Bio-compatibility

4. The positive effect of Sr on improving the viability of vascular cells was determined for the first time. This can be related to Sr being part of the human body. *It paves the way for using Mg-Sr based alloys for many biodegradable implant applications, such as cardiovascular and orthopedic implants.*
5. Enhanced biocompatibility of Mg-Sr alloys was observed in comparison to rare-earth-containing WE43 commercial alloy in in vivo testing. *This finding can guide the development of new biodegradable Mg alloys, of interest to major bio-companies.*

Mg-Sr-Ca alloys

Bio-corrosion resistance

6. Two surface active elements, Sr and Ca, were added in combination to develop a bio-corrosion resistant Mg alloy. It was seen that presence of Sr led to the in-situ development of a Sr-substituted hydroxyapatite. *This work showed that Sr consistently develops a Sr-HA layer on Mg alloys.*
7. In-situ formation of a thin layer of Sr-substituted HA was observed for the first time in animal study. This layer protects the surface of the implant and prevents fast degradation rates. *This finding shows a good match between in vitro and in vivo results, and the consistent formation of a Sr-HA layer both in vitro and in vivo.*
8. The idea of the third element effect, i.e. the effectiveness of an element at a lower level in making an alloy noble when it is combined with another element, was successfully used and confirmed in the Mg-0.3Sr-0.3Ca alloy. *This finding will help the development of cardiovascular implant alloys; Ca is an important alloying addition for Mg but at high levels is not well tolerated in the cardiovascular system. In the binary Mg-Ca alloys, Ca improves the bio-corrosion resistance at 0.6 wt.%, but in combination with Sr (the third element), its optimum alloying level is halved to 0.3 wt.%. The idea of the third element effect will be*

important in developing corrosion resistant alloys in general where elements cannot be used at high levels for various reasons, ranging from toxicity to cost.

9. The microstructures of the ternary Mg-Sr-Ca was systematically investigated; in the as-cast condition of the Mg-0.3Sr-0.3Ca alloy, a new Sr-Ca intermetallic phase was discovered. The crystal structure of new phase was determined via TEM analysis; it is hcp with lattice parameters $a = 6.42\text{\AA}$ and $c = 9.44\text{\AA}$. This is a new phase designated as a Ca-Sr(Mg) with Ca/Sr ratio 3/2 and its crystal structure is different from the binary $\text{Mg}_{17}\text{Sr}_2$ or Mg_2Ca found in the binary alloys and the Ca-Sr compounds previously known and listed by Pearson. The phase is likely metastable and forms under non-equilibrium conditions. It exists in a globular and dispersed morphology in the alloy, 1.5-2.0 μm in size, showing beneficial effects both on the bio-corrosion resistance and on the mechanical properties of the Mg-0.3Sr-0.3Ca alloy, due to its fine dispersion as well as its different chemical nature. *This finding establishes the Mg-Sr-Ca system as an alternative to Al-containing alloys for different applications. Also, it improves the microstructural knowledge of these alloys thus potentially helping future thermodynamic simulations, which are now limited to the equilibrium phases.*
10. The new Ca-Sr phase shows relatively good metallurgical stability in thermal treatment but transforms to the equilibrium phases during prolonged thermal exposure at 400 °C, leading to some property loss. *This highlighted the importance of having the Mg-Sr-Ca implant with the as-cast microstructure. Optimum manufacturing conditions for Mg-0.3Sr-0.3Ca, using lower temperatures and shorter times, maintains the enhanced mechanical properties during implantation and in-service mechanical performance of the implant. This is contrary to the mainstream idea of using thermo-mechanical processing to manufacture Mg-based implants.*

Bio-compatibility

11. The positive influence of Mg alloys with small amounts of Sr and Ca on viability of HUVECs was studied for the first time. Mg-0.3Sr-0.3Ca enhances the viability of the cells and shows better viability with longer exposure time. A low level of Sr and Ca does not affect the viability of these cells. *This finding is contrary to the idea of avoiding Ca-containing alloys for cardiovascular applications and paves the way for using Mg-Sr-Ca alloys for many biodegradable applications, such as cardiovascular and orthopedic implants.*

12. In vivo performance of Mg-Sr-Ca alloy as cardiovascular stent was evaluation for the first time in animal study. The new alloy developed in this study, Mg-0.3Sr-0.3Ca, shows good biological performance and performs better than the conventional alloy WE43, evaluated by major bio-companies for cardiovascular implant use. Specifically, it has higher potential to minimize the risk of thrombosis. *Similarly to what mentioned before, this result will help the development of biodegradable Mg alloys by major bio-companies.*